COUPLED DYNAMIC ANALYSIS OF MULTIPLE UNIT FLOATING OFFSHORE WIND TURBINE

A Dissertation

by

YOON HYEOK BAE

Submitted to the Office of Graduate Studies of
Texas A&M University
in partial fulfillment of the requirements for the degree of

DOCTOR OF PHILOSOPHY

Approved by:

Chair of Committee,	Moo-Hyun Kim
Committee Members,	John Niedzwecki
	Jun Zhang
	Alan Palazzolo
Head of Department,	John Niedzwecki

May 2013

Major Subject: Ocean Engineering

ABSTRACT

In the present study, a numerical simulation tool has been developed for the rotor-floater-tether coupled dynamic analysis of Multiple Unit Floating Offshore Wind Turbine (MUFOWT) in the time domain including aero-blade-tower dynamics and control, mooring dynamics and platform motion. In particular, the numerical tool developed in this study is based on the single turbine analysis tool FAST, which was developed by National Renewable Energy Laboratory (NREL). For linear or nonlinear hydrodynamics of floating platform and generalized-coordinate-based FEM mooring line dynamics, CHARM3D program, hull-riser-mooring coupled dynamics program developed by Prof. M.H. Kim's research group during the past two decades, is incorporated. So, the entire dynamic behavior of floating offshore wind turbine can be obtained by coupled FAST-CHARM3D in the time domain. During the coupling procedure, FAST calculates all the dynamics and control of tower and wind turbine including the platform itself, and CHARM3D feeds all the relevant forces on the platform into FAST. Then FAST computes the whole dynamics of wind turbine using the forces from CHARM3D and return the updated displacements and velocities of the platform to CHARM3D.

To analyze the dynamics of MUFOWT, the coupled FAST-CHARM3D is expanded more and re-designed. The global matrix that includes one floating platform and a number of turbines is built at each time step of the simulation, and solved to obtain the entire degrees of freedom of the system. The developed MUFOWT analysis tool is

able to compute any type of floating platform with various kinds of horizontal axis wind turbines (HAWT). Individual control of each turbine is also available and the different structural properties of tower and blades can be applied. The coupled dynamic analysis for the three-turbine MUFOWT and five-turbine MUFOWT are carried out and the performances of each turbine and floating platform in normal operational condition are assessed. To investigate the coupling effect between platform and each turbine, one turbine failure event is simulated and checked. The analysis shows that some of the malfunction of one turbine in MUFOWT may induce significant changes in the performance of other turbines or floating platform. The present approach can directly be applied to the development of the remote structural health monitoring system of MUFOWT in detecting partial turbine failure by measuring tower or platform responses in the future.

DEDICATION

This dissertation is dedicated, with love and respect, to my parents.

ACKNOWLEDGEMENTS

First and foremost, I would like to warmly express sincere appreciation to my advisor, Professor Moo-Hyun Kim, for his continuous support, invaluable advice, and warm encouragement throughout the course of this research. His insight and comments always helped me complete this thesis.

I would like to thank my committee members, Dr. Niedzwecki, Dr. Zhang, and Dr. Palazzolo, for their guidance and support throughout the course of this research.

I also want to extend my gratitude to the American Bureau of Shipping (ABS) for their technical and financial support and the National Renewable Energy Laboratory (NREL) for their essential resources during my Ph.D. study. Thanks also go to my friends and colleagues and the department faculty and staff for making my time at Texas A&M University a great experience.

Finally, thanks to my parents, parents-in-law and my sister's family for their love and encouragement and to my wife J.Y. Kim, for her patience and love.

TABLE OF CONTENTS

Page

LIST OF FIGURES

Page

LIST OF TABLES

Page

1. INTRODUCTION

1.1 Background and Literature Review

During the past century, people have depended on fossil fuels as their major source of energy. However, fossil fuels continue to be depleted and their negative environmental impact is very alarming. Therefore, the importance of increasing the use of clean renewable energy cannot be over emphasized for the secure future of all human beings. As a result, the number of wind turbines has rapidly increased all around the world. Wind energy resources have many benefits. The first and most important benefit is that wind energy is economically competitive. Today's rising oil and gas prices are a serious threat to the economies and industries in the United States, so building a new wind plant is the most competitive way to produce a new electricity generation source. Unlike most other energy resources, wind turbines do not consume water while fossil fuel and nuclear energy plants require large amounts of water for their cooling systems. Wind energy is inexhaustible and infinitely renewable and does not produce any carbon emissions.

As can be seen in Figure 1.1, the global cumulative wind energy capacity gradually increased over the year, and reached 237.7GW in 2011. The turbine size is also growing as the capacity increases in Figure 1.2. In the 1990's, the largest turbine produced 2MW and the diameter of the rotor was approximately 80m. Recently, the capacity has increased up to 8 ~ 10MW and the size of rotors has doubled to around 160m.

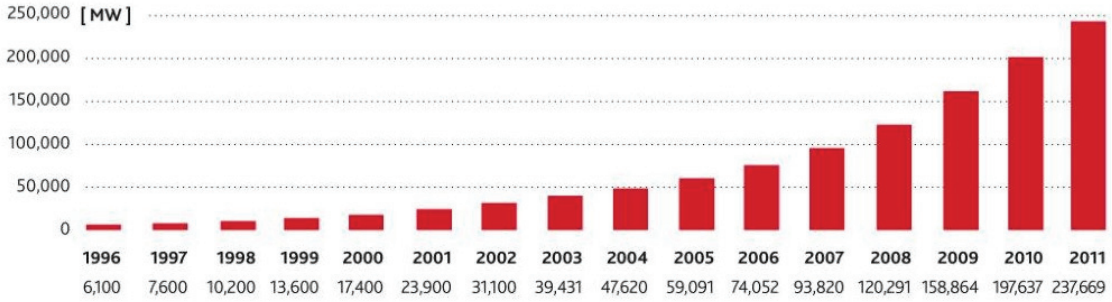

Figure 1.1 Global cumulative installed wind capacity (Global Wind Energy Council, 2011)

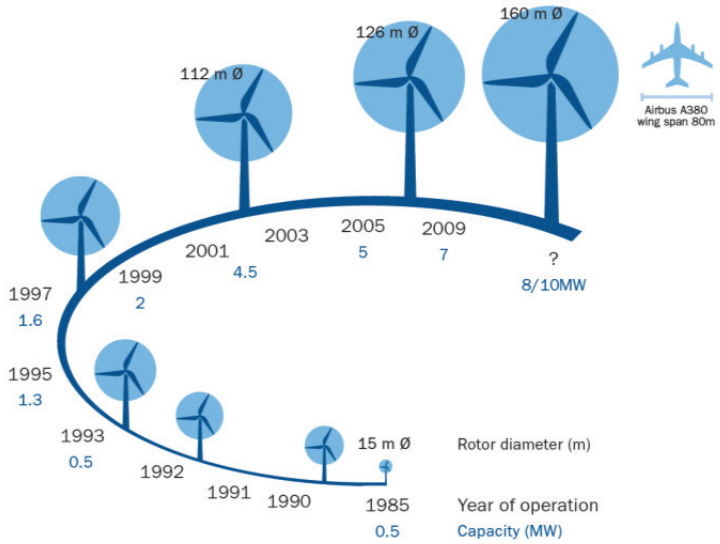

Figure 1.2 Size evolution of wind turbines over time (EWEA, 2010)

In the case of the United States, 5,116MW of wind power was created in 2010 and over 5,600MW of wind power is currently under construction. Total U.S. wind installations stand at 40,181MW, which represents 21% of global wind capacity. Furthermore, the U.S. government expects that wind energy will produce 20% of total energy by 2030. To implement the 20% wind scenario, new wind power installations

would increase to more than 16,000MW per year by 2018, and continue at that rate through 2030 as shown in Figure 1.3.

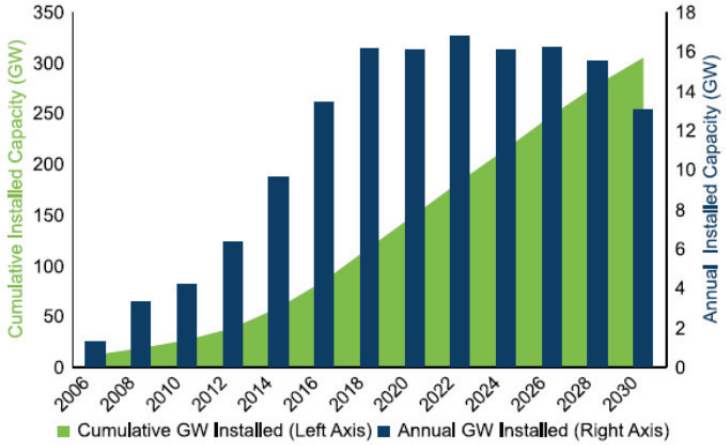

Figure 1.3 Annual and cumulative wind installations by 2030 in the U.S. (Courtesy of http://www.20percentwind.org/)

However, the on-land wind farms also have many negative features such as lack of available space, noise restriction, shade, visual pollution, limited accessibility in mountainous areas, community opposition, and regulatory problems. Therefore, many countries in Europe have started to build wind turbines in coastal waters, and so far most offshore wind farms have been installed in relatively shallow-water areas less than 40m deep by using bottom-fixed-type base structures.

Recently, several countries have started to plan offshore floating wind farms. Although they are considered to be more difficult to design, wind farms in deeper waters are, in general, less sensitive to space availability, noise restriction, visual pollution, and regulatory problems. They are also exposed to much stronger and steadier wind fields to

become more effective. Furthermore, in designing these floating wind farms, the existing technology and experience of offshore industry used for petroleum production has been helpful. In this regard, if technology and infrastructure is fully developed, offshore floating wind farms are expected to produce huge amounts of clean electricity at competitive prices compared to other energy sources (Henderson et al., 2002; Henderson et al., 2004; Musial et al., 2004; Tong, 1998; Wayman et al., 2006). Possible disadvantages of floating type wind farms include the complexity of blade controls due to platform motion, and a larger inertia loading on the tall tower caused by greater floater accelerations, etc. They are also directly exposed to the open ocean without any natural protection so they may have to endure harsher environments.

On the other hand, there are also merits of floating bases compared to fixed bases in the dynamic/structural point of view. In case of fixed offshore wind turbines (OWTs), the high-frequency excitations caused by rotating blades and tower flexibility may cause resonance at the system's natural frequencies. This is particularly so as water depth increases which may significantly shorten its fatigue life. For floating wind turbines, however, their natural frequencies of 6-DOFs motion are typically much lower than those rotor-induced or tower-flexibility-induced excitations (Roddier et al., 2009), so the possibility of dynamic resonance with the tower and blades is much less (Jonkman and Sclavounos, 2006; Withee, 2004). The TLP-type OWT is one exception (Bae et al., 2010; Jagdale and Ma, 2010). TLP-types are much stiffer in the vertical-plane modes compared to other floating wind turbines, so the effects of such high-frequency excitations from the tower and blades need to be checked.

Another concept for floating offshore wind farms is the Multiple Unit Floating Offshore Wind Turbine (MUFOWT). This model includes multiple turbines upon a single floating platform rather than the typical concept of the floating offshore wind turbine (FOWT) where each turbine has its own floating platform. The possible advantages and disadvantages of MUFOWT over single floating turbine were checked (Barltrop, 1993), and an effort was made to develop analytical tools for evaluating the performance of multiple turbine wind farm was made (Henderson et al., 1999)

Compared to the single unit floating wind turbine, MUFOWT has several advantages. It may reduce installation cost because only one mooring system is necessary for multiple turbines. From a stability point of view, MUFOWT provides a more stable condition than a single unit structure. This characteristic also enables higher towers and better energy capture. Better platform response in random sea environments can also be ensured because larger floating units usually tend to have less response. The easy access to MUFOWT is also one of the advantages compared to the single turbine unit. A larger floating platform may be equipped with a helicopter landing deck, so access by air can be available. On the other hand, there are also several disadvantages of the MUFOWT concept. One of the most serious problems is the interference between turbines, and possibility of performance drop due to the shade effect of the blades or tower. This disadvantage can be overcome by adopting a specific design of floater or arrangement of turbines. In some point, weathervaning design of floater is necessary to avoid excessive interference between turbines. In addition to the interference problem,

the MUFOWT is not suitable for shallow water area, because mooring design and power transport in shallow water depth will be difficult.

At the earlier stage of research about MUFOWT, such a large floating structure and multiple turbines are not regarded as cost-effective. However, technological developments and recent trends in the rapid increase in size of wind turbines make this concept more viable.

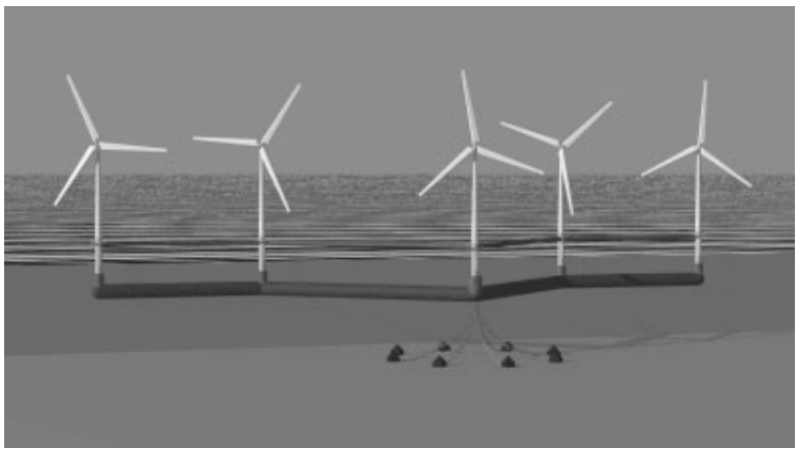

Figure 1.4 Concept design of Semi-submersible type MUFOWT (Henderson and Patel, 2003)

Figure 1.4 shows an example of a semi-submersible type MUFOWT which is suggested by a research project conducted by University College London (Henderson and Patel, 2003). This MUFOWT concept has five turbines upon on large semi-submerged pontoon. In order to minimize wave loads and the resulting platform motion, the main structure is located below the sea surface. It also has one turret mooring system at the center of the structure, and each turbine is located symmetrically about the anchor

position. This mooring concept enables the whole structure to rotate so that the series of turbines face the wind direction.

Similar semi-submersible types, but with different hull forms are also suggested (Henderson et al., 2000). Both weathervaning and non-weathervaning vessels are suggested as shown in Figure 1.5. As pointed out earlier, the weathervaning vessel always faces into the wind so a relatively expensive turret mooring system is required. On the other hand, a non-weathervaning model cannot rotate to face into the wind, and the possibility of wake interference from another turbine is very high. However, this model is more cost-effective compared to the weathervaning model. In order to compromise minimal fatigue loads and minimum pontoon cost, one of the fractal designs was recommended.

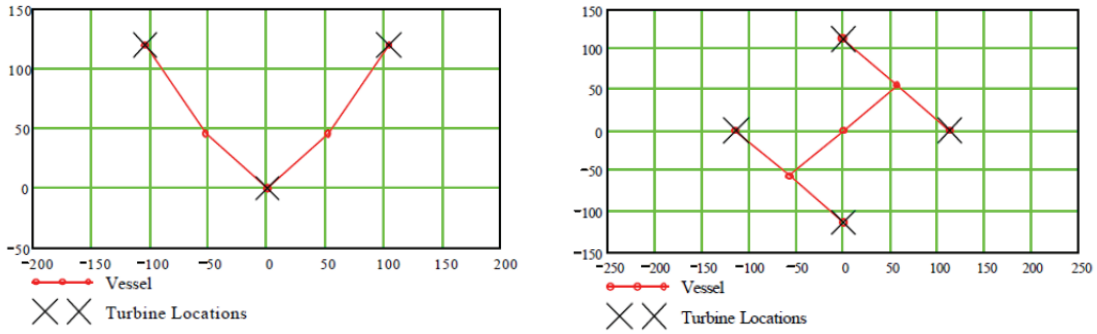

(a) Weathervaning model (b) Non-weathervaning model

Figure 1.5 Semi-submersible type MUFOWT (Henderson et al., 2000)

Recently, research concerning the feasibility for three turbines on one floating unit was carried out, and the model tests were performed (Lefranc and Torud, 2011). As can be seen in Figure 1.6, the proposed model has three inclined towers and the mooring

lines are connected to a turret at the vessel's geometric center. This research showed that the concept design proved to be feasible in water depth from 45m and deeper. Regarding cost effectiveness, the concept is comparable to today's solution when it comes to the cost of energy production.

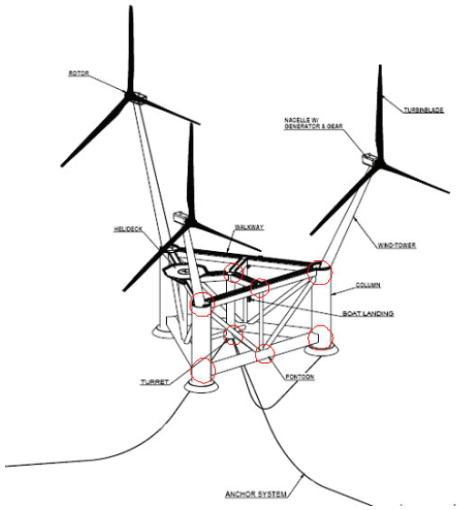

Figure 1.6 Next generation wind farm (Courtesy of http://www.windsea.no/)

1.2 Objective and Scope

The main objective of this research is to develop a coupled dynamic analysis tool for MUFOWT. As mentioned earlier, an analysis tool for large floating offshore wind farms was developed (Henderson, 2000) in the state/frequency domain and several different designs of MUFOWT were suggested. The developed tools were primarily used to obtain motion responses and loads for several locations of platform structures. However, these analysis tools did not include the mooring line analysis tool, hence the dynamic coupling effect between hull and mooring lines could not be accounted for.

Moreover, the turbine model used in those analysis tools was able to estimate fatigue damage but did not consider elasticity of tower and blades; this is proved to be very important to the response of turbine and platform. So, the effectiveness of analysis tools in this research was very limited.

Another design code which has been developed for years in the U.S. wind energy industry is FAST. The National Renewable Energy Laboratory (NREL) and its academic and industry partners have created aero-elastic simulators for horizontal axis wind turbines for both two- and three-bladed turbines. This design code was initially developed with a built-in aerodynamics code (Wilson et al., 1995) and later merged with the AeroDyn subroutine library of rotor-aerodynamics routines developed by NREL to compute the aerodynamic forces on the turbine blades (Wilson et al., 2000). Recently, FAST has been updated to accommodate a greater degree of freedom of turbines and hydrodynamic calculations for floating offshore wind turbines (Jonkman and Buhl Jr, 2005). So far, many of the wind energy industries in the world have used this FAST design code to evaluate their turbines and the code has been verified by the world's foremost certifying body for wind turbines, Germanischer Lloyd (GL) WindEnergie GmbH, located in Hamburg, Germany (Manjock, 2005). Since FAST can model many common turbine configurations and flexible elements using modal representation and analyze in the time domain, it is considered to be the most advanced design code in the wind energy industry to date.

However, the most up-to-date version of FAST has been optimized for land-based turbines or single-turbine floating wind farm analysis, so direct use of FAST for

analyzing MUFOWT is impossible. Furthermore, the hydrodynamic module inside FAST has several limitations and the mooring module can deal only with the quasi-static model of lines, so the dynamic behavior of mooring lines cannot be calculated during time domain simulation.

For this reason, a portion of the FAST algorithm is implemented into the floater-mooring coupled dynamic analysis program, CHARM3D, and vice versa so that the tower-floater coupling can be accurately achieved. By combining FAST and CHARM3D, the wind turbine design code FAST can include a more efficient hydrodynamic module and finite element dynamic mooring line module at the same time.

To achieve the objectives of this study, the combined design code FAST-CHARM3D will be extended in order to accommodate multiple turbines on a single floating platform. Of course, multiple turbine dynamics should be solved simultaneously with the time marching scheme as done by single turbine analysis. The research and development works which will be covered in this thesis will include

- Dynamic coupling between FAST and CHARM3D
- Development of coupled dynamic analysis tools for MUFOWT
- Design verification of MUFOWT platforms in time domain
- Dynamic load analysis in turbine failure conditions.

2. WAVE LOADS ON FLOATING PLATFORM

2.1 Introduction

In this section the wave loads and dynamic responses of floating platform are reviewed. In the beginning, the wave theory of first order is reviewed, and the review of diffraction theory with first order potential force and moment on floating platform follows. Finally, the Morison's formula for inertia and drag force in the time domain will be also presented.

2.2 Wave Theory

To derive wave theory, Boundary Value Problem (BVP) with proper kinematic and dynamic boundary conditions needs to be solved. The governing equation of fluid with assumption of irrotational, incompressible and inviscid properties can be defined by Laplace's equation:

$$\nabla^2 \Phi = 0 \tag{2.1}$$

To solve the Laplace equation, the proper boundary conditions in the domain should be defined. The common boundary conditions for ocean water wave problems are introduced and explained. On the free surface, water waves should satisfy two boundary conditions; kinematic and dynamic boundary conditions. The kinematic boundary condition indicates that water particles on the free surface should remain on the free surface and be formulated as below.

$$\frac{\partial \eta}{\partial t} + u\frac{\partial \eta}{\partial x} + v\frac{\partial \eta}{\partial y} - \frac{\partial \Phi}{\partial t} = 0 \qquad \text{at } z = \eta(x, y, t) \tag{2.2}$$

where $\eta(x, y, t)$ is the free surface elevation written in the spatial and time domain. The dynamic free surface boundary condition states that the pressure on the free surface must be the same as the atmospheric pressure and be constant along the free surface.

$$\rho\frac{\partial \Phi}{\partial t} + \frac{1}{2}\left(\Phi_x^2 + \Phi_y^2 + \Phi_z^2\right) + \rho g z = 0 \qquad \text{at } z = \eta(x, y, t) \tag{2.3}$$

For bottom boundary condition, the vertical component of velocity of fluid particle at the ocean bottom is zero and formulated as below.

$$\frac{\partial \Phi}{\partial z} = 0 \qquad \text{at } z = -d \tag{2.4}$$

where d is water depth. This boundary condition represents that the water particles at the bottom cannot penetrate the ocean bottom.

The exact solution of the Laplace equation with the given boundary conditions above is difficult to obtain due to nonlinear terms of the free surface boundary conditions. So the perturbation method with small wave amplitude assumption can be used to obtain an approximated solution of a certain order of accuracy. The following equations show the first and second order velocity potentials and free surface elevations.

First order velocity potential and free surface elevation:

$$\Phi^{(1)} = \mathrm{Re}\left[-\frac{igA}{\omega}\frac{\cosh k(z+d)}{\cosh kd}e^{i(kx\cos\theta + ky\sin\theta - \omega t)}\right] \tag{2.5}$$

$$\eta^{(1)} = A\cos(kx\cos\theta + ky\sin\theta - \omega t) \tag{2.6}$$

Second order velocity potential and free surface elevation:

$$\Phi^{(2)} = \mathrm{Re}\left[-\frac{3}{8}\omega A^2 \frac{\cosh 2k\left(z+d\right)}{\sinh^4 kd} e^{i(2kx\cos\theta+2ky\sin\theta-2\omega t)} \right] \tag{2.7}$$

$$\eta^{(2)} = A^2 \frac{\cosh kd}{\sinh^3 kd} \cos\left(2kx\cos\theta + 2ky\sin\theta - 2\omega t\right) \tag{2.8}$$

where A is the wave amplitude, ω is the wave frequency, k is the wave number, and θ is the incident wave heading angle.

In a random sea environment, a fully developed wave condition can be modeled as wave spectra by summation of regular wave trains and random phases. In the ocean engineering field, various wave spectra such as JONSWAP (Joint North Sea Wave Observation Project) and Pierson-Moskowitz are proposed and used. The simulated random wave time series from the given wave spectrum $S(\omega)$ can be expressed by superposition of a large number of linear wave components with random phases.

$$\eta\left(x,t\right) = \sum_{i=1}^{N} A_{\,i} \cos\left(k_i x + \omega_i t + \varepsilon_i\right) = \mathrm{Re}\left[\sum_{i=1}^{N} A_i e^{i(k_i x - \omega_i t + \varepsilon_i)} \right] \tag{2.9}$$

$$A_i = \sqrt{2S(\omega_i)\Delta\omega} \tag{2.10}$$

where, N and $\Delta\omega$ are the number of wave components and intervals of frequency division, and ε_i is a random phase angle generated by random function. To avoid the repetition of random wave realization with a limited number of wave components, some modification was made and re-written as below.

$$\eta(x,t) = \mathrm{Re}\left[\sum_{i=1}^{N} A_i e^{i(k_i x - \omega_i' t + \varepsilon_i)} \right] \tag{2.11}$$

where $\omega_i^{'} = \omega_i + \delta\omega_i$ and $\delta\omega_i$ is the random perturbation number uniformly distributed between $-\Delta\omega/2$ and $\Delta\omega/2$.

2.3 Wave Loads on Structures

It is important to predict wave loads on a structure in studying the dynamics of the floating platform. In deeper water, the diffraction of waves around the platform is significant. So, the diffraction theory is the most appropriate way to describe the wave loading on the platform. In case of a slender body, Morison's formula is also widely used. In extreme environmental conditions, viscous force may become important and should be taken into consideration. In this section, both the diffraction theory and Morison's formula are discussed and these will be used to compute the wave load in our study.

2.3.1 Diffraction and Radiation Theory

To see the interaction between incident waves and large floating structures, the boundary value problem is reviewed in this section. As we already mentioned, the total velocity potential Φ satisfies Laplace equations, free surface boundary conditions, and the bottom boundary condition. This total velocity potential Φ includes the incident potential Φ_I, diffraction potential Φ_D and radiation potential Φ_R and can be expressed by a perturbation series with respect to the wave slope parameter ε

$$\Phi = \sum_{n=1}^{\infty} \varepsilon^n \Phi^{(n)} = \sum_{n=1}^{\infty} \varepsilon^n \left(\Phi_I^{(n)} + \Phi_D^{(n)} + \Phi_R^{(n)} \right) \tag{2.12}$$

where, $\Phi^{(n)}$ represents the nth order solution of Φ, and solutions up to second order will be considered in this study.

To solve the wave and floating body interaction problem, an additional boundary condition, which is called body boundary condition, should also be considered. By introducing surface normal vector $\mathbf{n}$, the body boundary condition can be expressed as

$$\frac{\partial \Phi}{\partial \mathbf{n}} = V_n \qquad \text{on body surface} \tag{2.13}$$

where, V_n is the normal velocity vector of the body at its surface.

In addition, the diffraction (Φ_D) and radiation potential (Φ_R) also should satisfy the Sommerfeld radiation condition at the far field boundary.

$$\lim_{r\to\infty} \sqrt{r}\left(\frac{\partial \Phi_{D,R}}{\partial r} \pm ik\Phi_{D,R}\right) = 0 \tag{2.14}$$

where, r is the radial distance from the center of the floating body.

2.3.2 First Order Boundary Value Problem

The first order interaction of a monochromatic incident wave with a freely floating body will be reviewed in this section. The first order potential can be re-written by separating the time dependency explicitly as

$$\Phi^{(1)} = \varepsilon\left(\Phi_I^{(1)} + \Phi_D^{(1)} + \Phi_R^{(1)}\right) = \mathrm{Re}\left\{\left[\phi_I^{(1)}(x,y,z) + \phi_D^{(1)}(x,y,z) + \phi_R^{(1)}(x,y,z)\right]e^{-i\omega t}\right\} \tag{2.15}$$

The first order incident potential $\phi_I^{(1)}$ is the linear wave potential re-written as

$$\phi_I^{(1)}(x,y,z) = \mathrm{Re}\left[-\frac{igA}{\omega}\frac{\cosh(k(z+d))}{\cosh(kd)}e^{i\mathbf{k}\cdot\mathbf{x}}\right] \tag{2.16}$$

where, $\mathbf{K}$ is a vector wave number with Cartesian components $(k\cos\theta, k\sin\theta, 0)$, and $\mathbf{x}$ is the position vector in the fluid. Here θ is the angle of the incident wave relative to the positive x axis.

So, the boundary value problem governing the first order diffraction and radiation potentials can be summarized as

$$\nabla^2\phi_{D,R}^{(1)} = 0 \qquad \text{in the fluid } (z<0) \tag{2.17}$$

$$\left(-\omega^2 + g\frac{\partial}{\partial z}\right)\phi_{D,R}^{(1)} = 0 \qquad \text{on the free surface } (z=0) \tag{2.18}$$

$$\frac{\partial\phi_{D,R}^{(1)}}{\partial z} = 0 \qquad \text{on the bottom } (z=-d) \tag{2.19}$$

$$\frac{\partial\phi_{R}^{(1)}}{\partial n} = -i\omega\mathbf{n}\cdot\left(\boldsymbol{\xi}^{(1)} + \boldsymbol{\alpha}^{(1)}\times\mathbf{r}\right) \qquad \text{on the body surface} \tag{2.20}$$

$$\lim_{r\to\infty}\sqrt{r}\left(\frac{\partial}{\partial r} \pm ik\right)\phi_{D,R}^{(1)} = 0 \qquad \text{at far field} \tag{2.21}$$

where $\mathbf{r}$ represent the position vector on the body surface, r is the radial distance from the origin and $\mathbf{n}$ is the unit normal vector pointing into the fluid domain at the body surface. The first-order motion of the body in the translational ($\Xi^{(1)}$) and rotational ($\Theta^{(1)}$) directions have the forms

$$\Xi^{(1)} = \mathrm{Re}\left\{\boldsymbol{\xi}^{(1)}e^{-i\omega t}\right\} \qquad \boldsymbol{\xi}^{(1)} = \left\{\xi_1^{(1)}, \xi_2^{(1)}, \xi_3^{(1)}\right\} \tag{2.22}$$

$$\Theta^{(1)} = \mathrm{Re}\left\{\boldsymbol{\alpha}^{(1)}e^{-i\omega t}\right\} \qquad \boldsymbol{\alpha}^{(1)} = \left\{\alpha_1^{(1)}, \alpha_2^{(1)}, \alpha_3^{(1)}\right\} \tag{2.23}$$

where the subscripts 1,2 and 3 denote the translational (surge, sway and heave) and rotational (roll, pitch and yaw) modes with respect to the x, y and z axes respectively. The six degrees of freedom of first order motion can be also simplified as

$$\zeta_i = \xi_i^{(1)} \qquad \text{for } i = 1,2,3 \tag{2.24}$$

$$\zeta_i = \alpha_{i-3}^{(1)} \qquad \text{for } i = 4,5,6 \tag{2.25}$$

Based on that motion, the radiation potential, which represents the fluid disturbance due to the motion of the body, can be further decomposed as

$$\phi_R^{(1)} = \sum_{i=1}^{6} \zeta_i \phi_i^{(1)} \tag{2.26}$$

where ϕ_i represent the first order velocity potential of the rigid body motion with unit amplitude in the ith mode without incident waves. The body boundary condition of each mode can be also expressed by replacing $\phi_i^{(1)}$

$$\frac{\partial \phi_i^{(1)}}{\partial n} = n_i \qquad i = 1,2,3 \tag{2.27}$$

$$\frac{\partial \phi_i^{(1)}}{\partial n} = \left(\mathbf{r} \times \mathbf{n}\right)_{i-3} \qquad i = 4,5,6 \tag{2.28}$$

on the body surface.

The first order diffraction potential $\phi_D^{(1)}$ represents the disturbance to the incident wave due to the presence of the body in its fixed position. This velocity potential should satisfy the body surface boundary condition below.

$$\frac{\partial \phi_D^{(1)}}{\partial n} = -\frac{\partial \phi_I^{(1)}}{\partial n} \qquad \text{on the body surface} \tag{2.29}$$

2.3.3 First Order Potential Forces

Now, the first order hydrodynamic potential force on the floating structure can be obtained by solving the first order diffraction ($\phi_D^{(1)}$) and radiation ($\phi_R^{(1)}$) potentials. By adopting the perturbation method, the hydrodynamic pressure $P(t)$ can be expressed as

$$P^{(1)} = -\rho \frac{\partial \Phi^{(1)}}{\partial t} \tag{2.30}$$

The total force and moment on the body can be directly obtained by simple integration over the instantaneous wetted body surface $S(t)$.

$$\mathbf{F}(t)_i = \begin{cases} \iint_{S_b} P n_i dS & i = 1,2,3 \\ \iint_{S_b} P(\mathbf{r} \times \mathbf{n})_i \, dS & i = 4,5,6 \end{cases} \tag{2.31}$$

where, S_b is the body surface at rest.

The first order total force and moment including the hydrostatic term can now be expressed as

$$\mathbf{F}^{(1)} = \mathbf{F}_{HS}^{(1)} + \mathbf{F}_R^{(1)} + \mathbf{F}_{EX}^{(1)} \tag{2.32}$$

where subscript HS represents the hydrostatic restoring force and moment, R represents the force and moment from the radiation potential, and EX represents the wave exciting force and moment from the incident and diffraction potentials.

The hydrostatic restoring force and moment ($\mathbf{F}_{HS}^{(1)}$) are induced by hydrostatic pressure change due to the motion of the body. It can be expressed as

$$\mathbf{F}_{HS}^{(1)} = -\mathbf{K}\{\zeta^{(1)}\} \tag{2.33}$$

where, $\zeta^{(1)}$ is the first order motion of the floating body, and $\mathbf{K}$ represents the hydrostatic restoring stiffness.

The force and moment from the radiation potential ($\mathbf{F}_R^{(1)}$) comes from the first order motions of the floating body. The radiation potential ($\phi_R^{(1)}$) induces the added mass and radiation damping, and it can be expressed as

$$\mathbf{F}_R^{(1)} = \mathrm{Re}\left(\left[\mathbf{f}\right]\left\{\zeta^{(1)}\right\}\right) \tag{2.34}$$

where

$$\mathbf{f} = f_{ij} = -\rho\iint_{S_B}\frac{\partial\phi_i}{\partial n}\phi_j dS \qquad i,j = 1,2,\cdots,6 \tag{2.35}$$

The set of coefficients f_{ij} is complex and the real and imaginary parts are dependent on the frequency ω . The coefficients can be re-written as

$$f_{ij} = -\omega^2 M_{ij}^a - i\omega C_{ij} \tag{2.36}$$

So, the force and moment from the radiation potential can be expressed as

$$\mathbf{F}_R^{(1)} = \mathrm{Re}\left(\left[\mathbf{M}^a\right]\left\{\ddot{\zeta}^{(1)}\right\} + \left[\mathbf{C}\right]\left\{\dot{\zeta}^{(1)}\right\}\right) \tag{2.37}$$

where, $\mathbf{M}^a$ is the added mass coefficients and $\mathbf{C}$ is the radiation damping coefficients.

The last term $\mathbf{F}_{EX}^{(1)}$ represents the first order wave excitation forces and moments, which are derived by incident and diffraction wave potentials. It can be written as

$$\mathbf{F}_{EX}^{(1)} = \mathrm{Re}\left\{-\rho A e^{-i\omega t}\iint_{S_0}\left(\phi_I + \phi_D\right)\frac{\partial\phi_j}{\partial n}dS\right\} \qquad j = 1,2,\cdots,6 \tag{2.38}$$

where, A is wave amplitude. It is seen that the first order wave excitation forces and moments are proportional to wave amplitude which is frequency dependent. The first order wave exciting force from the unit wave amplitude is called Linear Transfer Function (LTF) which represents the relationship between incident wave elevation and the first order diffraction forces on the floating body.

2.3.4 Wave Loads in Time Domain

In this section, the time domain realization of the first and second wave forces and moments in a random sea environment will be presented. The first and second order hydrodynamic forces and moments on a body due to stationary Gaussian random seas can be expressed as a two-term Volterra series in the time domain as below

$$\mathbf{F}^{(1)}(t)+\mathbf{F}^{(2)}(t)=\int_{-\infty}^{\infty}h_1(\tau)\eta(t-\tau)d\tau+\int_{-\infty}^{\infty}\int_{-\infty}^{\infty}h_2(\tau_1,\tau_2)\eta(t-\tau_1)\eta(t-\tau_2)d\tau_1 d\tau_2 \quad (2.39)$$

where $\eta(t)$ is the ambient wave free surface elevation at a reference position, $h_1(\tau)$ is the linear impulse response function, and $h_2(\tau_1,\ \tau_2)$ is the quadratic impulse response function. The above equation can be rewritten in the form of the summation of the N frequency components as follows

$$\mathbf{F}_I^{(1)}(t)=\mathrm{Re}\left[\sum_{j=1}^{N}A_j\mathbf{L}(\omega_j)e^{i\omega t}\right] \quad (2.40)$$

$$\mathbf{F}_I^{(2)}(t)=\mathrm{Re}\left[\sum_{j=1}^{N}\sum_{k=1}^{N}A_jA_k^{*}\mathbf{D}(\omega_j,-\omega_k)e^{i\omega^{-}t}+\sum_{j=1}^{N}\sum_{k=1}^{N}A_jA_k\mathbf{S}(\omega_j,\omega_k)e^{i\omega^{+}t}\right] \quad (2.41)$$

where $\mathbf{L}(\omega_j)$ represents the linear force transfer function (LTF), and $\mathbf{D}(\omega_j, -\omega_k)$ and $\mathbf{S}(\omega_j, \omega_k)$ are the difference and the sum frequency quadratic transfer functions (QTF), respectively.

The time domain expression from radiation potential forces and moments has the following form

$$\mathbf{F}_R(t) = -\mathbf{M}^a(\infty)\ddot{\zeta}(t) - \int_{-\infty}^{t} \mathbf{R}(t-\tau)\dot{\zeta}(\tau)\,d\tau \tag{2.42}$$

where $\mathbf{M}^a(\infty)$ is the added mass at infinite frequency, and $\mathbf{R}(t)$ is called a retardation function or time memory function which is related to the frequency domain solution of the radiation problem as follows

$$\mathbf{R}(t) = \frac{2}{\pi}\int_0^{\infty} C(\omega)\frac{\sin \omega t}{\omega}\,d\omega \tag{2.43}$$

where $C(\omega)$ is the radiation damping coefficient in the Equation (2.36) at frequency ω.

The total wave loads in the time domain can now be obtained by summing each force component as follows

$$\mathbf{F}_{Total}(t) = \mathbf{F}_I(t) + \mathbf{F}_R(t) \tag{2.44}$$

where $\mathbf{F}_{Total}(t) = \mathbf{F}^{(1)}(t) + \mathbf{F}^{(2)}(t)$ is the total wave exciting force, $\mathbf{F}_I(t) = \mathbf{F}_I^{(1)}(t) + \mathbf{F}_I^{(2)}(t)$ is the sum of the Equation (2.40) and (2.41), $\mathbf{F}_R(t)$ is the radiation term from the Equation (2.42).

2.3.5 Morison's Formula

For slender cylindrical structures, the diffraction effect is usually negligible and the viscous effect becomes dominant. In that case, the inertia effect including the added mass and damping effect can be simply estimated by Morison's formula (Morison et al., 1950). This formula states that the wave load per unit length of the structure normal to the elemental section with diameter D which is small compared to the wave length is obtained by the sum of an inertial, added mass and drag force.

$$F_m = C_m \rho \frac{\pi D^2}{4} \dot{u}_n - C_a \rho \frac{\pi D^2}{4} \ddot{\zeta}_n + \frac{1}{2} \rho C_D D_S \left(u_n - \dot{\zeta}_n \right) \left| u_n - \dot{\zeta}_n \right| \tag{2.45}$$

where F_m denotes Morison's force, $C_m = 1 + C_a$ is the inertia coefficient, C_a is the added mass coefficient, C_D is the drag coefficient, D_S is the breadth or diameter of the structure, $\dot{u}_n$ and u_n are the acceleration and the velocity of the fluid normal to the body, respectively, and $\ddot{\zeta}_n$ and $\dot{\zeta}_n$ are the normal acceleration and the velocity of the body, respectively. The first two terms in Equation (2.45) are the inertia forces from the Froude-Krylov force and added mass effect. The last term represents the drag force in the relative velocity form. This relative-velocity form indicates that the drag force contributes to both the exciting force and damping force on the motion of the structure.

In this study, the viscous effects of slender members such as the cylindrical hull, TLP columns or truss members are computed by Morison's formula and are combined with the potential forces to compute the wave forces on the platform.

3. DYNAMICS OF MOORING LINES

3.1 Introduction

In this chapter, the dynamics of the mooring lines and theoretical background will be presented. The position of the floating wind turbine is maintained on the station by mooring systems. Traditionally, ships were moored by anchor chains from the bow, and floating production vessels such as FPSOs were moored by spread mooring which is utilized by a turret mooring system or a Single Point Mooring (SPM) system. In the case of a floating offshore platform such as TLP, taut vertical moorings or tendons, which are usually made of steel pipes, have been used for the mooring system. Steel wire ropes combined with a chain at each end also have been used for the spar platform. For ultra-deep water around 3,000m depth, synthetic mooring lines such as polyester lines are considered to be more efficient.

The basic concept of mooring systems for FOWTs is identical to the floating offshore oil & gas platforms. Slack catenary, taut catenary, or taut tension-leg mooring systems are considered to be common mooring systems in FOWTs. In addition to the station-keeping purpose, the mooring systems also provide the platforms with stability. For a TLP type platform design, the vertical tendons are main stability members so the failure of the vertical tendon system would cause the failure of the complete system. Therefore, the mooring system design of FOWT is one of the most important components for the dynamic behavior of the entire system as well as its stability.

So far, not many studies have been done concerning the dynamic behavior of mooring systems in FOWTs, and the effect of mooring systems has been estimated by quasi-static catenary equations. In shallow waters, this quasi-static method shows acceptable results because the total mass of mooring lines is negligible and the motion is small. However for deep water, the dynamics of mooring lines, including line inertia and the drag forces in the fluid, become more important, so finite-element mooring line analysis, which can include those effects, has been adopted in this study and is definitely preferred.

In this study, a three-dimensional elastic rod theory, which includes the line stretching, has been adopted to model the mooring lines (Garrett, 1982). The finite element method has been used to represent the analytic expression as a numerical form. The rod theory has some advantages in that the governing equation has been developed in a single global coordinate system and the geometric nonlinearity can be handled with ease and efficiency.

3.2 Theory of Rod

This theory describes the behavior of slender rods in terms of the position of the centerline of the rod. As illustrated in Figure 3.1, a position vector $\mathbf{r}(s,t)$ is introduced to define the space curve, which is a function of arc length s and time t. If we assume that the rod is inextensible, then the unit tangent vector to the space curve is $\mathbf{r}'$, and the principal normal vector is directed along $\mathbf{r}''$ and the bi-normal is directed along $\mathbf{r}'\times\mathbf{r}''$ where the prime symbol represents the differentiation with respect to the arc length.

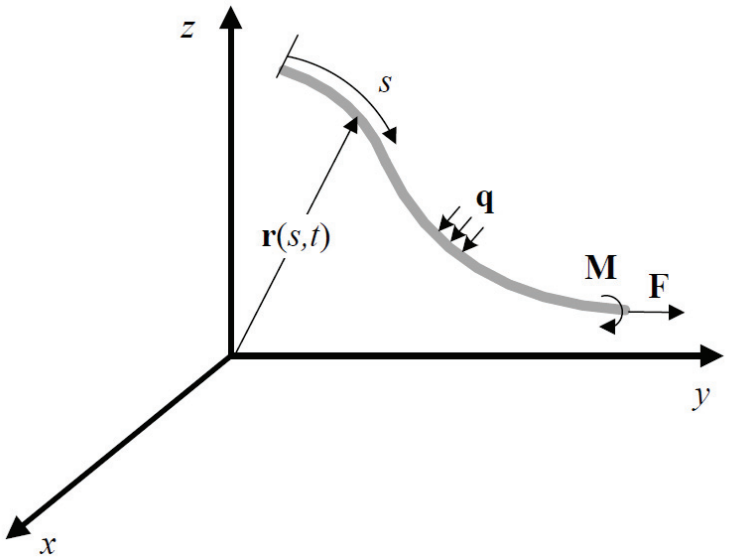

Figure 3.1 Coordinate system for slender rod

The equation of motion can be derived by equilibrium of the linear force and moment at the unit arc length of the rod as follows

$$\mathbf{F}' + \mathbf{q} = \rho \ddot{\mathbf{r}} \tag{3.1}$$

$$\mathbf{M}' + \mathbf{r}' \times \mathbf{F}' + \mathbf{m} = \mathbf{0} \tag{3.2}$$

where $\mathbf{q}$ is the applied force per unit length, ρ is the mass per unit length of the rod, $\mathbf{m}$ is the applied moment per unit length. $\mathbf{F}$ and $\mathbf{M}$ are the resultant force and moment along the centerline. The dot denotes the differentiation with respect to time.

The resultant moment $\mathbf{M}$ can be expressed as

$$\mathbf{M}' = \mathbf{r}' \times EI\mathbf{r}'' + H\mathbf{r}' \tag{3.3}$$

where EI is the bending stiffness, H is the torque. This relationship indicates that the bending moment is proportional to the curvature and is directed along the bi-normal direction. Substituting this relation into Equation (3.2), we have

$$\mathbf{r}' \times \left[\left(EI\mathbf{r}'' \right)' + \mathbf{F} \right] + H'\mathbf{r}' + H\mathbf{r}'' + \mathbf{m} = \mathbf{0} \tag{3.4}$$

and the scalar product of the above equation with $\mathbf{r}'$ yields

$$H' + \mathbf{m} \cdot \mathbf{r}' = \mathbf{0} \tag{3.5}$$

If we assume that there is no distributed torsional moment ($\mathbf{m} \cdot \mathbf{r}'$), and the torque in the lines is negligible, then the Equation (3.4) can be re-written as

$$\mathbf{r}' \times \left[\left(EI\mathbf{r}'' \right)' + \mathbf{F} \right] = \mathbf{0} \tag{3.6}$$

Introducing a scalar function $\lambda(s,t)$, which is called the Lagrangian multiplier, the $\mathbf{F}$ in the above equation can be written as

$$\mathbf{F} = -\left(EI\mathbf{r}'' \right)' + \lambda \mathbf{r}' \tag{3.7}$$

The scalar product of Equation (3.7) with $\mathbf{r}'$ results in

$$\lambda = \mathbf{F} \cdot \mathbf{r}' - \left(EI\mathbf{r}'' \right)' \cdot \mathbf{r}' \tag{3.8}$$

or

$$\lambda = T - EI\kappa^2 \tag{3.9}$$

where T is the tension and the κ is the curvature of the rod.

Combining Equation (3.7) with (3.1), the equation of motion for the rod become

$$-\left(EI\mathbf{r}'' \right)'' + \left(\lambda \mathbf{r}' \right)' + \mathbf{q} = \rho \ddot{\mathbf{r}} \tag{3.10}$$

In addition, $\mathbf{r}$ should satisfy the inextensible condition as

$$\mathbf{r}' \cdot \mathbf{r}' = 1 \tag{3.11}$$

If the rod is extensible, and the stretch is linear and small, the above condition (3.11) can be approximated by

$$\frac{1}{2}\left(\mathbf{r}'\cdot\mathbf{r}'-1\right)=\frac{T}{AE}\approx\frac{\lambda}{AE} \tag{3.12}$$

The above equation of motion of the rod and inextensible (or extensible) condition with initial and boundary conditions and applied force vector $\mathbf{q}$, are sufficient to determine the position vector $\mathbf{r}(s,t)$ and the Lagrangian multiplier $\lambda(s,t)$. The applied force vector $\mathbf{q}$, in most offshore applications, comes from the gravity of the rod and the hydrostatic and hydrodynamic forces from surrounding fluid. So it can be expressed as

$$\mathbf{q}=\mathbf{w}+\mathbf{F}^{\mathbf{s}}+\mathbf{F}^{\mathbf{d}} \tag{3.13}$$

where $\mathbf{w}$ is the weight of the rod per unit length, $\mathbf{F}^{\mathbf{s}}$ is the hydrostatic force and $\mathbf{F}^{\mathbf{d}}$ is the hydrodynamic force on the rod per unit length. The hydrostatic force can be written as

$$\mathbf{F}^{\mathbf{s}}=\mathbf{B}-\left(P\mathbf{r}'\right)' \tag{3.14}$$

where $\mathbf{B}$ is the buoyancy force on the rod per unit length, and P is the hydrostatic pressure at point $\mathbf{r}$ on the rod.

The hydrodynamic force $\mathbf{F}^{\mathbf{d}}$ can be derived by Morison's formula below

$$\begin{aligned}\mathbf{F}^{\mathbf{d}}&=-C_A\ddot{\mathbf{r}}^n+C_M\dot{\mathbf{V}}^n+C_D\left|\mathbf{V}^n-\ddot{\mathbf{r}}^n\right|\left(\mathbf{V}^n-\ddot{\mathbf{r}}^n\right)\\&=-C_A\ddot{\mathbf{r}}^n+\overline{\mathbf{F}}^{\mathbf{d}}\end{aligned} \tag{3.15}$$

where C_A is the added mass coefficient per unit length, C_M is the inertial coefficient per unit length per unit normal acceleration and C_D is the drag coefficient per unit length per

unit normal velocity. $\mathbf{V}^n$ and $\dot{\mathbf{V}}^n$ are fluid velocity and acceleration normal to the rod centerline respectively. They can be expressed as

$$\mathbf{V}^{\mathrm{n}} = \left(\mathbf{V} - \dot{\mathbf{r}}\right) - \left[\left(\mathbf{V} - \dot{\mathbf{r}}\right) \cdot \mathbf{r}'\right] \mathbf{r}' \tag{3.16}$$

$$\dot{\mathbf{V}}^{\mathrm{n}} = \dot{\mathbf{V}} - \left(\mathbf{V} \cdot \dot{\mathbf{r}}\right) \cdot \mathbf{r}' \tag{3.17}$$

where $\dot{\mathbf{V}}$ and $\mathbf{V}$ are the total fluid particle's acceleration and velocity at the centerline of the rod without disturbance by the rod. $\ddot{\mathbf{r}}^n$ and $\dot{\mathbf{r}}^n$ are the rod acceleration and velocity normal to its centerline and can be obtained by

$$\dot{\mathbf{r}}^{\mathrm{n}} = \dot{\mathbf{r}} - \left(\dot{\mathbf{r}} \cdot \mathbf{r}'\right) \mathbf{r}' \tag{3.18}$$

$$\ddot{\mathbf{r}}^{\mathrm{n}} = \ddot{\mathbf{r}} - \left(\ddot{\mathbf{r}} \cdot \mathbf{r}'\right) \mathbf{r}' \tag{3.19}$$

The equation of motion of the rod subjected to its weight, hydrostatic and hydrodynamic forces in water, combining Equations (3.13) through (3.15) with (3.1) becomes

$$\rho \ddot{\mathbf{r}} + C_a \rho_w \ddot{\mathbf{r}}^n + \left(EI\mathbf{r}''\right)'' - \left(\tilde{\lambda}\mathbf{r}'\right)' = \tilde{\mathbf{w}} + \overline{\mathbf{F}}^d \tag{3.20}$$

where

$$\tilde{\lambda} = T + P - EI\kappa^2 = \tilde{T} - EI\kappa^2 \tag{3.21}$$

$$\tilde{\mathbf{w}} = \mathbf{w} + \mathbf{B} \tag{3.22}$$

$$\tilde{T} = T + P \tag{3.23}$$

$\tilde{T}$ is the effective tension in the rod, $\tilde{\mathbf{w}}$ is the effective weight or the wet weight.

The Equation (3.20) together with the line stretch condition in Equation (3.12), are the governing equations for the statics or dynamics of the rod in fluid.

4. DYNAMICS OF HORIZONTAL AXIS WIND TURBINES

4.1 Introduction

The dynamics response of three-bladed, horizontal axis wind turbines (HAWT) can be analyzed by structural modeling with proper geometry, coordinate systems and degrees of freedom (DOFs). Thus, accurate structural models are necessary to analyze wind energy systems. To deal with multiple components of wind turbines such as floating platform, towers, blades and Rotor Nacelle Assembly (RNA), Kane's method (originally called Lagrangian form of d'Alembert's principle) is used to set up equations of motion which can be handled by numerical integration. This method can greatly simplify the equations of motion. Consequently the equations are easier to solve than other dynamic approaches using methods of Newton or Lagrange. Furthermore, computation time can be also reduced by using fewer terms than other conventional approaches. This chapter revisits the steps to establish the equations of motion for HAWT which is employed by computational design code FAST (Jonkman, 2003; Wilson et al., 2000). First, wind turbine geometry with various rigid bodies is defined, and then coordinate systems and degrees of freedom are discussed. Since FAST models the blades and tower as flexible bodies, the deflections and vibrations are presented with the numerical model of elastic bodies. Aerodynamic load calculations, including aerodynamic lift, drag, and pitching moment of the airfoil section along the wind turbine blades, are carried out by AeroDyn, and the details of aerodynamics are not presented in this study. Finally, the equations of motion, which describe the kinematic and kinetics of

wind turbine motion and force-acceleration relations of the entire wind turbine system, are presented by Kane's equations of motion.

4.2 Mechanical Components and Coordinate Systems

The FAST design code models a floating wind turbine with six rigid and five flexible bodies. The six rigid bodies include the floating platform, nacelle, tower-top base plate, armature, hub and gears. In detail, the tower is rigidly attached to the floating platform and the top of the tower is fixed to a base plate which supports a yaw bearing and nacelle. The nacelle assembly can be allowed to tilt and the low speed shaft (LSS) connects the gearbox to the rotor. The rotor assembly consists of hub, blades, and tip brakes. In terms of DOFs, platform rigid body motion accounts for six DOFs, nacelle yaw, rotor furl, generator azimuth, tail furl accounts for four DOFs respectively.

The five flexible bodies are the three blades, tower and drive train. The blades flexibility accounts for 1^{st}-flapwise, 2^{nd}-flapwise, and edgewise DOFs, so a total of three DOFs are necessary to describe one blade. In the case of tower, two fore-aft, and two side-to-side DOFs are accounted for, and the remaining one DOF is for drive train flexibility. To sum up, 24 DOFs are required for one floating wind turbine with 3 blades, and the DOFs will be further extended for MUFOWT.

To describe the kinematics and kinetics expressions of the wind turbine, several reference frames formed by orthogonal sets of unit vectors are employed in FAST. The major coordinate systems used for the FAST design code are listed in Table 4.1.

Table 4.1 Coordinate system of wind turbine

Unit Vector Set	Description
z	Inertial coordinates
a	Tower base / Platform coordinate
t	Tower element-fixed coordinate
b	Tower top / base plate coordinate
d	Nacelle / yaw coordinate
rf	Rotor-furl coordinate
c	Shaft coordinate
e	Azimuth coordinate
f	Teeter coordinate
g	Hub / delta-3 coordinate
g'	Hub (prime) coordinate
i	Coned coordinate
j	Blade / pitched coordinate
Lj	Blade coordinate system aligned with local structural axes
n	Blade element-fixed coordinate
m	Blade element-fixed coordinate for aerodynamics loads
te	Trailing edge coordinate
tf	Tail-furl coordinate
p	Tail fin coordinate

Since a complete set of coordinate systems is defined, the transformation of fixed quantities from one coordinate system to any other coordinate system is available. Examples of simple transformation matrices used in FAST are shown below.

From tower base (Platform) to inertial:

$$\begin{Bmatrix} z_1 \\ z_2 \\ z_3 \end{Bmatrix} = \begin{bmatrix} \cos(q_6) & 0 & \sin(q_6) \\ 0 & 1 & 0 \\ -\sin(q_6) & 0 & \cos(q_6) \end{bmatrix} \begin{bmatrix} 1 & 0 & 0 \\ 0 & \cos(q_5) & -\sin(q_5) \\ 0 & \sin(q_5) & \cos(q_5) \end{bmatrix} \begin{bmatrix} \cos(q_4) & -\sin(q_4) & 0 \\ \sin(q_4) & \cos(q_4) & 0 \\ 0 & 0 & 1 \end{bmatrix} \begin{Bmatrix} a_1 \\ a_2 \\ a_3 \end{Bmatrix} \tag{4.1}$$

where q_4, q_5, and q_6 are roll, pitch and yaw angle of floating platform.

From tower top to tower base (Platform):

$$\begin{Bmatrix} a_1 \\ a_2 \\ a_3 \end{Bmatrix} = \begin{bmatrix} \cos(\theta_7) & -\sin(\theta_7) & 0 \\ \sin(\theta_7)\cos(\theta_8) & \cos(\theta_7)\cos(\theta_8) & -\sin(\theta_8) \\ \sin(\theta_7)\sin(\theta_8) & \cos(\theta_7)\sin(\theta_8) & \cos(\theta_8) \end{bmatrix} \begin{Bmatrix} b_1 \\ b_2 \\ b_3 \end{Bmatrix} \tag{4.2}$$

where θ_7 is longitudinal angle of tower top slope, θ_8 is lateral angle of tower top slope.

From nacelle yaw to tower top:

$$\begin{Bmatrix} b_1 \\ b_2 \\ b_3 \end{Bmatrix} = \begin{bmatrix} \cos(q_{11}) & 0 & \sin(q_{11}) \\ 0 & 1 & 0 \\ -\sin(q_{11}) & 0 & \cos(q_{11}) \end{bmatrix} \begin{Bmatrix} d_1 \\ d_2 \\ d_3 \end{Bmatrix} \tag{4.3}$$

where q_{11} is nacelle yaw angle.

From shaft tilt to nacelle yaw:

$$\begin{Bmatrix} d_1 \\ d_2 \\ d_3 \end{Bmatrix} = \begin{bmatrix} \cos(\theta_T) & -\sin(\theta_T) & 0 \\ \sin(\theta_T) & \cos(\theta_T) & 0 \\ 0 & 0 & 1 \end{bmatrix} \begin{Bmatrix} c_1 \\ c_2 \\ c_3 \end{Bmatrix} \tag{4.4}$$

where θ_T is shaft tilt angle.

From azimuth to shaft tilt:

$$\begin{Bmatrix} c_1 \\ c_2 \\ c_3 \end{Bmatrix} = \begin{bmatrix} 1 & 0 & 0 \\ 0 & \cos(q_{13}+q_{14}) & -\sin(q_{13}+q_{14}) \\ 0 & \sin(q_{13}+q_{14}) & \cos(q_{13}+q_{14}) \end{bmatrix} \begin{Bmatrix} e_1 \\ e_2 \\ e_3 \end{Bmatrix} \tag{4.5}$$

where q_{13} is azimuth angle and q_{14} is zero azimuth offset due to the drive train flexibility.

Since the delta-3 angle and teeter angle for 3 bladed turbines are assumed to be zero,

$$\begin{Bmatrix} e_1 \\ e_2 \\ e_3 \end{Bmatrix} = \begin{Bmatrix} f_1 \\ f_2 \\ f_3 \end{Bmatrix} = \begin{Bmatrix} g_1 \\ g_2 \\ g_3 \end{Bmatrix} \tag{4.6}$$

From blade-oriented hub to hub:

$$\begin{Bmatrix} g_1 \\ g_2 \\ g_3 \end{Bmatrix} = \begin{bmatrix} 1 & 0 & 0 \\ 0 & \cos\left(\frac{2\pi}{N_B}\right) & -\sin\left(\frac{2\pi}{N_B}\right) \\ 0 & \sin\left(\frac{2\pi}{N_B}\right) & \cos\left(\frac{2\pi}{N_B}\right) \end{bmatrix} \begin{Bmatrix} g_1' \\ g_2' \\ g_3' \end{Bmatrix} \tag{4.7}$$

where N_B is blade number. $(N_B = 1,2,3)$

From coning to blade-oriented hub:

$$\begin{Bmatrix} g_1' \\ g_2' \\ g_3' \end{Bmatrix} = \begin{bmatrix} \cos(\beta) & 0 & \sin(\beta) \\ 0 & 1 & 0 \\ -\sin(\beta) & 0 & \cos(\beta) \end{bmatrix} \begin{Bmatrix} i_1 \\ i_2 \\ i_3 \end{Bmatrix} \tag{4.8}$$

where β is coning angle.

From blade pitch to coning:

$$\begin{Bmatrix} i_1 \\ i_2 \\ i_3 \end{Bmatrix} = \begin{bmatrix} \cos(\theta_P) & \sin(\theta_P) & 0 \\ -\sin(\theta_P) & \cos(\theta_P) & 0 \\ 0 & 0 & 1 \end{bmatrix} \begin{Bmatrix} j_1 \\ j_2 \\ j_3 \end{Bmatrix} \tag{4.9}$$

where θ_P is blade pitch angle.

From blade twist to blade pitch

$$\begin{Bmatrix} j_1 \\ j_2 \\ j_3 \end{Bmatrix} = \begin{bmatrix} \cos(\theta_S) & \sin(\theta_S) & 0 \\ -\sin(\theta_S) & \cos(\theta_S) & 0 \\ 0 & 0 & 1 \end{bmatrix} \begin{Bmatrix} Lj_1 \\ Lj_2 \\ Lj_3 \end{Bmatrix} \tag{4.10}$$

where θ_S is structural twist angle of blade.

There are 24 DOFs for three-bladed floating wind turbines, and each DOF is tabulated in Table 4.2. All of the wind turbine motion can be described by those variables.

Table 4.2 Degree of freedom variables

Variable	Description
q_1	Platform surge
q_2	Platform sway
q_3	Platform heave
q_4	Platform roll
q_5	Platform pitch
q_6	Platform yaw
q_7	Longitudinal tower top displacement for natural mode 1
q_8	Latitudinal tower top displacement for natural mode 1

Table 4.2 Continued

Variable	Description
q_9	Longitudinal tower top displacement for natural mode 2
q_{10}	Latitudinal tower top displacement for natural mode 2
q_{11}	Nacelle yaw angle
q_{12}	Rotor furl angle
q_{13}	Generator azimuth angle
q_{14}	Drive train rotational flexibility
q_{15}	Tail furl angle
q_{16}	Blade 1 flapwise tip displacement for natural mode 1
q_{17}	Blade 1 edgewise tip displacement
q_{18}	Blade 1 flapwise tip displacement for natural mode 2
q_{19}	Blade 2 flapwise tip displacement for natural mode 1
q_{20}	Blade 2 edgewise tip displacement
q_{21}	Blade 2 flapwise tip displacement for natural mode 2
q_{22}	Blade 3 flapwise tip displacement for natural mode 1
q_{23}	Blade 3 edgewise tip displacement
q_{24}	Blade 3 flapwise tip displacement for natural mode 2

Blades can be declined, or angled slightly downwind as denoted by the coning angle β . Similarly, each blade can be pitched or twisted independently so the transformation matrices (4.8) ~ (4.10) can be used for any blade with each coning angle, pitch angle, and twisted angle together with the reference frame specified for each blade.

4.3 Blade and Tower Flexibility

The flexibility of blades and towers in FAST is implemented by cantilevered beams, fixed at one end to either the hub or the platform, and free at the other end. Both have continuous distributed mass and stiffness, and the flexibility of structures is roughly estimated by the normal mode shape summation method. By this simplification, the total number of DOFs can be reduced from infinity to N, the number of dominant normal modes, and the longitudinal or lateral deflection of the flexible beam can be expressed by $u(z,t)$ as a function of distance z along the beam and time t.

$$u(z,t) = \sum_{a=1}^{N} \phi_a(z) q_a(t) \tag{4.11}$$

where $\phi_a(z)$ represents the normal mode shape and $q_a(t)$ denotes the generalized coordinate.

In case of the tower deflection, both longitudinal and lateral directions are represented by two modes which require two DOFs in each direction. Components of the longitudinal and lateral displacement of the tower top consist of the contributions from the first and second mode shapes. They are related to the tower DOFs as follows

$$u_7 = q_7 + q_9 \tag{4.12}$$

$$u_8 = q_8 + q_{10} \tag{4.13}$$

where u_7 is the total tower top fore-aft displacement, and u_8 is the total tower top side-to-side displacement. The tower top rotation angles can be also expressed as

$$\theta_7 = -(\alpha_7 q_7 + \alpha_9 q_9) \tag{4.14}$$

$$\theta_8 = \alpha_8 q_8 + \alpha_{10} q_{10} \tag{4.15}$$

where θ_7 is a rotation about $\mathbf{a}_3$, θ_8 is a rotation about $\mathbf{a}_1$. α is the first derivative of the mode shapes.

Blade deflection is modeled with two vibration modes for out-of-plane direction and one mode for in-plane direction. This means that a total of three DOFs is required for one blade. The current position of the local blade element can be expressed in root-fixed coordinates as

$$\mathbf{u}(z,t) = u(z,t)i_1 + v(z,t)i_2 + \left[r(z) + w(z,t)\right]i_3 \tag{4.16}$$

where the vector $\mathbf{u}$ is the vector position of the local blade element, i_3 is along the blade, i_1 is in the out-of-plane direction, i_2 is in the in-plane direction, and $r(z)$ is the distance along the undeformed blade to the current blade element.

4.4 Kinematics

Once the geometry, coordinate system, and DOFs are set up, then the kinematic expression of the wind turbine system can be derived. This step is necessary to build kinetics expression, and develop Kane's equations of motion. In this kinematics expression, the vectors from any references frame can be transformed to a common coordinate system and the acceleration of any point in the body can be expressed using velocities and angular velocities. The velocities and angular velocities of one frame with respect to another, say of frame B with respect to frame A, will be denoted by ${}^{A}\mathbf{v}^{B}$ and ${}^{A}\boldsymbol{\omega}^{B}$ respectively.

The reference frames in wind turbine systems are presented in Figure 4.1(a). Based on the given frames, the angular velocity of the tower base in the inertial frame can be expressed by the summation of angular velocity of rotational motion of the platform (roll, pitch and yaw) and is given by

$$^{E}\boldsymbol{\omega}^{X} = \dot{q}_4\mathbf{z}_1 + \dot{q}_5\mathbf{z}_2 + \dot{q}_6\mathbf{z}_3 \tag{4.17}$$

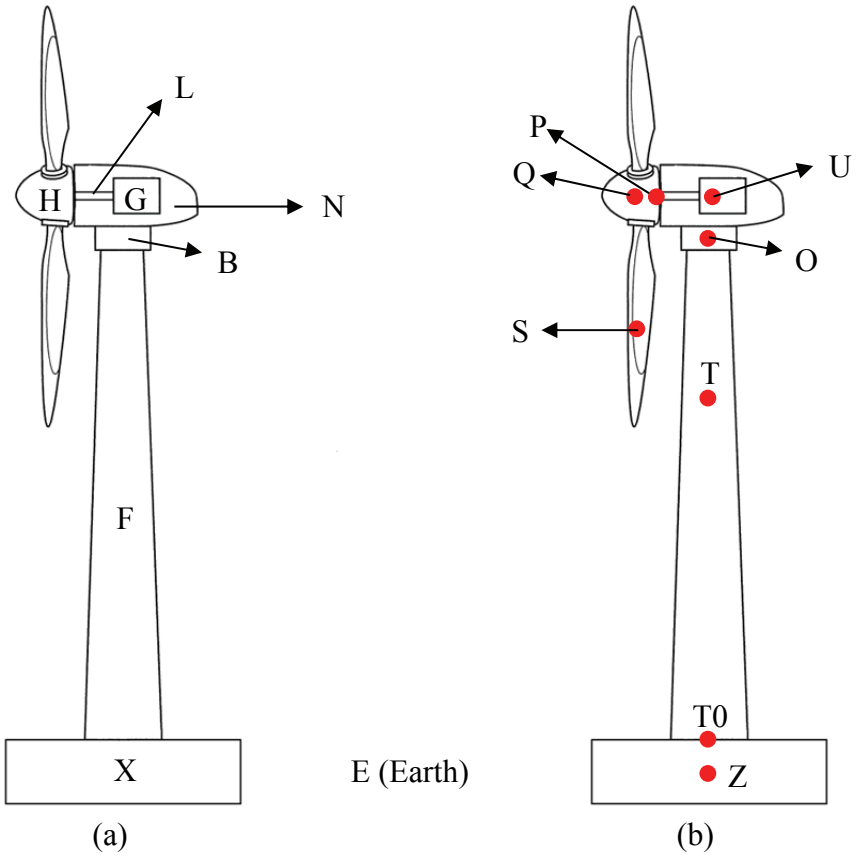

Figure 4.1 Turbine reference frames (a) and reference points (b)

The angular velocity of the tower top base plate in the inertial frame can be expressed by the summation of angular velocity of longitudinal and lateral direction and is given by

$$^{X}\boldsymbol{\omega}^{B} = \dot{\theta}_8 \mathbf{a}_1 + \dot{\theta}_7 \mathbf{a}_3 \tag{4.18}$$

The angular velocity of the nacelle relative to the tower-top base plate depends on the rate of yaw

$$^{B}\boldsymbol{\omega}^{N} = \dot{q}_{11} \mathbf{d}_2 \tag{4.19}$$

The angular velocity of azimuth angle is

$$^{N}\boldsymbol{\omega}^{L} = \left(\dot{q}_{13} + \dot{q}_{14}\right) \mathbf{e}_1 \tag{4.20}$$

Once the angular velocities of each reference frame are written, the angular velocity of the low-speed shaft can be expressed in the inertial frame by combining together.

$$\begin{aligned} ^{E}\boldsymbol{\omega}^{L} &= {}^{E}\boldsymbol{\omega}^{X} + {}^{X}\boldsymbol{\omega}^{B} + {}^{B}\boldsymbol{\omega}^{N} + {}^{N}\boldsymbol{\omega}^{L} \\ &= \dot{q}_4 \mathbf{z}_1 + \dot{q}_5 \mathbf{z}_2 + \dot{q}_6 \mathbf{z}_3 + \dot{\theta}_8 \mathbf{a}_1 + \dot{\theta}_7 \mathbf{a}_3 + \dot{q}_{11} \mathbf{d}_2 + \left(\dot{q}_{13} + \dot{q}_{14}\right) \mathbf{e}_1 \end{aligned} \tag{4.21}$$

Since, there is no angular velocity difference between the low-speed shaft and hub because of the absence of a teeter pin, the angular velocity of hub can be written as

$$^{E}\boldsymbol{\omega}^{H} = {}^{E}\boldsymbol{\omega}^{L} \tag{4.22}$$

Similarly, the velocity of the platform reference point (Z) depicted in Figure 4.1(b), which is dependent on the platform velocity in the inertial frame, is

$$^{E}\mathbf{v}^{Z} = \dot{q}_1 \mathbf{z}_1 + \dot{q}_2 \mathbf{z}_2 + \dot{q}_3 \mathbf{z}_3 \tag{4.23}$$

The velocity of the tower base in the inertial frame is

$$ {}^{E}\mathbf{v}^{T0} = {}^{E}\mathbf{v}^{Z} + {}^{E}\boldsymbol{\omega}^{X} \times \mathbf{r}^{ZT0} \tag{4.24} $$

The velocity of the tower top base plate (O) in the tower base frame without axial deflection is

$$ {}^{E}\mathbf{v}^{O} = {}^{E}\mathbf{v}^{T0} + \dot{u}_7 \mathbf{a}_1 + \dot{u}_8 \mathbf{a}_3 \tag{4.25} $$

where $\dot{u}_7$ is the tower top fore-aft deflection velocity, and $\dot{u}_8$ is the tower top side-to-side deflection velocity. Those deflection velocities consider the axial-reduction terms. The axial reduction of the tower is the combined result of assuming the flexible beam with a fixed length and the fact that the free end of a cantilever beam must move closer to the fixed end when the beam deflects laterally. A detailed derivation of tower deflection in Figure 4.2 is presented by J. Jonkman. (Jonkman, 2003)

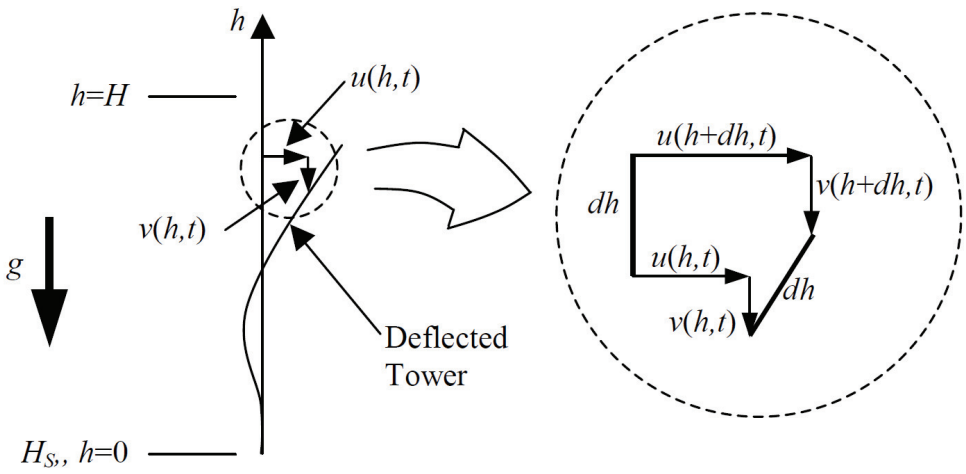

Figure 4.2 Tower deflection geometry (Jonkman, 2003)

The velocity of point T on the flexible tower in the inertial frame is

$$ {}^{E}\mathbf{v}^{T} = {}^{E}\mathbf{v}^{T0} + \left[\dot{q}_7\phi_{1T}(h) + \dot{q}_9\phi_{2T}(h)\right]\mathbf{a}_1 + \left[\dot{q}_8\phi_{1T}(h) + \dot{q}_{10}\phi_{2T}(h)\right]\mathbf{a}_3 \tag{4.26} $$

where h is the elevation of point T which ranges from zero to H. The elevation h equals zero at the top of the rigid part of the tower.

The velocity of the nacelle center of mass (U) in the inertial frame is

$$ {}^{E}\mathbf{v}^{U} = {}^{E}\mathbf{v}^{O} + {}^{E}\boldsymbol{\omega}^{N} \times \mathbf{r}^{OU} \tag{4.27} $$

where ${}^{E}\boldsymbol{\omega}^{N}$ is the angular velocity of the nacelle in the inertial frame $\left({}^{E}\boldsymbol{\omega}^{N} = {}^{E}\boldsymbol{\omega}^{X} + {}^{X}\boldsymbol{\omega}^{B} + {}^{B}\boldsymbol{\omega}^{N}\right)$, and $\mathbf{r}^{OU}$ is the position vector pointing from the tower-top base plate to the nacelle center of mass.

The velocity of the hub in the inertial frame is

$$ {}^{E}\mathbf{v}^{P} = {}^{E}\mathbf{v}^{O} + {}^{E}\boldsymbol{\omega}^{N} \times \mathbf{r}^{OP} \tag{4.28} $$

Similarly, the velocities of the blade axes intersection point (Q) and the hub center of mass in the inertial frame are

$$ {}^{E}\mathbf{v}^{Q} = {}^{E}\mathbf{v}^{P} + {}^{E}\boldsymbol{\omega}^{H} \times \mathbf{r}^{PQ} \tag{4.29} $$

and

$$ {}^{E}\mathbf{v}^{C} = {}^{E}\mathbf{v}^{Q} + {}^{E}\boldsymbol{\omega}^{H} \times \mathbf{r}^{QC} \tag{4.30} $$

Finally, the velocity of any point S on blade 1 in the inertial frame is

$$ {}^{E}\mathbf{v}^{S} = {}^{E}\mathbf{v}^{Q} + {}^{H}\mathbf{v}^{S} + {}^{E}\boldsymbol{\omega}^{H} \times \mathbf{r}^{QS} \tag{4.31} $$

where ${}^{H}\mathbf{v}^{S}$ is the velocity of point S on blade 1 with respect to the rotating frame fixed in the hub, and $\mathbf{r}^{QS}$ is the position vector connecting any point S on the deflected blade 1 to the blade axes intersection point Q that can be expressed as

$$ \mathbf{r}^{QS} = u(r,t)\mathbf{i}_1 + v(r,t)\mathbf{i}_2 + \left[r + R_H - w(r,t)\right]\mathbf{i}_3 \tag{4.32} $$

The ${}^{H}\mathbf{v}^{S}$ can be obtained by time derivative of $\mathbf{r}^{QS}$

$${}^{H}\mathbf{v}^{S} = \dot{u}(r,t)\mathbf{i}_1 + \dot{v}(r,t)\mathbf{i}_2 - \dot{w}(r,t)\mathbf{i}_3 \tag{4.33}$$

So, the velocity of any point S on blade 1 in the inertial frame can be written as a summation of the derived equation above

$$\begin{aligned}{}^{E}\mathbf{v}^{S} = {} & \dot{q}_1\mathbf{z}_1 + \dot{q}_2\mathbf{z}_2 + \dot{q}_3\mathbf{z}_3 + (\dot{q}_4\mathbf{z}_1 + \dot{q}_5\mathbf{z}_2 + \dot{q}_6\mathbf{z}_3)\times\mathbf{r}^{ZT0} + \\ & (\dot{q}_7 + \dot{q}_9)\mathbf{a}_1 + (\dot{q}_8 + \dot{q}_{10})\mathbf{a}_3 + (\dot{q}_4\mathbf{z}_1 + \dot{q}_5\mathbf{z}_2 + \dot{q}_6\mathbf{z}_3 + \dot{\theta}_8\mathbf{a}_1 + \dot{\theta}_7\mathbf{a}_3 + \dot{q}_{11}\mathbf{d}_2)\times\mathbf{r}^{OP} + \\ & [\dot{q}_4\mathbf{z}_1 + \dot{q}_5\mathbf{z}_2 + \dot{q}_6\mathbf{z}_3 + \dot{\theta}_8\mathbf{a}_1 + \dot{\theta}_7\mathbf{a}_3 + \dot{q}_{11}\mathbf{d}_2 + (\dot{q}_{13} + \dot{q}_{14})\mathbf{e}_1]\times\mathbf{r}^{PQ} + \\ & [\dot{q}_4\mathbf{z}_1 + \dot{q}_5\mathbf{z}_2 + \dot{q}_6\mathbf{z}_3 + \dot{\theta}_8\mathbf{a}_1 + \dot{\theta}_7\mathbf{a}_3 + \dot{q}_{11}\mathbf{d}_2 + (\dot{q}_{13} + \dot{q}_{14})\mathbf{e}_1]\times\mathbf{r}^{QS} + {}^{H}\mathbf{v}^{S}\end{aligned} \tag{4.34}$$

This velocity can be simply expressed as a generalized form

$${}^{E}\mathbf{v}^{A} = \left(\sum_{r=1}^{24} {}^{E}\mathbf{v}_r^{A}\dot{q}_r\right) + {}^{E}\mathbf{v}_t^{A} \tag{4.35}$$

where ${}^{E}\mathbf{v}_r^{A}$ is the r^{th} partial velocity associated with point A, and ${}^{E}\mathbf{v}_t^{A}$ is the sum of all other terms. The angular velocity of any reference frame A in the inertial frame can also be expressed as

$${}^{E}\boldsymbol{\omega}^{A} = \left(\sum_{r=1}^{24} {}^{E}\boldsymbol{\omega}_r^{A}\dot{q}_r\right) + {}^{E}\boldsymbol{\omega}_t^{A} \tag{4.36}$$

where ${}^{E}\boldsymbol{\omega}_r^{A}$ is the r^{th} partial angular velocity associated with point A, and ${}^{E}\boldsymbol{\omega}_t^{A}$ is the sum of all other terms.

The acceleration of any point in the inertial frame can be derived by time derivatives of the ${}^{E}\mathbf{v}^{A}$ as

$${}^{E}\mathbf{a}^{A} = \frac{d}{dt}\left({}^{E}\mathbf{v}^{A}\right) = \left(\sum_{r=1}^{24} {}^{E}\mathbf{v}_r^{A}\ddot{q}_r\right) + \left[\sum_{r=1}^{24}\frac{d}{dt}\left({}^{E}\mathbf{v}_r^{A}\right)\dot{q}_r\right] + \frac{d}{dt}\left({}^{E}\mathbf{v}_t^{A}\right) \tag{4.37}$$

or it can be expressed in a similar form as the velocity form:

$$ {}^{E}\mathbf{a}^{A} = \left(\sum_{r=1}^{24} {}^{E}\mathbf{v}_{r}^{A} \ddot{q}_{r} \right) + {}^{E}\mathbf{a}_{t}^{A} \tag{4.38} $$

where,

$$ {}^{E}\mathbf{a}_{t}^{A} = \left[\sum_{r=1}^{24} \frac{d}{dt}\left({}^{E}\mathbf{v}_{r}^{A} \right) \dot{q}_{r} \right] + \frac{d}{dt}\left({}^{E}\mathbf{v}_{t}^{A} \right) \tag{4.39} $$

4.5 Generalized Active Forces

Using partial velocity vectors derived above as base vectors (direction vectors), it is useful to project forces along these vectors. Those projected forces are called generalized forces. Consider a set of forces F^{X_i} $\left(i = 1, 2, ..., N\right)$ applied at points X_i, then the generalized forces are obtained by adding the generalized forces from the individual forces as

$$ F_r = \sum_{i=1}^{N} {}^{E}\mathbf{v}_{r}^{X_i} \cdot \left(F^{X_i} \right) \qquad \left(r = 1, 2, ..., n\right) \tag{4.40} $$

where N is the number of rigid bodies in the system, and n is the number of DOFs.

We can obtain the kinematic expressions of points X_i using the velocity at the center of mass of rigid body G as

$$ {}^{E}\mathbf{v}^{X_i} = {}^{E}\mathbf{v}^{G} + {}^{E}\boldsymbol{\omega}^{G} \times \mathbf{r}^{GX_i} \tag{4.41} $$

where, ${}^{E}\boldsymbol{\omega}^{G}$ is the angular velocity associated with the rigid body, and $\mathbf{r}^{GX_i}$ is the position vector of the center of mass of the rigid body relative to the center of mass G.

By differentiating Equation (4.41) with respect to the generalized coordinate r, then

$$ {}^{E}\mathbf{v}_r^{X_i} = {}^{E}\mathbf{v}_r^{G} + {}^{E}\boldsymbol{\omega}_r^{G} \times \mathbf{r}^{GX_i} \qquad (r = 1, 2, ..., n) \tag{4.42} $$

Substituting Equation (4.42) into (4.40) gives

$$ \begin{aligned} F_r &= \sum_{i=1}^{N} \left({}^{E}\mathbf{v}_r^{G} + {}^{E}\boldsymbol{\omega}_r^{G} \times \mathbf{r}^{GX_i} \right) \cdot F_i \\ &= \sum_{i=1}^{N} {}^{E}\mathbf{v}_r^{G} \cdot F_i + \sum_{i=1}^{N} \left({}^{E}\boldsymbol{\omega}_r^{G} \times \mathbf{r}^{GX_i} \right) \cdot F_i \\ &= {}^{E}\mathbf{v}_r^{G} \cdot \left(\sum_{i=1}^{N} \cdot F_i \right) + {}^{E}\boldsymbol{\omega}_r^{G} \cdot \left(\sum_{i=1}^{N} \mathbf{r}^{GX_i} \times F_i \right) \end{aligned} \tag{4.43} $$

We can rewrite this in the form

$$ F_r = {}^{E}\mathbf{v}_r^{G} \cdot \mathbf{F} + {}^{E}\boldsymbol{\omega}_r^{G} \cdot \mathbf{T} \tag{4.44} $$

where $\mathbf{F}$ and $\mathbf{T}$ are the resultant force and moment induced by the set of applied forces F^{X_i}, respectively.

The all resultant forces and moments acting on elements of the floating wind turbine contribute to the total generalized active forces. These forces include the hydrodynamic forces, mooring restoring forces, aerodynamic forces, elastic forces from the tower, blades, and drive train flexibility, elastic forces from the nacelle yaw spring, gravitational forces, generator forces, and damping forces.

$$ F_r = F_r\big|_{Hydro} + F_r\big|_{Mooring} + F_r\big|_{Aero} + F_r\big|_{Elastic} + F_r\big|_{Gravity} + F_r\big|_{Generator} + F_r\big|_{Damping} \tag{4.45} $$

The detailed derivations of all generalized active forces are beyond the scope of this study.

4.6 Generalized Inertia Forces

Along with the generalized active forces, which are presented above, generalized inertia forces can be also defined. Similarly, a generalized inertia force is defined as a projection of inertia force along a partial velocity vector.

$$F_r^* = \sum_{i=1}^{N} {}^E\mathbf{v}_r^{X_i} \cdot \left(-m_i \, {}^E\mathbf{a}^{X_i}\right) \qquad (r = 1, 2, ..., n) \tag{4.46}$$

where, as before, F_r^* is the inertia force on points X_i and ${}^E\mathbf{v}_r^{X_i}$ is the r[th] partial velocity associated with rigid body, ${}^E\mathbf{a}^{X_i}$ is the acceleration of points X_i. Using Equation (4.42), the partial velocity ${}^E\mathbf{v}_r^{X_i}$ can be replaced as

$$\begin{aligned} F_r^* &= \sum_{i=1}^{N} \left({}^E\mathbf{v}_r^G + {}^E\boldsymbol{\omega}_r^G \times \mathbf{r}^{GX_i} \right) \cdot \left(-m_i \, {}^E\mathbf{a}^{X_i}\right) \\ &= \sum_{i=1}^{N} {}^E\mathbf{v}_r^G \cdot \left(-m_i \, {}^E\mathbf{a}^{X_i}\right) + {}^E\boldsymbol{\omega}_r^G \times \mathbf{r}^{GX_i} \cdot \left(-m_i \, {}^E\mathbf{a}^{X_i}\right) \\ &= {}^E\mathbf{v}_r^G \cdot \sum_{i=1}^{N} \left(-m_i \, {}^E\mathbf{a}^{X_i}\right) + \sum_{i=1}^{N} {}^E\boldsymbol{\omega}_r^G \times \mathbf{r}^{GX_i} \cdot \left(-m_i \, {}^E\mathbf{a}^{X_i}\right) \\ &= {}^E\mathbf{v}_r^G \cdot \sum_{i=1}^{N} \left(-m_i \, {}^E\mathbf{a}^{X_i}\right) + {}^E\boldsymbol{\omega}_r^G \cdot \sum_{i=1}^{N} \left(-m_i \mathbf{r}^{GX_i} \times {}^E\mathbf{a}^{X_i}\right) \\ &= {}^E\mathbf{v}_r^G \cdot \mathbf{F}^* + {}^E\boldsymbol{\omega}_r^G \cdot \mathbf{T}^* \end{aligned} \tag{4.47}$$

where $\mathbf{F}^*$ and $\mathbf{T}^*$ are force and moment passing through the center of mass respectively and written as

$$\mathbf{F}^* = -M\mathbf{a}^G \tag{4.48}$$

$$\mathbf{T}^* = -\mathbf{I} \cdot \boldsymbol{\alpha} - \boldsymbol{\omega} \times \left(\mathbf{I} \cdot \boldsymbol{\omega}\right) \tag{4.49}$$

where M is the mass of rigid body, $\mathbf{I}$ is the central inertia dyadic of the rigid body, $\mathbf{a}^G$ is the acceleration of center of mass, $\boldsymbol{\omega}$ and $\boldsymbol{\alpha}$ are the angular velocity and angular acceleration of the rigid body respectively.

For the floating wind turbine model in FAST, the generalized inertia forces are separately calculated from the rigid body components with mass, then summed up together to get the total generalized inertia forces.

$$F_r^* = F_r^*\big|_{Platform} + F_r^*\big|_{Tower} + F_r^*\big|_{Nacelle} + F_r^*\big|_{Hub} + F_r^*\big|_{Blades} \tag{4.50}$$

The detail derivations of all generalized inertia forces are beyond the scope of this study so are not presented.

4.7 Kane's Equations

FAST uses Kane's method to derive the dynamic equations of motion. Once the equation of motion is set up, it can be solved by numerical integration. Kane's method provides an elegant formulation of the dynamical equations of motion, and it simply state that the sum of the generalized active forces and the generalized inertia forces, for each generalized coordinate, is zero. That is

$$F_r + F_r^* = 0 \qquad \left(r = 1, 2, ..., n\right) \tag{4.51}$$

Kane first published the above equation in 1961 (Kane, 1961). Intuitively, the Kane's equations can be interpreted as the sum of a projection of the applied and inertia forces along the directions of the partial velocity vectors is zero.

By substituting the kinematic expressions in the previous section into Equation (4.51), we can obtain a set of n coupled dynamic equations of motion of the entire floating wind turbine system, which can be written as

$$\sum_{s=1}^{n} C_{rs}\ddot{q}_s + f_r\left(\dot{q}_r, q_r\right) = 0 \qquad \left(r = 1,2,...,n\right) \tag{4.52}$$

The first term in Equation (4.52) includes the known coefficient C_{rs}, and the acceleration terms, while the second term includes the lower order terms as a function of velocity and displacement of each degree of freedom. This equation is expanded into matrix form as

$$\begin{bmatrix} C_{11} & C_{12} & \cdots & \cdots & \cdots & C_{1n} \\ C_{21} & C_{22} & & \vdots & & C_{2n} \\ \vdots & & \ddots & & & \vdots \\ \vdots & \cdots & \cdots & C_{rs} & \cdots & \vdots \\ \vdots & & & \vdots & \ddots & \vdots \\ C_{n1} & C_{n2} & \cdots & \cdots & \cdots & C_{nn} \end{bmatrix} \begin{Bmatrix} \ddot{q}_1 \\ \ddot{q}_2 \\ \vdots \\ \ddot{q}_s \\ \vdots \\ \ddot{q}_n \end{Bmatrix} = \begin{Bmatrix} -f_1(\dot{q}_1, q_1) \\ -f_2(\dot{q}_2, q_2) \\ \vdots \\ -f_r(\dot{q}_r, q_r) \\ \vdots \\ -f_n(\dot{q}_n, q_n) \end{Bmatrix} \tag{4.53}$$

At each time step, the right hand side of Equation (4.53) is filled up using the fourth-order Adams-Bashforth predictor method; the Gauss elimination technique is then applied to obtain the accelerations of the entire DOFs. These accelerations are then used as the estimate for the next step. Finally, a fourth-order Adams-Mounton corrector is used to make the final estimate and to determine the accelerations. Once the motion and applied load are specified by solving the equations of motion, then the local loads at various point of the wind turbine can be calculated by performing simple summations of these loads.

4.8 Coupling between FAST and CHARM3D

CHARM3D is 3D hull-mooring-riser fully coupled static/dynamic analysis tool which was developed by Prof. M.H. Kim's research group during the past two decades (Kim et al., 2001; Ran et al., 1999; Tahar and Kim, 2003; Yang and Kim, 2010). The CHARM3D has been verified through numerous comparisons against experiments and field data during the past decade. Figure 4.3 shows a simple example that CHAMR3D can handle. The hydrodynamic coefficients including added mass, radiation damping, first and second order wave forces and mean drift forces of floater are obtained by a 3D diffraction/radiation preprocessor WAMIT in the frequency domain, and then transferred to CHARM3D for the time domain calculation.

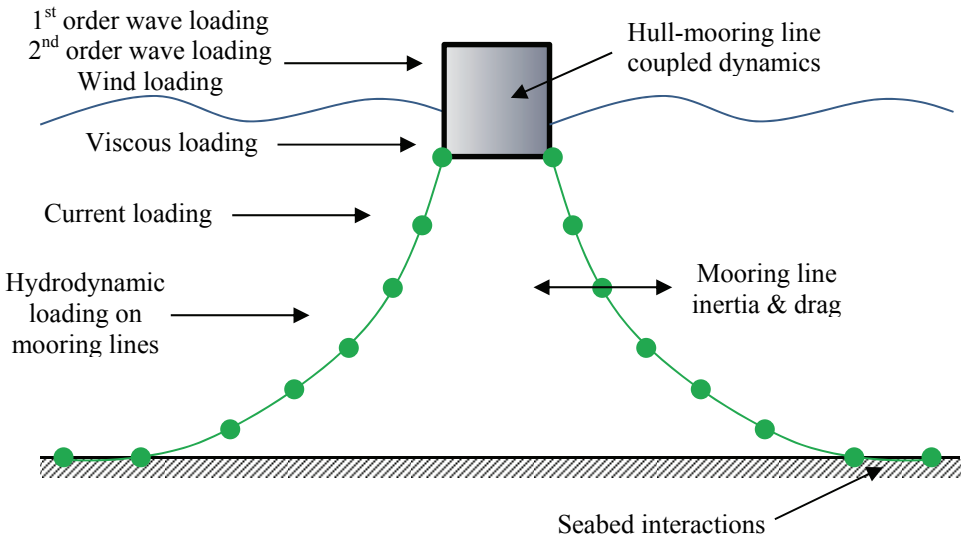

Figure 4.3 Coupled hull and mooring, riser analysis

In CHARM3D, the floating platform is assumed to be a rigid body undergoing motion in waves, winds, and currents, and the mooring lines are modeled as a higher-order finite element model. The mooring line dynamics due to the wave kinematics and its inertia and drag can be also included in the analysis. The entire mooring/riser dynamics and hull motions are solved simultaneously in a combined system matrix at each time step.

The equation of motion of a floating body in the time domain can be expressed as below.

$$[M + M^a(\infty)]\ddot{\zeta} = \mathbf{F}_I(t) + \mathbf{F}_c(t,\dot{\zeta}) + \mathbf{F}_n(t,\dot{\zeta}) + \mathbf{F}_m(t,\zeta) + \mathbf{F}_{hs}(\zeta) \tag{4.54}$$

where, $\mathbf{F}_I(t)$ is wave exciting force, $\mathbf{F}_c(t,\dot{\zeta})$ is radiation damping force, $\mathbf{F}_n(t,\dot{\zeta})$ is nonlinear viscous drag force, $\mathbf{F}_m(t,\zeta)$ is mooring restoring force and $\mathbf{F}_{hs}(\zeta)$ is hydrostatic force. M and $M^a(\infty)$ are the floating body mass and added mass at infinite frequency respectively.

At the initial stage of coupling, the platform added mass at infinite frequency, $M^a(\infty)$ and hydrostatic coefficients are transferred to FAST from CHARM3D. During the time marching simulation, FAST calculates all the dynamics of blade, rotor, tower including floating platform, and CHARM3D feeds the required forces of the platform into FAST. Those forces are properly fed into the generalized active forces in Equation (4.45), and the platform added mass transferred to FAST is used to calculate the generalized inertia force of the platform inside the FAST. The forces calculated by CHARM3D include the hydrodynamic wave force (first-order wave-frequency and

second-order sum- and difference-frequency), viscous force of Morison members, radiation damping force in the form of convolution integral, and mooring restoring force. The mooring restoring force can be estimated from the top tension of each mooring line and its directional cosine. The nonlinear viscous drag forces on Morison members are evaluated at the instantaneous body position and up to the instantaneous free-surface elevation. Then FAST computes the entire dynamics of wind turbine including platform response using the forces from CHARM3D and returns the updated displacement and velocity of platform to CHARM3D. Then CHARM3D recursively calculates the updated forces based on the new position and velocity of platform. Figure 4.4 shows the schematic diagram of coupling between CHARM3D and FAST. A possibly simpler coupling approach through transmitted forces and moments at the tower base was also experimented by Shim and Kim (Shim and Kim, 2008) and it was seen that it cannot fully account for the entire features of the more complicated couplings between the rotor and floater.

The time step of the CHARM3D side should be determined by the time step of the FAST side since FAST requires platform forces, which are generated by CHARM3D, at every internal time step. So, both modules should have the similar time step or CHARM3D can have a slightly larger time step. The time step of the CHARM3D side should be carefully determined so that CHARM3D may not feed large variation of mooring restoring force to FAST.

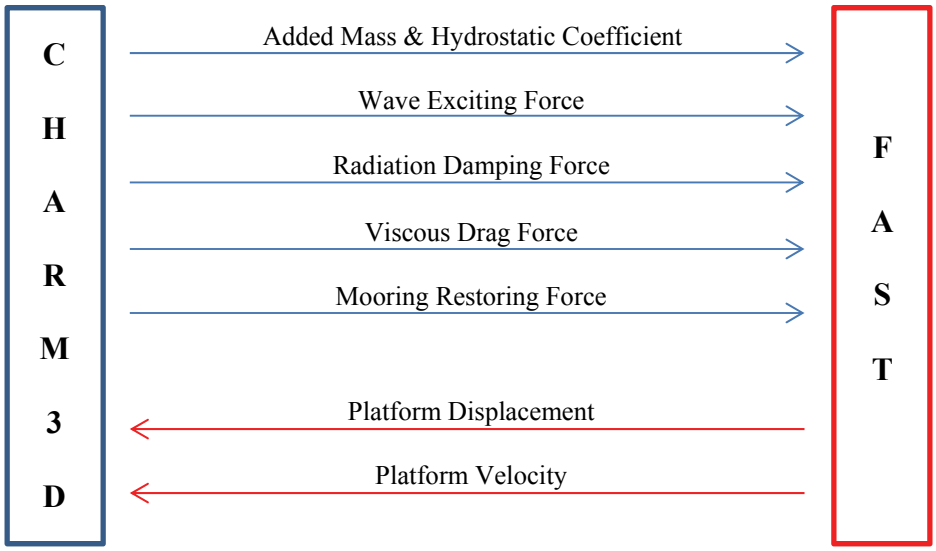

Figure 4.4 Data transfer between CHARM3D and FAST

5. DYNAMICS OF A MULTIPLE UNIT FLOATING OFFSHORE WIND TURBINE

5.1 Introduction

In this chapter, the dynamic equation of motion for multiple unit offshore wind turbines in the time domain is established by utilizing the equations of motion for single floating wind turbines. The dynamic behavior of MUFOWT can be derived from full DOFs of single floating wind turbines including 6-DOFs of floating platform, and additional wind turbine DOFs with proper platform-turbine coupling terms. The entire MUFOWT system equations of motion are built in one global coefficient matrix with forcing functions, and then solved simultaneously at each time step. Assuming that every degree of freedom for a three-bladed turbine in FAST is turned on, the total DOFs of MUFOWT can be expressed as $6+18\times N$, where N is total number of turbines. The generalized inertia and active forces from each turbine should be independently taken into account and applied to the floating platform at the same time, but the generalized inertia and active force of a floating platform should be included only once. The coupled terms between a floating platform and each turbine in the coefficient matrix should be derived by accounting for every effect of generalized inertia and active forces from both bodies. In the case of the coupling terms between one turbine and another one, the coefficients are set to zero because a direct kinematic or kinetic relationships between each turbine does not exist.

5.2 Equations of Motion

The equations of motion for MUFOWT can be basically derived by summation of equations of motion from the single wind turbine. Assuming that there are total N turbines in one floating platform as can be seen in Figure 5.1, the total generalized active forces and the generalized inertia forces of N turbines and the floating platform are now derived.

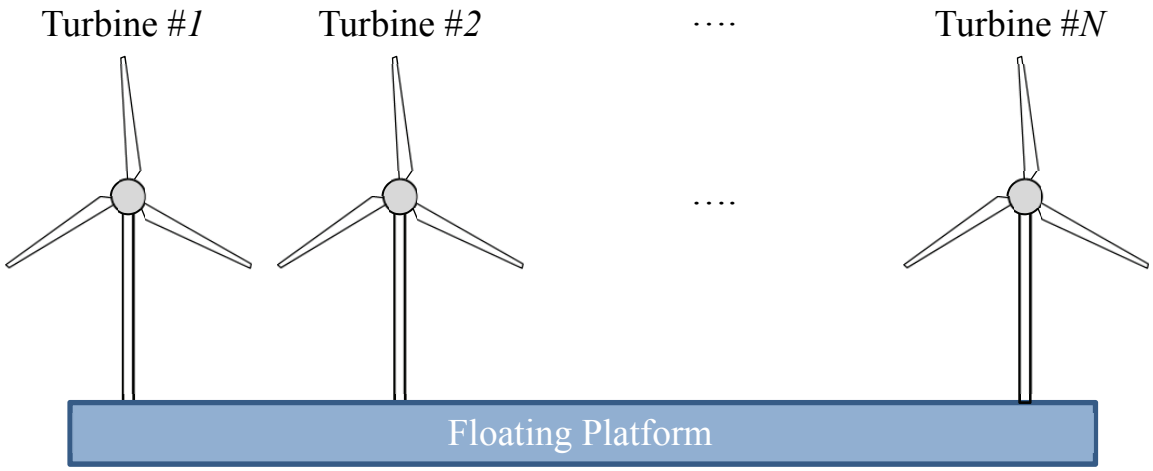

Figure 5.1 Schematic configuration of MUFOWT

5.2.1 Generalized Active Force

The generalized active force on the whole MUFOWT system can be divided into turbine part and floating platform part. For turbines on top of the platform, the generalized active force can be obtained separately from each turbine. Aero dynamic, elastic, gravity, generator, and damping force for each turbine are summed up

individually and arranged one by one. Then the generalized active force of each turbine without floating platform can be expressed as

$$\begin{cases} F_r^{Turbine\#1} = F_r\big|_{Aero}^{Turbine\#1} + F_r\big|_{Elastic}^{Turbine\#1} + F_r\big|_{Gravity}^{Turbine\#1} + F_r\big|_{Generator}^{Turbine\#1} + F_r\big|_{Damping}^{Turbine\#1} \\ F_r^{Turbine\#2} = F_r\big|_{Aero}^{Turbine\#2} + F_r\big|_{Elastic}^{Turbine\#2} + F_r\big|_{Gravity}^{Turbine\#2} + F_r\big|_{Generator}^{Turbine\#2} + F_r\big|_{Damping}^{Turbine\#2} \\ \vdots \\ F_r^{Turbine\#N} = F_r\big|_{Aero}^{Turbine\#N} + F_r\big|_{Elastic}^{Turbine\#N} + F_r\big|_{Gravity}^{Turbine\#N} + F_r\big|_{Generator}^{Turbine\#N} + F_r\big|_{Damping}^{Turbine\#N} \end{cases} \tag{5.1}$$

So, the total generalized active forces of N turbines excluding floating platform can be written as a summation of Equation (5.1).

$$F_r^{Total\ Turbines} = F_r^{Turbine\#1} + F_r^{Turbine\#2} + \cdots + F_r^{Turbine\#N} \tag{5.2}$$

The generalized active force on the floating platform should be taken into account separately from the turbines because the platform is not individually arranged but positioned as a whole body and expressed as

$$F_r^{Platform} = F_r\big|_{Hydro} + F_r\big|_{Mooring} \tag{5.3}$$

This means that the generalized active force on the platform comes from hydrodynamic force and mooring line restoring force, and should be accounted for only once.

By combining Equations (5.2) and (5.3), the total generalized active forces on the MUFOWT can be established as shown below in Equation (5.4).

$$
\begin{aligned}
F_r &= F_r^{Total\ Turbine} + F_r^{Platform} = F_r^{Turbine\#1} + F_r^{Turbine\#2} + \cdots + F_r^{Turbine\#N} + F_r^{Platform} \\
&= F_r\big|_{Aero}^{Turbine\#1} + F_r\big|_{Elastic}^{Turbine\#1} + F_r\big|_{Gravity}^{Turbine\#1} + F_r\big|_{Generator}^{Turbine\#1} + F_r\big|_{Damping}^{Turbine\#1} \\
&\quad + F_r\big|_{Aero}^{Turbine\#2} + F_r\big|_{Elastic}^{Turbine\#2} + F_r\big|_{Gravity}^{Turbine\#2} + F_r\big|_{Generator}^{Turbine\#2} + F_r\big|_{Damping}^{Turbine\#2} \\
&\quad + \cdots \\
&\quad + F_r\big|_{Aero}^{Turbine\#N} + F_r\big|_{Elastic}^{Turbine\#N} + F_r\big|_{Gravity}^{Turbine\#N} + F_r\big|_{Generator}^{Turbine\#N} + F_r\big|_{Damping}^{Turbine\#N} \\
&\quad + F_r\big|_{Hydro} + F_r\big|_{Mooring}
\end{aligned}
\tag{5.4}
$$

5.2.2 Generalized Inertia Force

Similarly, the generalized inertia force can be also expressed for MUFOWT. First, the generalized inertia forces from each turbine are obtained. The inertial loadings of each turbine, such as tower, nacelle, hub and blades are calculated based on the mass and inertia properties of each component and summarized with respect to the tower base origin for each turbine. The generalized inertia force of each turbine can be expressed as

$$
\begin{cases}
F_r^{*\ Turbine\#1} = F_r^*\big|_{Tower}^{Turbine\#1} + F_r^*\big|_{Nacelle}^{Turbine\#1} + F_r^*\big|_{Hub}^{Turbine\#1} + F_r^*\big|_{Blades}^{Turbine\#1} \\
F_r^{*\ Turbine\#2} = F_r^*\big|_{Tower}^{Turbine\#2} + F_r^*\big|_{Nacelle}^{Turbine\#2} + F_r^*\big|_{Hub}^{Turbine\#2} + F_r^*\big|_{Blades}^{Turbine\#2} \\
\qquad\qquad\qquad\qquad\qquad\qquad \vdots \\
F_r^{*\ Turbine\#N} = F_r^*\big|_{Tower}^{Turbine\#N} + F_r^*\big|_{Nacelle}^{Turbine\#N} + F_r^*\big|_{Hub}^{Turbine\#N} + F_r^*\big|_{Blades}^{Turbine\#N}
\end{cases}
\tag{5.5}
$$

Thus, total generalized inertia forces of turbines without floating platform are

$$
F_r^{*\ Total\ Turbine} = F_r^{*\ Turbine\#1} + F_r^{*\ Turbine\#2} + \cdots + F_r^{*\ Turbine\#N} \tag{5.6}
$$

If we include the generalized inertia force from the floating platform obtained by the platform mass property, then the total generalized inertia force of MUFOWT can be expressed as below.

$$
\begin{aligned}
F_r^* &= F_r^{*\,Total\ Turbine} + F_r^*\big|_{Platform} = F_r^{*\,Turbine\#1} + F_r^{*\,Turbine\#2} + \cdots + F_r^{*\,Turbine\#N} + F_r^*\big|_{Platform} \\
&= F_r^*\big|_{Tower}^{Turbine\#1} + F_r^*\big|_{Nacelle}^{Turbine\#1} + F_r^*\big|_{Hub}^{Turbine\#1} + F_r^*\big|_{Blades}^{Turbine\#1} \\
&\quad + F_r^*\big|_{Tower}^{Turbine\#2} + F_r^*\big|_{Nacelle}^{Turbine\#2} + F_r^*\big|_{Hub}^{Turbine\#2} + F_r^*\big|_{Blades}^{Turbine\#2} \\
&\quad + \cdots \\
&\quad + F_r^*\big|_{Tower}^{Turbine\#N} + F_r^*\big|_{Nacelle}^{Turbine\#N} + F_r^*\big|_{Hub}^{Turbine\#N} + F_r^*\big|_{Blades}^{Turbine\#N} \\
&\quad + F_r^*\big|_{Platform}
\end{aligned}
\tag{5.7}
$$

Note that the inertia force from the platform is only accounted for once to obtain the total generalized inertia force of MUFOWT system.

The velocity vectors inside the above generalized forces should be calculated based on the tower base position vectors which are uniquely determined by the location of each turbine base relative to the platform reference point.

$$
{}^E\mathbf{v}^{T0}\big|_{Turbine\#N} = {}^E\mathbf{v}^Z + {}^E\boldsymbol{\omega}^X \times \mathbf{r}^{ZT0}\big|_{Turbine\#N} \tag{5.8}
$$

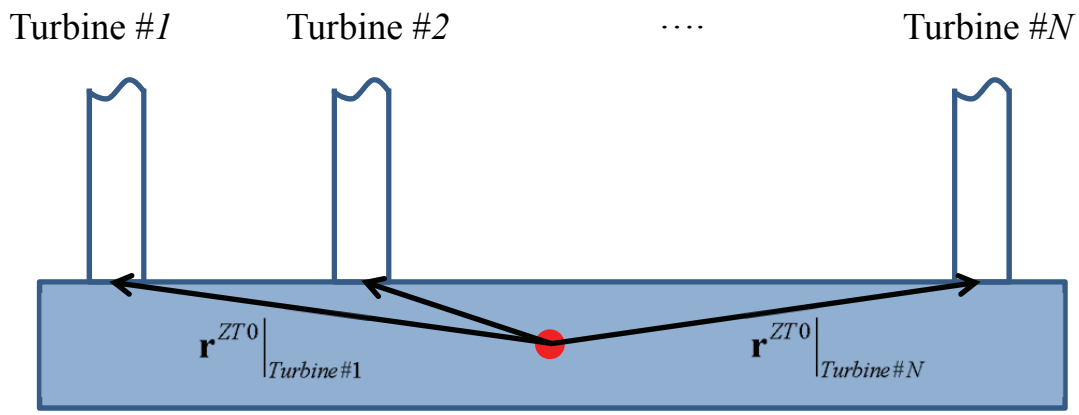

Figure 5.2 Tower base position vectors

For example, the relative velocity vector of tower base position in Equation (5.8) is determined by a different tower base position vector of $\mathbf{r}^{ZT0}$ in Figure 5.2.

Once the tower base velocity, acceleration, and partial velocity vectors for each turbine are derived based on the different tower base position vector above, the consecutive kinematic vectors such as tower top, nacelle, hub and blade vectors are determined successively. Finally, the total equations of motion of MUFOWT can be established using Kane's equation as we did in the single turbine analysis.

5.3 Coefficient Matrix of Kane's Dynamics

In case of a three-bladed single floating turbine, the coefficient matrix $[C_{rs}]$ in Equation (4.53) can be expressed by components from the floating platform to the blades.

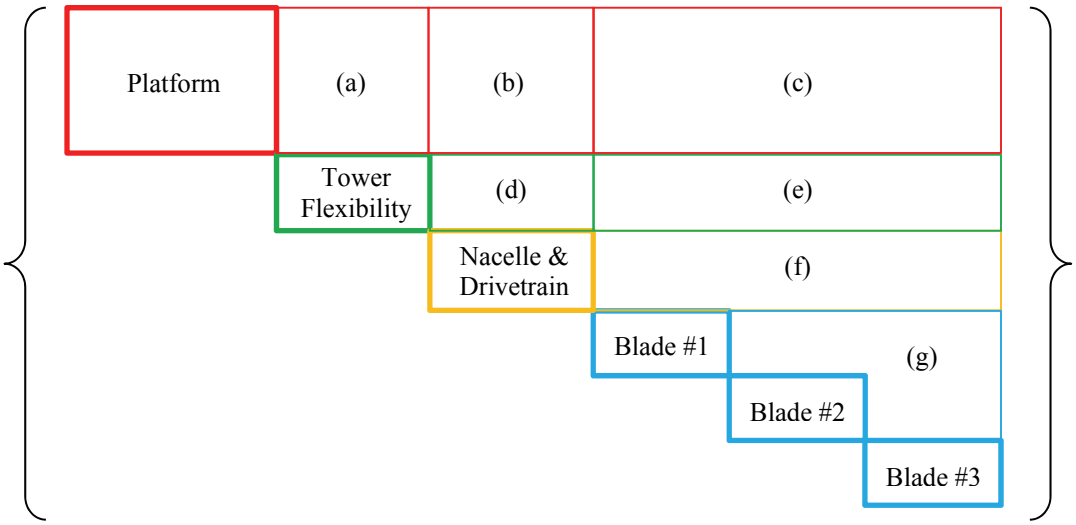

Figure 5.3 Coefficient matrix of single turbine and platform

The coefficient matrix in Figure 5.3 shows that the dynamic responses of turbine part, including tower, nacelle and blades, are coupled with the platform DOFs as there are off-diagonal terms between platform and turbine which are represented by (a) ~ (c) terms. The off-diagonal terms denoted by (d) ~ (g) terms represent the dynamic coupling between turbine components. For example, the terms (d) represent the coupling between tower flexibility and the nacelle dynamics, and (f) denote the coupling between nacelle or drivetrain and blades. It is seen that there is no dynamic coupling between each blade, so the off-diagonal terms (g) are null matrix. This is true because there is no direct kinematic or kinetic relationship between each blade as their dynamics can be transmitted to another blade only through the hub.

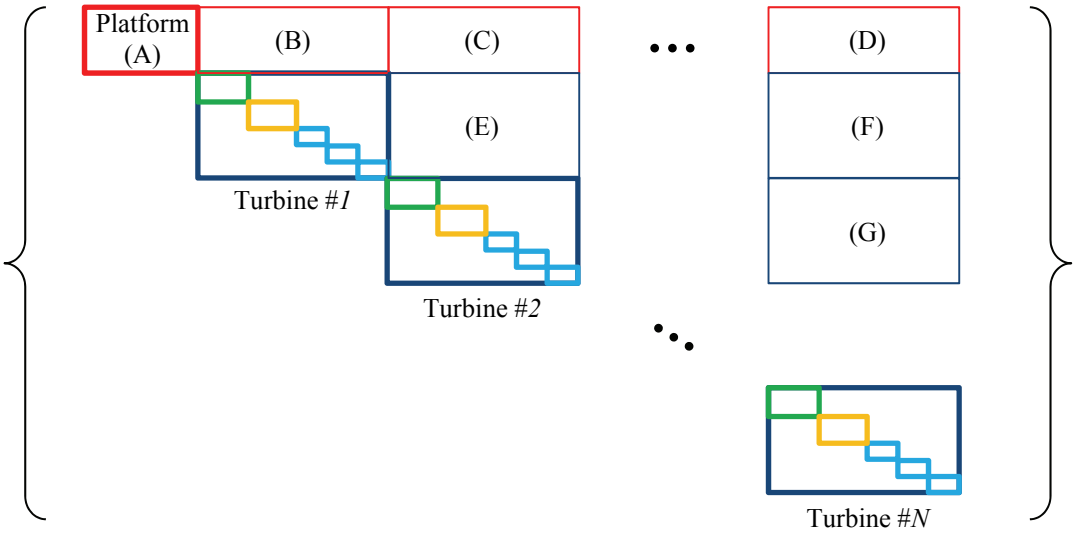

Figure 5.4 Coefficient matrix of multiple turbines and platform

In the case of MUFOWT, it is expected that the dynamic coupling terms between one turbine and another do not exist since the turbine response of one turbine can affect another turbine only through the floating platform. In this regard, the dynamic coupling terms between the floating platform and each turbine are important and should be properly taken into consideration. So, the coefficient matrix $\left[C_{rs}\right]$ for MUFOWT can be depicted as in Figure 5.4.

In this global coefficient matrix, the off-diagonal terms (B) and (C) represent the dynamic coupling between the floating platform and turbine #1 and turbine #2 respectively. As mentioned above, the off-diagonal terms (E) ~ (G), which represent the dynamic coupling between one turbine and another, are null matrix. The only way to interact between two turbines is through the floating platform which is represented in terms (B) ~ (D). If there are connecting structural members between two separated turbine towers, such as brace or truss, then the coupling terms between the two turbines (E) ~ (G) should not be zero.

As pointed out earlier, the coefficient matrixes for each turbine are determined based on the different tower base position vectors as well as the dependent platform coupling terms (B) ~ (D).

5.4 Force Vector of Kane's Dynamics

The right hand side of Equation (4.53) would be forcing terms as a function of displacement and velocity of each degree of freedom. The forcing function represented by $-f_r\left(\dot{q}_r, q_r\right)$ for a single floating turbine is depicted in Figure 5.5.

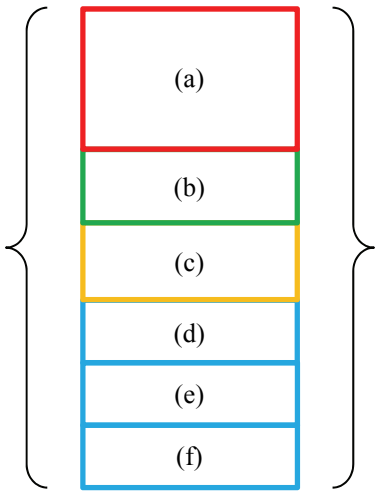

Figure 5.5 Forcing vector of single turbine and platform

where, (a) is the platform loading, which includes the loadings from the turbine part, (b) is the tower top fore-aft or side-to-side loading, (c) is the nacelle and drivetrain loading, (d) ~ (f) represent the blade loadings. In case of a floating wind turbine, the hydrodynamic loading due to radiation damping, hydrodynamic wave loading, hydrostatic loading, viscous loading, and mooring line restoring loading should be included in these (a) terms. Hydrodynamic added mass effect is not included in this part, but included in the coefficient matrix in the previous section. Aerodynamic loading on the blades should be positioned in (d) ~ (f). In a similar way, the force vector for MUFOWT can be established.

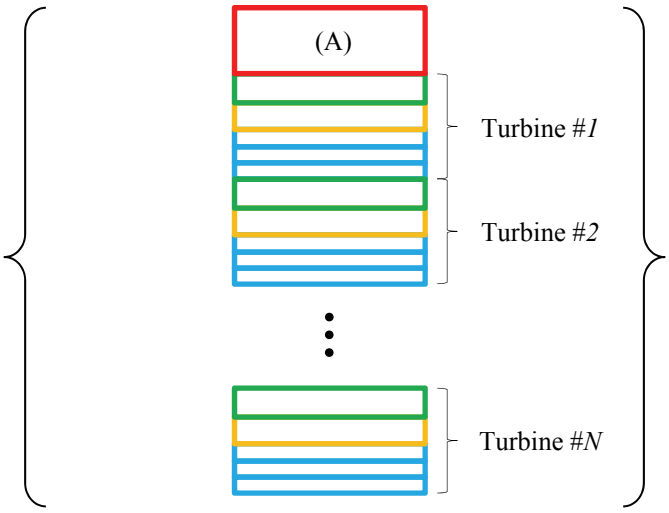

Figure 5.6 Forcing vector of multiple turbines and platform

The forcing term (A) in Figure 5.6 includes the hydrodynamic, hydrostatic loading, viscous loading, mooring line restoring loading, and the loading from each turbine. Additional loading terms on each turbine should be followed. Those turbine loading terms are also uniquely determined based on the position of the tower base.

5.5 Equations of Motion in FAST

The floating wind turbine solver FAST is basically designed to analyze a single floating wind turbine. Thus, the maximum DOFs for a three-bladed turbine are limited to 24. In this study, all of the global variables inside the FAST, including the AeroDyn module, are expanded so that it can afford one more dimension. For example, single variables are converted to the one dimensional array, and n dimensional variables are expanded to $n+1$ dimensional variables. One additional space is allocated for turbine ID

so all the inside calculations can be done for different turbines. One of the challenges in this work is to combine individual equations of motion for each turbine into global equations of motion. Since FAST is designed to build a full coefficient matrix $[C_{rs}]$ for a single turbine, rigorous modification work has been done in order to build a global matrix and solve the entire MUFOWT system simultaneously at given time step.

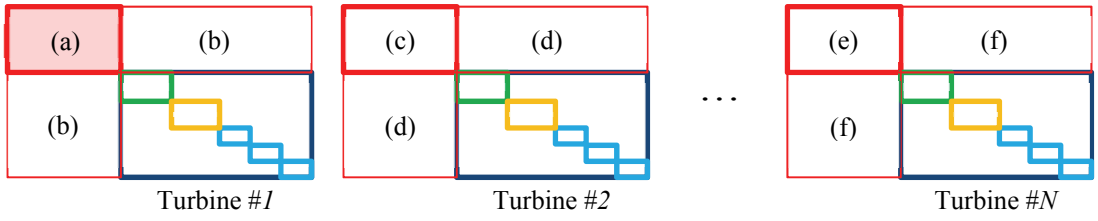

Figure 5.7 Series of coefficient matrices

As can be seen in Figure 5.7, FAST starts to build the coefficient matrix for turbine *#1* including the dynamic effect of floating platform, then repeat building the next coefficient matrix for turbine *#2*. The first step for filling up the coefficient matrix for turbine *#1* is quite a normal procedure, but attention should be paid for the next step to establish the coefficient matrix for turbine *#2* through turbine *#N*.

Since the inertia terms of the floating platform are already taken into account when the first coefficient matrix is built in (a), the platform inertia due to its mass and added mass should be eliminated from the (c) and (e) terms. This does not mean that those terms are null matrix because those portions still include the inertia loadings from the turbine. So, the coefficient matrix of (a), (c) and (e) can be expressed as

$$[C_{rs}]_{(a)} = [C_{rs}]_{Platform} + [C_{rs}]_{Hydro} + [C_{rs}]_{Tower\#1} + [C_{rs}]_{Nacelle\#1} + [C_{rs}]_{Rotor\#1} + [C_{rs}]_{Hub\#1} + [C_{rs}]_{Blades\#1} \tag{5.9}$$

$$[C_{rs}]_{(c)} = [C_{rs}]_{Tower\#2} + [C_{rs}]_{Nacelle\#2} + [C_{rs}]_{Rotor\#2} + [C_{rs}]_{Hub\#2} + [C_{rs}]_{Blades\#2} \tag{5.10}$$

$$[C_{rs}]_{(e)} = [C_{rs}]_{Tower\#N} + [C_{rs}]_{Nacelle\#N} + [C_{rs}]_{Rotor\#N} + [C_{rs}]_{Hub\#N} + [C_{rs}]_{Blades\#N} \tag{5.11}$$

On the other hand, the dynamic coupling terms between platform and turbines, such as (b), (d) and (f) should contain the platform inertia terms including hydro added mass term because the platform inertia has to influence all turbines.

$$[C_{rs}]_{(b)} = [C_{rs}]_{Platform} + [C_{rs}]_{Tower\#1} + [C_{rs}]_{Nacelle\#1} + [C_{rs}]_{Rotor\#1} + [C_{rs}]_{Hub\#1} + [C_{rs}]_{Blades\#1} \tag{5.12}$$

$$[C_{rs}]_{(d)} = [C_{rs}]_{Platform} + [C_{rs}]_{Tower\#2} + [C_{rs}]_{Nacelle\#2} + [C_{rs}]_{Rotor\#2} + [C_{rs}]_{Hub\#2} + [C_{rs}]_{Blades\#2} \tag{5.13}$$

$$[C_{rs}]_{(f)} = [C_{rs}]_{Platform} + [C_{rs}]_{Tower\#N} + [C_{rs}]_{Nacelle\#N} + [C_{rs}]_{Rotor\#N} + [C_{rs}]_{Hub\#N} + [C_{rs}]_{Blades\#N} \tag{5.14}$$

Finally, the global coefficient matrix with N turbines can be made by combining every coefficient matrix as a formation of Figure 5.4. Turbine inertia terms, (c) and (e), should be added to the platform inertia matrix in turbine #*1* represented by (A) in Figure 5.4. The other terms like (B) through (D) in Figure 5.4 are assigned by (b) ~ (f) as expressed below so that the global matrix has 6 platform DOFs plus $18 \times N$ turbines DOFs.

$$[C_{rs}]_{(A)} = [C_{rs}]_{(a)} + [C_{rs}]_{(c)} + \cdots + [C_{rs}]_{(e)} \tag{5.15}$$

$$[C_{rs}]_{(B)} = [C_{rs}]_{(b)} \tag{5.16}$$

$$[C_{rs}]_{(C)} = [C_{rs}]_{(d)} \tag{5.17}$$

$$[C_{rs}]_{(D)} = [C_{rs}]_{(f)} \tag{5.18}$$

The global force vector can also be made in a similar way. As can be seen in Figure 5.8, each force vector is built one by one and then combined so that it forms a global force vector.

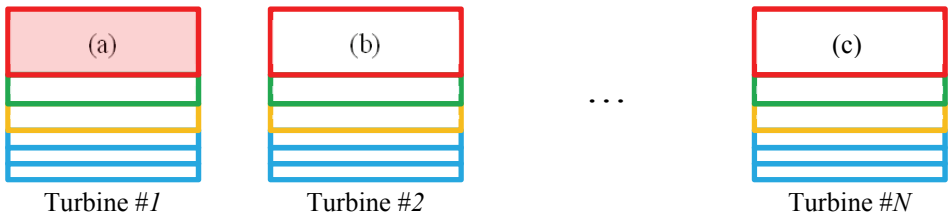

Figure 5.8 Series of forcing vectors

The platform loading terms in the turbine #2 vector through the turbine #N vector, represented by (b) and (c) terms in Figure 5.8, should not include the platform loadings such as hydrodynamic, hydrostatic, viscous, and mooring restoring forces. Those loadings are already included in the force vector in (a). Similarly, the terms (b) and (c) still contain the turbine loading portions.

$$\begin{aligned} -f_r(\dot{q}_r, q_r)\big|_{(a)} = &-f_r(\dot{q}_r, q_r)\big|_{Platform} - f_r(\dot{q}_r, q_r)\big|_{Hydro} - f_r(\dot{q}_r, q_r)\big|_{Tower\#1} - f_r(\dot{q}_r, q_r)\big|_{Nacelle\#1} \\ &- f_r(\dot{q}_r, q_r)\big|_{Hub\#1} - f_r(\dot{q}_r, q_r)\big|_{Blades\#1} - f_r(\dot{q}_r, q_r)\big|_{Aero\#1} \end{aligned} \tag{5.19}$$

$$-f_r\left(\dot{q}_r,q_r\right)\Big|_{(b)} = -f_r\left(\dot{q}_r,q_r\right)\Big|_{Tower\#2} - f_r\left(\dot{q}_r,q_r\right)\Big|_{Nacelle\#2} - f_r\left(\dot{q}_r,q_r\right)\Big|_{Hub\#2} - f_r\left(\dot{q}_r,q_r\right)\Big|_{Blades\#2} - f_r\left(\dot{q}_r,q_r\right)\Big|_{Aero\#2} \tag{5.20}$$

$$-f_r\left(\dot{q}_r,q_r\right)\Big|_{(c)} = -f_r\left(\dot{q}_r,q_r\right)\Big|_{Tower\#N} - f_r\left(\dot{q}_r,q_r\right)\Big|_{Nacelle\#N} - f_r\left(\dot{q}_r,q_r\right)\Big|_{Hub\#N} - f_r\left(\dot{q}_r,q_r\right)\Big|_{Blades\#N} - f_r\left(\dot{q}_r,q_r\right)\Big|_{Aero\#N} \tag{5.21}$$

Finally, the global force vector in Figure 5.6 can be made by summation of the platform loading terms, and distributing all the other turbine force vectors successively. The forcing term (A) in Figure 5.6 is going to be

$$-f_r\left(\dot{q}_r,q_r\right)\Big|_{(A)} = -f_r\left(\dot{q}_r,q_r\right)\Big|_{(a)} - f_r\left(\dot{q}_r,q_r\right)\Big|_{(b)} - \cdots - f_r\left(\dot{q}_r,q_r\right)\Big|_{(c)} \tag{5.22}$$

Once the global coefficient matrix and force vector are established, then the built-in Gauss elimination solver inside the FAST can handle those global equations of motion for MUFOWT.

5.6 Consideration of the Shade Effect

The interference or shade effect of turbines in the MUFOWT is one of the biggest concerns in designing the size and capacity of a platform. Figure 5.9 shows the considerable wake effect observed behind the Horns Rev offshore wind farm west of Denmark. Due to this wake effect between turbines, the efficiency of the power production will be significantly decreased and the dynamic loadings of downstream turbines will be increased.

Figure 5.9 Wake turbulence behind individual wind turbines (Courtesy of Vattenfall Wind Power, Denmark)

To minimize this wake effect, turbines are typically arranged with enough spacing. The distance between wind turbines is commonly determined by the rotor diameter and local wind conditions. One of the research suggests spacing turbines between 5 and 10 rotor diameters apart. If prevailing winds are generally from the same direction, turbines may be installed 3 or 4 rotor diameters apart in the direction perpendicular to the prevailing winds. Under multidirectional wind conditions, a space from 5 to 7 rotor diameters is recommended (Global Energy Concepts and AWS Truewind LLC, 2005) between each turbine as can be seen in Figure 5.10.

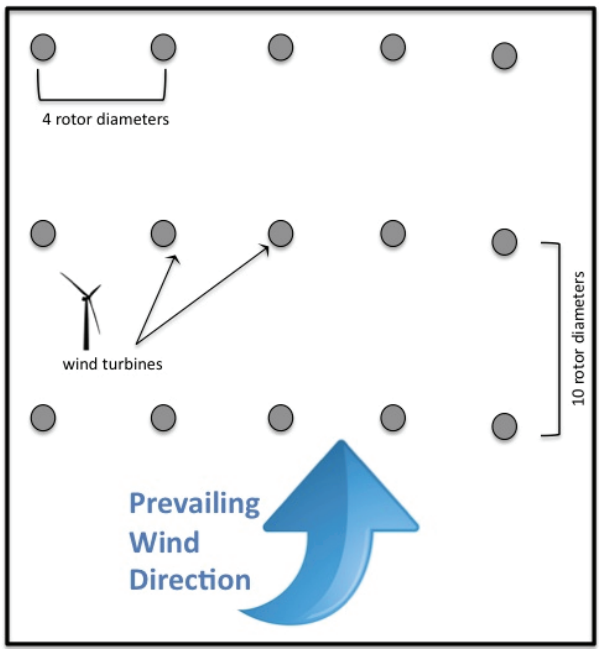

Figure 5.10 Turbine spacing recommendation (Courtesy of http://en.openei.org/)

It is known that the power loss of a downstream turbine can reach up to 40% in full wake conditions; if various wind directions are considered the overall loss of power is around 8% for onshore wind farms and 12% for offshore farms (Barthelmie et al., 2009; Barthelmie et al., 2008). Hence, the accurate simulation of the wake effect between neighboring turbines on a wind farm is very important. Recently, the performances of several numerical wake models for offshore wind farm design have been proposed and evaluated (Rados et al., 2001). More recently, the numerical computation using CFD program with Actuator Line Method and Actuator Disc Method are performed (Ivanell et al., 2007; Mikkelsen, 2003). However, the wake effects and how they impact wind turbines and plant performance have not been well understood due to the complex behavior of turbulent wind field at downstream side.

That shade effect could be a big concern in the MUFOWT design as well, since the size of a platform is limited compared to the land site, and some of the rotors could be partly located at a shadow area of the other turbines. This aspect has been addressed by the CFD analysis and the model test was conducted by WindSea AS in Norway. As introduced in the chapter 1, their semi-submersible platform supports two upwind turbines and one downwind turbine (3.6MW each). They proved that the turbulent wind field at the aft turbine is moderated and smaller than the one in land-based wind turbines.

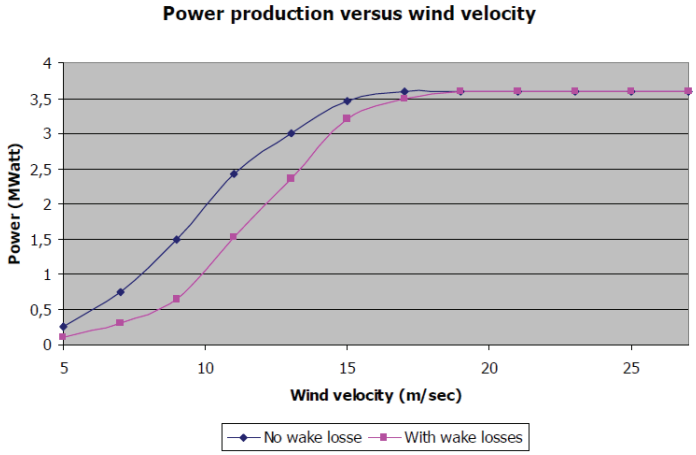

Figure 5.11 Power production for downwind turbine (Lefranc and Torud, 2011)

According to their research (Lefranc and Torud, 2011), the loss of a power production due to the wake effect is significant for the low wind velocity range while for high velocity condition, the power production does not make big differences, as can be seen in Figure 5.11. The upper line represents the power production of the downwind turbine without any shade effect, while the lower line is for the downwind turbine accounting the shade effect from the two upwind turbines. Risø calculated the annual

reduction ratio of a power production for the shaded turbine, and it was estimated at 25%. If the front turbines are included in the efficiency estimation, then the reduction ratio with a downtime of 15% is estimated to be 7%. This reduction factor is strongly dependent on turbine properties, turbine position and given environmental conditions thus an optimal arrangement of turbines and a proper site installation may reduce those negative shade effects.

If the power reduction ratio and the increased turbulence intensity of the shaded turbine are known parameters from the experiment, the wake effect can be partially included in the numerical simulations by applying different wind field input for each turbine. For example, the wake effect on the rear turbine in Figure 5.12 can be numerically simulated with reduced wind velocity and increased turbulence intensity of the separated rear-side wind field.

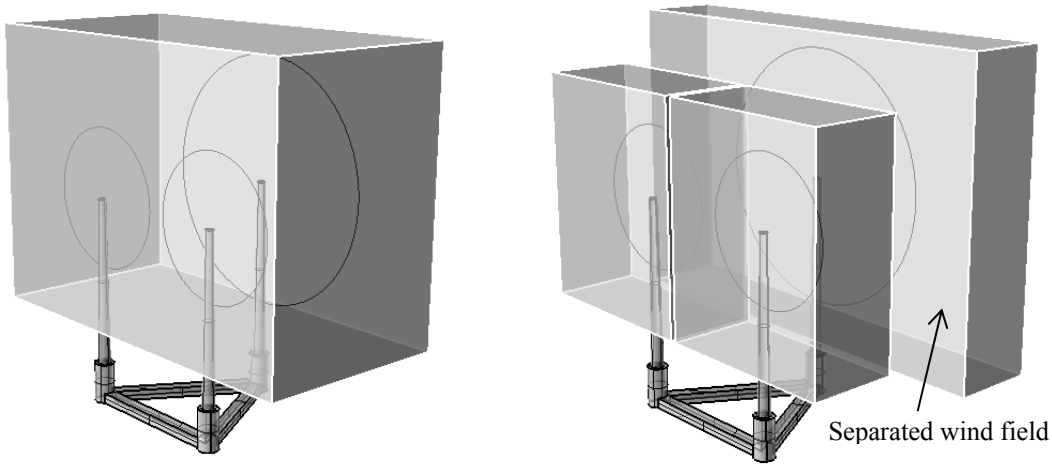

(a) (b)

Figure 5.12 Global wind field (a) and separated wind field (b)

In this study, numerical wake effects between neighboring turbines are not assessed because of the uncertainty and the complexity. Instead, the arrangement of turbines is determined so as to maximize the exposed area of each turbine and minimize the overlapped areas.

6. CASE STUDY I: SINGLE-TURBINE HYWIND SPAR*

6.1 Introduction

Recently, considerable research progress has been made in the single turbine floating platform area. Several different kinds of floating platforms are suggested as a turbine base platform and their performance and cost effectiveness are checked (Butterfield et al., 2007). Most general types of floating platforms for single wind turbines are classified into three categories based on the physical properties that are used to ensure static stability. The first type is a Spar-buoy type platform. This type of platform achieves stability by ballast weights hung below a central buoyancy tank which make a very low center of gravity for the whole system. The second type is a tension leg platform (TLP) type which achieves stability through mooring line tension. The last type is a barge or semi-submersible type. Stability in this type is achieved by the distributed buoyancy and righting arm that may generate positive restoring moment for the platform. Recently, it is regarded that the semi-submersible platform has become more popular because of better response characteristics in an ocean environment compared to a barge.

In this chapter, the performances of a single turbine platform are assessed before we move on to multiple turbine case studies. The Hywind spar type designed for 320m water depth is selected as a floating platform and NREL's 5MW baseline turbine is mounted on top of the platform (Jonkman, 2010). The present analysis method integrates

* Part of this chapter is reprinted with permission from "Aero-elastic-control-floater-mooring coupled dynamic analysis of floating offshore wind turbines" and "Influence of control strategy to FOWT hull motions by aero-elastic-control-floater-mooring coupled dynamic analysis" by Bae and Kim, 2011. Proceedings of the 21st (2011) International Offshore and Polar Engineering Conference, Copyright [2011] by the International Society of Offshore and Polar Engineers (ISOPE)

rotor dynamics and control, aero-dynamics, tower elasticity, floater dynamics, and mooring-line dynamics to investigate the full dynamic coupling among them in the time domain. The corresponding rotor-floater-mooring coupled dynamic analysis computer program is developed by combining the respective modules. For the dynamics and control of blade and tower, the primary design code of wind turbines, FAST, developed by the National Renewable Energy Laboratory (NREL), is employed (Jonkman and Buhl Jr, 2005). The portion of the FAST algorithm is modified to include some features of the floater-mooring coupled dynamic analysis program, CHARM3D, and vice versa so that the full coupling of rotor and floater can be accurately achieved.

The work presented in this chapter is based on the two conference proceedings (Bae et al., 2011a; Bae et al., 2011b) presented in the 21st International Offshore and Polar Engineering Conference.

6.2 Numerical Model for 5MW Hywind Spar

The adopted model of the 5MW turbine is the NREL offshore 5MW baseline wind turbine which has been adopted as the reference model for the integrated European UpWind research program. The Hywind floating platform in this case study is the 'OC3-Hywind' spar-buoy type platform which is slightly different from the actual turbine used by Statoil of Norway. The detailed specifications of 5MW turbine and Hywind spar hull are summarized in Tables 6.1 and 6.2. The characteristics of the mooring system are tabulated in Table 6.3.

Table 6.1 Specification of 5MW turbine

Item	Unit	Value
Tower height	m	90.0
Rotor diameter	m	126.0
Tower diameter (top)	m	3.87
Tower diameter (bottom)	m	6.5
Elevation to Tower Base above SWL	m	10
Elevation to Tower Top above SWL	m	87.6
Overall Tower mass	kg	249,718
Total wind turbine weight (except for platform)	kg	599,718
CM Location of Tower above SWL	m	43.4
Tower Structural Damping Ratio (All modes)	%	1

Table 6.2 Specification of Hywind spar platform

Item	Unit	Value
Depth to Platform Base below SWL	m	120.0
Elevation to Platform Top Above SWL	m	10
Depth to Top of Taper Below SWL	m	4
Depth to Bottom of Taper Below SWL	m	12
Platform Diameter Above Taper	m	6.5
Platform Diameter Below Taper	m	9.4
Platform Mass, including Ballast	kg	7,466,330
CM Location Below SWL	m	89.9155
Platform Roll Inertia about CM	$kg \cdot m^2$	4,229,230,000
Platform Pitch Inertia about CM	$kg \cdot m^2$	4,229,230,000
Platform Yaw Inertia about Platform Centerline	$kg \cdot m^2$	164,230,000

The Hywind spar is moored by three catenary lines. To increase the yaw stiffness of the platform, the lines are attached to the hull via a delta connection. This delta-connection effect is included in the time domain simulation by adding the corresponding yaw spring stiffness.

Table 6.3 Specification of Hywind spar mooring system

Item	Unit	Value
Number of Mooring Lines	ea	3
Angle Between Adjacent Lines	deg	120
Depth to Anchors Below SWL (Water Depth)	m	320
Depth to Fairleads Below SWL	m	70.0
Radius to Anchors from Platform Centerline	m	853.87
Radius to Fairleads from Platform Centerline	m	5.2
Unstretched Mooring Line Length	m	902.2
Mooring Line Diameter	m	0.09
Equivalent Mooring Line Mass Density	kg/m	77.7066
Equivalent Mooring Line Weight in Water	N/m	698.094
Equivalent Mooring Line Extensional Stiffness	N	384,243,000
Additional Yaw Spring Stiffness	Nm/rad	98,340,000

Each mooring line is modeled by 20 higher-order finite elements with an unstretched length of 902.2m. Illustrations of mooring line arrangement are shown in Figure 6.1.

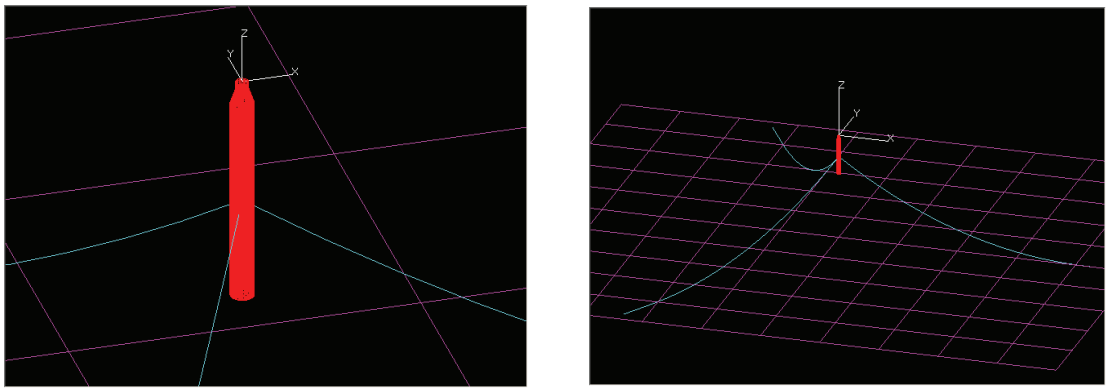

Figure 6.1 Hywind spar mooring line arrangement

6.3 Hydrodynamic Coefficients in the Frequency Domain

Wave forces and hydrodynamic coefficients for the submerged portion of the hull are calculated by using the potential-based 3D diffraction/radiation panel program (Lee et al., 1991). The submerged body has two planes of symmetry and each quadrant has 3,900 panels as can be seen in Figure 6.2.

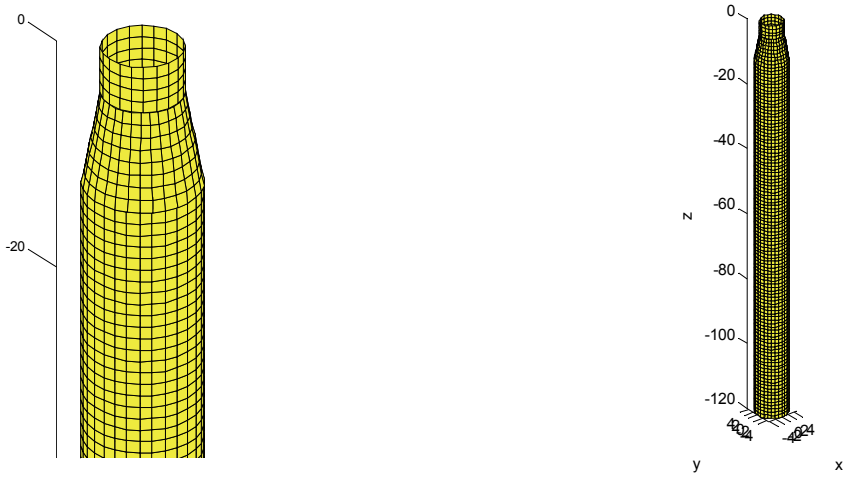

Figure 6.2 Discretized panel model of floating body (Hywind spar)

Second-order mean drift forces are also calculated to generate slowly-varying drift forces and motions through Newman's approximation method. The viscous drag force of the hull is included by employing two Morison members for the upper and lower sections. The drag coefficient C_D is taken to be 0.6 which is typical for a cylinder at high Reynolds numbers.

The viscous loadings on Morison members are calculated at the body's instantaneous position up to the instantaneous free surface at each time step. The wave particle kinematics above MWL are generated by using a uniform extrapolation technique. The nonlinear viscous drag forces also contribute to the nonlinear slowly varying motions. The time-series generation of the input wave field and the corresponding first-order wave-frequency and second-order slowly varying wave forces and spar motions are based on the two-term Volterra-series expansion (Kim et al., 1999; Kim and Yue, 1991). For the design of offshore floating platforms, 3-hour simulations are usually required for the survival condition. However, in the case of the FOWT design, a 1-hour simulation length is usually recommended.

The natural frequencies of the Hywind spar platform are given in Table 6.4. It is seen that all the natural frequencies are located below the lowest wave frequency of appreciable energy except the yaw mode. However, yaw motions will be small anyway due to the minimal wave-induced yaw moments on the vertical-cylinder hull.

Table 6.4 Natural frequencies of platform motions (Hywind spar)

Mode	rad/s	Mode	rad/s
Surge	0.05	Sway	0.05
Heave	0.20	Roll	0.22
Pitch	0.22	Yaw	0.71

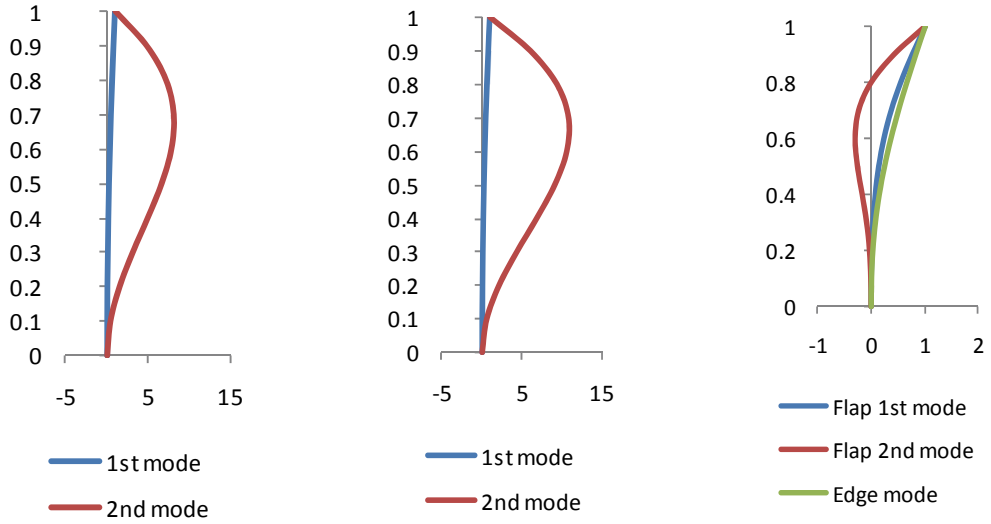

(a) (b) (c)

Figure 6.3 Normalized mode shapes of (a) tower fore-aft, (b) tower side-to-side and (c) blades

The flexibility of the tower is included by using a linear modal representation as suggested in FAST. As shown in Figure 6.3, two fore-aft and two side-to-side mode shapes of tower and two flap-wise modes and one edgewise mode of blades are used for the coupled dynamic analysis. The natural frequencies of those elastic modes at 17.11m/s steady wind are tabulated in Table 6.5. The tower base is located at the 10m

height from the MWL so the flexibility of the tower begins from that height. The rated power is 5MW, and the rotor diameter is 126m.

Table 6.5 Natural frequencies of tower and blade at 17.11 m/s steady wind

Mode	rad/s
1st tower fore-aft mode	2.33
2nd tower fore-aft mode	16.22
1st tower side-to-side mode	2.31
2nd tower side-to-side mode	14.34
Blade 1st flapwise	4.51
Blade 2nd flapwise	12.63
Blade 1st edgewise	6.86

6.4 Coupled Dynamic Analysis in the Time Domain

In this study, the effects of more rigorous aerodynamic loading, flexible tower/blade, rotating blades, and blade pitch-angle control on floater motions and mooring tensions are investigated in the time domain by comparing the coupled and uncoupled numerical models. The coupled analysis is carried out by using the FAST-CHARM3D hybrid program, and the tower-blade portion and floater portion are dynamically interacting at each time step by exchanging dynamic and kinematic information. In the uncoupled analysis, the tower-blade portion is modeled by another rigid body with equivalent wind loading, in the way typical offshore oil and gas platforms are analyzed. The equivalent mean wind loading on the swept area of blades is

determined from that of the coupled analysis by adjusting the blade drag coefficient as shown in Table 6.6.

Table 6.6 Wind load for uncoupled dynamics

Item	Value
Rotor Diameter	126 m
Swept Area	12468.98 m^2
Drag Coefficient	0.168
Uncoupled Mean Wind Load	374.5 kN

Table 6.7 Environmental conditions (Hywind spar)

Item	Value
Reference Wind Speed at 10m	13 m/s
Mean Wind Speed at Hub Height	17.11 m/s
Water Depth	320 m
Wave Heading	0 deg
Significant Wave Height	5.0 m
Peak Wave Period	8.69 sec

The wind and wave are collinear and their headings are fixed at 0 degree; currents are not considered in the present study for convenience. The JONSWAP wave spectrum is used with a significant wave height of 5 m and peak wave period of 8.69s. As for wind, a 1-hour mean wind speed (at 10 m height) of 13 m/s is used and a time

dependent wind velocity is generated from the corresponding API wind spectrum. The environmental condition is summarized in Table 6.7.

During the time-marching procedure, several control methods are working together to maximize and optimize the power capture. In this study, blade-pitch control and variable-speed-torque control methods are adopted. Some modifications of the conventional control strategies typically used for land-based turbines are applied to reduce large resonant motions and eliminate negative damping of the platform pitch mode. Otherwise, unacceptably large resonant motions would occur because the blade-pitch-angle-control-induced excitations act very close to pitch-heave natural frequencies.

In Figures 6.4 ~ 6.9, 6-DOFs motions of the coupled and uncoupled cases are compared to observe the effects of rotor-tower coupling. Due to the symmetry of the hull geometry and the head-direction of wind and wave, sway-roll-yaw motions of the uncoupled case are zero, but the corresponding motions of the coupled case show non-zero displacements because of the interaction between the hull and wind turbine. Due to the aero-loading on blades and gyroscopic effects of blade rotation, there exist non-zero mean values of sway, roll and yaw in coupled analysis.

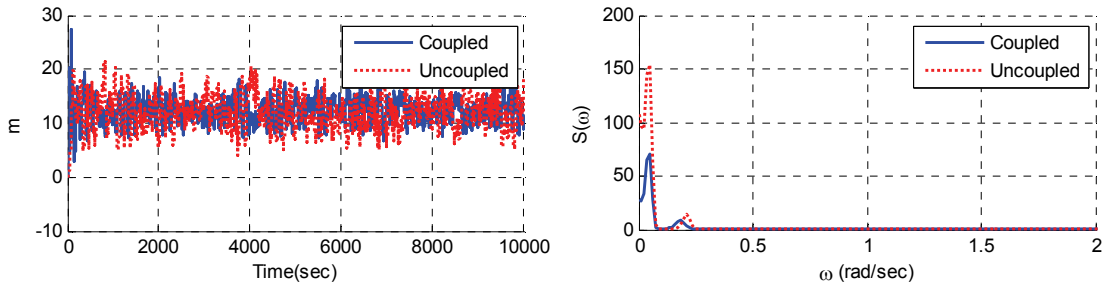

(a) (b)

Figure 6.4 Surge motion (a) and spectra (b) (Hywind spar)

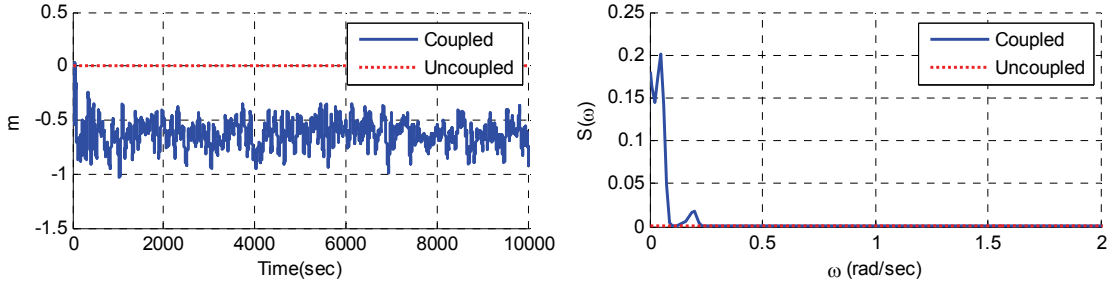

(a) (b)

Figure 6.5 Sway motion (a) and spectra (b) (Hywind spar)

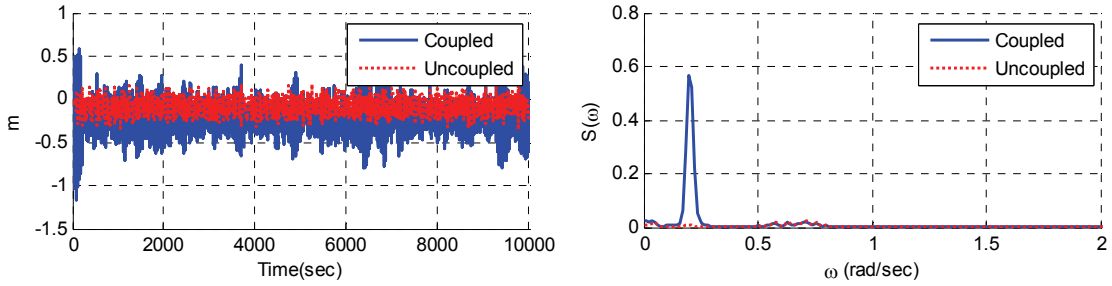

(a) (b)

Figure 6.6 Heave motion (a) and spectra (b) (Hywind spar)

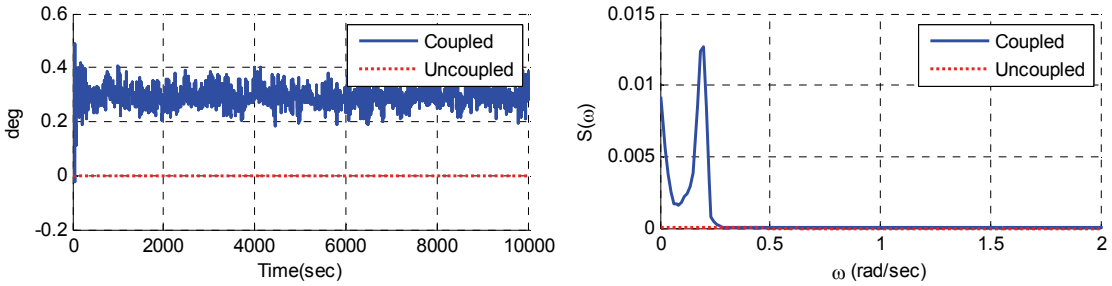

(a) (b)

Figure 6.7 Roll motion (a) and spectra (b) (Hywind spar)

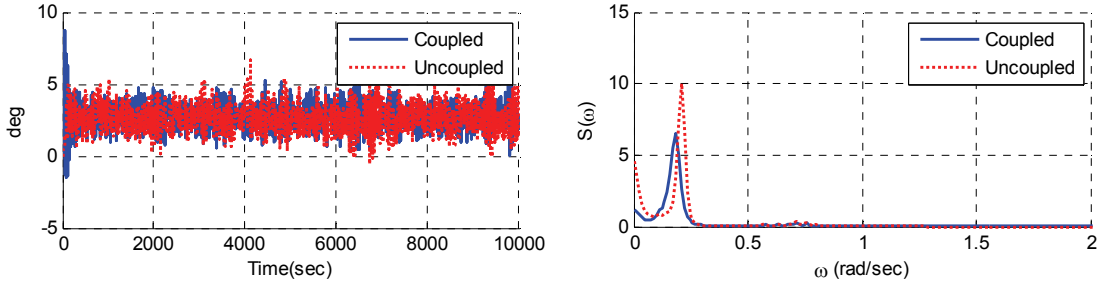

(a) (b)

Figure 6.8 Pitch motion (a) and spectra (b) (Hywind spar)

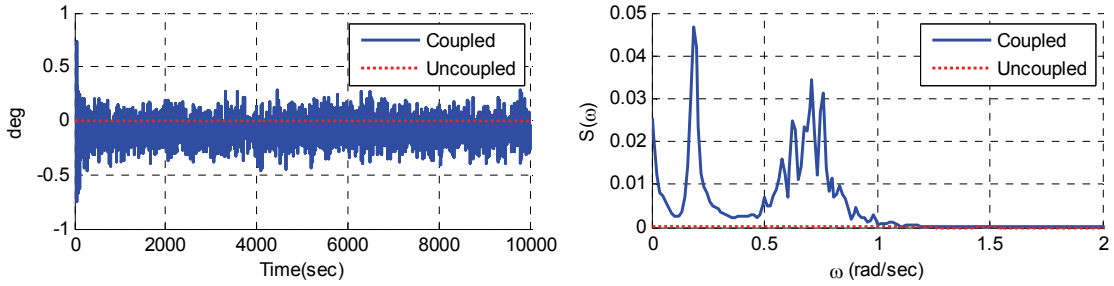

(a) (b)

Figure 6.9 Yaw motion (a) and spectra (b) (Hywind spar)

An interesting phenomenon we can observe is that the uncoupled surge and pitch responses are slightly greater than the corresponding coupled responses. For instance, the maximum surge displacement in the uncoupled case is 21.7m, but that of the coupled case is only 20.3m. A similar trend can be observed in pitch responses. The standard deviations of surge and pitch motions in the uncoupled case are 48% and 14% higher than those of the coupled case, respectively. This trend is actually opposite to that of a TLP-type FOWT (Bae and Kim, 2011). This phenomenon can be explained by the blade-pitch-control action of the coupled case. Assuming that equivalent winds are applied to the rotor for both cases, the platform of the uncoupled case will be fully

actuated by the incident wind. However, in the coupled case, the turbine starts to adjust its blade-pitch angle to regulate the incoming wind effect. This pitch-to-feather action plays a role in mitigating the wind loading and the corresponding platform response. Moreover, in the rotor-floater coupled analysis, the relative wind velocity with respect to the platform motion is used to calculate the wind loading but the relative-wind-velocity effect is ignored in the uncoupled analysis. Also, in the coupled analysis, the instantaneous wind loading is applied at the instantaneous tower-blade position thus acting in all directions including heave direction. On the other hand, in the uncoupled analysis, the wind loading is applied only to the mean position of tower and blade, and thus only the horizontal wind loading (and the corresponding pitch moment) is applied to the center of the equivalent disk. For this reason, the coupled heave motions are appreciably greater than the uncoupled heave motions as can be seen in Figure 6.6. In the coupled case, there exist non-zero transverse motions due to the gyroscopic effect of blade rotation and the influence of the blade pitch-angle control. This phenomenon cannot be obtained from the uncoupled analysis. The statistics of hull responses are tabulated in Table 6.8.

Table 6.8 Platform motion statistics (Hywind spar)

		Max.	**Min**	**Mean**	**SD**
Surge (m)	Uncoupled	2.17E+01	4.14E+00	1.20E+01	3.04E+00
	Coupled	2.03E+01	6.77E+00	1.23E+01	2.06E+00
Sway (m)	Uncoupled	8.61E-06	-9.53E-06	-7.30E-08	2.29E-06
	Coupled	-3.32E-01	-1.05E+00	-6.27E-01	1.21E-01

Table 6.8 Continued

		Max.	Min	Mean	SD
Heave (m)	Uncoupled	1.97E-01	-3.58E-01	-7.99E-02	7.54E-02
	Coupled	4.58E-01	-8.33E-01	-2.33E-01	1.68E-01
Roll (deg)	Uncoupled	3.52E-06	-3.16E-06	-1.01E-08	9.86E-07
	Coupled	4.21E-01	1.77E-01	2.96E-01	3.72E-02
Pitch (deg)	Uncoupled	6.72E+00	-5.16E-01	2.63E+00	8.81E-01
	Coupled	6.35E+00	-1.12E-01	2.76E+00	7.75E-01
Yaw (deg)	Uncoupled	9.17E-07	-8.87E-07	-2.13E-08	1.12E-07
	Coupled	3.39E-01	-4.58E-01	-8.74E-02	1.07E-01

The differences in hull motions between the coupled and uncoupled cases directly affect the top-tension statistics of tethers which are summarized in Table 6.9. The mooring lines arrangement is depicted in Figure 6.10. The upwind-side lines such as lines #2 and #3 will have higher tensions as can be seen in Figures 6.12 ~ 6.13, and the tension of downwind-side line #1 in Figure 6.11 will be decreased due to the surge offset. Due to more severe surge slow-drift motions in the uncoupled analysis, the maximum top tensions of lines are increased by 3~6%.

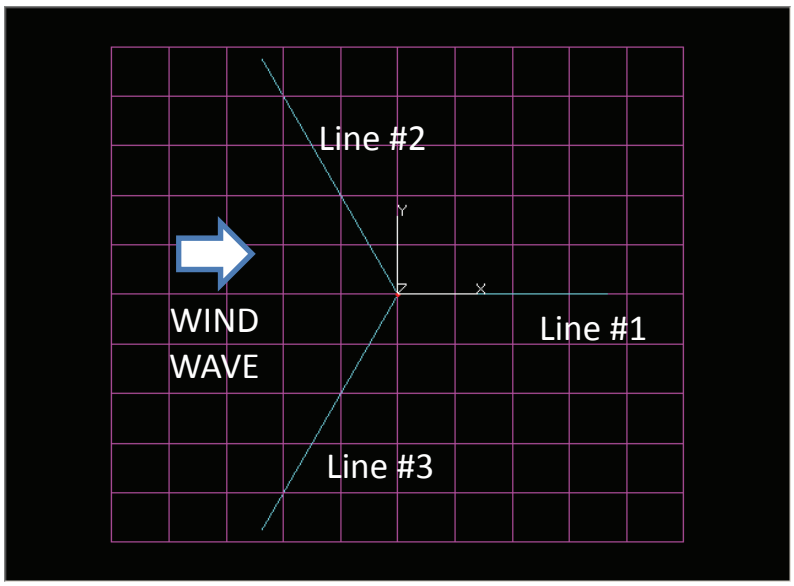

Figure 6.10 Top view of mooring-line arrangement (Hywind spar)

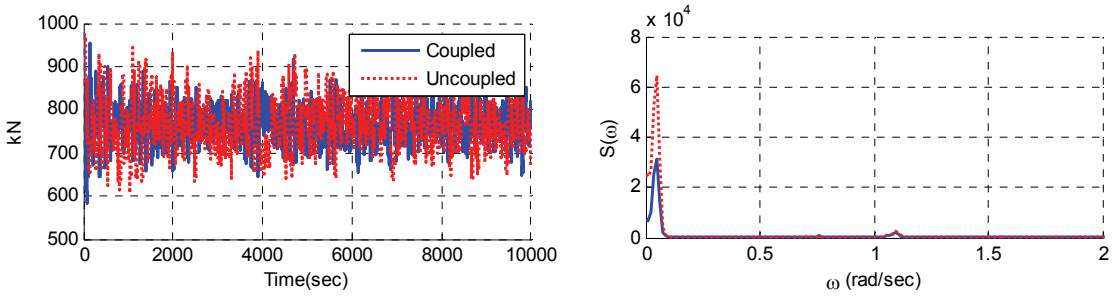

(a) (b)

Figure 6.11 Top-tension (a) and spectra (b) of Line #1 (Hywind spar)

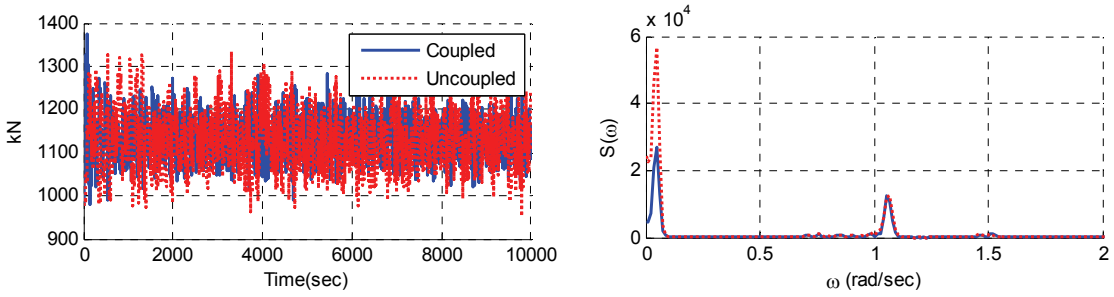

(a) (b)

Figure 6.12 Top-tension (a) and spectra (b) of Line #2 (Hywind spar)

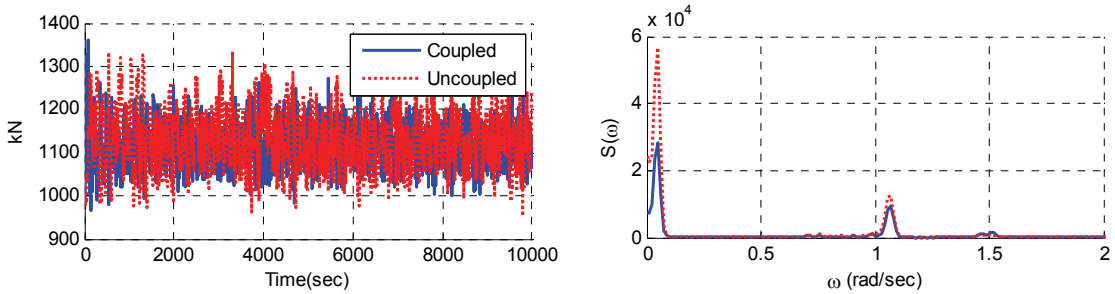

(a) (b)

Figure 6.13 Top-tension (a) and spectra (b) of Line #3 (Hywind spar)

Table 6.9 Mooring line top tension statistics (Hywind spar)

		Max.	Min	Mean	SD
Line #1 (kN)	Uncoupled	9.52E+02	6.07E+02	7.65E+02	5.34E+01
	Coupled	8.98E+02	6.41E+02	7.59E+02	3.73E+01
Line #2 (kN)	Uncoupled	1.33E+03	9.51E+02	1.13E+03	5.62E+01
	Coupled	1.29E+03	9.94E+02	1.13E+03	4.13E+01
Line #3 (kN)	Uncoupled	1.33E+03	9.51E+02	1.13E+03	5.62E+01
	Coupled	1.27E+03	9.89E+02	1.12E+03	4.21E+01

Fore-aft accelerations at 3-different locations of the tower were also investigated and the coupled and uncoupled cases are compared in Figures 6.14 ~ 6.16. For the coupled case, the total acceleration at a given height is calculated by the summation of the local tower acceleration from elastic vibration and the global acceleration due to the hull motion. Phase differences between the local-tower acceleration and global acceleration were considered and included in the calculation of the total acceleration. In the uncoupled analysis, the entire system is treated as a rigid body so only the global accelerations are considered at the respective heights.

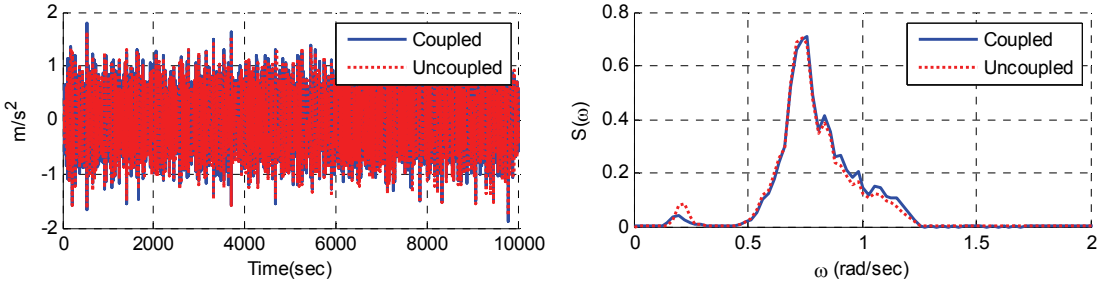

(a) (b)

Figure 6.14 Tower-acceleration (a) and spectra (b) at 85.66m from MWL

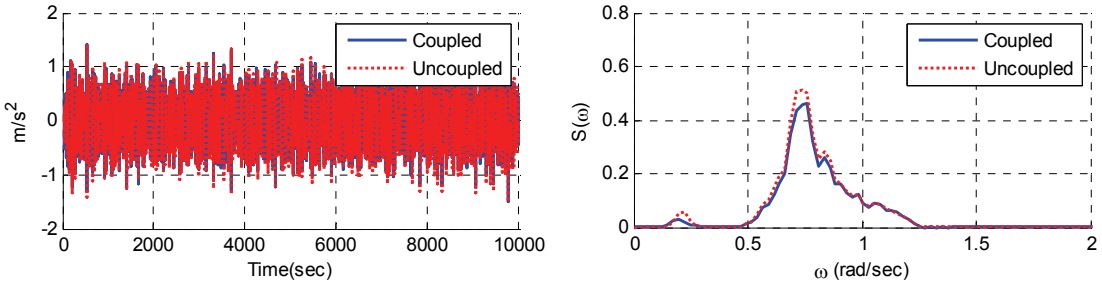

(a) (b)

Figure 6.15 Tower-acceleration (a) and spectra (b) at 58.50m from MWL

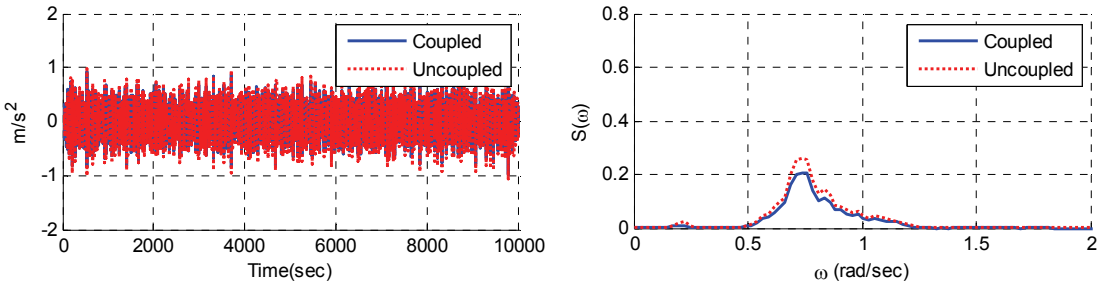

(a) (b)

Figure 6.16 Tower-acceleration (a) and spectra (b) at 11.94m from MWL

The statistics of the tower fore-aft accelerations in Table 6.10 show that the maximum acceleration of the coupled analysis is increased by 10.4% at the top position

compared to the uncoupled case. On the contrary, the maximum uncoupled acceleration of tower at the middle position is increased by 23.8% compared to the coupled case. Similarly, the maximum uncoupled tower acceleration is larger than that of the coupled case by 8.9% at the near bottom position. These phenomena can be explained by the tower elastic modes of the coupled analysis. The tower top is accelerated more by tower elastic bending modes, while the tower base is accelerated mostly by the surge acceleration of the platform itself.

Table 6.10 Tower acceleration statistics (Hywind spar)

		Max.	Min	Mean	SD
85.66m (m/s^2)	Uncoupled	1.63E+00	-1.76E+00	1.06E-04	4.48E-01
	Coupled	1.80E+00	-1.89E+00	9.46E-05	4.56E-01
58.50m (m/s^2)	Uncoupled	1.39E+00	-1.51E+00	8.71E-05	3.83E-01
	Coupled	1.14E+00	-1.22E+00	1.83E-04	2.97E-01
11.94m (m/s^2)	Uncoupled	9.76E-01	-1.07E+00	5.48E-05	2.72E-01
	Coupled	9.28E-01	-9.82E-01	8.60E-05	2.42E-01

6.4 Influence of Control Strategies

6.4.1 Two Control Strategies

For the NREL 5MW turbine, two control systems are designed to work. A generator-torque controller and a blade-pitch controller are working in the below-rated and above-rated wind-speed range respectively.

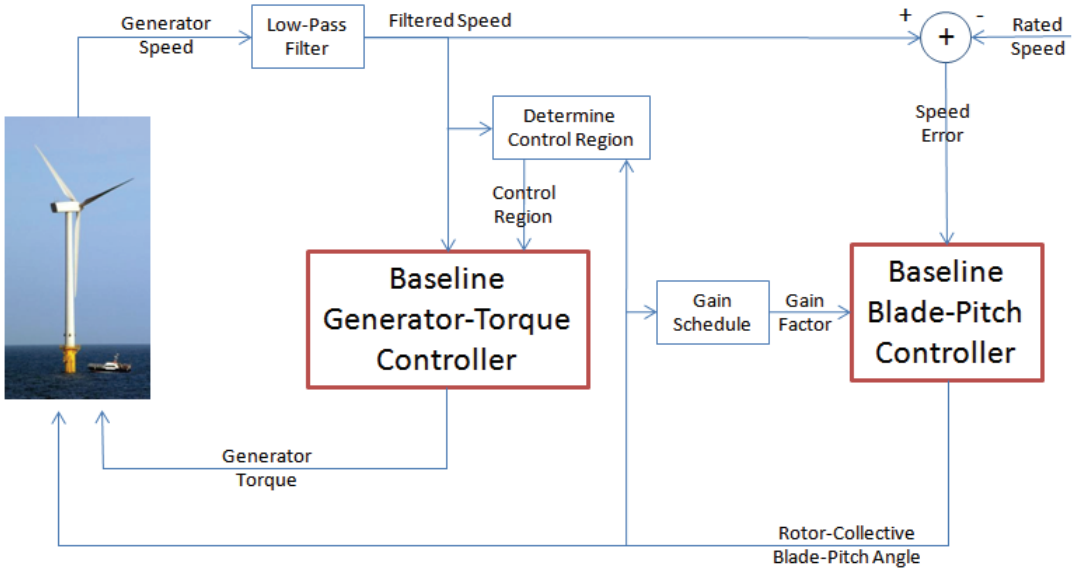

Figure 6.17 Two control strategies (Hywind spar)

The generator-torque controller is designed to maximize power capture and the blade-pitch controller is designed to regulate generator speed by gain-scheduled proportional-integral (PI) control. The schematic diagram of the two control strategies is depicted in Figure 6.17.

The controllers determine its feedback order such as generator torque of blade-pitch angle by measuring the filtered shaft speed. The measured shaft speed is then compared with the target shaft speed. The error between measured and target shaft speed can be expressed as the equation of motion for the rotor-speed error.

$$\left[I_{Drivetrain} + \frac{1}{\Omega_0}\left(-\frac{\partial P}{\partial \theta}\right) N_{Gear} K_d \right] \ddot{\varphi} + \left[\frac{1}{\Omega_0}\left(-\frac{\partial P}{\partial \theta}\right) N_{Gear} K_p - \frac{P_0}{\Omega_0^2} \right] \dot{\varphi}$$
$$+ \left[\frac{1}{\Omega_0}\left(-\frac{\partial P}{\partial \theta}\right) N_{Gear} K_i \right] \varphi = 0$$

where $I_{Drivetrain}$ is a drivetrain inertia and P and P_0 are mechanical power and rated mechanical power respectively. θ is a full-span rotor-collective blade-pitch angle and Ω_0 is a rated low-speed shaft rotational speed. $\partial P / \partial \theta$ stands for a sensitivity of aerodynamic power to rotor-collective blade pitch. K_d, K_p and K_i are the blade-pitch controller proportional, integral, and derivative gains respectively.

It is known that the rotor-speed-error responds as a second-order system as shown in the above equation (Jonkman, 2008). For the 5MW baseline, NREL recommended the optimal gain values of proportional (K_p = 0.01882681s) and integral (K_i = 0.008068634) gains at a minimum blade pitch setting for the baseline wind turbines. The derivative gain K_d is set to zero because it gives better performance than other values. Based on these gains, the blade-pitch control system uses a new gain according to the blade pitch angle input. Note that the negative damping represented by the $-P_0 / \Omega_0^2$ term is introduced in the speed error response and should be compensated by the proportional gain in the blade-pitch controller.

6.4.2 Modification of Control Strategies

The blade-pitch response of this control strategy can be evaluated for a land-based turbine. The step variation of input wind speed is applied to the land-based turbine and the response of blade-pitch angle is investigated. The current control parameter (conventional control strategy) gives a very fast and accurate response of blade-pitch angle. This strategy is very good for land-based turbines or TLP-type offshore wind

turbines since they have minimal rotational motion and very high pitch natural frequencies (Bae and Kim, 2011). However, if the pitch/roll natural frequency of a floating platform is low and close to the pitch-angle-actuator frequency, such as spar-type or semisubmersible-type FOWTs, the interaction between the platform pitch motion and the variation of thrust force due to the blade-pitch control action may cause serious resonance. In order to avoid this resonance, the pitch-angle-actuator frequency must be lowered by detuning the gain values.

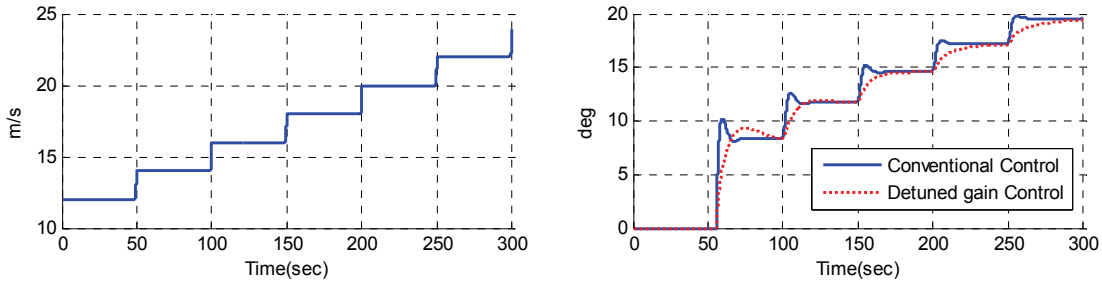

(a) (b)

Figure 6.18 Step wind input (a) and blade pitch angle (b) (Land-based)

According to Larsen and Hanson (Larsen and Hanson, 2007), the lowest controller-response natural frequency should be less than the platform's pitch natural frequency to avoid the negatively damped platform motion. By detuning gain values, one can reduce the controller-response natural frequency and ensure the platform motions remain positively damped. In Figure 6.18(b), the pitch angle of conventional control reaches its target pitch angle very fast in response to the variation of step input wind speed. If we reduce the gain values, then the overall reaction of the pitch-angle actuator is changed. It takes longer to reach the target pitch angle and the gradient of

pitch angle variation is small compared to that of conventional control. When it comes to control quality, the conventional control shows a larger transient overshoot in the lower wind-speed range, while the modified gain control shows relatively smaller or no transient overshoots.

In addition to this detuned-gain modification, the negative damping term can also be reduced to zero if the variable-speed-torque control changes the Region 3 from a constant generator power to a constant generator-torque. Region 3 is one of the control regions where the generator torque is computed as a tabulated function of the filtered generator speed; it was originally designed to produce a constant generator power. This modification may reduce the negative damping term of the speed-error equation but it could also affect the quality of the generated power output. With the same step variation of input wind speed, and keeping the same gain values, the trends of conventional and constant-torque control are compared.

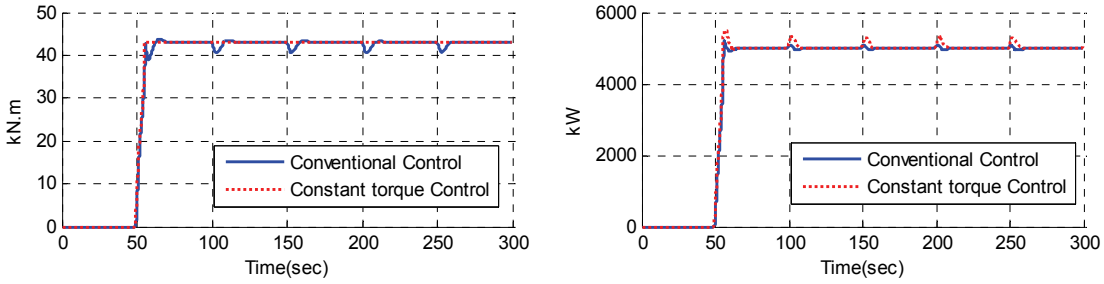

(a) (b)

Figure 6.19 Generator torque (a) and generator power (b) (Land-based)

Figure 6.19(a) shows that the modification of Region 3 produces constant generator torque regardless of the change of input wind speed. However, the generated

power has a relatively larger overshoot at every initial stage of wind-speed variation compared to the conventional-control case. This kind of power surge may have negative effects on the generator or other electric devices in the turbine.

As already pointed out, the two modifications of control strategy explained earlier are in fact not necessary for the land-based or TLP-type wind turbines. However, in the case of the Hywind spar, the modifications are quite essential since the hull motions can be greatly amplified without them. This is particularly so since the conventional-control-induced excitation frequencies are very close to the surge/sway and roll-pitch natural frequencies. However, by modifying the control strategy as explained above, the detrimental resonance effects can be avoided. In order to see the effects of modifications on the Hywind spar, similar tests are carried out with the same step wind input.

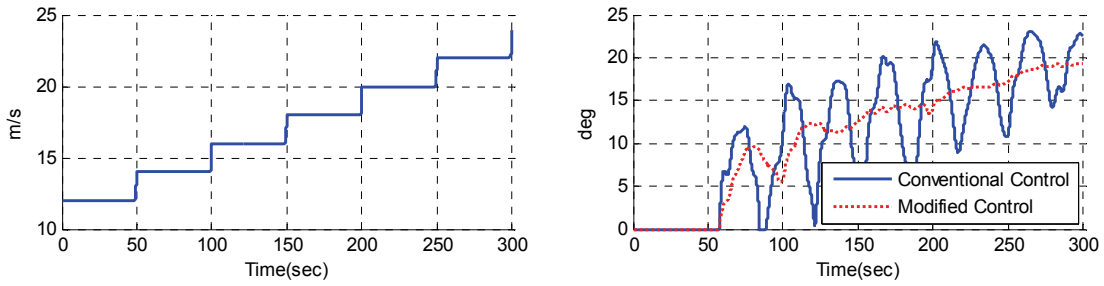

(a) (b)

Figure 6.20 Step wind input (a) and blade pitch angle (b) (Hywind spar)

Figure 6.20(b) shows the comparison of the pitch-angle variation between the conventional and modified control strategies. We can see that the pitch angle changes very hastily with significantly amplified amplitudes with the conventional-control

strategy. The conventional-control-induced excitation frequencies are very close to the pitch natural frequency of the Hywind spar. As a result, large platform pitch responses occur, as can be seen in Figure 6.21. The blade-pitch controller tries to catch up with the variation of input wind and it consequently produces a variation of thrust force in the frequency range similar to platform pitch resonance.

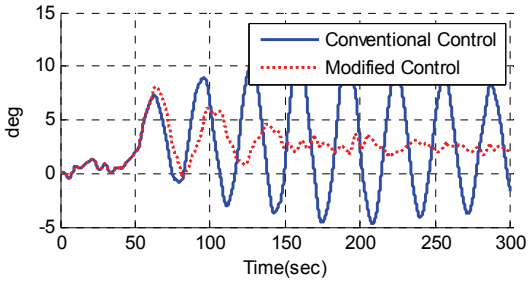

Figure 6.21 Platform pitch motion for two control strategies

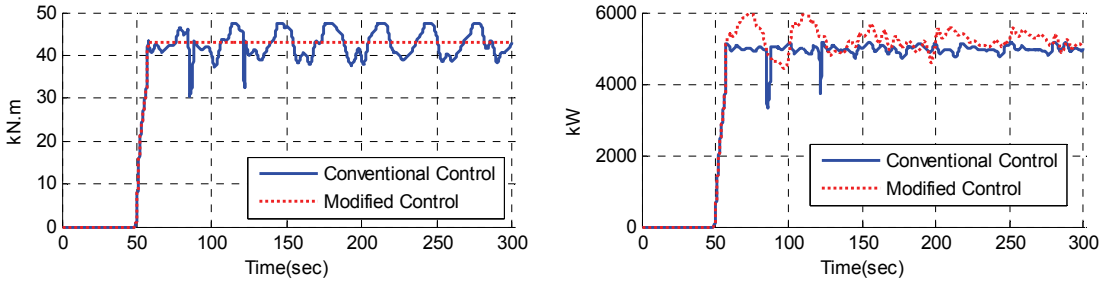

(a) (b)

Figure 6.22 Generator torque (a) and generator power (b) for two control strategies

To avoid this kind of resonance, the modified control strategy is applied to the same Hywind spar platform; it is seen in Figure 6.21 that the platform pitch response is greatly reduced as a result. However, the generator power surge of the modified control

may have a negative effect (see Figure 6.22(b)) as a result as explained above. Thus a further check needs to be done to deal with this effect.

6.4.3 Response in Random Sea Environment

So far, the effect of control strategy on the global performance of FOWTs has been investigated under the simple step-wind environment. In this section, we have considered a typical wind-wave environment as a more realistic random input to the respective control systems. The time-varying wind speed at hub height is generated based on the API wind spectrum ranging 5s to 3,600s. If the aerodynamic loading is to be generated in a strict manner, the full-wind-field data inside the blade-swept area need to be used, but in the present study only the variation of the wind velocity in the vertical direction is considered assuming that the sideways variation can be neglected. The random waves are generated from the JONSWAP spectra and 1-hour simulations were carried out. Total time domain simulation is for 4,000s, including initial 400s of ramp time. Statistics are obtained based on those time series from 400s to 4,000s after eliminating the effect of initial transient responses. The environmental condition used for the simulation is the same as the previous section in Table 6.7.

In Figure 6.23, the blue (solid) line shows the variation of blade pitch angle as a result of applying the conventional control strategy. It shows a lot of fluctuation. From time to time, the blade pitch angle hits 0 degree which means the controller tries to capture a maximum lift force from the blade. This random pitch-angle action is primarily concentrated in the frequency range between 0.15~0.23 rad/s. The frequency range

coincides with the pitch/roll/heave natural frequencies of the Hywind spar (see Table 6.4). Therfore, it is expected that large pitch/heave motions will occur as a result of the blade-pitch-angle control.

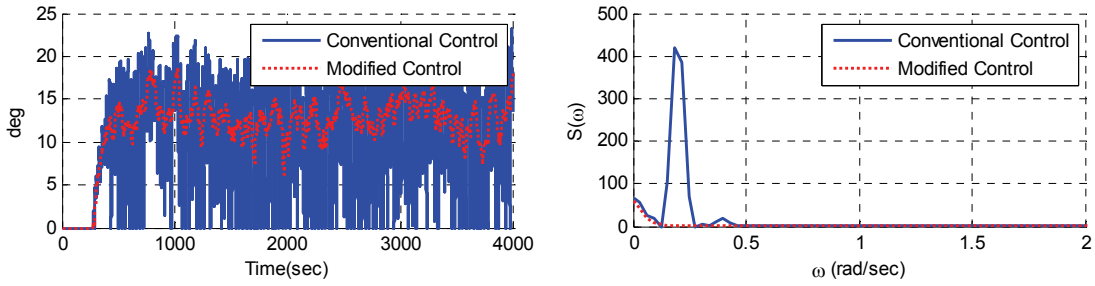

(a) (b)

Figure 6.23 Blade pitch angle (a) and spectra (b) for two control strategies

The corresponding time history of the thrust force measured at the low-speed shaft point is given by the blue line in Figure 6.24. At this point, the thrust force is affected by the aerodynamic force which is regulated by the blade-pitch controller. The trend is very similar to the blade pitch-angle variation. The high peak is also shown at the same frequency range.

If the two modifications are applied to the retuned control system, the duty cycle of blade-pitch is reduced noticeably, as can be seen on the dotted red line in Figure 6.23. The actuation frequency is much lower than the pitch-roll-heave resonance frequencies. The resulting pitch motions will be smaller, so the blade-pitch controller needs to spend less effort to adjust. Compared to the conventional control case in Figure 6.23(b), the peak frequency is located at a much smaller frequency.

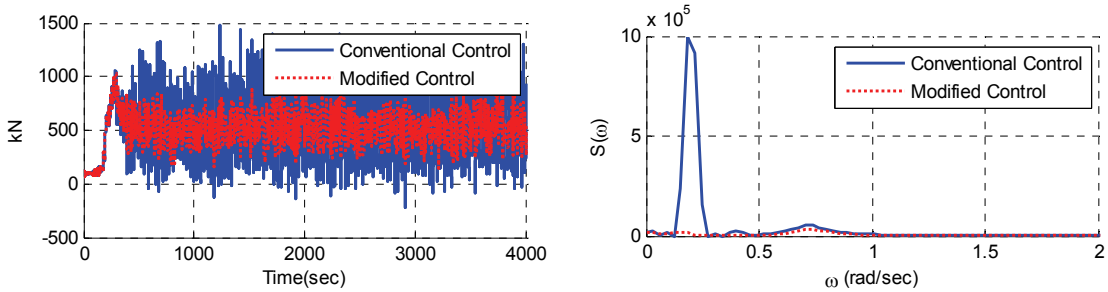

(a) (b)

Figure 6.24 Shaft thrust force (a) and spectra (b) for two control strategies

The major contribution of the thrust force is aerodynamic loading. The thrust force directly affects the floater pitch motion. In the case of conventional control, the blade-action-induced thrust force is again greatly amplified in the range of 0.15~0.23 rad/s for the same reason. The harmful resonance disappears when the modified control scheme is applied as shown in Figure 6.24.

The same kind of improvement of performance can also be seen in the 6-DOFs platform motions (Figures 6.25 ~ 6.30) by applying the modified control strategy. Without such modification, the platform motions become too large, especially in heave and pitch modes, so they are not acceptable in the design. The sway, roll and yaw are also appreciably influenced by the blade-control action. The results typically illustrate that the blade-control scheme strongly influences platform motions and the phenomenon can only be explained by use of the rotor-floater-mooring fully-coupled time-domain simulation program. The same phenomenon has also been observed in an experiment with spar-type FOWT (Nielsen et al., 2006).

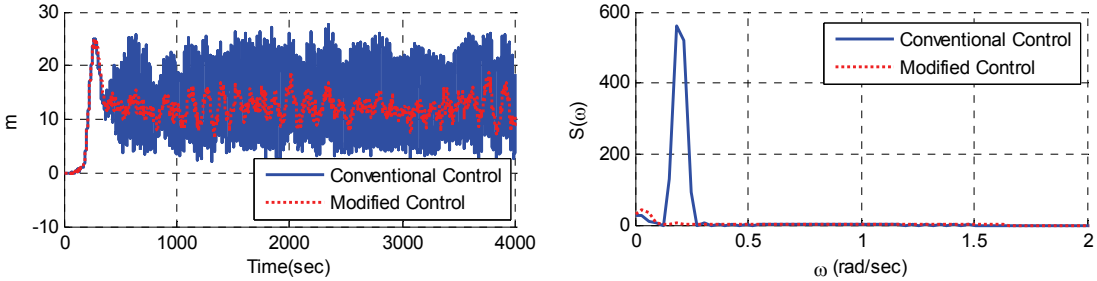

(a) (b)

Figure 6.25 Surge motion (a) and spectra (b) for two control strategies

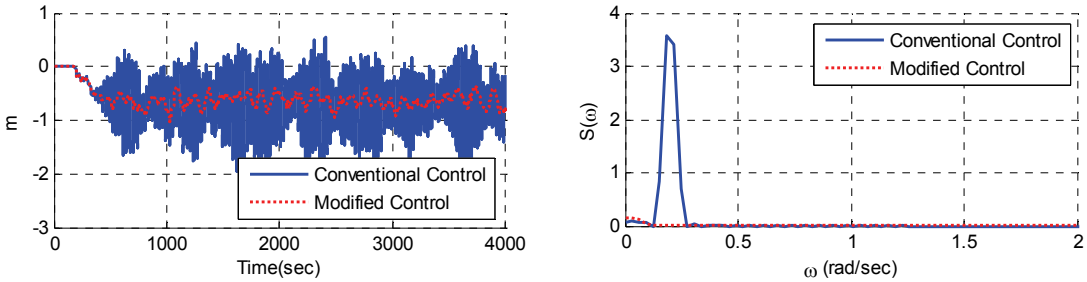

(a) (b)

Figure 6.26 Sway motion (a) and spectra (b) for two control strategies

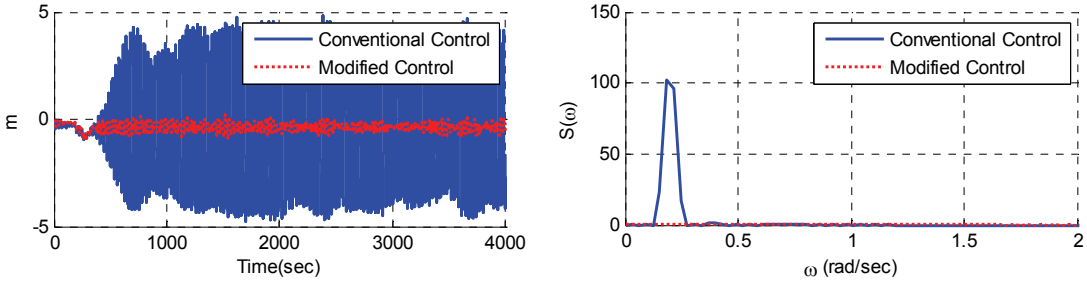

(a) (b)

Figure 6.27 Heave motion (a) and spectra (b) for two control strategies

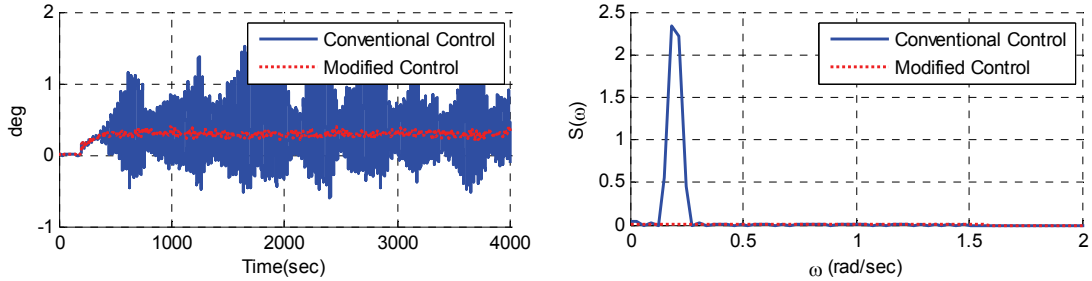

(a) (b)

Figure 6.28 Roll motion (a) and spectra (b) for two control strategies

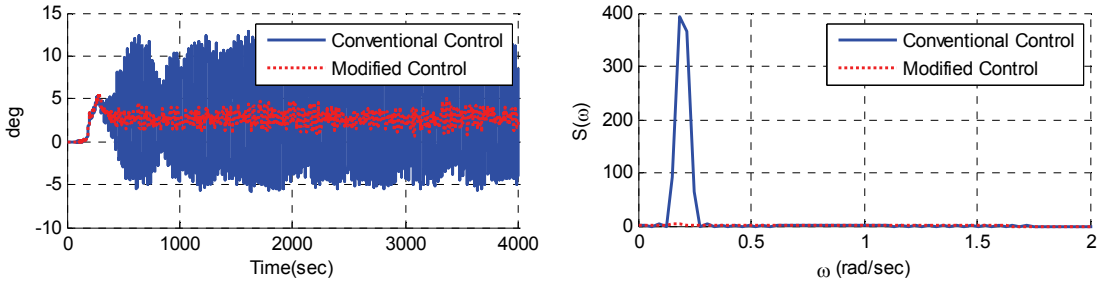

(a) (b)

Figure 6.29 Pitch motion (a) and spectra (b) for two control strategies

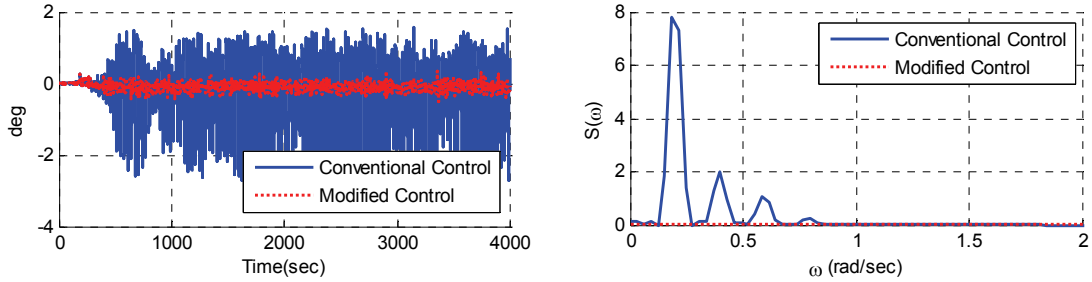

(a) (b)

Figure 6.30 Yaw motion (a) and spectra (b) for two control strategies

A gyroscopic effect can also be seen in the case of conventional control in Figure 6.30. This gyroscopic yaw moment comes not from the aerodynamic loads on the rotor but from the spinning inertia of the rotor combined with large pitch motion.

Table 6.11 shows the statistics of the Hywind spar motion in the given random environment. All the 6-DOFs motions with conventional control strategy show very large maximum and standard-deviation values due to the control-actuated pitch/heave resonance.

Table 6.11 Statistics of platform motion in two control strategies

		Max.	Min	Mean	SD
Surge (m)	Conventional	2.76E+01	2.21E+00	1.39E+01	6.76E+00
	Modified	1.87E+01	6.52E+00	1.22E+01	1.98E+00
Sway (m)	Conventional	5.38E-01	-2.09E+00	-7.03E-01	5.44E-01
	Modified	-3.64E-01	-1.02E+00	-6.34E-01	1.17E-01
Heave (m)	Conventional	4.83E+00	-4.74E+00	-5.04E-01	2.84E+00
	Modified	1.71E-01	-9.21E-01	-3.64E-01	1.75E-01
Roll (deg)	Conventional	1.52E+00	-6.08E-01	3.84E-01	4.36E-01
	Modified	4.03E-01	1.97E-01	2.97E-01	3.44E-02
Pitch (deg)	Conventional	1.30E+01	-5.79E+00	3.26E+00	5.55E+00
	Modified	5.05E+00	6.78E-01	2.74E+00	7.10E-01
Yaw (deg)	Conventional	1.56E+00	-3.08E+00	1.77E-02	9.48E-01
	Modified	3.41E-01	-4.95E-01	-9.38E-02	1.11E-01

The comparisons of the rotor speed and generated power output between the two cases are also shown in Figures 6.31 ~ 6.32. The rotor speed with conventional control is also greatly affected by platform pitch resonance combined with blade pitch actuation. The power output from the conventional control had numerous power drops during the simulation time. The reason for this sudden drop is the instantaneous reduction in the

relative wind speed due to large pitch backward motions. Thus, the time frame of these sudden drops coincides with that of the 0-degree blade-pitch angle. In the case of the modified control, the number and range of power drops are significantly reduced but a nontrivial power overshoot also exists as a minor side effect. Nevertheless, the overall quality of the generated power with the modified control strategy is much better than that of the other case.

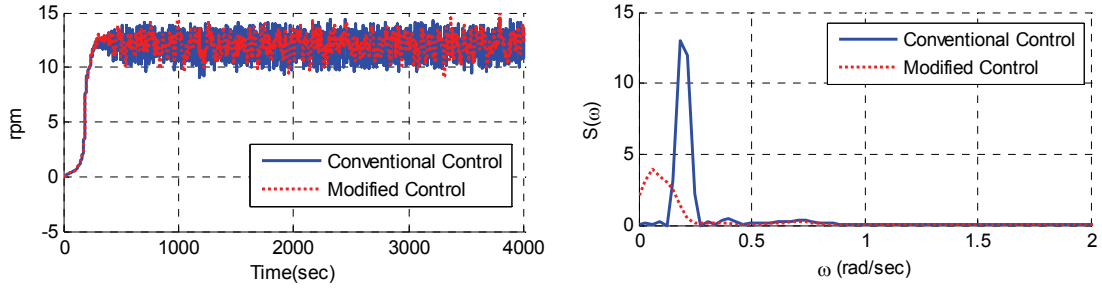

(a) (b)

Figure 6.31 Rotor speed (a) and spectra (b) for two control strategies

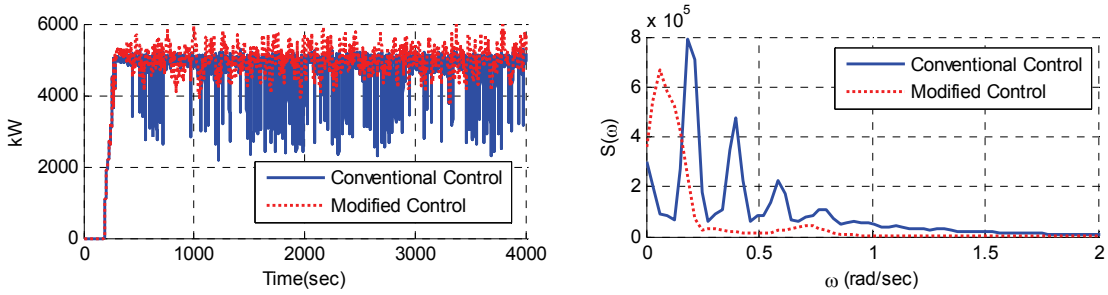

(a) (b)

Figure 6.32 Generator power (a) and spectra (b) for two control strategies

The fore-aft shear force, axial force, and fore-aft bending moment at the tower base (Figures 6.33 ~ 6.35) are important to the structural design of a tower. The general

tendency of the time histories of the shear, axial forces, and bending moment at the tower base is similar to that of platform motion. It is seen that large forces and moments are transferred to the position in case of the conventional control and the location of the peak is consistent with that of platform motion. The maximum shear force and bending moment with the conventional control is more than 70% higher than that of the modified control. The higher standard deviation of the shear force means more vulnerability to fatigue failure which may happen when the blade control system is poorly designed. The negative sign of axial force stands for the compression force that may be a concern for buckling failure.

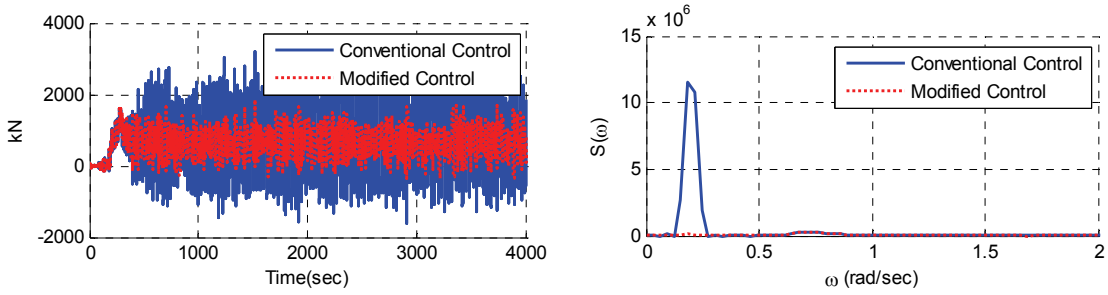

(a) (b)

Figure 6.33 Tower-base fore-aft shear force (a) and spectra (b) for two control strategies

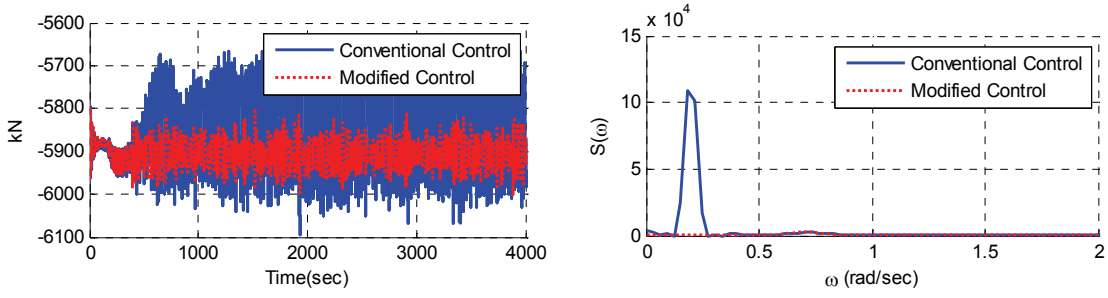

(a) (b)

Figure 6.34 Tower-base axial force (a) and spectra (b) for two control strategies

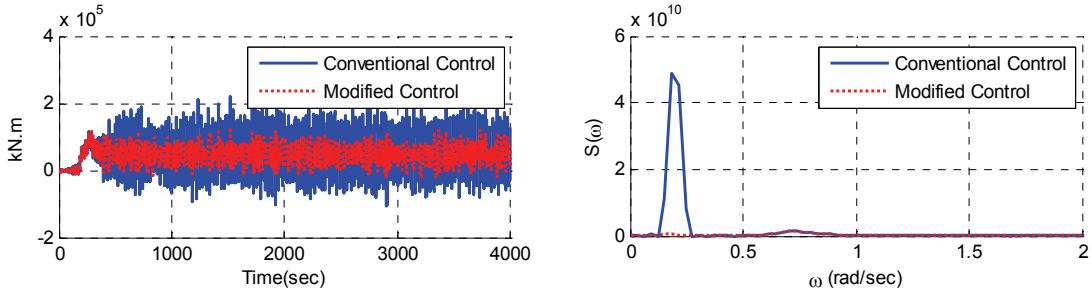

(a) (b)

Figure 6.35 Tower-base pitch bending moment (a) and spectra (b) for two control strategies

The structural loading on the blade root location was also investigated in this study. Since the configuration of the blades attached to the rotor hub is a kind of cantilever beam, the highest shear force and bending moment are expected at the blade-root location. Based on the elastic blade configurations, two shear forces, flapwise and edgewise, at the root location were selected for comparison as shown in Figures 6.36 ~ 6.37.

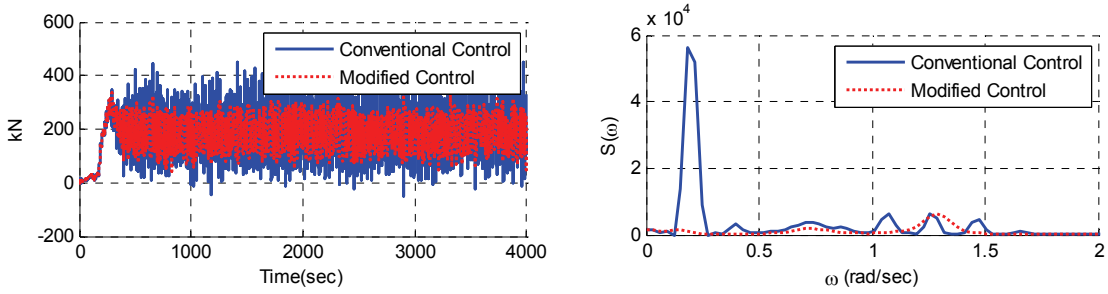

(a) (b)

Figure 6.36 Flapwise shear force at blade root (a) and spectra (b) for two control strategies

In the frequency domain, the flapwise shear force with conventional control shows a high peak around the platform pitch resonance frequency, and small peaks around 1P frequency of 1.27 rad/s. 1P represents the once per revolution frequency of the rotor. In case of modified control, 1P frequency is dominant.

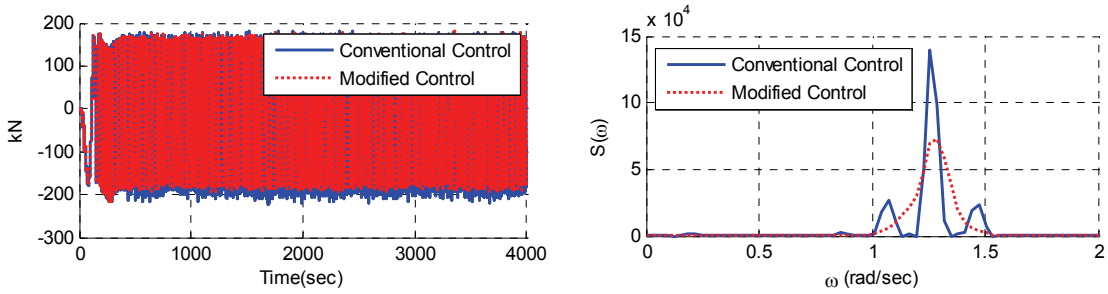

(a) (b)

Figure 6.37 Edgewise shear force at blade root (a) and spectra (b) for two control strategies

In the case of edgewise direction in Figure 6.37, the shear force is more strongly associated with the rotation of the blade. This shear force shows a clear peak at the 1P frequency. The shear forces in the frequency domain show a different trend between the two control strategies. The modified control shows a smoother transition around the 1P frequency while the conventional control shows sharper and higher peaks at 1P frequency with minor peaks nearby. These differences are mostly due to the different actuator speed of the blade pitch which results in a smooth transition with a low speed actuator (modified) and a sharper transition with a rapid actuator (conventional). The maximum flapwise shear force with the conventional control is nearly 39% greater than that of the modified control.

The differences in hull motions between the conventional control and modified control directly affect the top-tension statistics of mooring lines. The mooring-line arrangement is depicted in Figure 6.10. The wind-wave direction is along the x (in the direction of line #1 and between taut-side lines #2 and #3). The upwind-side lines such as line #2 and #3 will have higher tensions and the tension of the downwind-side line #1 will be smaller due to the mean surge offset

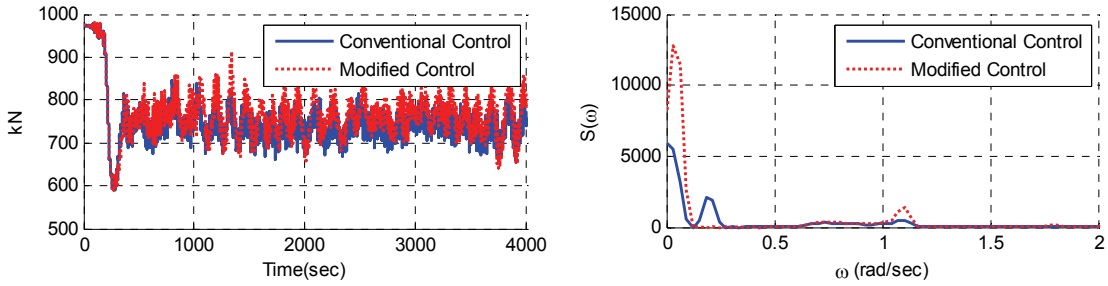

(a) (b)

Figure 6.38 Top-tension of Line #1 (a) and spectra (b) for two control strategies

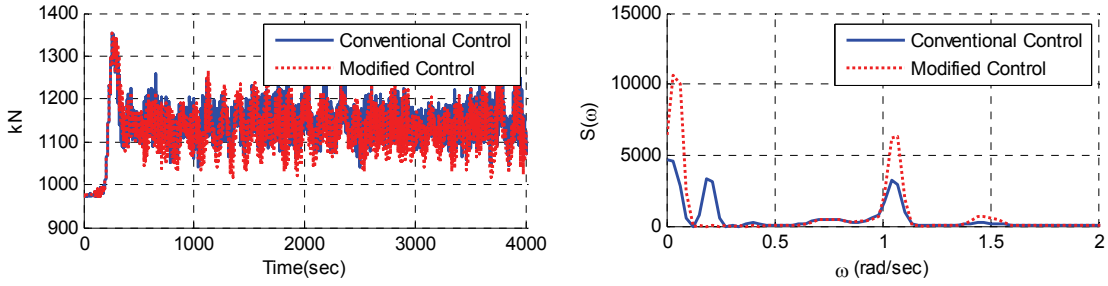

(a) (b)

Figure 6.39 Top-tension of Line #2 (a) and spectra (b) for two control strategies

The standard deviations of top tensions from upwind lines with modified control are 18 ~ 21% greater than those of the conventional control case. This trend is quite

opposite to the previous results. An increase at the lowest frequency due to modified control can be expected since the blade-action was intentionally moved to lower frequency. The three lowest natural frequencies of the mooring lines are estimated to be 0.36, 0.72, and 1.07 rad/s. In this case, the peak around 1.07 rad/s in Figures 6.38 ~ 6.39 corresponds to the third lowest mooring dynamics mode. Interestingly, the peak of modified control is slightly larger than that of the conventional control. In terms of mooring line tension, the modified control is less efficient than the conventional control despite the significant advantage in floater motions. These responses can be captured only by a full mooring dynamics model; an alternative quasi-static mooring analysis model cannot get those high peaks as can be seen in Figure 6.40.

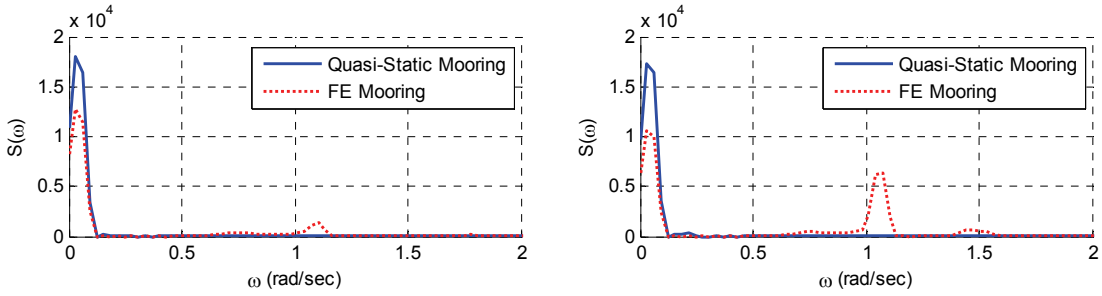

Figure 6.40 Spectra of top-tension of Line #1 (a) and Line #2 (b) for quasi-static and FE mooring

6.5 Discussion

In case of the Hywind spar, it is seen that the rotor-floater coupling effects decrease the maximum horizontal offsets and mooring-line tensions but heave motions are increased due to the time-varying wind loading caused by the time-varying blade

pitch angle and relative wind velocity against the moving tower. The tower top accelerations are, however, increased due to the effects of tower flexibility which in turn will greatly affect the corresponding inertial loading on nacelle and blades. This may be of important concern for the structural robustness and fatigue life of the system.

In addition, the influence of two different control strategies (conventional and modified) on the global performance of floating offshore wind turbines, especially for a Hywind spar platform, was investigated. The conventional control scheme that gives fast and accurate feedback response is designed for land-based or TLP-type wind turbines. If the pitch stiffness of a FOWT is small, such as that of spar-type or semi-submersible-type floaters, the control-induced excitations may cause resonance which can significantly increase the floater responses. This was clearly demonstrated in the present time-domain simulations by using a fully coupled dynamic analysis program. In such a case, a modified control strategy is necessary to avoid the resonance effect. By detuning the gain values and modifying the Region 3 control method, better control strategy can be devised. Applying the modified control strategy showed that the 6-DOFs floater motions and tower-base/blade-root shear forces and bending moments are noticeably reduced and the corresponding turbine performance, such as generated power quality, is also appreciably improved. However, the modified control may induce slightly higher mooring line tension. In conclusion, the time-domain aero-elastic-control-floater-mooring coupled dynamic analysis computer program was successfully developed. It can be used for checking the global performance and robustness of any type of FOWTs for

any kind of environment, control scheme, and mooring system and can also be very helpful in the design of more reliable and innovative FOWTs in the future.

7. CASE STUDY II: THREE-TURBINE SEMI-SEBMERSIBLE

7.1 Introduction

In the previous chapters, the theory and numerical methods for multiple turbines on one platform were discussed. By expanding the coefficient matrix $[C_{rs}]$ and the number of degrees of freedom, the FAST-CHARM3D coupled tool can analyze the multiple turbines on one platform, including tower and blade elasticity in time domain. Since there is no real MUFOWT structure at this moment, the floating platform and mounted turbines were selected considering their hydrostatic stability and turbine size. As a preprocessor, WAMIT was used to obtain hydrodynamic coefficients such as added mass, radiation damping and first-order wave force.

In terms of aero dynamics, the effects of dynamic aero loadings were considered separately in individual turbines. However, the aerodynamic interference and shade effect between adjacent turbines were not considered in this study because of the complexity and uncertainty of their aerodynamic effect on the turbulent wind field. Instead, the turbines were positioned with enough spacing in side-by-side and fore-aft directions. The water depth was set to 300m, and 6 catenary mooring lines were attached in the fairlead position to avoid platform drift in a wind-wave-current environment. In this case study, two 1.5MW turbines and one 5MW turbine were adopted and arranged on top of a triangular-shaped semi-submersible platform. Overall platform responses including mooring line tension and turbine performances were assessed. To see the integrated platform responses, one turbine fault scenario was simulated and the resultant

overall platform responses as well as the performances of other turbines were checked and presented.

7.2 Configuration of the Platform, Mooring System and Turbines

The floating platform used in this case study was triangular with three vertical columns and three horizontal pontoons as seen in Figure 7.1. The left two columns support 1.5MW turbines each, and the right column supports one 5MW turbine. The properties of 5MW turbine are in Table 6.1, and the properties of 1.5MW turbine are specified in WindPACT studies conducted by NREL (Malcolm et al., 2002).

To satisfy the static equilibrium of the platform in calm water, the ballast water was filled inside the platform.

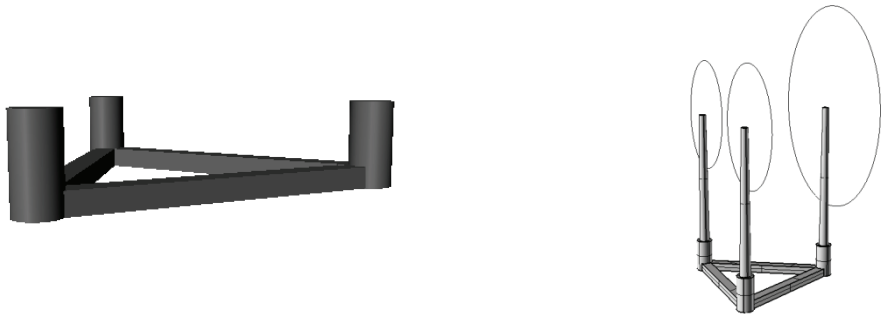

(a) (b)

Figure 7.1 Triangular platform geometry (a) and system configuration (b)

Since the weight of the two front 1.5MW turbines was lighter than that of rear 5MW turbine, more ballast water should be filled out in the front columns. The column diameter was 10m each, and the distance between each column was 79.67m. The

platform draft was 20m, and the width and height of each pontoon was 6m and 5m respectively. Figure 7.2 shows the dimensions of the triangular platform.

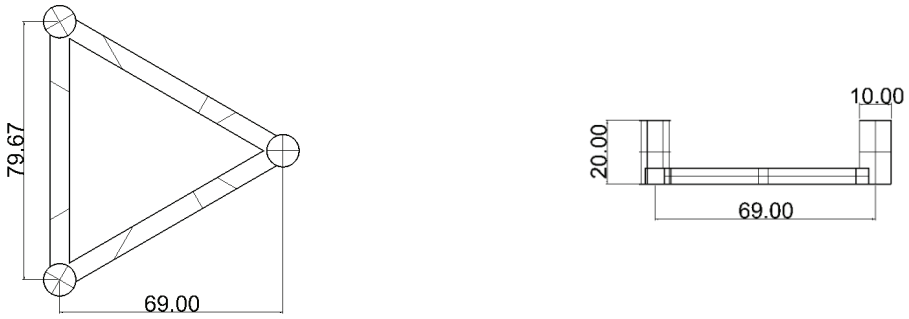

(a) (b)

Figure 7.2 Platform dimensions from top (a) and side (b) (Triangular platform)

The platform hull weight was estimated with the submerged surface area and given plate thickness (15mm). The mass properties of the platform, including mass moment of inertia, were calculated considering the displaced steel platform and ballast water. The details of the platform properties are tabulated in Table 7.1.

Table 7.1 Specification of triangular platform

Item	Unit	Value
Depth to Platform Base below SWL	m	20.0
Column Diameter	m	10.0
Length between Columns	m	79.67
Pontoon Width	m	6.0
Pontoon Height	m	5.0
Platform Weight, including Ballast	N	98,246,039

Table 7.1 Continued

Item	Unit	Value
Platform Buoyancy	N	113,607,091
Platform CM Location Below SWL	m	15.0
Platform Roll Inertia about CM	$kg \cdot m^2$	7,051,945,158
Platform Pitch Inertia about CM	$kg \cdot m^2$	6,200,218,656
Platform Yaw Inertia about Platform Centerline	$kg \cdot m^2$	13,099,535,514

In case of the mooring system, two catenary mooring lines were installed at each corner, making a total of six mooring lines in this system. Each mooring line consisted of a chain-steel wire-chain combination with a total length of 644.6m. The mooring line top tensions were estimated based on the equilibrium relation between the platform weight and buoyancy. The details of the mooring system properties are tabulated in Table 7.2.

Table 7.2 Specification of mooring system (Triangular platform)

Item	Unit	Value
Number of Mooring Lines	ea	6
Angle Between Adjacent Lines	deg	60
Depth to Anchors Below SWL (Water Depth)	m	300
Depth to Fairleads Below SWL	m	20.0
Unstretched Mooring Line Length	m	644.6
Mooring Line Diameter (Chain)	m	0.382
Mooring Line Mass Density (Chain)	kg/m	381.374
Mooring Line Mass in Water (Chain)	kg/m	322.638

Table 7.2 Continued

Item	Unit	Value
Mooring Line Extensional Stiffness (Chain)	kN	1.328E6
Mooring Line Diameter (Steel wire)	m	0.163
Mooring Line Mass Density (Steel wire)	kg/m	90.041
Mooring Line Mass in Water (Steel wire)	kg/m	79.334
Mooring Line Extensional Stiffness (Steel wire)	kN	240192

The arrangements of six mooring lines are presented in Figure 7.3.

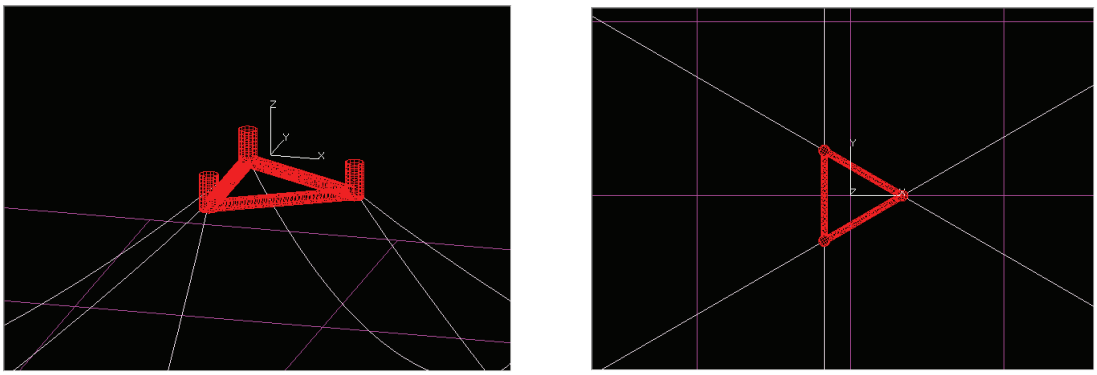

Figure 7.3 Mooring line configurations (Triangular platform)

7.3 Hydrodynamic Coefficients in the Frequency Domain

The hydrodynamic coefficients, including added mass, radiation damping, and linear wave forces, were obtained by WAMIT. Figure 7.4 shows the discretized panel distribution of the floater. The submerged body has one plane of symmetry and each side has 1,155 panels. Second-order sum and difference frequency effects were not included in this simulation for simplicity. The viscous drag force of the hull and mooring line was

not considered in the frequency domain analysis, but will be accounted for in the following time domain analysis using Morison's equation.

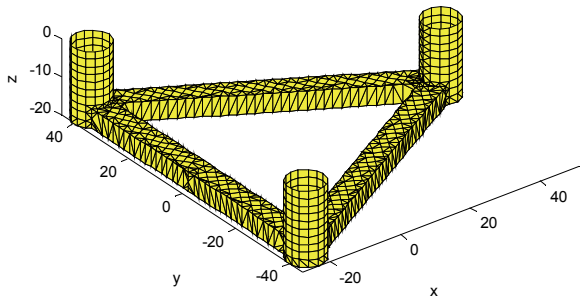

Figure 7.4 Discretized panel model of floating body (Triangular platform)

The hydrodynamic added mass and radiation damping in frequency domain are presented in Figures 7.5 and 7.6 respectively.

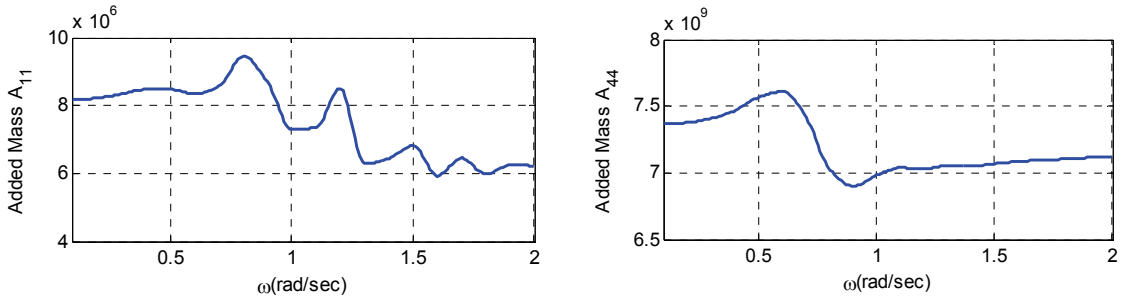

Figure 7.5 Added mass (Triangular platform)

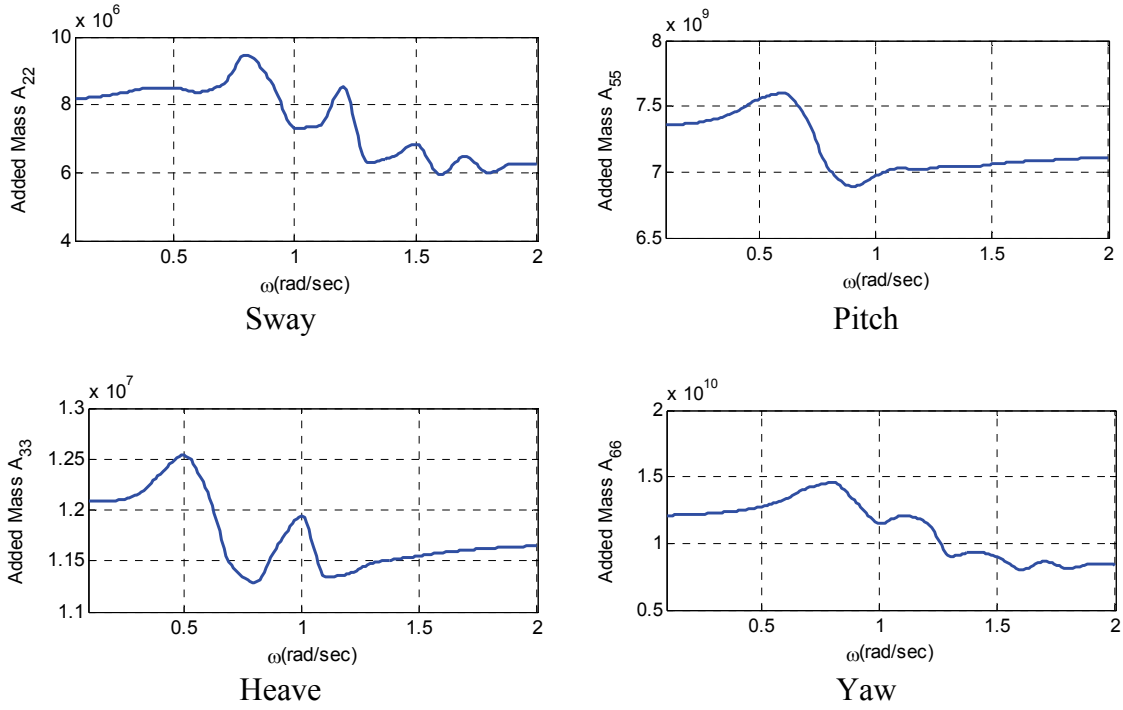

Figure 7.5 Continued

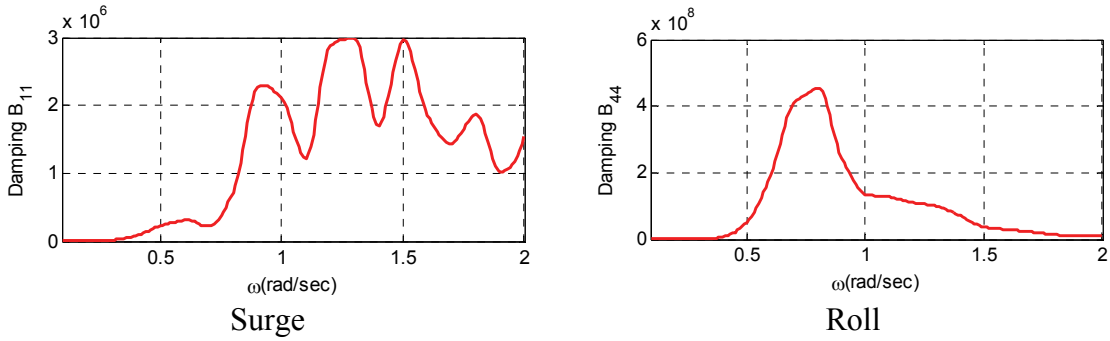

Figure 7.6 Radiation damping (Triangular platform)

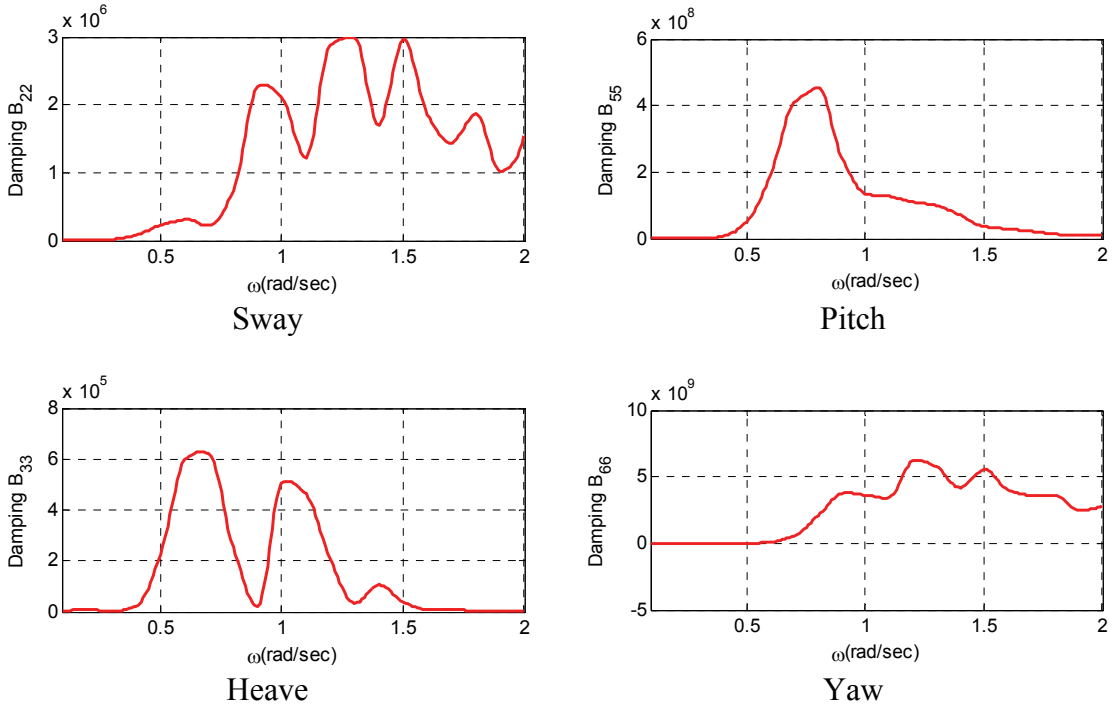

Figure 7.6 Continued

7.4 Time Marching Simulation in Normal Operational Condition

So far, the mass and stiffness properties of the floating platform and wind turbine system were determined and the hydrodynamic coefficients were also obtained from WAMIT. To see the dynamic responses of MUFOWT, floater-rotor-mooring coupled dynamic analysis of multiple turbines on one platform was carried out in the time domain. By performing this time domain analysis, a more rigorous analysis was made of the entire wind turbine system including blade aero dynamics with time-varying random wind field, elastic modes of tower and blades, FEM based mooring lines and nonlinear viscous loading of platform.

7.4.1 Viscous Damping Modeling

One of the advantages of the time domain analysis is that a numerical model can include the viscous damping effect. In FAST-CHARM3D, the viscous damping is calculated by placing an equivalent truss or plate members inside the submerged platform model where the diameter of the member is small compared to the wave length.

To include this effect, the Morison's formula in Equation (7.1) was used.

$$F_n = C_m \rho \forall \dot{u}_n - C_a \rho \forall \ddot{x}_n + \frac{1}{2} \rho S C_d (u_n - \dot{x}_n)\left|u_n - \dot{x}_n\right| \tag{7.1}$$

The symbols $\forall$ and S represent the displaced volume and projected area; the fluid density is ρ. C_a is the added mass coefficient, C_m is the inertia coefficient and C_d is the drag coefficient. $\dot{u}_n$ and u_n are the acceleration and velocity of fluid normal to the body, and $\ddot{x}_n$ and $\dot{x}_n$ are the acceleration and velocity of a floating body in the normal direction, respectively.

In the case of the three-turbine platform, the viscous drag force of the hull was represented by employing three truss members for each column; this acted along every normal direction of the column, and two plate members (vertical and horizontal) for each pontoon, which act in the normal direction of the plate as well. The drag coefficient C_d was taken to be 0.6 for the cylindrical column and 1.28 for the rectangular pontoon. The first two inertial loading terms in Equation (7.1) were not used because the incident-diffraction potential force and hull added mass were already calculated and included in Equation (4.54).

In addition to the hull viscous members above, the dynamic loadings on tethers were also calculated by Morison's equation. For the calculation of the loading on tethers, the inertia coefficient C_m in Equation (7.1) was taken to be 2 and the drag coefficients C_d were set to 1.3 for the wire and 2.4 for the chain. The drag coefficients for all the Morison members are tabulated in Table 7.3.

Table 7.3 Drag coefficients of Morison members (Triangular platform)

Location	C_d	**Viscous model**	**No. of members**
Columns	0.6	Truss	3
Pontoons	1.28	Horizontal plate	3
		Vertical plate	3
Chain Mooring	2.4	Slender rod	6
Wire Mooring	1.3	Slender rod	6

7.4.2 System Identification and Free Decay Test

To check the 6-DOFs platform natural frequencies, free decay tests in the time domain were carried out. In the time domain analysis, nonlinear viscous drag by platform and mooring line dynamics were included, but the tower and blades elasticity were not considered and every part of turbine was assumed to be a rigid body without any flexibility. In addition to that, the environmental loadings were not applied, which means the free decay test was simulated in calm water without wind and waves. Figure 7.7 shows the time history and spectra of the free decay test in every mode, respectively.

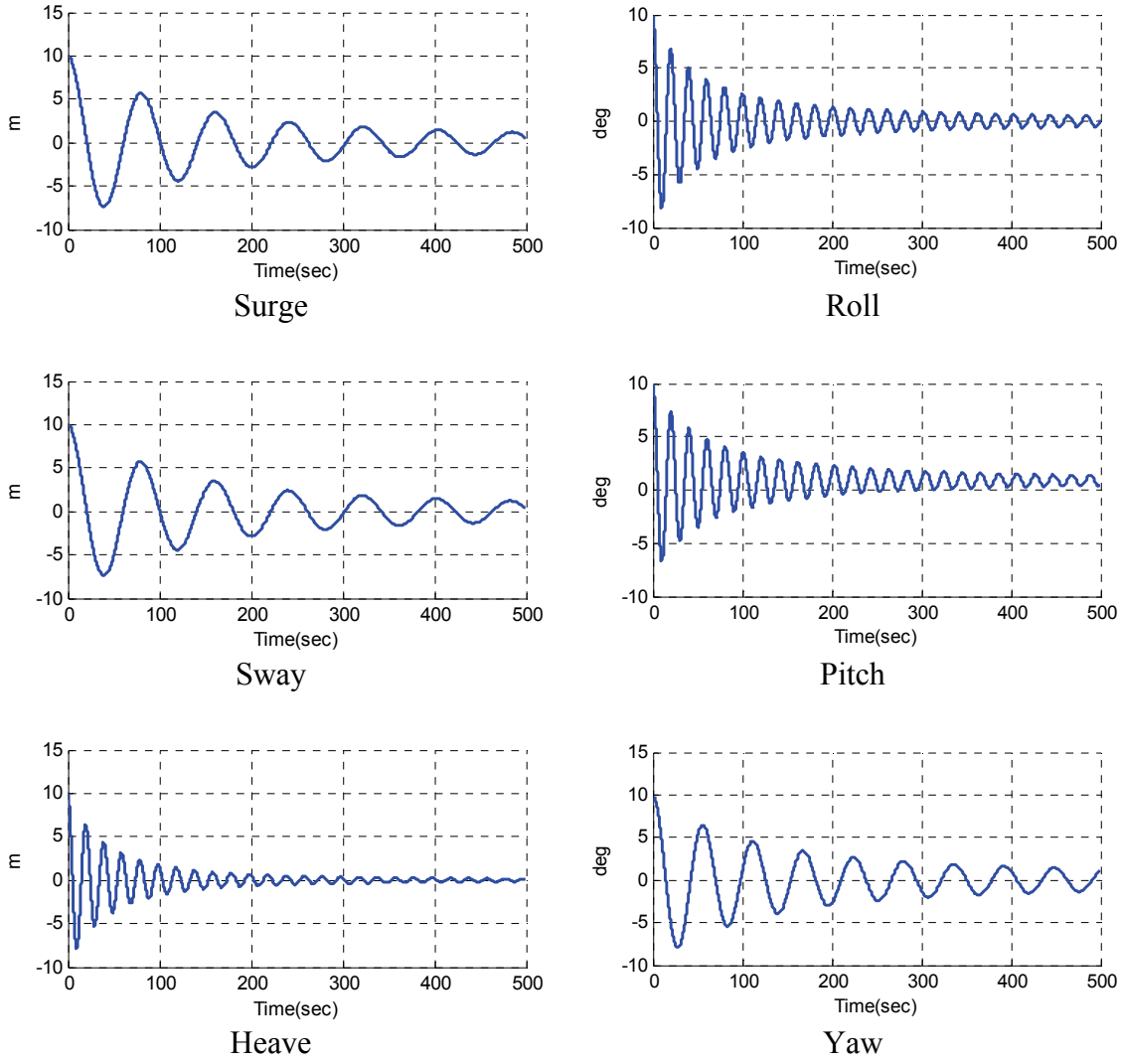

Figure 7.7 Free decay test (Triangular platform)

For surge, sway and heave tests, the platform was initially moved to a 10m position along the positive direction then released at that position. In the case of roll, pitch and yaw, the platform was released from the positive 10 degrees. The natural periods can be read from the time duration of one full cycle of the platform motion. The

natural frequencies, calculated in this free decay test, included the effect of the viscous drag from the hull and mooring lines as pointed out above.

It is seen that the natural frequencies of surge, sway and yaw, tabulated in Table 7.4, were positioned away from the wave frequency range so that the platform could avoid the resonance. Heave, roll and pitch natural frequencies were relatively close to the wave frequency range, but still had enough margins to the peak wave frequency. Thus, this design of floating system, including three turbines, is acceptable in an offshore wind-wave environment.

Table 7.4 Natural frequencies of triangular platform

	Surge	**Sway**	**Heave**	**Roll**	**Pitch**	**Yaw**
Period (sec)	80.2	79.5	19.4	19.9	20.1	55.7
Freq. (rad/s)	0.08	0.08	0.32	0.32	0.31	0.11

Even though the platform geometry had only one plane symmetry, it was seen that the natural frequency of surge and sway, or roll and pitch are nearly identical to each other.

7.4.3 Responses in Random Wind and Wave Environment

So far, the system identification works was done without consideration of structural elasticity and aero dynamic loading on the blades. It turned out that the current MUFOWT model can support 3 turbines with proper platform natural frequencies. The mooring system was also well designed to give a proper restoring force and moment to

the floating platform. In this section, a fully working MUFOWT in wind-wave environment was simulated. For simplicity, the directions of wind and wave were aligned (collinear) and set to zero degree. Mean wind speed at 90m height, which corresponds to the hub height of 5MW turbine, was set to 15m/s, which was higher than the rated wind speed. The environmental conditions are tabulated in Table 7.5.

Table 7.5 Environmental conditions (Triangular platform)

Item	Unit	Value
Mean Wind Speed At 90m Height	m/s	15
Water Depth	m	300
Wave Heading	deg	0
Significant Wave Height	m	5.0
Peak Wave Period	sec	8.688
Overshoot parameter	-	2.4
Cut-in / Cut-out Wave Frequencies	rad/s	0.15 / 1.2

The full field wind data was generated by TurbSim (Jonkman, 2009), and the wind velocities at different hub heights between 1.5MW and 5MW turbines were calculated separately. The random waves were generated base on the JONSWAP wave spectrum with significant wave height of 5m, peak period of 8.688sec, and overshoot parameter of 2.4. The current was not considered in this case study for simplicity. The time step of the CHARM3D side, which included the numerical integration of mooring line equations, was set to 0.01 seconds, and that of the FAST side, which included the computation of aerodynamics, elastic modes of tower and blades and platform dynamics,

was set to 0.005 seconds. So, at every two time step of FAST, the CHARM3D fed the mooring restoring and all other external loadings on the platform. The total simulation time was 1,000 seconds, including the initial 100 seconds of ramp time, in order to minimize the transient effect of responses in the beginning.

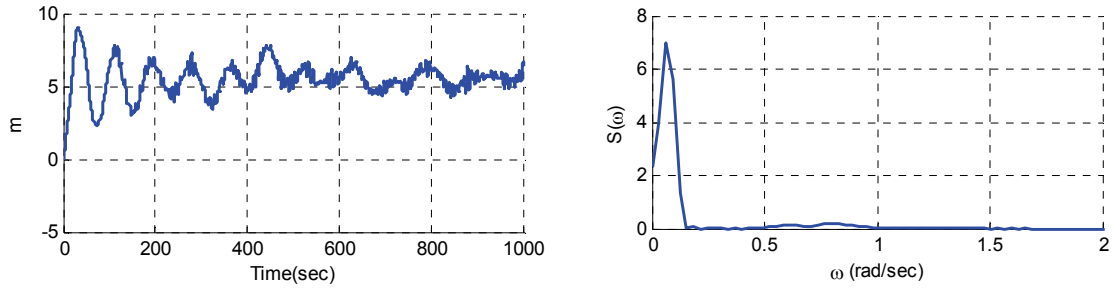

(a) (b)

Figure 7.8 Surge motion (a) and spectrum (b) (Triangular platform)

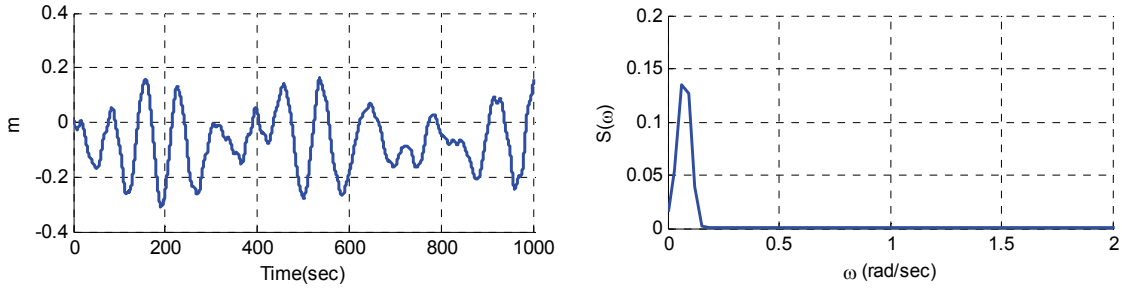

(a) (b)

Figure 7.9 Sway motion (a) and spectrum (b) (Triangular platform)

The surge and sway responses in Figures 7.8 ~ 7.9 show that the floating platform motions were primarily dependent on the low frequency, which was derived by wind. The contribution of wave was relatively small.

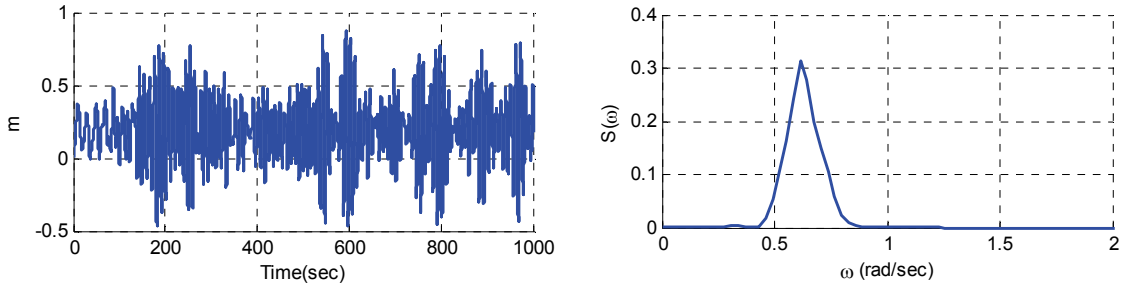

(a) (b)

Figure 7.10 Heave motion (a) and spectrum (b) (Triangular platform)

In the case of heave, the platform response was primarily affected by wave energy as can be seen in Figure 7.10. The roll and pitch responses in Figures 7.11 ~ 7.12 show a high peak around its natural frequency of 0.32 rad/s. Since the wave energy in this frequency range was not significant, no severe resonances occurred for both roll and pitch motions.

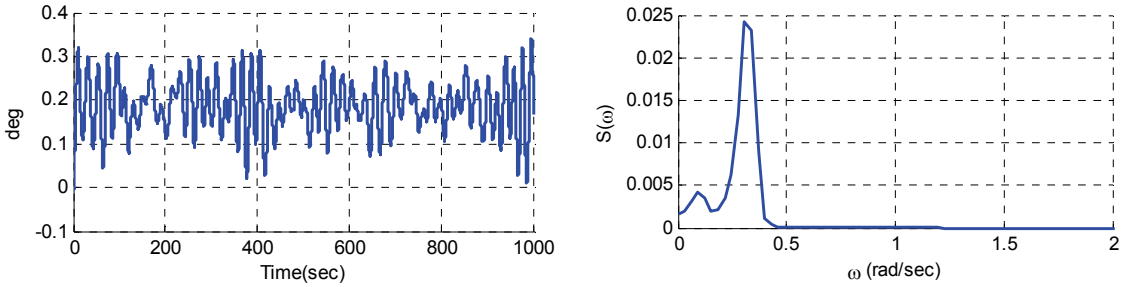

(a) (b)

Figure 7.11 Roll motion (a) and spectrum (b) (Triangular platform)

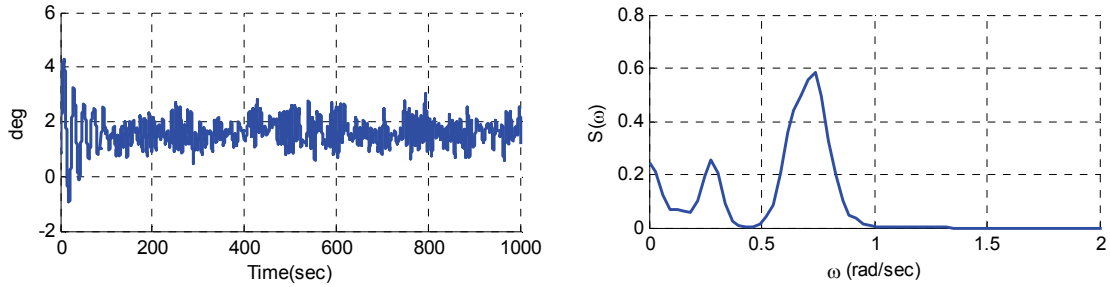

(a) (b)

Figure 7.12 Pitch motion (a) and spectrum (b) (Triangular platform)

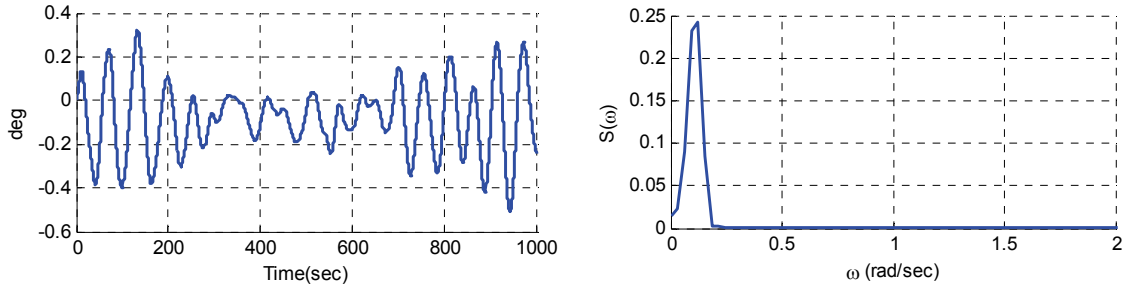

(a) (b)

Figure 7.13 Yaw motion (a) and spectrum (b) (Triangular platform)

Figure 7.13 shows that the mean yaw angle was not zero. This yaw offset also could be seen in a single floating wind turbine due to the tower base torsional moment which was induced by a rotating inertia of the rotor and a gyroscopic effect. In the case of a multiple turbines platform, the total torsional moment becomes bigger, so the resultant yaw response will be significantly increased. So, it is important to design a floating platform of MUFOWT considering the appreciable yaw moment from all turbines.

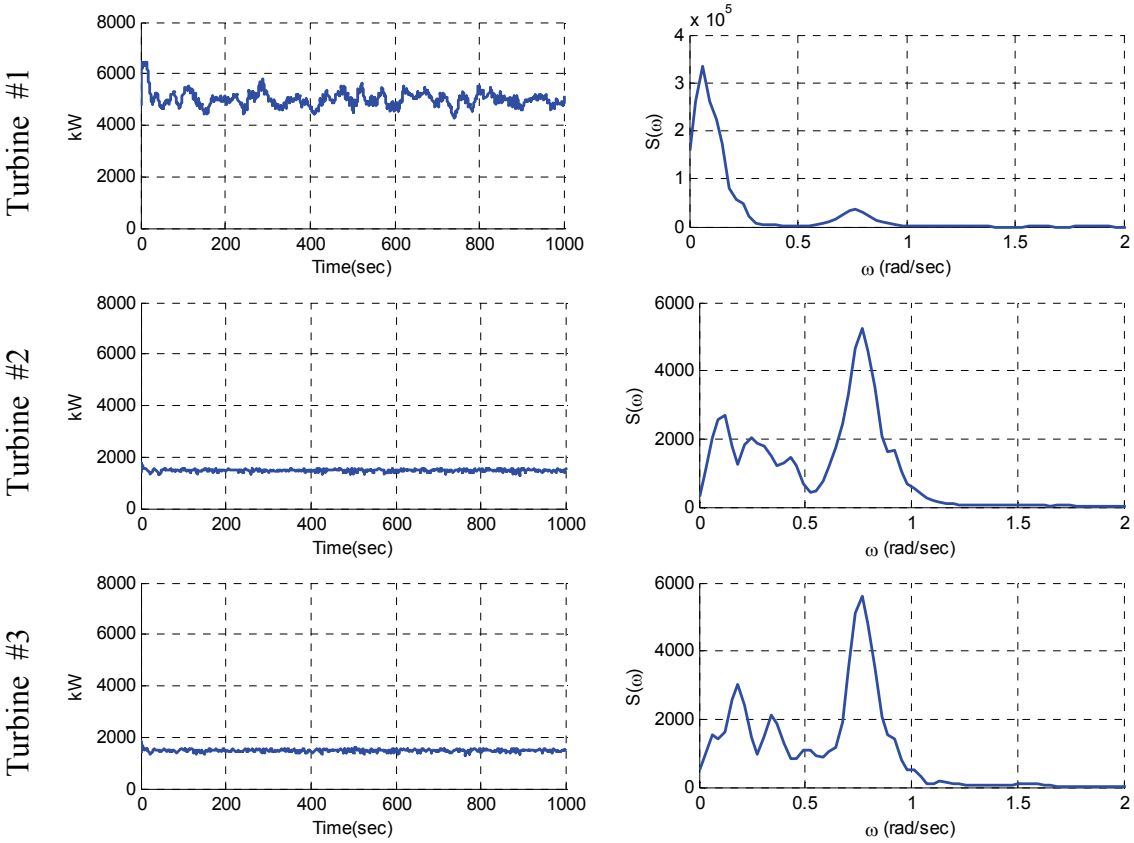

Figure 7.14 Generator power (a) and spectra (b) (Triangular platform)

In addition to the platform responses, the turbine outputs were also checked and presented. The electric power output in Figure 7.14 shows that turbine #1 generated rated power of 5MW, and the other turbines normally generated 1.5MW power during the entire simulation time.

Figure 7.15 shows the variation in blade pitch angle. It is seen that the variation of the 1.5MW blade angle was more active because the rated rotor speed was much faster than that of the 5MW turbine. Overall, it was apparent that blade pitch variation

was mostly dependent on the low frequency excitation from wind and a minor contribution from wave energy.

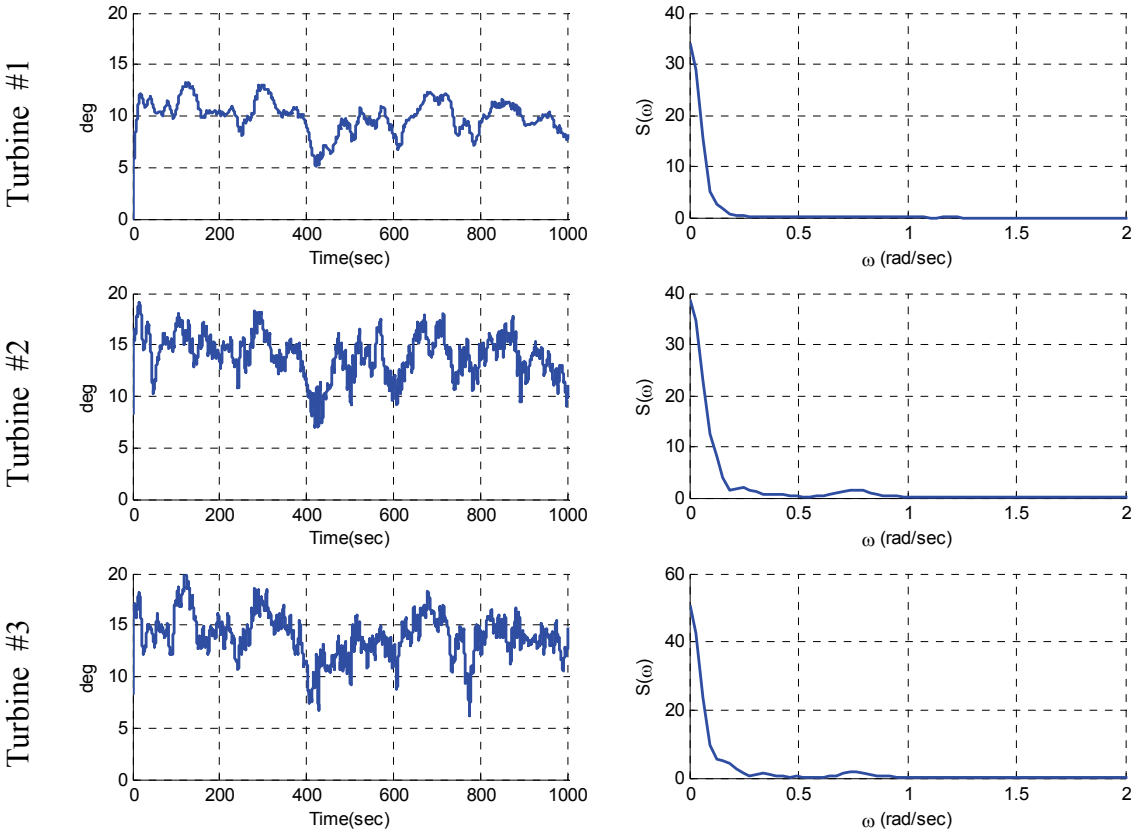

Figure 7.15 Blade pitch angle (a) and spectra (b) (Triangular platform)

The blade pitch and the generator torque controller used in this three-turbine case followed the same method that Hywind spar turbine had adopted. Otherwise, the platform responses as well as the turbine performance could experience similar instability observed in Hywind spar case because the pitch natural frequency of this semi-submersible platform was also very low, and there was possibility of negative

damping due to the conventional blade pitch controller. For convenience, the controller gains were adopted from the recommended values by NREL (Jonkman, 2008).

Since the structural specifications were different between the 1.5MW and 5MW turbines, the tower base loads were also different. As can be seen in Figure 7.16, the variation and magnitude of the 5MW tower base load was much greater than that of the 1.5MW turbine.

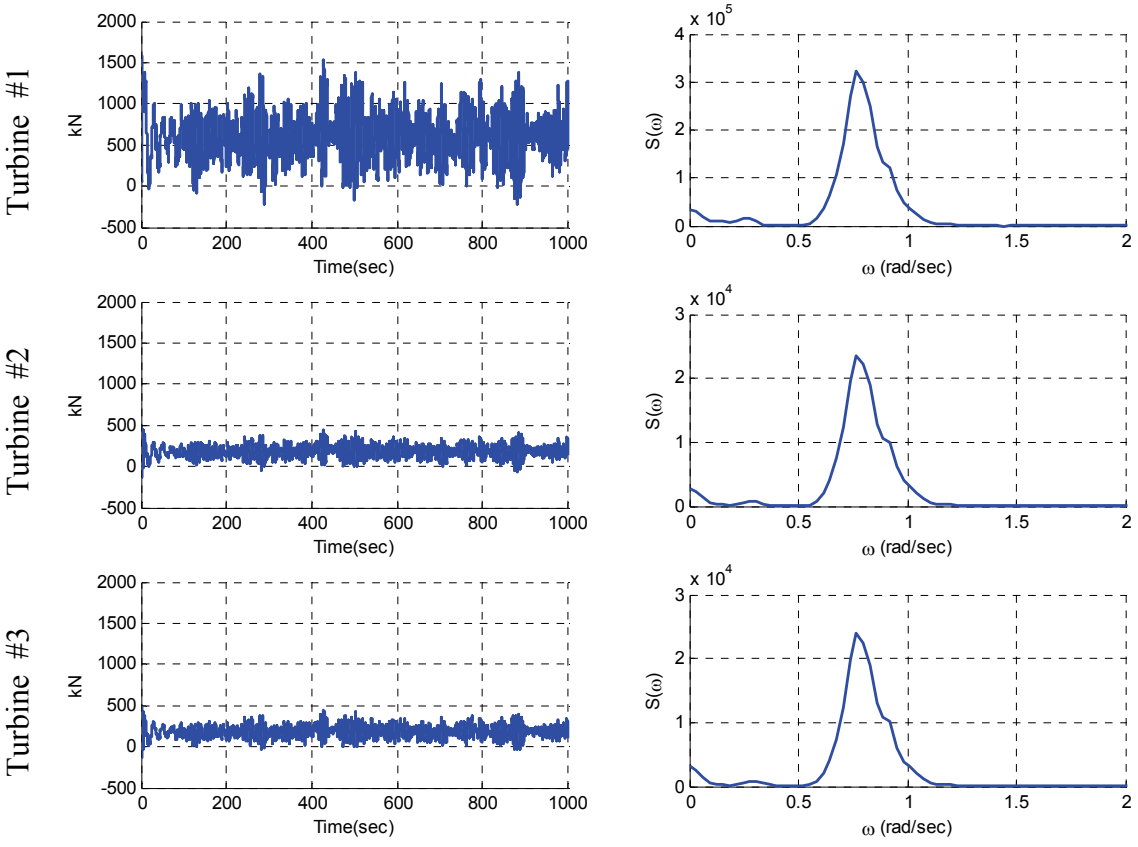

Figure 7.16 Tower base fore-aft shear force (a) and spectra (b) (Triangular platform)

Thus, proper structural design at the tower base becomes essential to ensure structural integrity. In the case of the tower base in-line shear force, the responses were very sensitive to the wave energy frequency range.

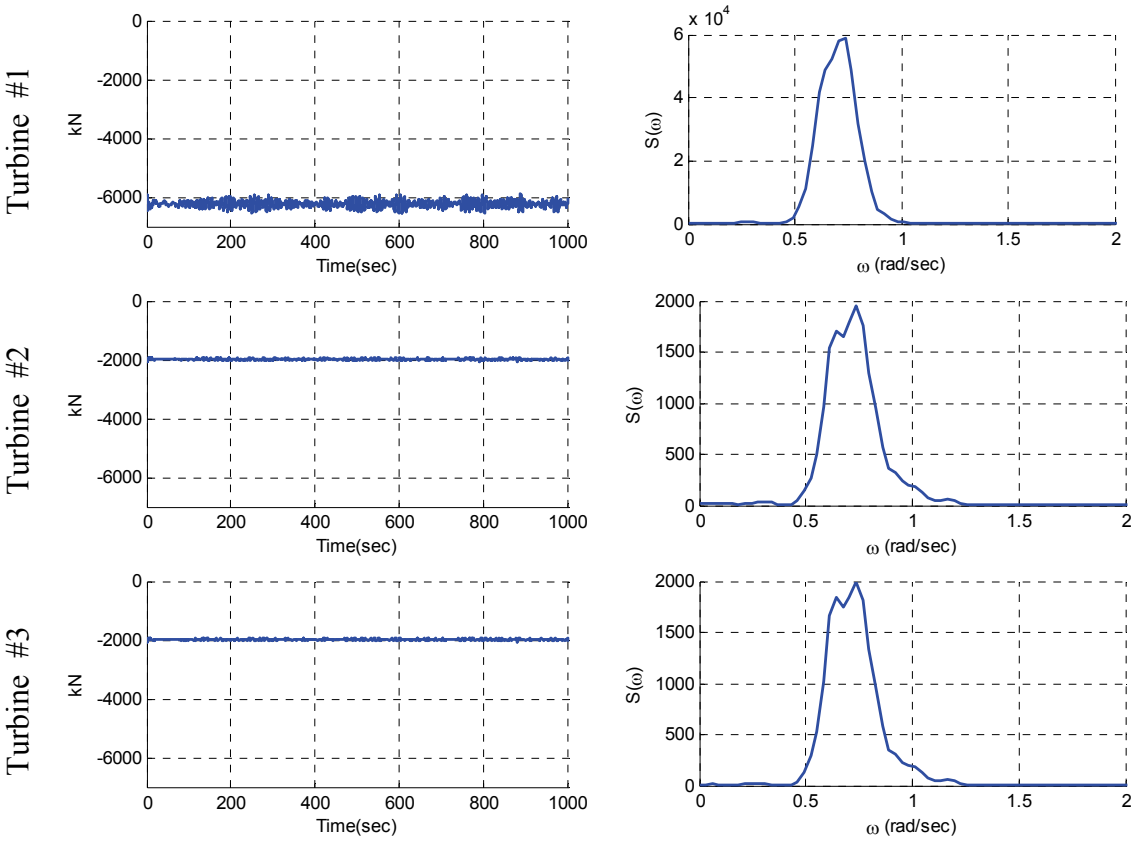

Figure 7.17 Tower base axial force (a) and spectra (b) (Triangular platform)

The tower base axial force in Figure 7.17 shows the difference in tower weight between 1.5MW and 5MW unit. Similarly, the axial forces are also dependent on the wave frequency range. The standard deviation of axial force from the 5MW turbine is 121.8 kN, and that of 1.5MW turbine is 24.2 kN, which means the repetitive vertical

loading on the 5MW tower base is more severe than that of the 1.5MW turbine; thus the fatigue failure of tower could become an issue for a large scale turbine.

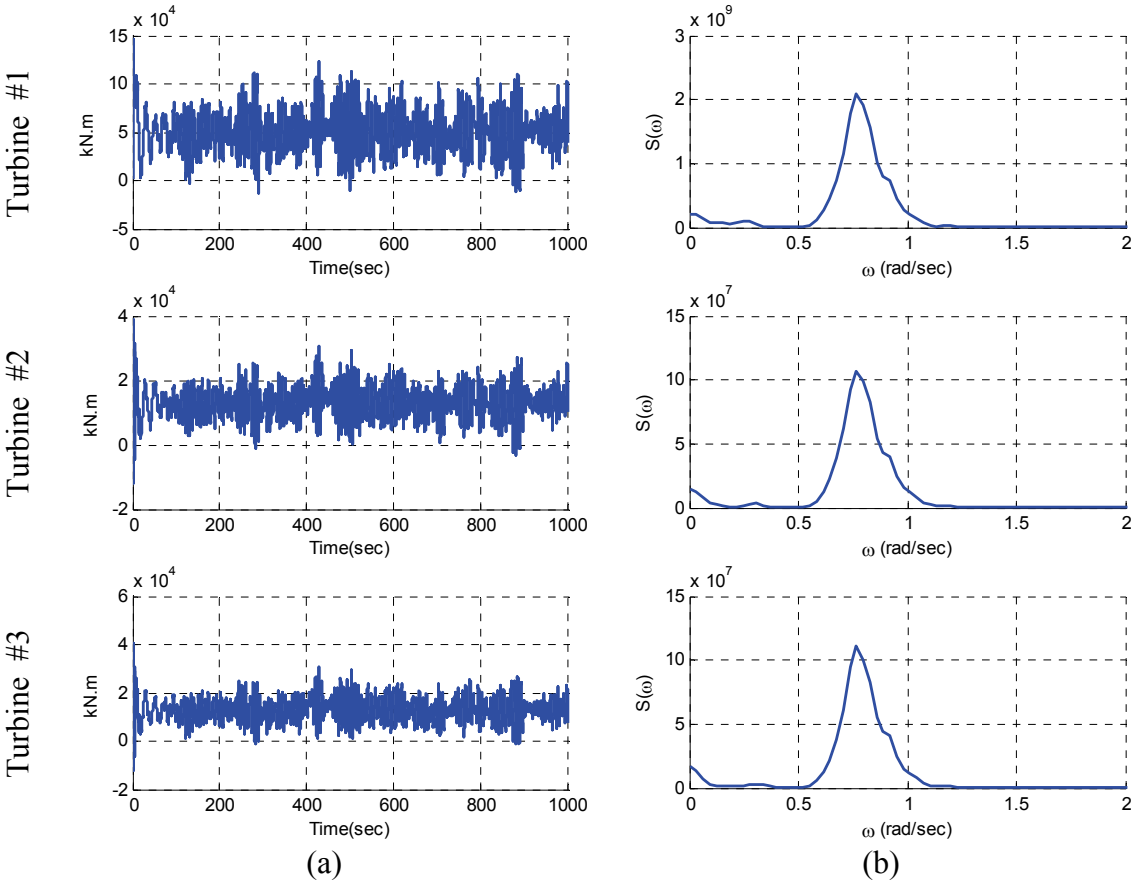

Figure 7.18 Tower base pitch moment (a) and spectra (b) (Triangular platform)

The tower base fore-aft moments and its spectra are depicted in Figure 7.18. It shows that the fore-aft moments at the tower base were affected by wave energy, similar to the fore-aft shear forces.

Due to the scale effect, the tower base torsional moment of the 5MW turbine was much greater than that of the 1.5MW turbine as seen in Figure 7.19. Also, the tower base

of the 5MW turbine was more vulnerable to torsional fatigue failure compared to the 1.5MW turbine due to the severe repetitive loads from the upper turbine. Interestingly, the tower base torsional moment was more affected by low frequency excitation from the wind, while the shear or axial force was primarily affected by wave loadings.

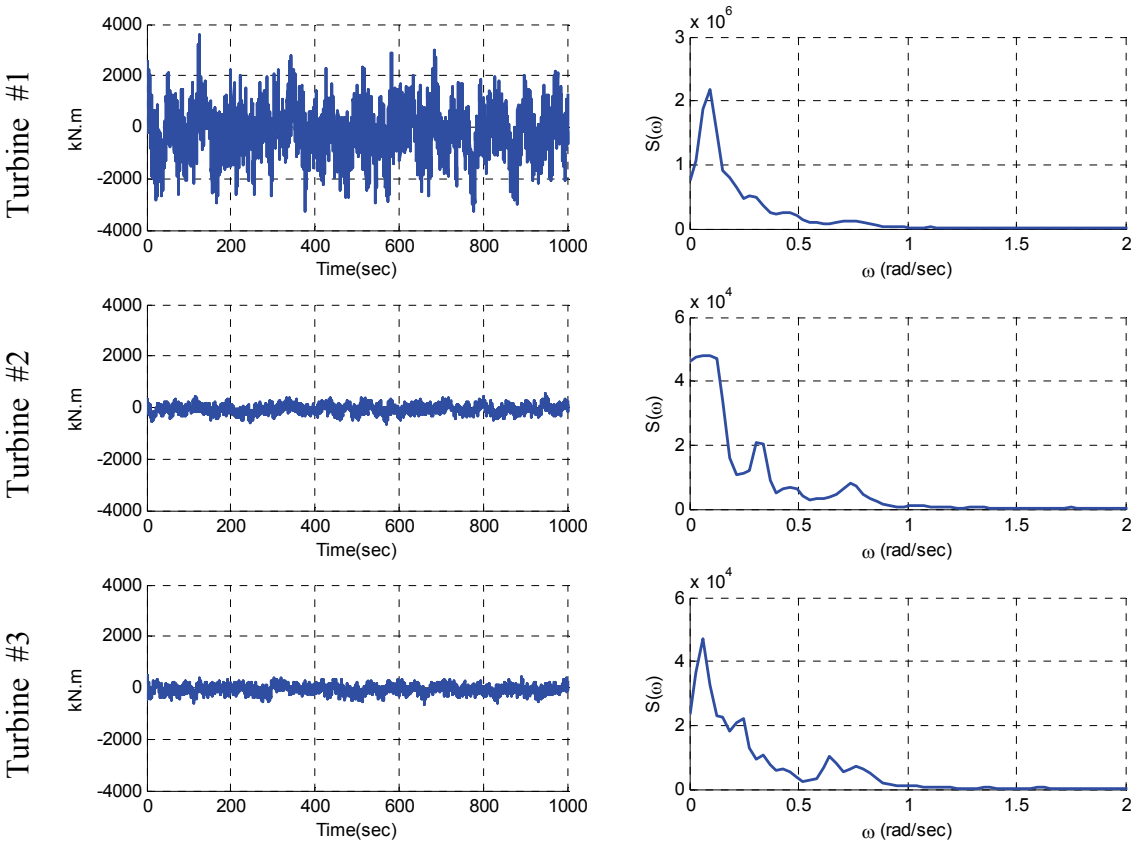

Figure 7.19 Tower base torsional moment (a) and spectra (b) (Triangular platform)

7.5 One Turbine Failure Simulation

7.5.1 Blade Pitch Control Failure of One Turbine

In this section, a more rigorous and sophisticated simulation of MUFOWT with the failure of one turbine was carried out and the platform responses, as well as turbine performances, were checked. The failure of the turbine was implemented by locking the blade pitch angle at 30 degrees for the smaller turbine #2 in Figure 7.20 (a). In detail, the blade pitch angle of turbine #2 suddenly went out of control, started to increase at 500 seconds, and then stopped in one minute. The blade pitch angle was locked at 30 degrees, which was insufficient to rotate the blades.

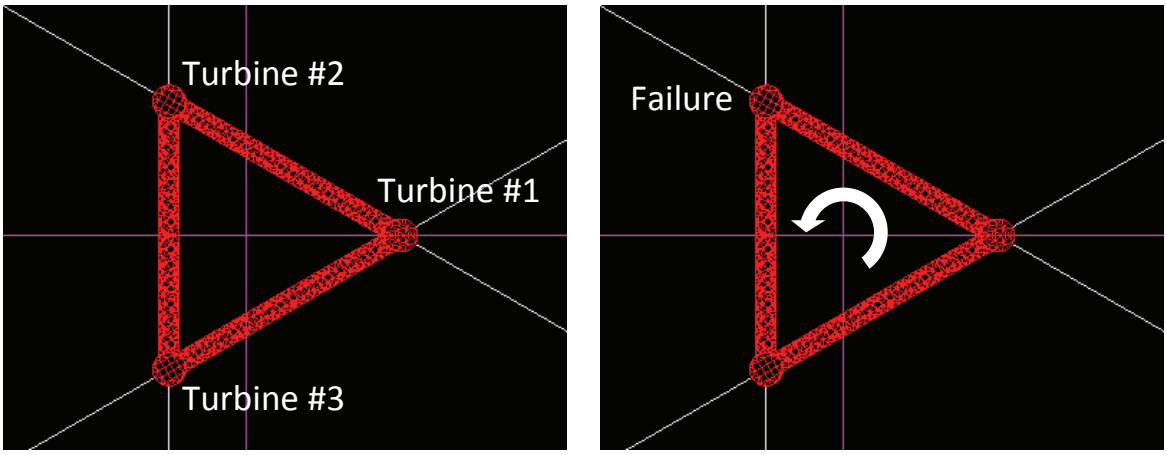

(a) (b)

Figure 7.20 Turbine location (a) and turbine failure (b) (Triangular platform)

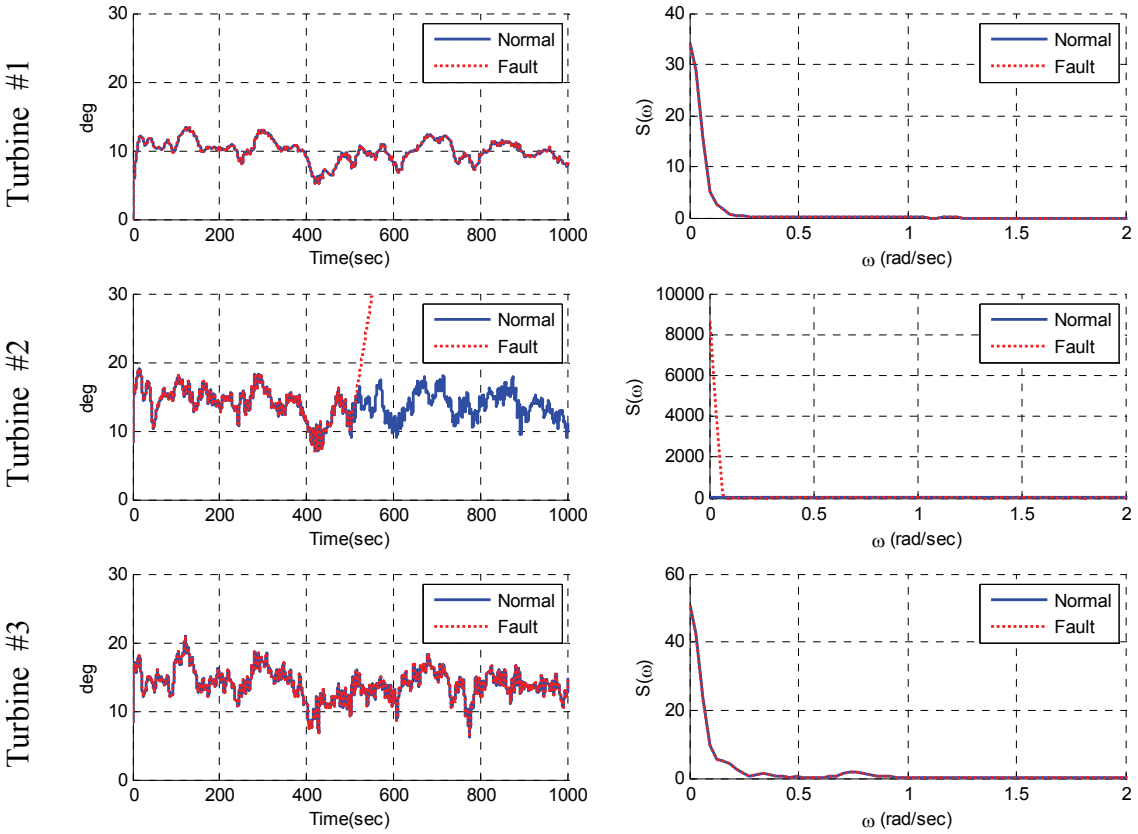

Figure 7.21 Blade pitch angle (a) and spectra (b) with blade control failure (Triangular platform)

During the first 500 seconds, the simulation performed normally. All turbines and platform were well balanced and worked without any disturbance. After 500 seconds, turbine #2 lost its thrust force due to the decreased angle of attack of the blades in turbine #2. As a result, the floating platform may experience unexpected yaw moment as seen in Figure 7.20 (b). Figure 7.21 shows the change of blade pitch angle of each turbine; it is seen that the pitch angle suddenly increases up to 30 degrees at 500 seconds and locked turbine #2.

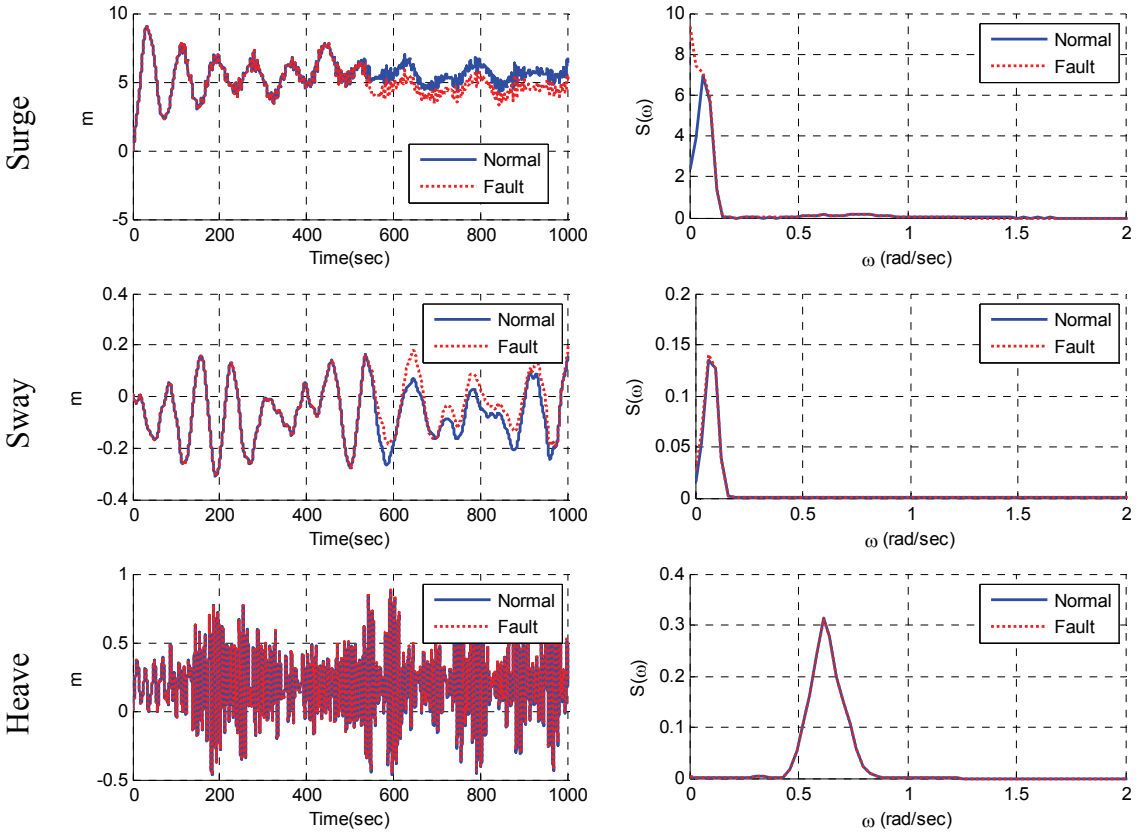

Figure 7.22 Platform translational motions (a) and spectra (b) with blade control failure (Triangular platform)

Due to the failure of turbine #2, the overall aerodynamic drag forces from each turbine were reduced; thus the mean surge offset after 500 seconds also decreased from 5.5m to 4.8m. As can be seen in Figure 7.22, the variation of heave is relatively small compared to the other modes.

In Figure 7.23, the platform yaw response shows very rapid change from -0.11 degree to +1.23 degree in a few minutes. The amount of yaw angle change seems relatively small, but this small variation usually induced a very large translational offset

at the turbine location because the MUFOWT platform was bigger than the single turbine platform.

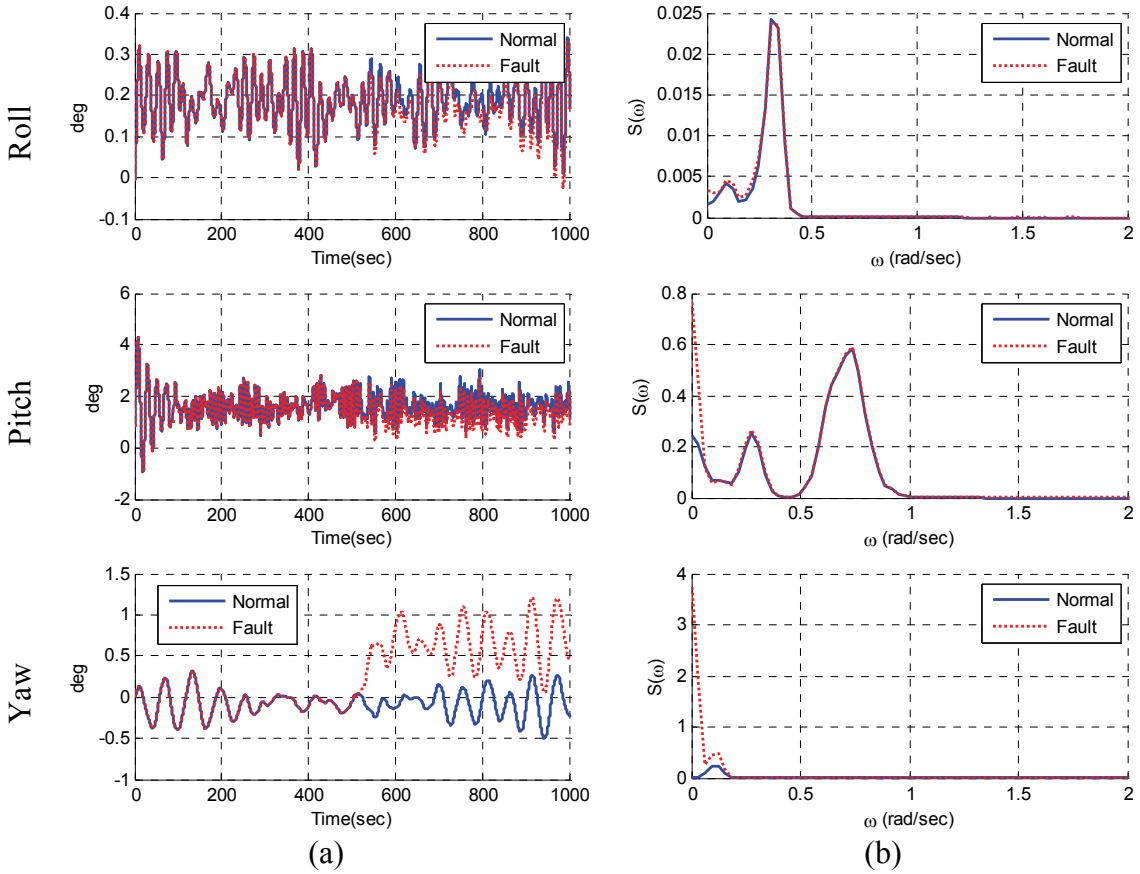

Figure 7.23 Platform rotational motions (a) and spectra (b) with blade control failure (Triangular platform)

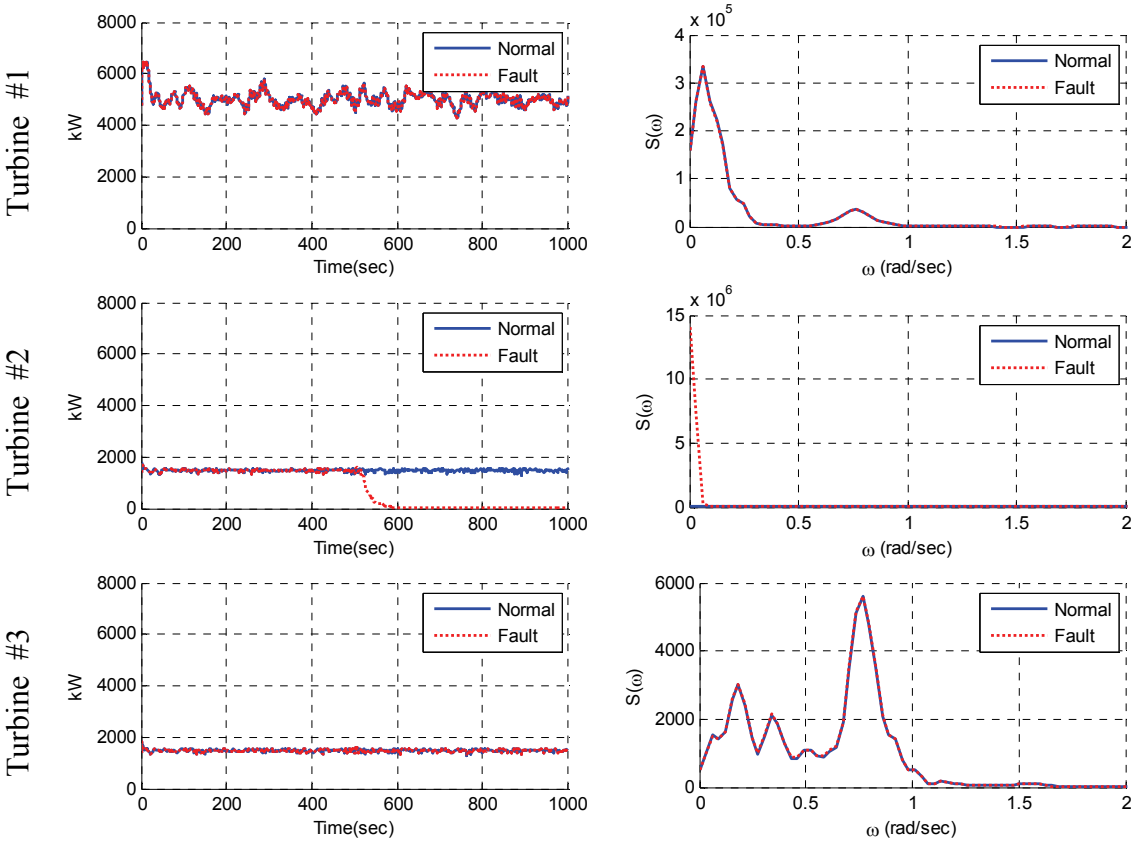

Figure 7.24 Generator power (a) and spectra (b) with blade control failure (Triangular platform)

As for the electric power output in Figure 7.24, turbine #1 produced 5MW rated power normally, while turbine #2 produced very low electric power around 500 kW after the locking of the blade pitch angle. This sudden drop in electric power was mainly due to the slow rotation of rotor due to the feathered blade pitch angle.

The responses of tower base force and moment in Figure 7.25 were also checked as below. As expected, the fore-aft shear forces at the tower base for turbine #2 decreased appreciably. For example, the mean shear force of turbine #2 dropped from

185.0 kN to 77.7 kN after the blade pitch failure. This drop of fore-aft shear force is main reason for the unbalanced yaw loading on the platform.

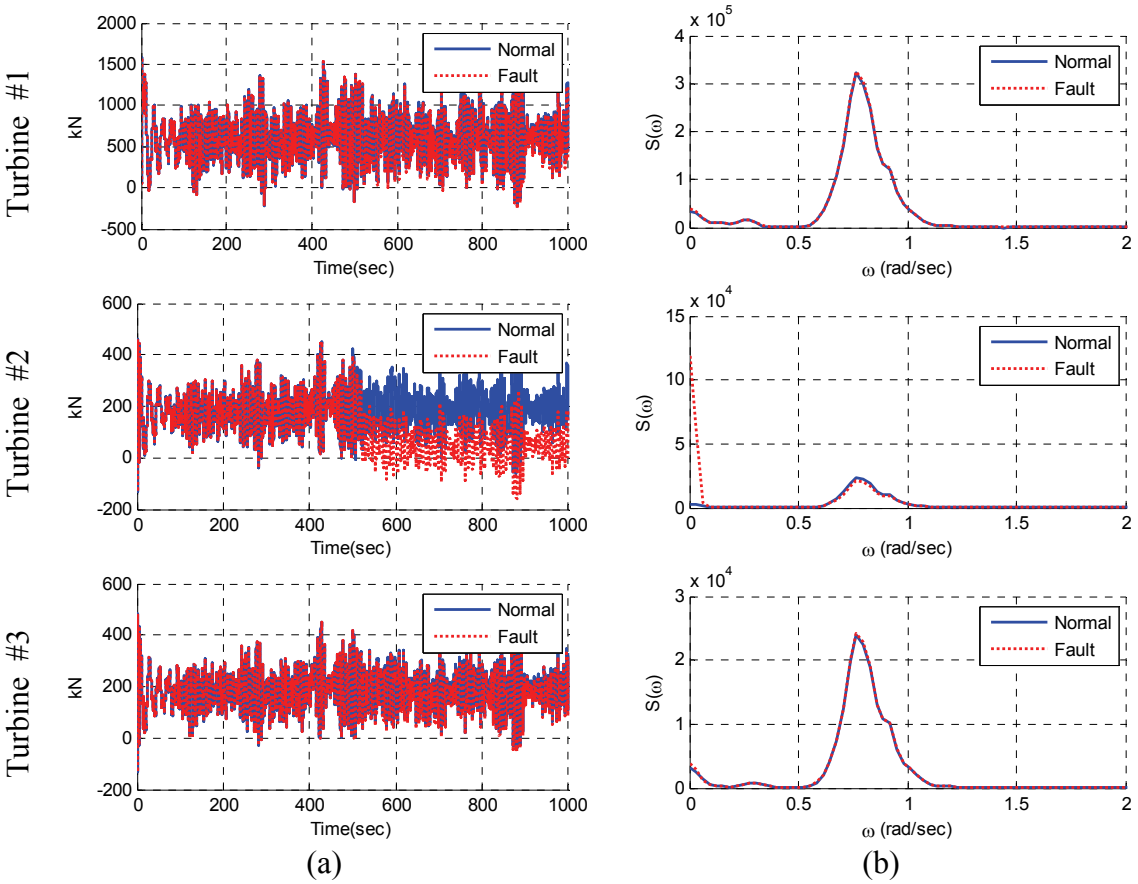

Figure 7.25 Tower base fore-aft shear force (a) and spectra (b) with blade control failure (Triangular platform)

In the frequency domain, it was seen that after failure at 500 seconds, the low frequency response was dominant for the tower base fore-aft shear force. It can be explained that the blade pitch angle was fixed; after that time, the turbine blade could not control the inflow aero loading and was fully affected by random wind which made a very low frequency response of the tower base shear force of turbine #2.

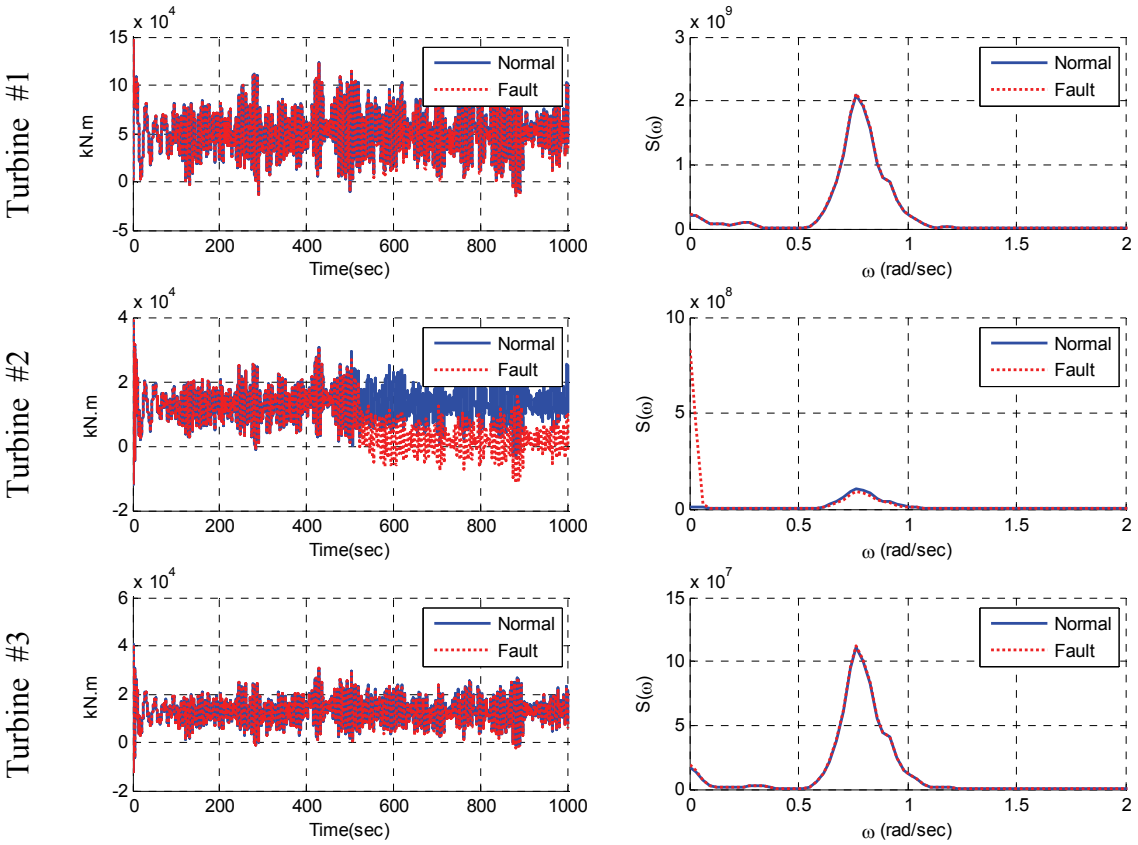

Figure 7.26 Tower base pitch moment (a) and spectra (b) with blade control failure (Triangular platform)

Similar phenomena can be also seen in the tower base pitch moment in Figure 7.26 and tower base torsional moment in Figure 7.27. The mean tower base pitch moment of turbine #2 decreased by 68.1% due to the loss of drag force. The maximum tower base torsional moment also decreased by 25.9% after locking the blade pitch angle. The changes in tower base loadings from other turbines (#1 and #3) were not that significant.

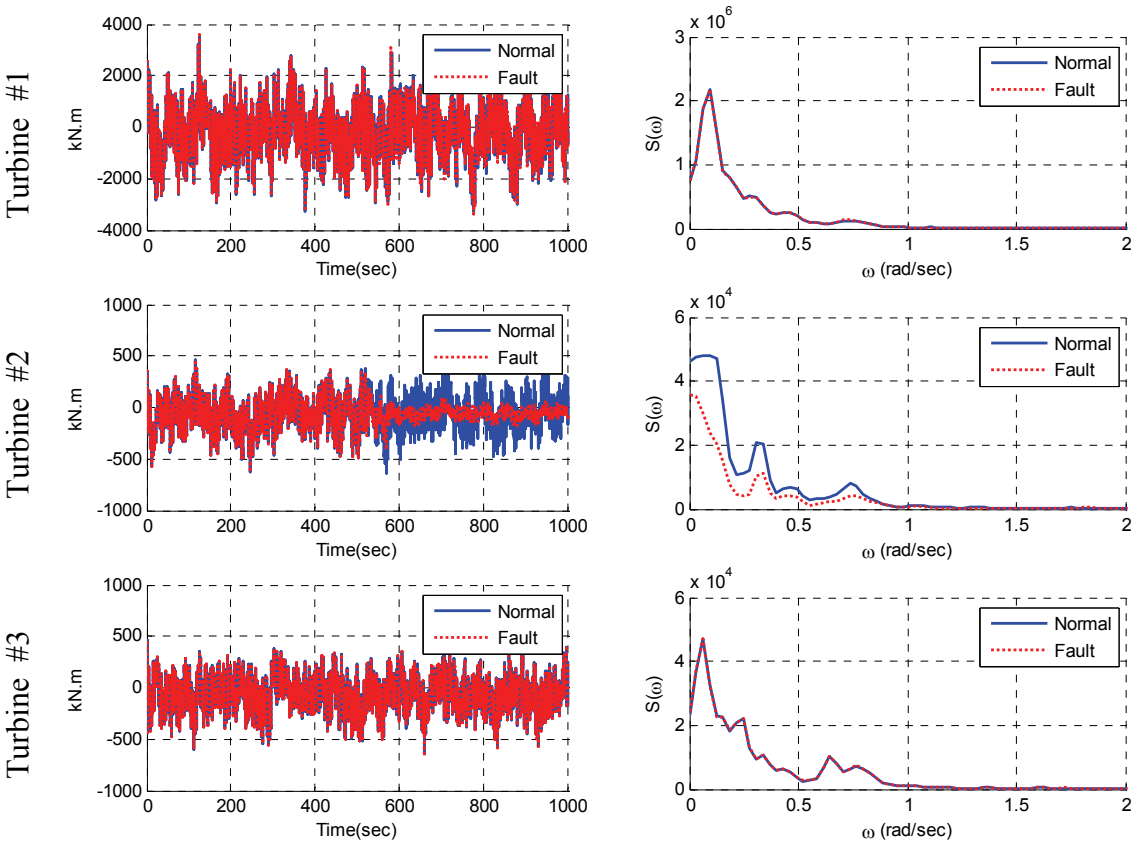

Figure 7.27 Tower base torsional moment (a) and spectra (b) with blade control failure (Triangular platform)

The failure of turbines also affects the mooring line top tensions. To see the time series of top tensions and its spectrum, each line is numbered as seen in Figure 7.28. In case of lee-side mooring lines such as #1 and #2 in Figure 7.29, the top tensions after failure event are increased while the weather-side lines including #4 and #5 in Figure 7.30 show less top tension after the failure of turbines. This change is mainly due to the variation of total thrust force on the platform and reduced surge offset. Side lines (#3 and #6) show relatively less change compared to the other lines because those lines are not directly related to the platform surge drift.

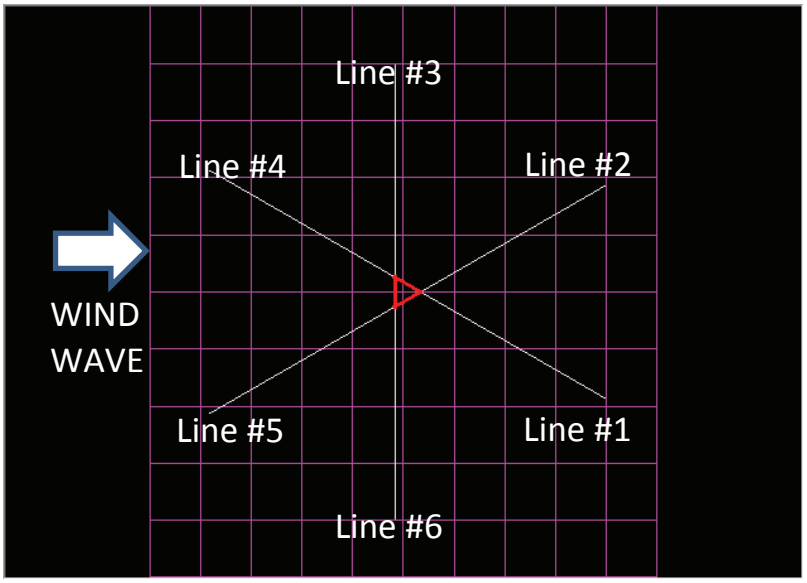

Figure 7.28 Top view of mooring-line arrangement (Triangular platform)

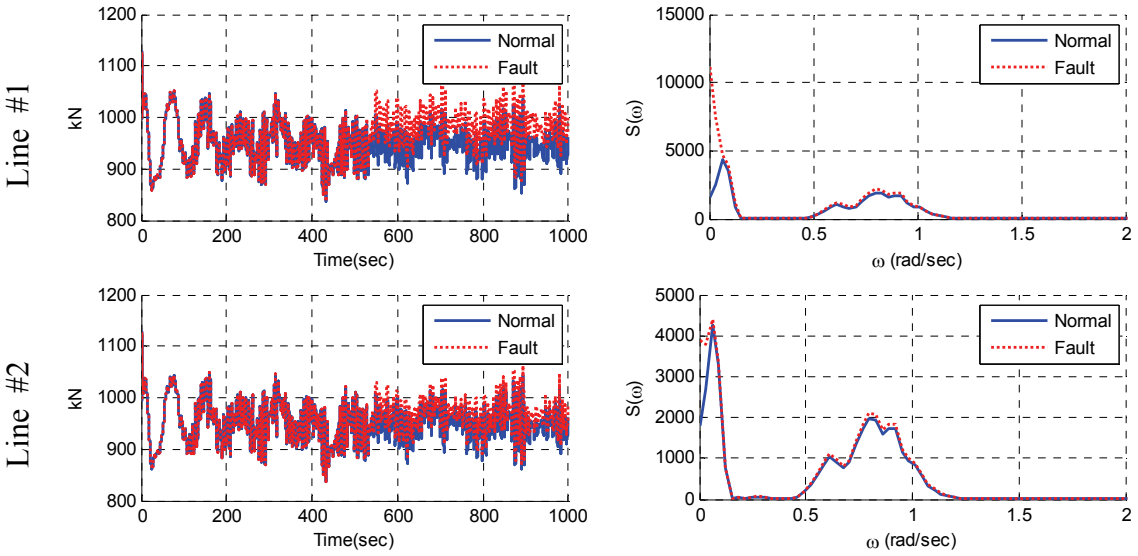

Figure 7.29 Top-tension (a) and spectra (b) of Line #1~#3 (Triangular platform)

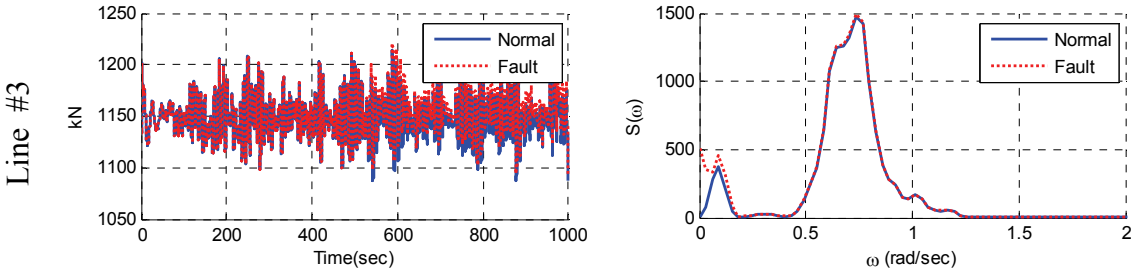

(a) (b)

Figure 7.29 Continued

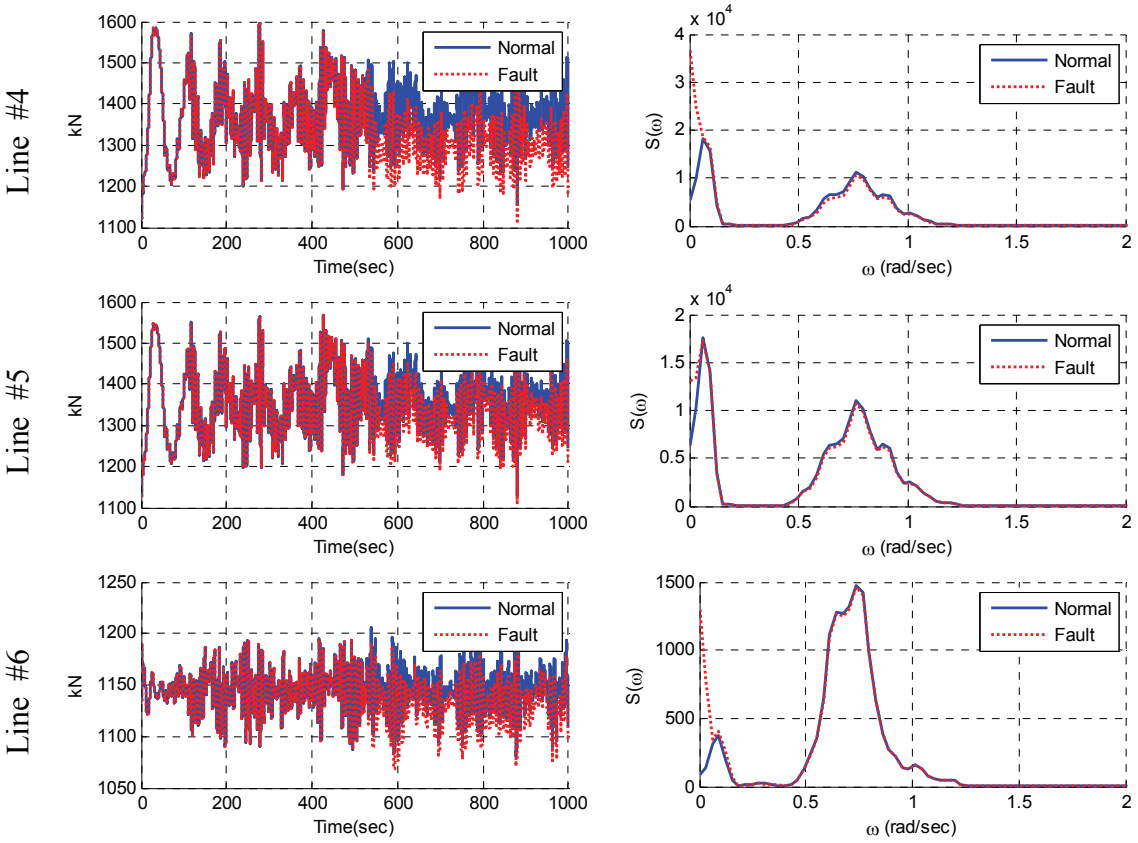

(a) (b)

Figure 7.30 Top-tension (a) and spectra (b) of Line #4~#6 (Triangular platform)

The overall performances of the three-turbine semi-submersible has been numerically computed and presented in this section. The time domain responses,

including aero-elastic-hydro-mooring dynamics for multiple turbines, can be analyzed through the developed tool. All the turbine outputs and platform responses have been solved simultaneously, so every possible wind turbine dynamic and interaction between each turbine and platform can be captured without any time consuming and complicated derivations.

7.5.2 Partial Blade Broken Failure of One Turbine

The NREL's 5MW baseline wind turbine has three blades. The blade structural model is based on the structural properties of the 62.6m-long LM Glassfiber blade used in the DOWEC study and properly modified by NREL (Jonkman, 2007). The overall blade mass is 17,740 kg per blade, and the structural damping ratio is 0.477% in all modes of the isolated blade. Table 7.6 summarizes the blade structural properties.

Table 7.6 Blade structural properties

Item	Unit	Value
Length (w.r.t. Root Along Preconed Axis)	m	61.5
Mass Scaling Factor	%	4.536
Overall (Integrated) Mass	kg	17,740
Second Mass moment of Inertia (w.r.t. Root)	$kg \cdot m^2$	11,776,047
First Mass Moment of Inertia (w.r.t. Root)	$kg \cdot m$	363,231
CM Location (w.r.t. Root Along Preconed Axis)	m	20.475
Structural Damping Ratio (All Modes)	%	0.477465

Similar to the blade structural properties, the blade aerodynamic properties are also defined based on the DOWEC blades. The details are explained by J. Jonkman (Jonkman, 2007).

The developed time-domain tool for wind turbine-floater-tether coupled dynamic analysis has been used in this study to assess the transient, global, and local effects when a blade tip is suddenly damaged. The details of tower/blade properties and control schemes are the same as those of NREL's 5MW Baseline wind turbine. The wind speed at hub height is set to 15m/s with vertical or horizontal variations, i.e. full-field wind data is used in this study considering random variation along both horizontal and vertical directions inside the blade swept area. The blade breaking zones were determined based on the blade node number. To minimize the instability of the simulation, the blade breaking zones were selected from the node number 15 to 17. Table 7.7 shows the selected blade length and node number.

Table 7.7 Damaged blade length and node number

Node number	Location from the Apex	Element Length	Element Mass
15	56.1667 m	2.7334 m	248.21 kg
16	58.9000 m	2.7332 m	193.63 kg
17	61.6333 m	2.7334 m	132.17 kg

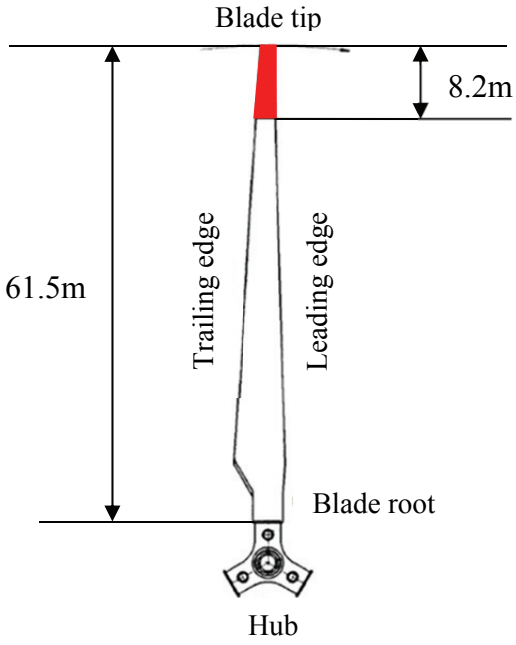

Figure 7.31 Blade length and broken zone

The total simulation time was set to 1,000 seconds, and the breaking event occurred at 500 seconds of time frame. To minimize the transient responses of the floater in the beginning, the wave loading was gradually increased to the actual values during the ramping time of 100s. However, ramping was not applied to wind loading. Instead, the blade was initially rotated with the given wind loading and thus the initial transient effect associated with the wind loading on the blade was very minimal. The statistics were calculated after the ramping period (100 seconds).

To simulate the broken blade, both the aerodynamic and structural dynamic properties were changed at a given breaking time, i.e. the blade element mass and aerodynamic forces in the broken range were set to zeros at the time of the breaking

event. Figure 7.31 shows the broken zone of the blade. The total loss of blade element mass was equivalent to 574 kg, and the length was about 8m.

The simulation result showed that the platform responses are not significantly influenced by the partially broken blade because the semi-submersible platform was very compliant, and the mass scale between turbine and platform was quite different. In the case of the single turbine TLP-type FOWT, the platform responses, especially for roll, pitch and yaw motions, were appreciably influenced by the partially broken blade.

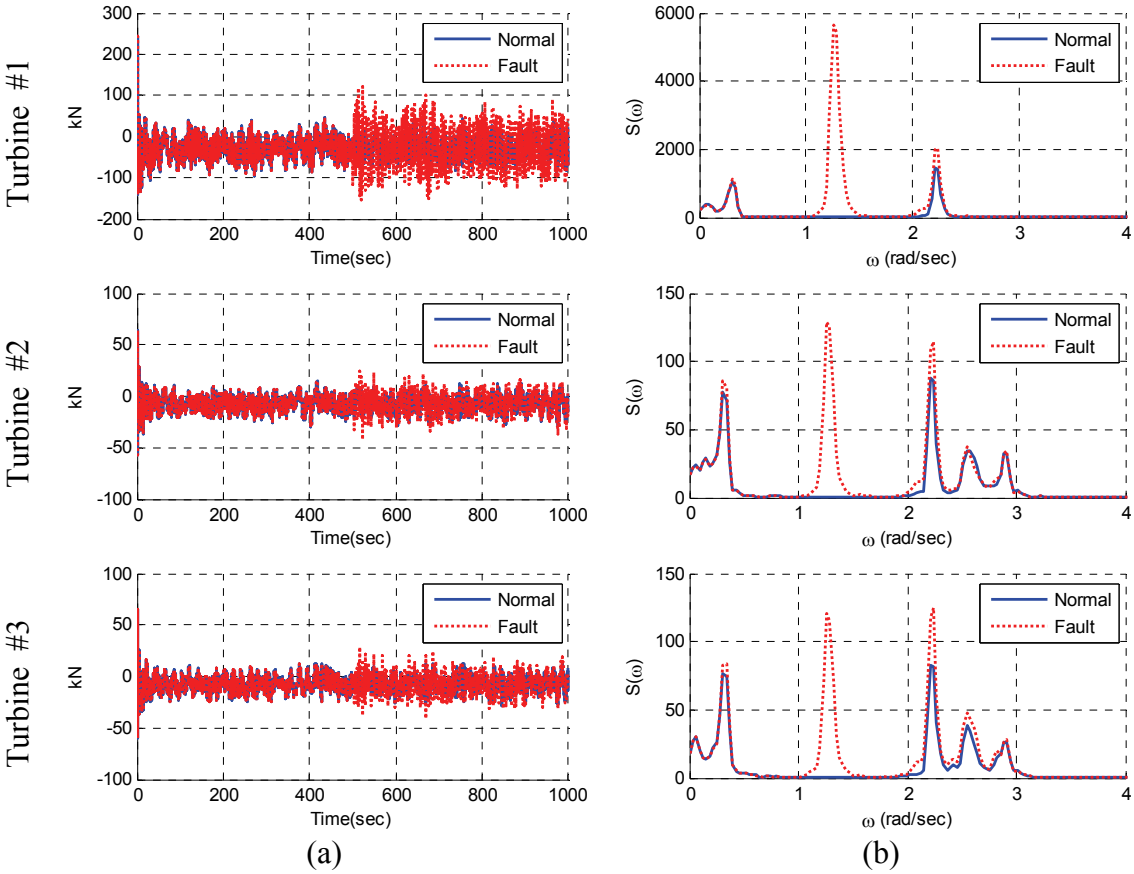

Figure 7.32 Tower base side-to-side shear force (a) and spectra (b) with partially broken blade

However, local structural responses such as tower base loads were influenced by the broken blade as presented in Figures 7.32 ~ 7.34.

Since the blade from the turbine #1 was broken during the simulation, the imbalance load on the rotor induced a 1P (1.27 rad/s) frequency response as can be seen in Figure 7.32. Interestingly, that 1P frequency response also showed up in turbines #2 and #3. For turbines #2 and #3; this 1P response was solely from turbine #1 because the rotor speed that generated the 1P frequency of turbine #1 was different from the other turbines. That is, the 1P frequency of turbines #2 and #3 was around 2.15 rad/s, which is also shown in the responses.

Table 7.8 Tower base side-to-side shear force statistics with partially broken blade

		Max.	**Min**	**Mean**	**SD**
Turbine #1 (kN)	Normal	4.34E+01	-9.10E+01	-2.70E+01	2.11E+01
	Partially Broken	1.23E+02	-1.53E+02	-2.65E+01	4.50E+01
Turbine #2 (kN)	Normal	1.28E+01	-2.90E+01	-7.10E+00	6.55E+00
	Partially Broken	2.47E+01	-4.17E+01	-7.05E+00	9.12E+00
Turbine #3 (kN)	Normal	1.37E+01	-2.84E+01	-7.34E+00	6.32E+00
	Partially Broken	2.85E+01	-4.02E+01	-7.30E+00	9.30E+00

In Table 7.8, the maximum shear force and standard deviation of turbine #1 after breaking increased by 182.8% and 113.0% respectively. Furthermore, the maximum forces of turbines #2 and #3 also increased by 93.8% ~ 108.6%. This result indicated that the partially broken blade of one turbine strongly affected the responses of other turbines. The statistics in Table 7.8 were obtained after breaking event at 500 seconds.

Tower base roll moments in Figure 7.33 also showed a similar trend with shear forces. As mentioned above, both 1.27 rad/s (1P of turbine #1) and 2.15rad/s (1P of turbines #2 and #3) showed up simultaneously so the structural properties of the tower base in the MUFOWT platform should be carefully designed by considering every possible response from the other turbines. The lowest tower bending mode of turbine #1 shows up near 2.2 rad/s, and this response can be also detected in the other turbines such as #2 and #3. This result confirmed that the dynamic coupling between each turbine was successfully implemented in the developed program for the MUFOWT analysis.

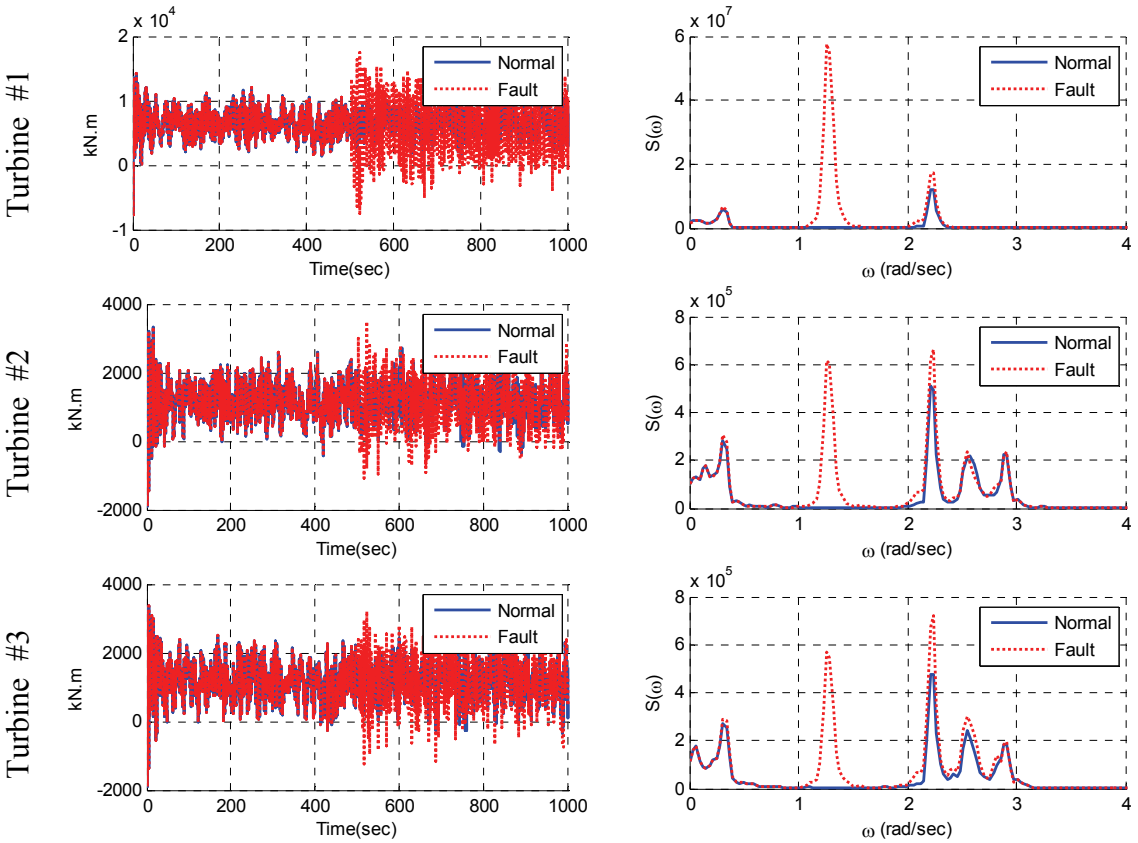

Figure 7.33 Tower base roll moment (a) and spectra (b) with partially broken blade

Table 7.9 Tower base roll moment statistics with partially broken blade

		Max.	Min	Mean	SD
Turbine #1 (kN·m)	Normal	1.11E+04	1.07E+03	6.43E+03	1.69E+03
	Partially Broken	1.75E+04	-7.48E+03	6.39E+03	4.28E+03
Turbine #2 (kN·m)	Normal	2.70E+03	-3.41E+02	1.15E+03	4.77E+02
	Partially Broken	3.49E+03	-1.07E+03	1.15E+03	6.52E+02
Turbine #3 (kN·m)	Normal	2.65E+03	-3.50E+02	1.17E+03	4.61E+02
	Partially Broken	3.65E+03	-1.26E+03	1.17E+03	6.71E+02

Similarly, the maximum roll moment and standard deviation of normal turbines (#2 and #3) in Table 7.9 also showed appreciable increases after the braking event at 500 seconds.

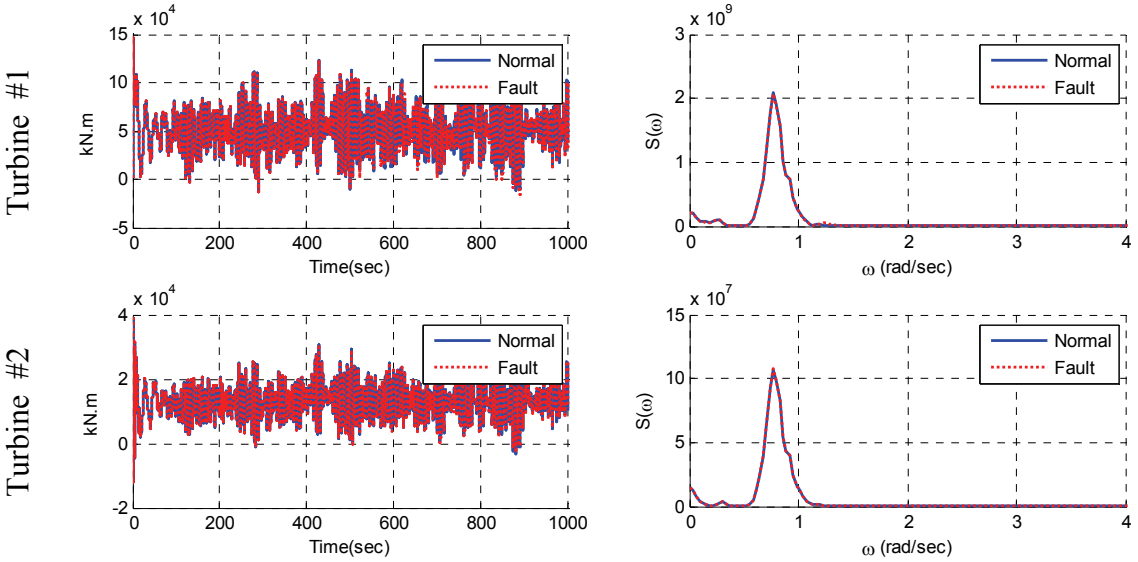

Figure 7.34 Tower base pitch moment (a) and spectra (b) with partially broken blade

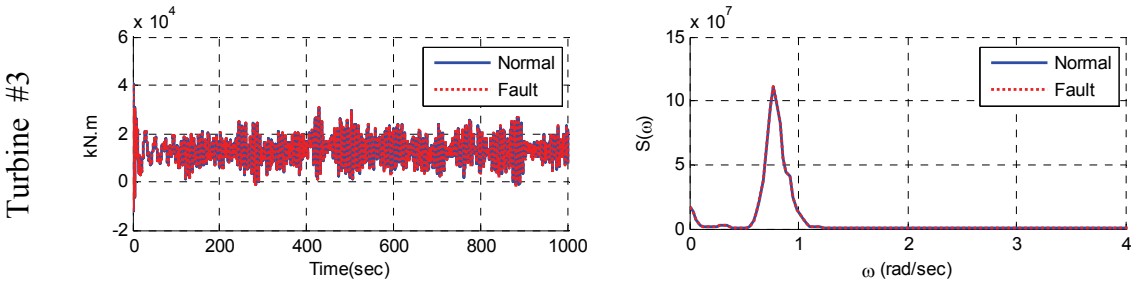

(a) (b)

Figure 7.34 Continued

The variations of tower base pitch moment in Figure 7.34 were relatively small. The statistics in Table 7.10 showed that the standard deviations of every tower base moment increased only 0.4 ~ 0.6%, while the maximum moments of all turbines decreased by 0.8 ~ 1.3%. In fore-aft direction, the reduced blades drag due to the loss of partial elements resulted in these decreases. It revealed that the loss of partial blade element did not make significant differences in the tower base fore-aft (pitch) moment.

Table 7.10 Tower base pitch moment statistics with partially broken blade

		Max.	Min	Mean	SD
Turbine #1 (kN·m)	Normal	1.13E+05	-1.18E+04	5.16E+04	2.25E+04
	Partially Broken	1.12E+05	-1.53E+04	5.17E+04	2.26E+04
Turbine #2 (kN·m)	Normal	2.93E+04	-3.18E+03	1.32E+04	5.19E+03
	Partially Broken	2.91E+04	-3.02E+03	1.31E+04	5.21E+03
Turbine #3 (kN·m)	Normal	2.94E+04	-1.42E+03	1.32E+04	5.21E+03
	Partially Broken	2.91E+04	-2.53E+03	1.32E+04	5.24E+03

The 1P response from the broken blade was also shown in the tower base torsional moment response as can be seen in Figure 7.35. However, that 1P did not show up in turbines #2 and #3 anymore because the yaw excitation of turbine #1 generated most of the sway or roll excitations for the other turbines, and contributed negligibly small yaw excitations. The statistics of tower base torsional moment in Table 7.11 also show that the variations of moment from turbines #2 and #3 were not that great and only those of turbine #1 increased noticeably. For example, the maximum torsional moment and standard deviation increased by 32.3% and 58.7%. It tells us that the modes of lateral direction such as sway and roll are primarily influenced by the imbalance of rotor blades. To investigate more severe breaking event and the resultant coupling effects, fully broken blade case are presented in the next section.

Table 7.11 Tower base torsional moment statistics with partially broken blade

		Max.	**Min**	**Mean**	**SD**
Turbine #1 (kN·m)	Normal	3.00E+03	-3.29E+03	-1.54E+02	9.25E+02
	Partially Broken	3.97E+03	-5.52E+03	-9.31E+01	1.47E+03
Turbine #2 (kN·m)	Normal	5.17E+02	-6.45E+02	-5.00E+01	1.55E+02
	Partially Broken	5.05E+02	-6.39E+02	-5.01E+01	1.55E+02
Turbine #3 (kN·m)	Normal	4.41E+02	-6.44E+02	-7.19E+01	1.48E+02
	Partially Broken	4.46E+02	-6.52E+02	-7.20E+01	1.48E+02

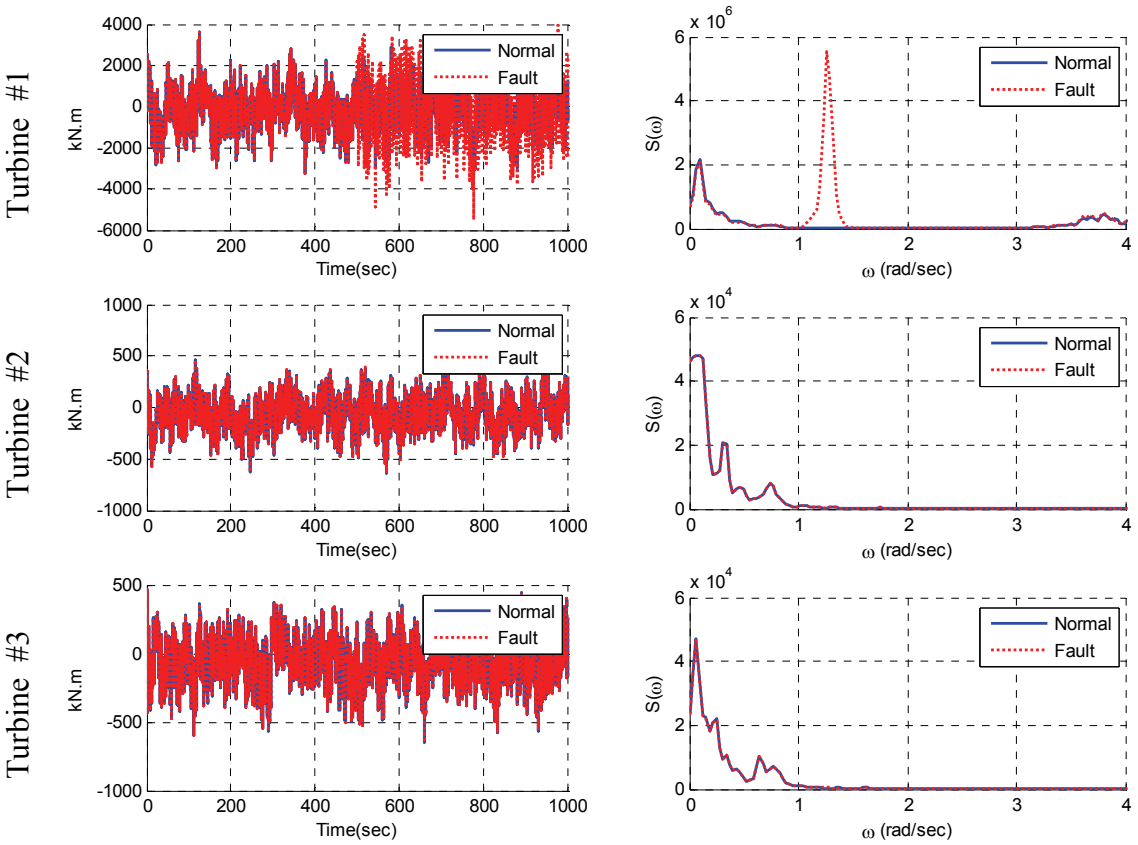

Figure 7.35 Tower base torsional moment (a) and spectra (b) with partially broken blade

The mooring line top tensions in this partially broken blade case were also investigated and presented in Figures 7.36 ~ 7.37. The mooring line arrangement was depicted in Figure 7.28.

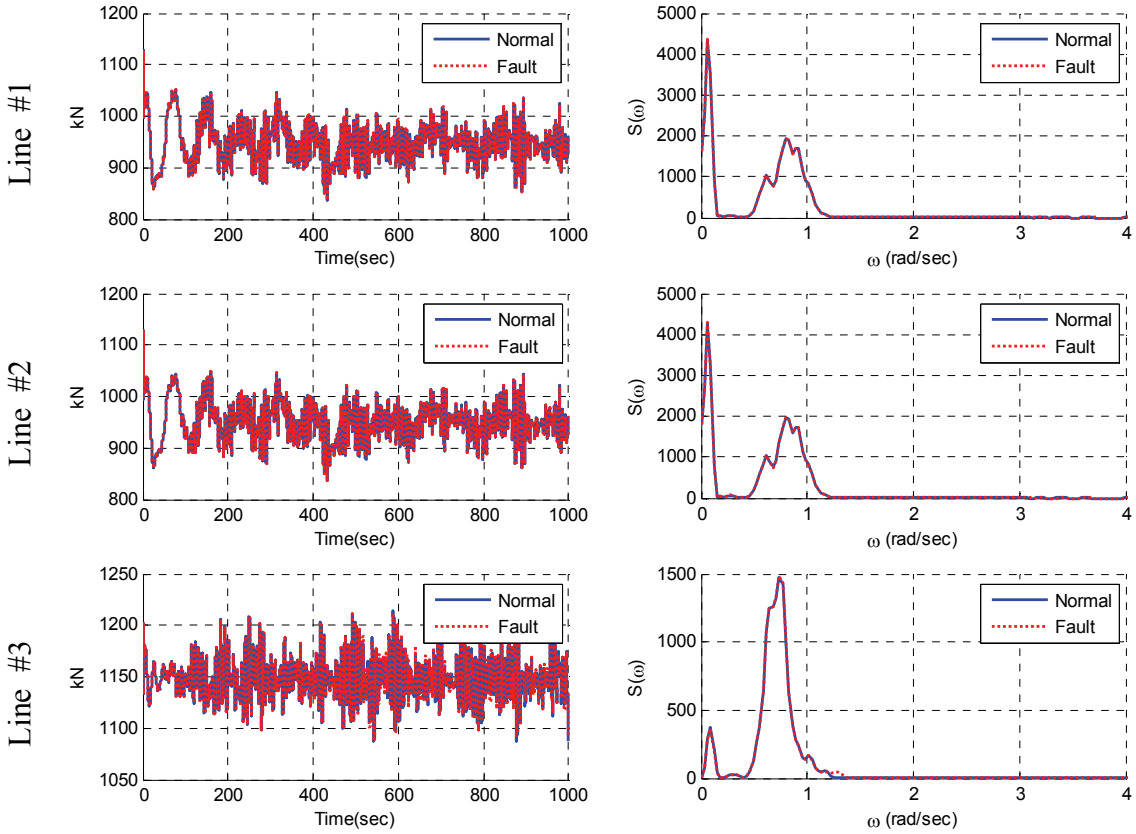

Figure 7.36 Top-tension (a) and spectra (b) of Line #1~#3 with partially broken blade

Except for the minor 1P response in line #3 tensions, the top tension responses did not make significant differences between before and after the breaking event. The statistics of top tensions were obtained after 500 seconds and tabulated in Table 7.12.

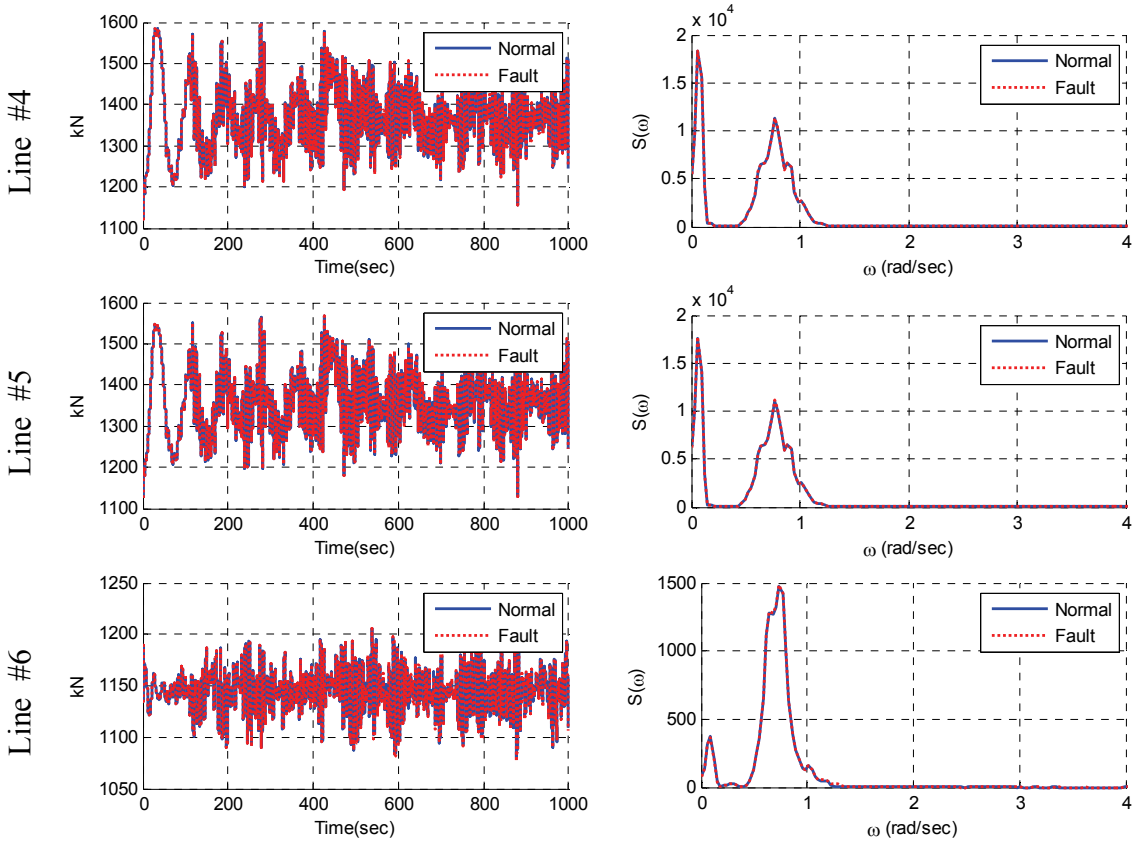

Figure 7.37 Top-tension (a) and spectra (b) of Line #4~#6 with partially broken blade

In the case of the other lines in Figure 7.37, the trends were similar to that of Figure 7.36. The statistics in Table 7.12 showed that there were no significant changes in top tensions in partially broken blade case. The standard deviations of side lines (#3 and #6) increased only by 0.9~ 1% and that of the other lines increased less than 0.5%. Thus, it was regarded that the effects of partially broken blade on the mooring line top tensions in this semi-submersible platform were minor compared to the side-to-side tower base responses.

Table 7.12 Mooring line top tension statistics with partially broken blade

		Max.	Min	Mean	SD
Line #1 (kN)	Normal	1.04E+03	8.60E+02	9.49E+02	3.04E+01
	Partially Broken	1.04E+03	8.59E+02	9.49E+02	3.04E+01
Line #2 (kN)	Normal	1.04E+03	8.60E+02	9.49E+02	3.04E+01
	Partially Broken	1.04E+03	8.59E+02	9.49E+02	3.04E+01
Line #3 (kN)	Normal	1.21E+03	1.09E+03	1.15E+03	2.22E+01
	Partially Broken	1.21E+03	1.09E+03	1.15E+03	2.24E+01
Line #4 (kN)	Normal	1.57E+03	1.16E+03	1.37E+03	6.48E+01
	Partially Broken	1.56E+03	1.15E+03	1.37E+03	6.50E+01
Line #5 (kN)	Normal	1.55E+03	1.13E+03	1.36E+03	6.50E+01
	Partially Broken	1.56E+03	1.13E+03	1.36E+03	6.53E+01
Line #6 (kN)	Normal	1.21E+03	1.08E+03	1.15E+03	2.22E+01
	Partially Broken	1.21E+03	1.08E+03	1.15E+03	2.24E+01

7.5.2 Full Blade Broken Failure of One Turbine

In this section, more severe failure case with 100% loss of the one blade was simulated and assessed. All the conditions were same as the previous partially broken case but the entire elements of one blade were eliminated at 500 seconds. Consequently, the aero dynamic loadings on that blade also should be removed. The overall mass removed from the broken blade was equivalent to 17,740 kg. Compared to the partially broken case, the platform and turbine responses considerably increased due to the imbalanced blade mass and unbalanced excitation of the aero dynamic loadings.

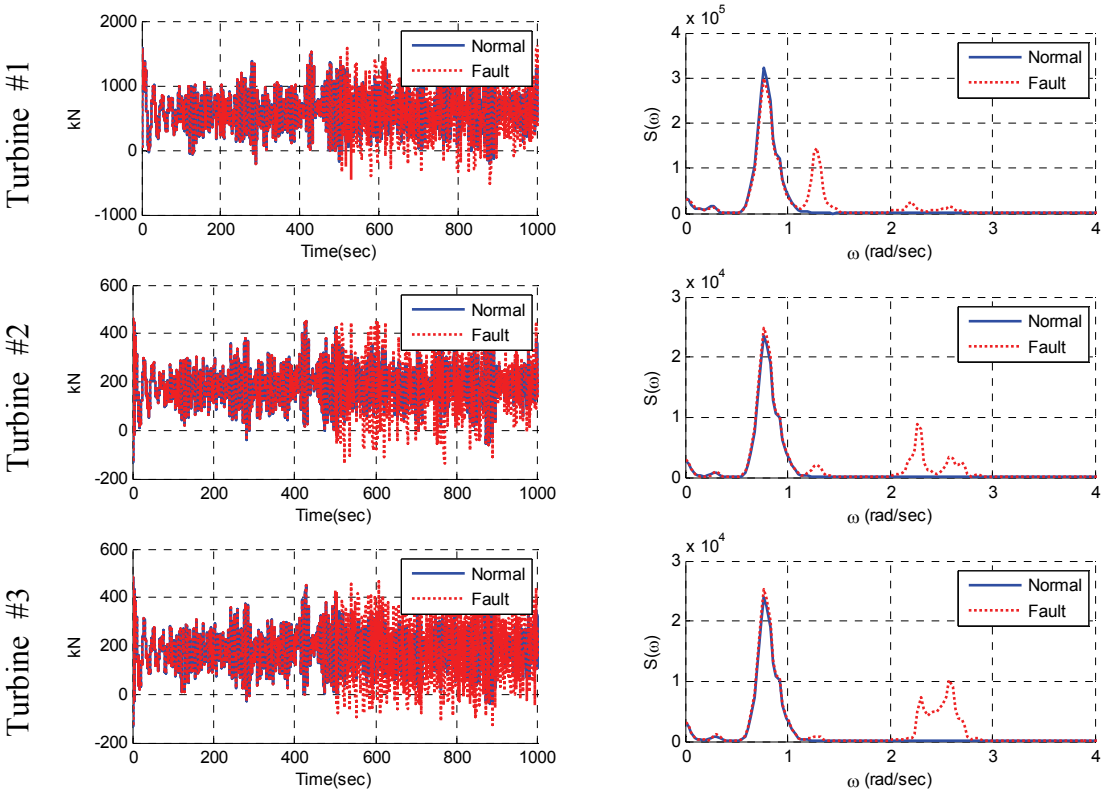

Figure 7.38 Tower base fore-aft shear force (a) and spectra (b) with fully broken blade

Interestingly, the tower base fore-aft shear forces after breaking showed clear coupling between turbines. The 1P excitation of the turbine #1 in Figure 7.38 could be also seen in turbines #2 and #3, and two lowest tower bending modes around 2 ~ 3 rad/s also showed up in each turbine.

Table 7.13 showed that the maximum fore-aft shear force of the turbine #1 increased nearly 17.3%. Another turbine's maximum also increased by 16.9 ~ 20.1%. In the case of a partially broken blade in the previous section, the variation of a fore-aft

shear force was not noticeable, whereas the excessive rotation of the unbalanced-blade in this case could induce even for the in-line (fore-aft) shear force variations.

Table 7.13 Tower base fore-aft shear force statistics with fully broken blade

		Max.	Min	Mean	SD
Turbine #1 (kN)	Normal	1.38E+03	-2.19E+02	6.07E+02	2.81E+02
	Fully Broken	1.62E+03	-5.22E+02	6.00E+02	3.54E+02
Turbine #2 (kN)	Normal	4.23E+02	-6.05E+01	1.85E+02	7.68E+01
	Fully Broken	5.08E+02	-1.37E+02	1.80E+02	1.03E+02
Turbine #3 (kN)	Normal	4.18E+02	-3.70E+01	1.85E+02	7.71E+01
	Fully Broken	4.89E+02	-1.27E+02	1.80E+02	1.13E+02

As already expected, the tower base side-to-side shear forces as well as roll moments showed great changes after 500 seconds. The tower base frequency responses in Figure 7.39(b) indicated that the unbalanced vibration responses were composed of both 1P excitations from the blades and the tower base side-to-side bending modes from two turbines. The most dominant component was the lowest bending mode of the 5MW tower near the 2.2 rad/s. The statistics in Table 7.14 shows the considerable increase of the shear forces. In real situations, these changes might result in the progressive collapse of the tower and the entire system.

Table 7.14 Tower base side-to-side shear force statistics with fully broken blade

		Max.	Min	Mean	SD
Turbine #1 (kN)	Normal	4.34E+01	-9.10E+01	-2.70E+01	2.11E+01
	Fully Broken	2.33E+03	-2.28E+03	-2.84E+01	7.18E+02
Turbine #2 (kN)	Normal	1.28E+01	-2.90E+01	-7.10E+00	6.55E+00
	Fully Broken	5.93E+02	-6.13E+02	-7.05E+00	1.78E+02
Turbine #3 (kN)	Normal	1.37E+01	-2.84E+01	-7.34E+00	6.32E+00
	Fully Broken	6.15E+02	-6.25E+02	-7.45E+00	1.80E+02

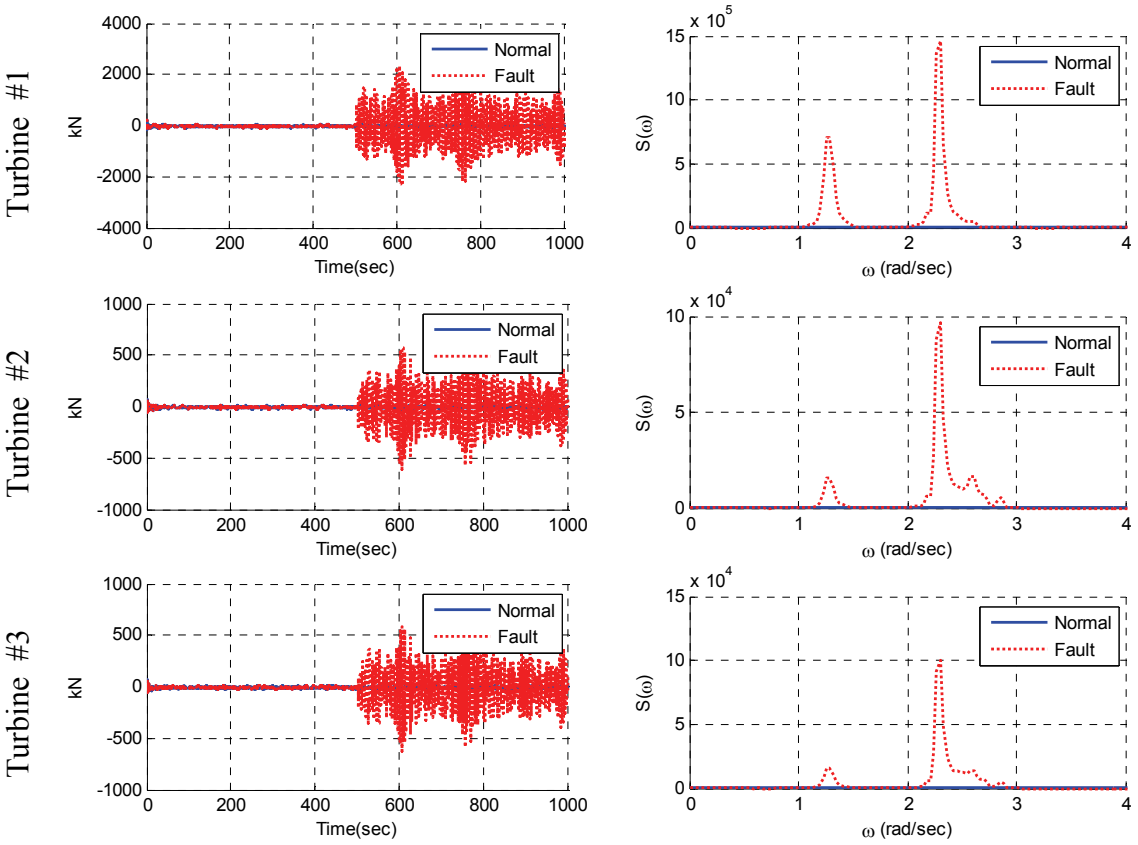

Figure 7.39 Tower base side-to-side shear force (a) and spectra (b) with fully broken blade

The changes in the tower base pitch moment in Figure 7.40 were very similar to the fore-aft shear forces in Figure 7.38. Again, it was very hard to observe the variations in the tower base pitch moment for the partially broken blade case, but in this fully broken case, clear effects could be observed. The 1P response of the 5MW turbine and two tower base bending modes were dominant components in this simulation.

Table 7.15 shows that the maximum tower base pitch moment increased up to 33.2%, and the standard deviation of the moment also increased by 59.0%. The maximum of another turbines also increased by 22.9 ~ 25.2%. Under the blade-broken situations, the tower base and turbine structure could be exposed to higher possibility of fatigue failure.

Table 7.15 Tower base pitch moment statistics with fully broken blade

		Max.	**Min**	**Mean**	**SD**
Turbine #1 (kN·m)	Normal	1.13E+05	-1.18E+04	5.16E+04	2.25E+04
	Fully Broken	1.51E+05	-4.64E+04	5.26E+04	3.58E+04
Turbine #2 (kN·m)	Normal	2.93E+04	-3.18E+03	1.32E+04	5.19E+03
	Fully Broken	3.67E+04	-9.87E+03	1.29E+04	7.28E+03
Turbine #3 (kN·m)	Normal	2.94E+04	-1.42E+03	1.32E+04	5.21E+03
	Fully Broken	3.61E+04	-9.64E+03	1.29E+04	8.33E+03

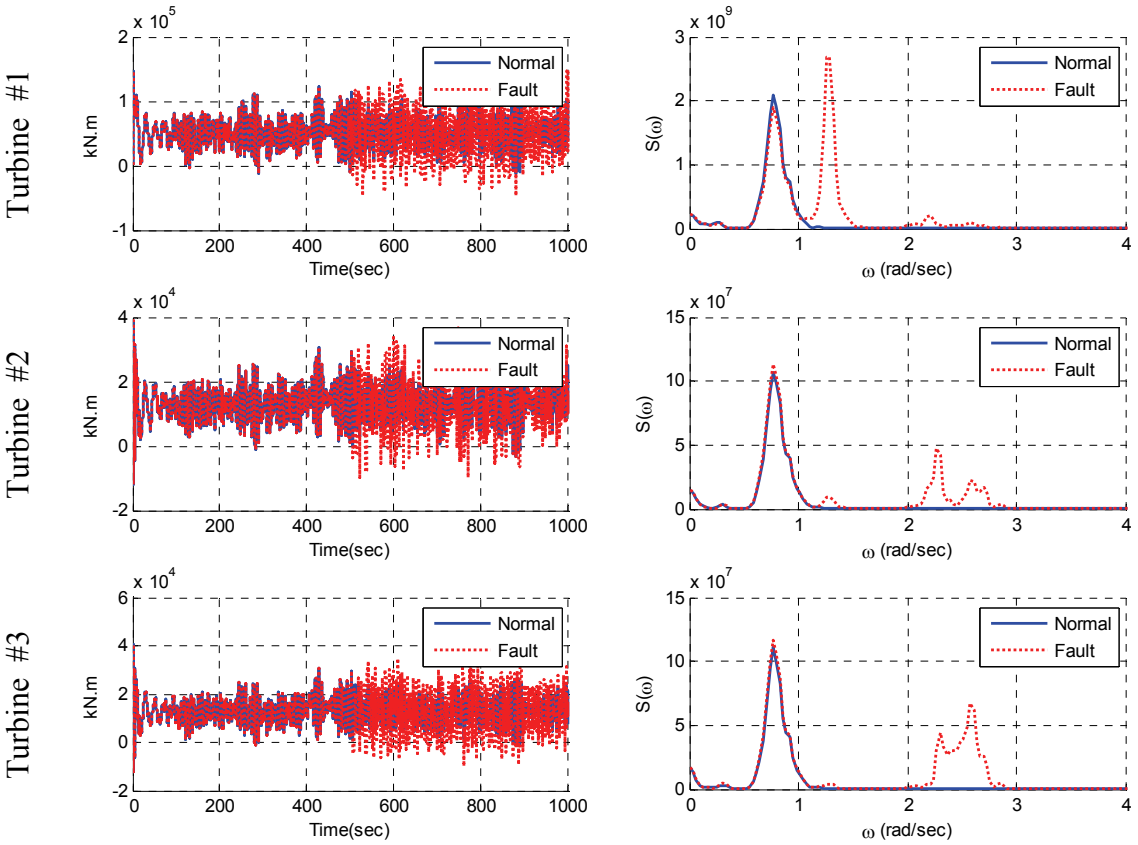

Figure 7.40 Tower base pitch moment (a) and spectra (b) with fully broken blade

In the case of tower base torsional moment under the full blade breaking, the maximum torsional moment of the turbine #1 was around 5.7 times greater than that of the normal case as can be seen in Figure 7.41 and Table 7.16. The responses of the turbine #1 were the most serious changes, while other turbines showed relatively mild changes. If the structural safety factor of the tower base design was not enough to cover those variations, then the serious failure of the turbines were expected.

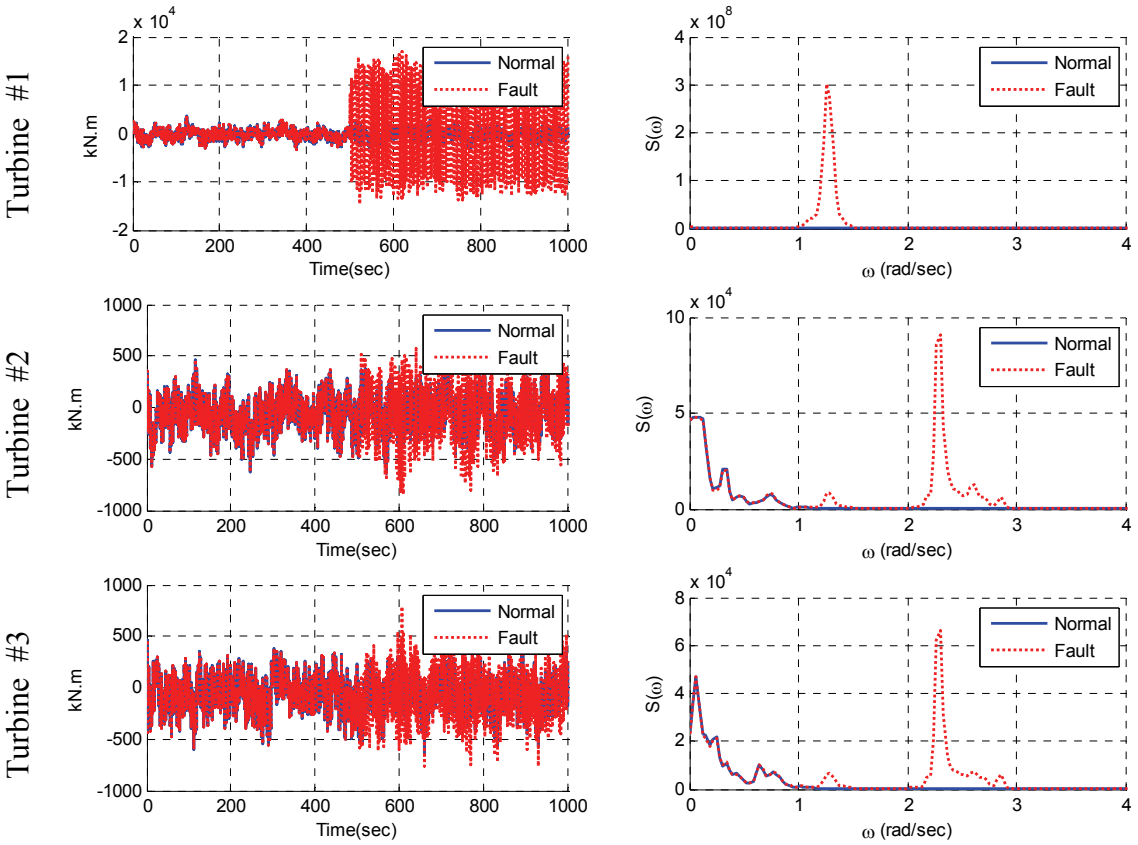

Figure 7.41 Tower base torsional moment (a) and spectra (b) with fully broken blade

One of the interesting responses in torsional moment was that the tower base side-to-side excitation of turbine #1 could be observed in the tower base torsional responses in turbines #2 and #3. Since the tower center lines were not necessarily located at the platform origin in the case of MUFOWT, the linear excitation from one tower base might result in the angular responses in the other tower base and vice versa as can be seen in Figure 7.42.

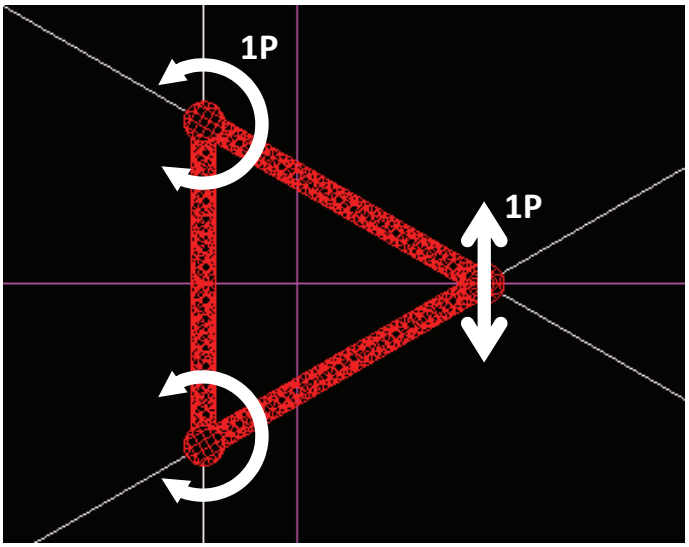

Figure 7.42 Transition of the side-to-side excitation of turbine #1

Table 7.16 Tower base torsional moment statistics with fully broken blade

		Max.	Min	Mean	SD
Turbine #1 (kN·m)	Normal	3.00E+03	-3.29E+03	-1.54E+02	9.25E+02
	Fully Broken	1.71E+04	-1.46E+04	6.40E+02	8.87E+03
Turbine #2 (kN·m)	Normal	5.17E+02	-6.45E+02	-5.00E+01	1.55E+02
	Fully Broken	7.01E+02	-8.48E+02	-4.98E+01	2.26E+02
Turbine #3 (kN·m)	Normal	4.41E+02	-6.44E+02	-7.19E+01	1.48E+02
	Fully Broken	7.91E+02	-7.61E+02	-7.12E+01	2.05E+02

The mooring line top tensions in this emergency case were also investigated and presented in Figures 7.43 ~ 7.44.

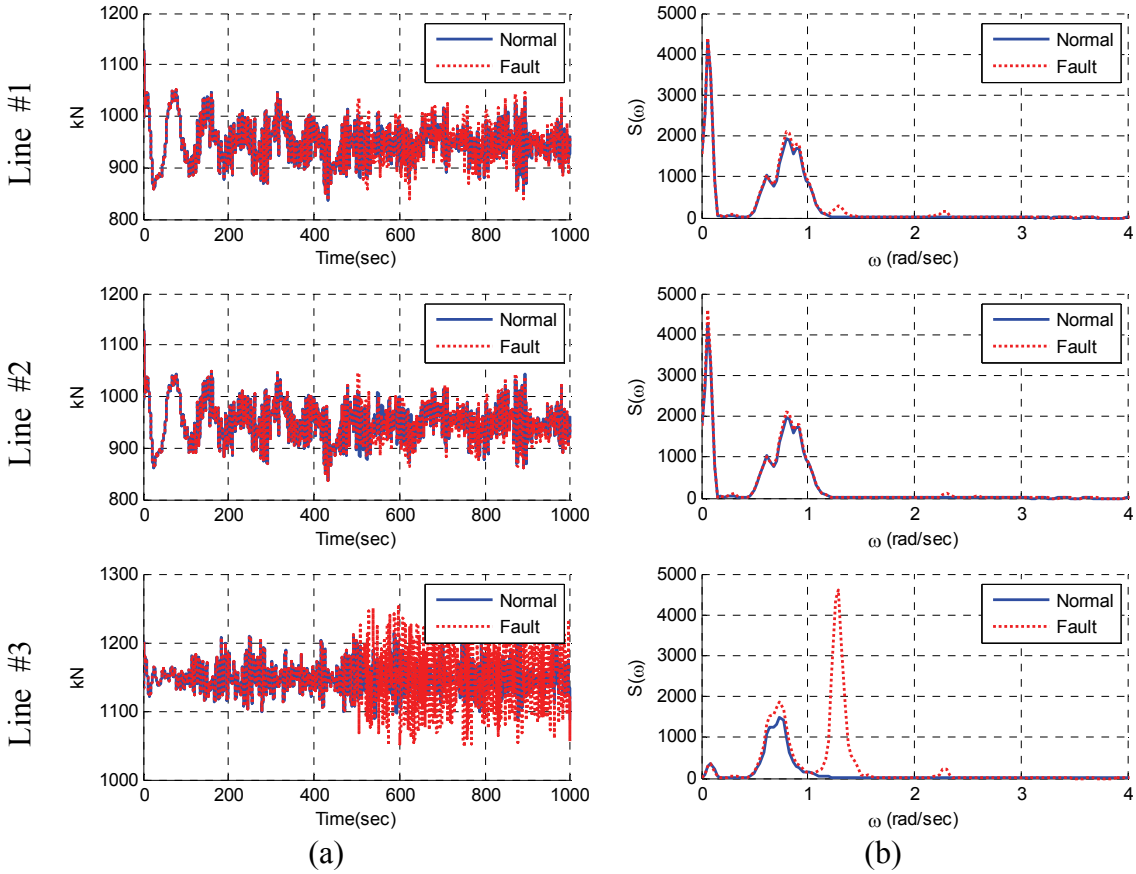

Figure 7.43 Top-tension (a) and spectra (b) of Line #1~#3 with fully broken blade

Two lee-side lines #1 and #2 did not make significant differences and the only minor responses in 1P frequency showed up. However, the top tensions of lines #3 and #6 which was located at the side direction showed noticeable changes. The 1P excitation was the primary source of the excitation from the rotor and the rest of the responses from the tower base bending modes were relatively small. The maximum top tension of the line #3 increased by only 3.7%, but the standard deviation after breaking event was 101.1% higher than that of the normal case. Thus, it was regarded that the mooring lines

under this situation were more vulnerable to the fatigue failures rather than the breaking failures from the axial tensions.

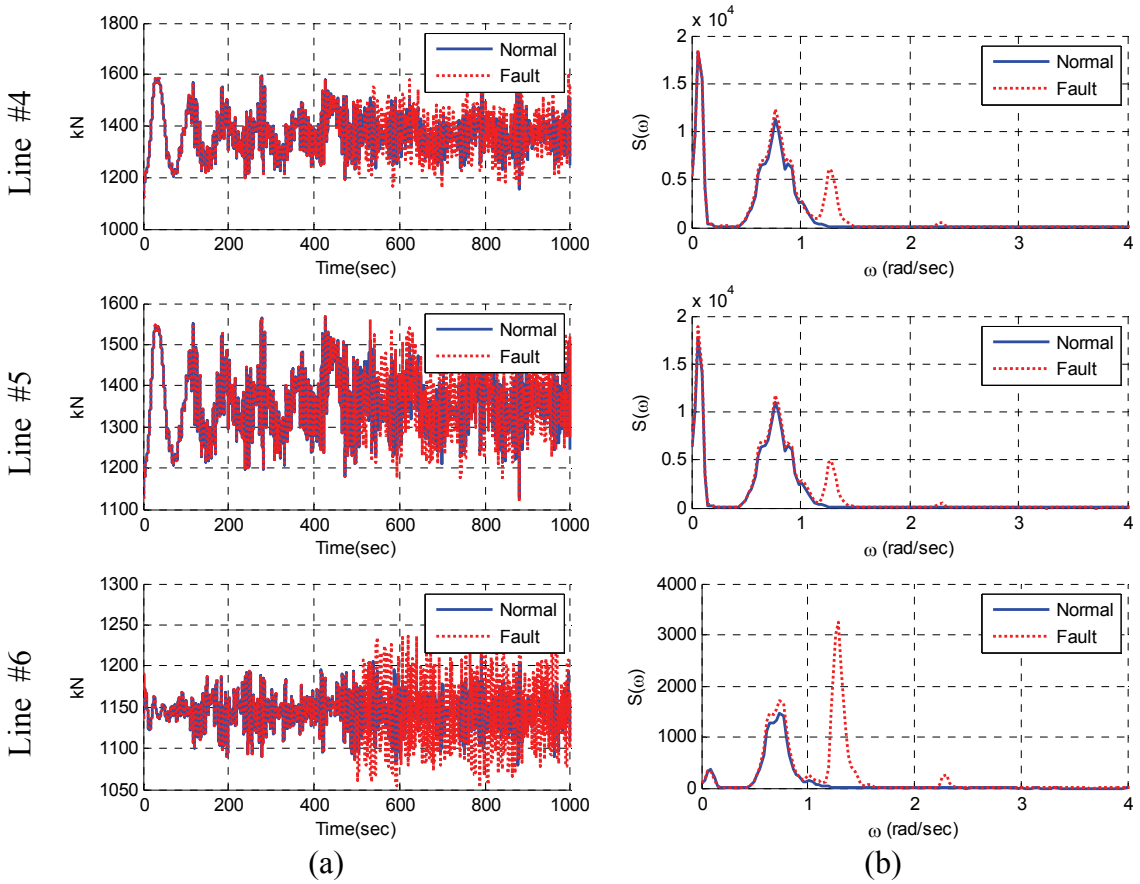

Figure 7.44 Top-tension (a) and spectra (b) of Line #4~#6 with fully broken blade

In the case of weather-side lines such as lines #4 and #5, the 1P responses in tension was relatively small compared to the side lines, but still more clear than those of the lee-side lines. Similarly, the standard deviations of those weather-side lines after breaking increased around 21.5 ~ 24.5%, which was still larger than the increased rate of

the maximum tensions. The statistics were obtained after the full breaking at 500 seconds, and tabulated in Table 7.17.

Table 7.17 Mooring line top tension statistics with fully broken blade

		Max.	Min	Mean	SD
Line #1 (kN)	Normal	1.04E+03	8.54E+02	9.47E+02	2.96E+01
	Fully Broken	1.05E+03	8.39E+02	9.48E+02	3.32E+01
Line #2 (kN)	Normal	1.04E+03	8.60E+02	9.49E+02	3.04E+01
	Fully Broken	1.05E+03	8.61E+02	9.48E+02	3.28E+01
Line #3 (kN)	Normal	1.21E+03	1.09E+03	1.15E+03	2.22E+01
	Fully Broken	1.26E+03	1.05E+03	1.15E+03	4.47E+01
Line #4 (kN)	Normal	1.57E+03	1.16E+03	1.37E+03	6.48E+01
	Fully Broken	1.63E+03	1.16E+03	1.37E+03	8.07E+01
Line #5 (kN)	Normal	1.55E+03	1.13E+03	1.36E+03	6.50E+01
	Fully Broken	1.57E+03	1.12E+03	1.37E+03	7.90E+01
Line #6 (kN)	Normal	1.21E+03	1.08E+03	1.15E+03	2.22E+01
	Fully Broken	1.25E+03	1.05E+03	1.14E+03	3.91E+01

7.6 Discussion

The dynamic responses of the three-turbine MUFOWT has been simulated and investigated in this chapter. The hydrodynamic coefficients were obtained by WAMIT and the time domain analysis was carried out using the FAST-CHARM3D analysis tool specifically designed for multiple-turbine platform.

In this case study, it was seen that the effect due to the partial loss of blade pitch control or partial loss of blade element can significantly affect the responses of the

whole system. Specifically, the loss of blade pitch control of one turbine may induce platform yaw moment which can seriously impact the other turbines due to the yaw error. In the case of a partially broken blade, the tower-base forces and moments, especially for sway and roll directions, were the most serious changes compared to normal responses. Due to the rotational imbalance with damage, the 1P excitation and responses were more pronounced in the tower and blade dynamics. Interestingly, the 1P excitation from the broken turbine may influence the other normal turbines, and vice versa. To avoid collapse of the entire system due to the partially broken blade, the structural integrity, especially for the yaw-related responses, should be carefully checked. More severe case with fully broken blade case was also investigated. Under this environment, the excessive unbalanced forces generated by rotor could influence not only the side-to-side responses, but also the fore-aft responses. Furthermore, this case also changed the mooring line top tensions specifically for the side lines.

The present approach for MUFOWT can directly be applied to the development of remote structural health monitoring systems to detect partial blade failure by measuring tower or platform responses.

8. CASE STUDY III: FIVE-TURBINE SEMI-SEBMERSIBLE

8.1 Introduction

In the previous chapter, the triangular shape MUFOWT platform with three 5MW turbines were numerically modeled and analyzed. The developed MUFOWT analysis tool was successfully utilized and demonstrated every aspect of the combined dynamic behaviors of multiple turbines. The fault scenario with one or two turbine failures was also simulated. It was shown that the failure of turbines may induce unexpected yaw moment of the floating turbine resulting in significant changes in the turbine structural load or mooring line top tensions.

In this case study, a bigger MUFOWT platform with 5 wind turbines was introduced and simulated. Two 5MW turbines were located at the rear side, and three 5MW turbines positioned at the front. To minimize the static trim angle of the platform, more ballast water filled the aft tank in a way similar to the previous chapter. To confirm the dynamic coupling between the turbine and platform, an emergency scenario with a partially broken blade was presented. All the dynamic responses, including each turbine and platform, have been presented and analyzed in this chapter.

8.2 Configuration of the Platform, Mooring System and Turbines

The selected MUFOWT platform has five cylindrical columns where each turbine is mounted plus seven submerged pontoons as can be seen in Figure 8.1. The column spacing was selected to avoid the interruption between turbines. The horizontal

distance from the fore turbine to the rear turbine was set to 140m, and the maximum distance from the upper and lower turbines was 280m. The column depth was 20m, and the diameter 10m so that the top side of the column can provide the 5MW tower base with the proper margins. Figure 8.2 shows the dimensions of the platform.

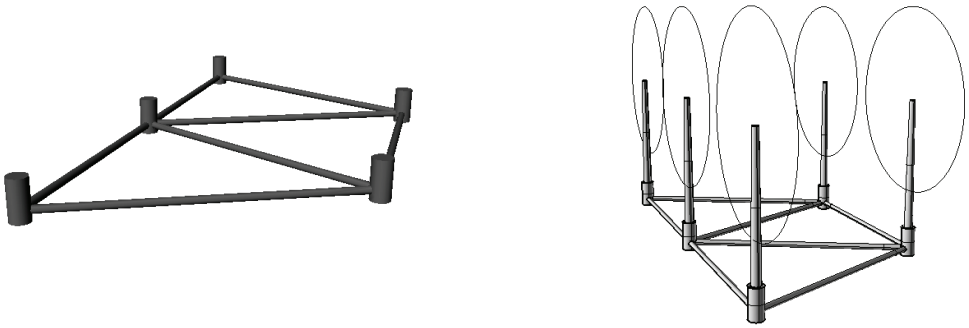

(a) (b)

Figure 8.1 Rectangular platform geometry (a) and system configuration (b)

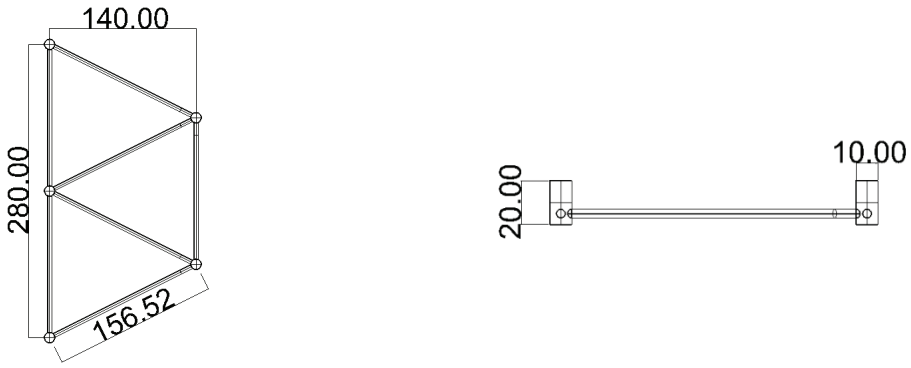

(a) (b)

Figure 8.2 Platform dimensions from top (a) and side (b) (Rectangular platform)

The platform hull weight was calculated based on the submerged surface area and given plate thickness (15mm). The mass properties of the platform, including mass

moment of inertia, were calculated by considering the displaced steel platform and ballast water. The details of platform properties are tabulated in Table 8.1.

The overall hydrostatic equilibrium was met using a different ballast height as similarly treated in the three-turbine platform. In the case of the five-turbine platform, the ballast water height at the rear tank is higher than that of the front tanks because the turbines mounted on top of the cylinder were the same for all columns and the rear side has only two turbines.

Table 8.1 Specification of rectangular platform

Item	Unit	Value
Depth to Platform Base below SWL	m	20.0
Column Diameter	m	10.0
Length between Columns (vertical)	m	140.0
Length between Columns (lateral)	m	156.52
Pontoon Width	m	4.0
Pontoon Height	m	4.0
Platform Weight, including Ballast	N	164,515,390
Platform Buoyancy	N	202,426,451
Platform CM Location Below SWL	m	15.1
Platform Roll Inertia about CM	$kg \cdot m^2$	1.14479E11
Platform Pitch Inertia about CM	$kg \cdot m^2$	56,616,813,871
Platform Yaw Inertia about Platform Centerline	$kg \cdot m^2$	1.63311E11

This five-turbine MUFOWT platform was moored by 4 catenary mooring lines. The material used in the mooring line was the same as the one used in the previous chapter. The mooring line arrangements are depicted in Figure 8.3.

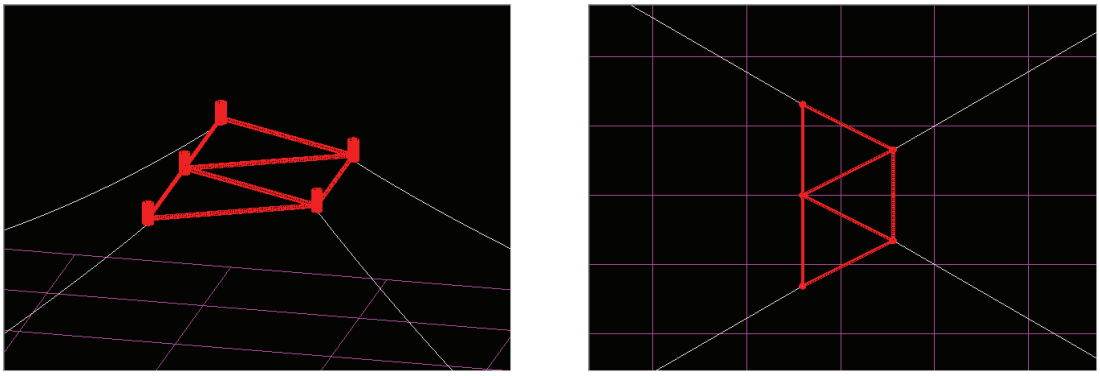

Figure 8.3 Mooring line configuration (Rectangular platform)

8.3 Hydrodynamic Coefficients in Frequency Domain

The hydrodynamic coefficients such as added mass, radiation damping and first order hydrodynamic force were obtained from WAMIT.

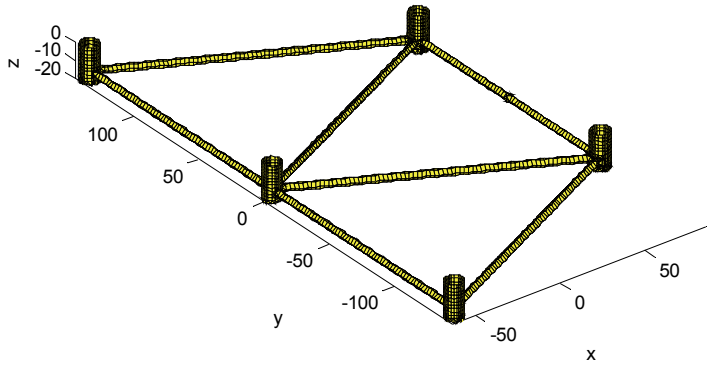

Figure 8.4 Discretized panel model of floating body (Rectangular platform)

Similar to the triangular platform in the previous chapter, the platform has one axis symmetric, and each side has 3,849 panels. Figure 8.4 shows the discretized panel model of the rectangular floater. The calculated hydrodynamic added mass and radiation damping in frequency domain are presented in Figures 8.5 and 8.6 respectively.

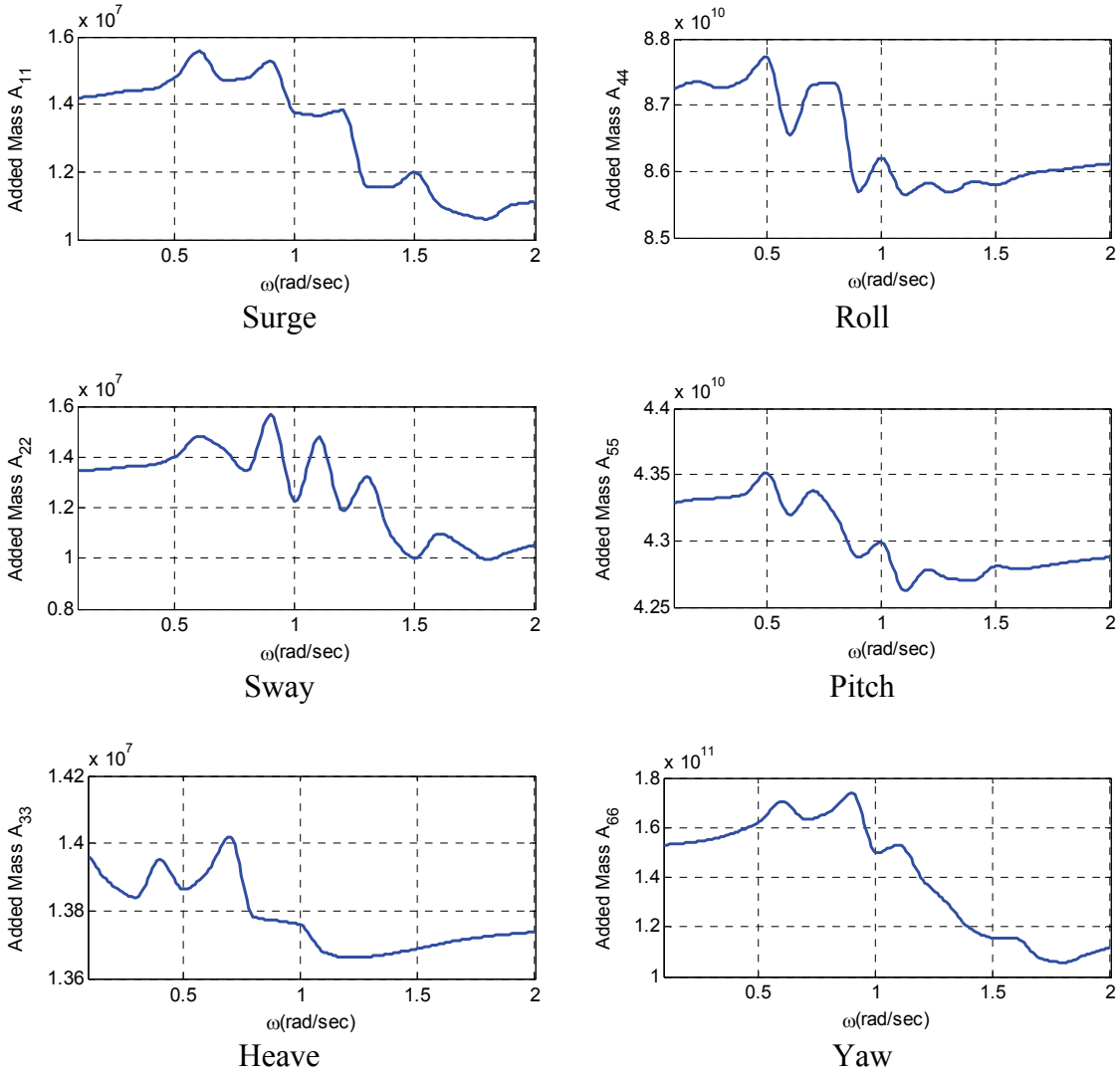

Figure 8.5 Added mass (Rectangular platform)

In addition to the added mass and radiation damping, hydrostatic stiffness of the platform can also be obtained from WAMIT. This type of semi-submersible platform should have enough hydrostatic restoring force and moment which can be confirmed by calculated hydrostatic coefficients. Otherwise, the platform in still water may not be stable or cannot maintain its upright position.

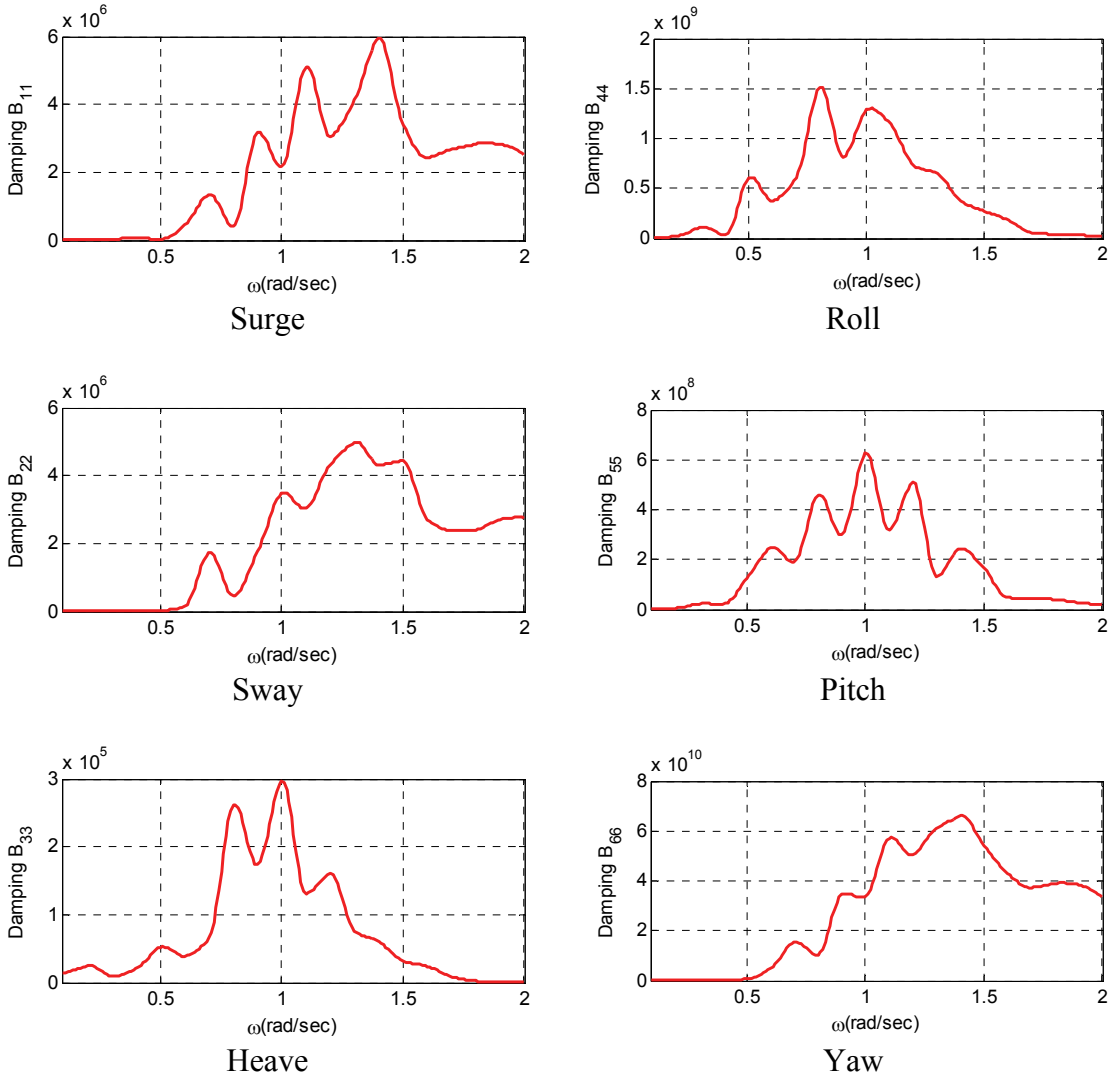

Figure 8.6 Radiation damping (Rectangular platform)

8.4 Time Marching Simulation in Normal Operational Condition

In this section, the time domain analysis with given hydrodynamic data derived by WAMIT has been carried out. Four higher-order FEM based mooring lines have been modeled and the dynamics of the mooring lines have also been accounted for. At each time step, the developed MUFOWT analysis tool based on FAST refers to CHARM3D once to provide all the external loadings including the mooring line restoring force. By repeating this data exchange, the progressive time marching solution of entire system can be obtained.

8.4.1 Viscous Damping Modeling

As already pointed out, one of the advantages of the time domain analysis is that numerical model can include the nonlinear viscous effect. In FAST-CHARM3D, the viscous damping is calculated by placing equivalent truss or plate members inside the submerged platform model where the diameter of the member is small compared to the wave length.

In the case of the five turbines platform, the viscous drag force of the hull was represented by employing five vertical truss members for each column which acts along every normal direction of the column, and seven truss members for each pontoon. The drag coefficient C_d is taken to be 0.6 for the cylindrical. In addition to the hull viscous members above, the dynamic loadings on tethers were also calculated by Morison's equation. For the calculation of the loading on tethers, the inertia coefficient C_m was

taken to be 2 and the drag coefficients C_d were set to 1.3 for the wire and 2.4 for the chain. The drag coefficients for all the Morison members are tabulated in Table 8.2.

Table 8.2 Drag coefficients of Morison members (Rectangular platform)

Location	C_d	Viscous model	No. of members
Columns	0.6	Truss	5
Pontoons	0.6	Truss	7
Chain Mooring	2.4	Slender rod	4
Wire Mooring	1.3	Slender rod	4

8.4.2 System Identification and Free Decay Test

To check the 6-DOFs platform natural frequencies, free decay tests in the time domain were carried out and presented in Figure 8.7. Similar to the three turbines case, the whole system was assumed as a rigid body, thus no elastic or aerodynamic responses were included in this free decay test. However, all the viscous effects from the hull or mooring lines have been considered and included in the simulation.

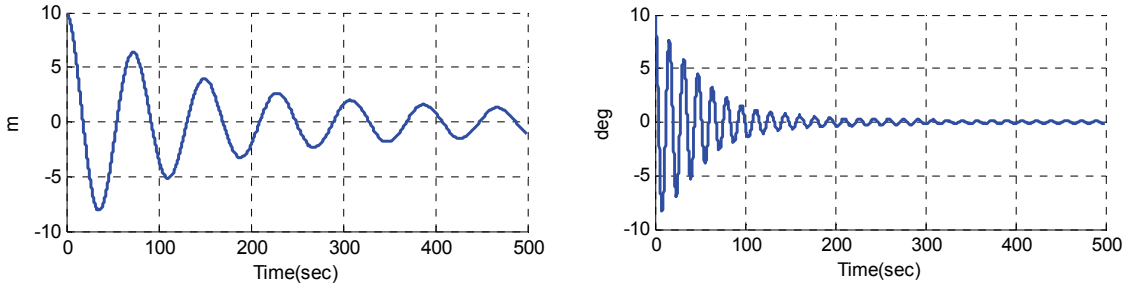

Surge Roll

Figure 8.7 Free decay test (Rectangular platform)

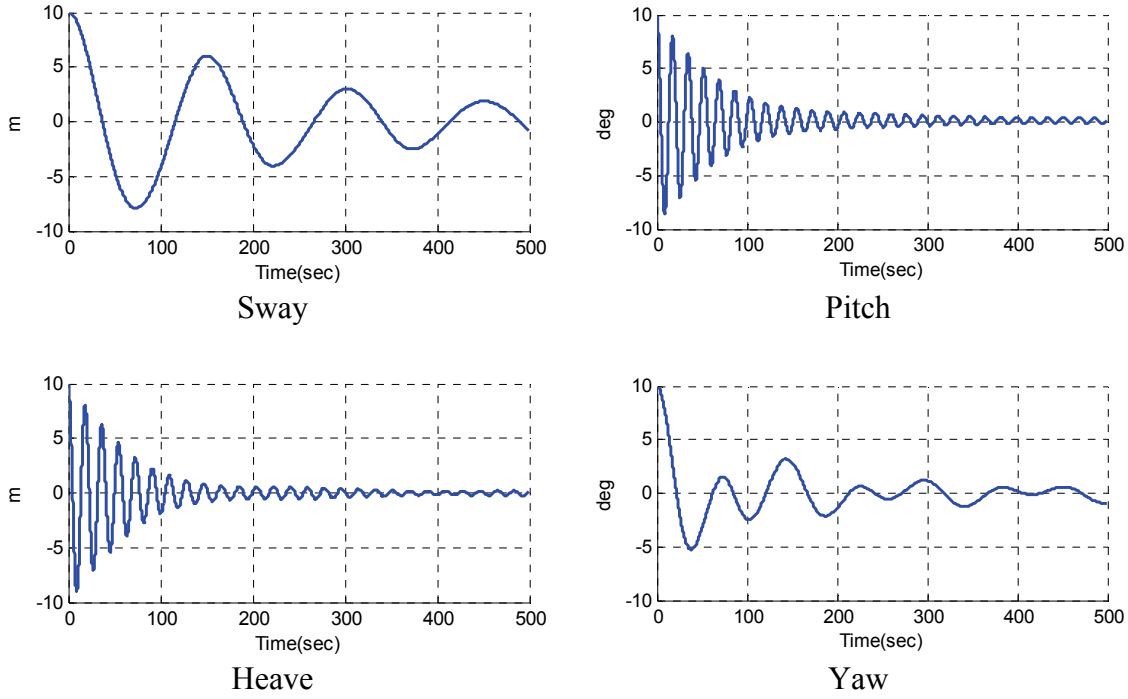

Figure 8.7 Continued

The floating platform was released from the 10m offset distance in case of surge, sway and heave and a 10 degree angle for roll, pitch and yaw. The natural periods or frequencies can be estimated by measuring the period of free decay oscillations.

Table 8.3 Natural frequencies of rectangular platform

	Surge	**Sway**	**Heave**	**Roll**	**Pitch**	**Yaw**
Period	72.6	151.0	18.1	15.9	17.2	73.1
Freq. (rad/s)	0.09	0.04	0.35	0.40	0.37	0.09

Table 8.3 shows the natural frequencies of 6-DOFs of platform motion. Heave, roll and pitch natural frequencies are relatively close to the wave energy range, but still

look reasonable in that those are far below the peak wave energy range. In case of surge, sway and yaw, the natural frequencies are quite low, and the resonances can be safely avoided.

8.4.3 Responses in Random Wind and Wave Environments

After checking the natural frequencies of the system a fully coupled time domain analysis of MUFOWT was performed. All the environmental conditions are the same as those in the previous three turbines case study tabulated in Table 7.5.

The time step of the CHARM3D side in this study was set to 0.01 seconds, and that of the FAST side, which included the computation of aerodynamics, elastic modes of tower and blades and platform dynamics, was set to the same time step. So, at every time step of FAST, the CHARM3D fed the mooring restoring and all other external loadings on the platform. The total simulation time was 1,000 seconds, including the initial 100 seconds of ramp time in order to minimize the transient effect of responses. All 6-DOFs of platform responses are presented in Figures 8.8 ~ 8.13.

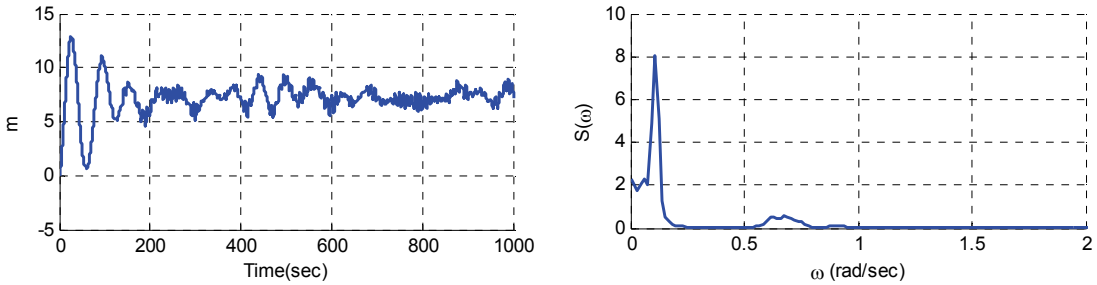

(a) (b)

Figure 8.8 Surge motion (a) and spectrum (b) (Rectangular platform)

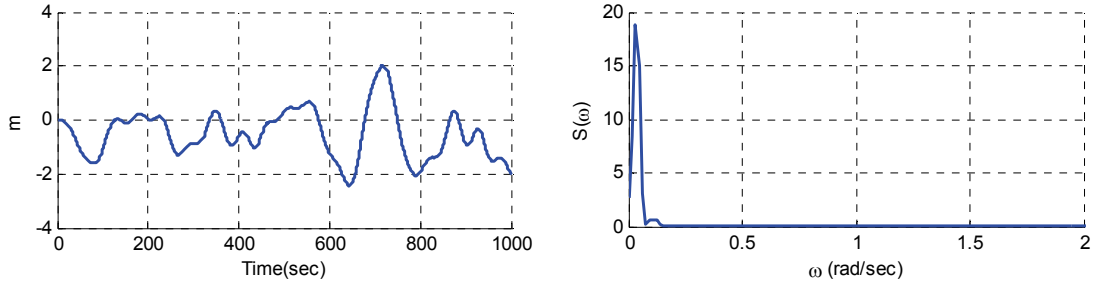

(a) (b)

Figure 8.9 Sway motion (a) and spectrum (b) (Rectangular platform)

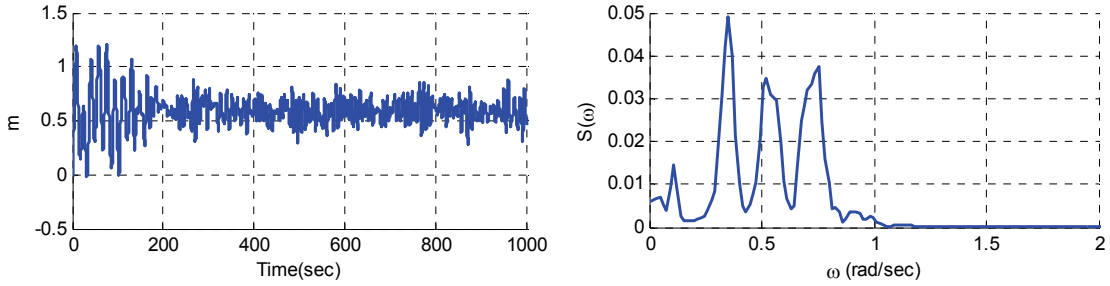

(a) (b)

Figure 8.10 Heave motion (a) and spectrum (b) (Rectangular platform)

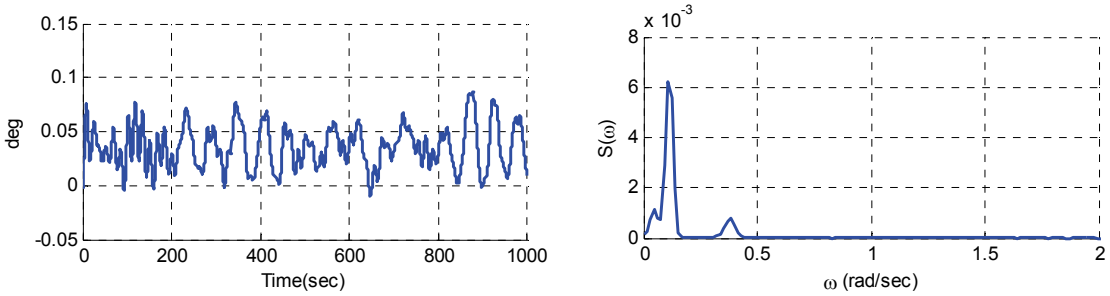

(a) (b)

Figure 8.11 Roll motion (a) and spectrum (b) (Rectangular platform)

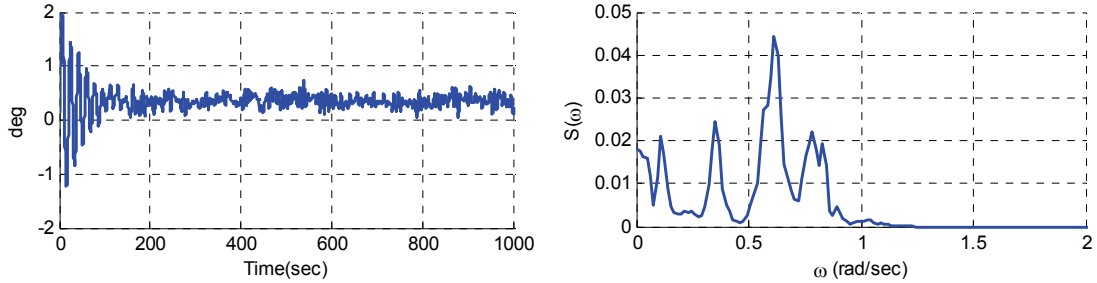

(a) (b)

Figure 8.12 Pitch motion (a) and spectrum (b) (Rectangular platform)

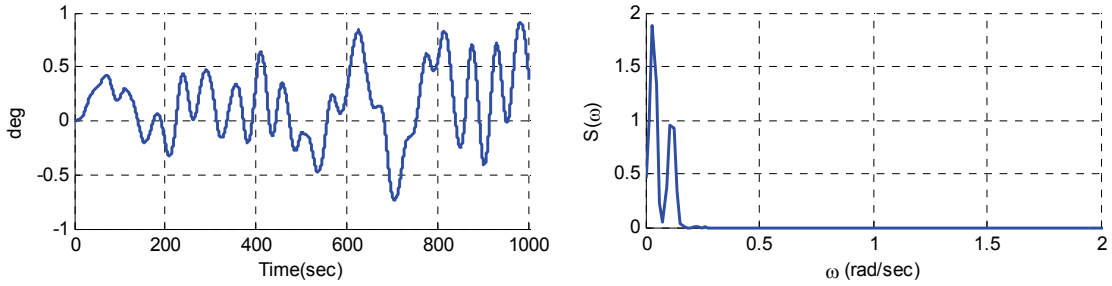

(a) (b)

Figure 8.13 Yaw motion (a) and spectrum (b) (Rectangular platform)

As can be seen in the Figures above, most platform responses are located at below 0.5 rad/s except for heave and pitch. So, attention should be paid and a clear check done for heave and pitch to ensure a good performance of the platform in wind and wave environments.

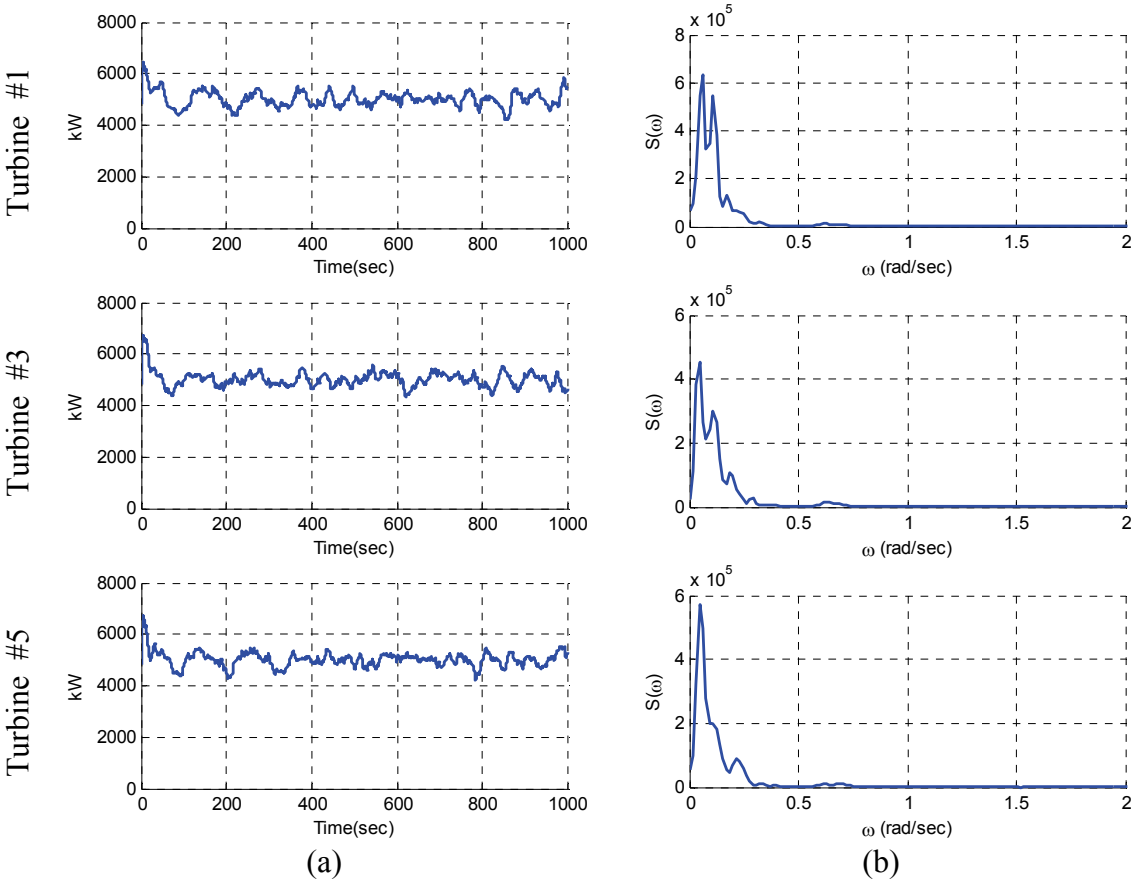

Figure 8.14 Generator power (a) and spectra (b) (Rectangular platform)

The performance of each turbine was also investigated. In normal operational condition, all turbines generate rated power of 5MW; the selected output is depicted in Figure 8.14. Now that the wind speed at hub height (15 m/s) is higher than the rated wind speed (11.4 m/s), the power generated in this turbine shows only small variations around rated power. If the wind velocity is near the rated wind speed, then the generated power may have serious fluctuations due to lowered wind velocity and reduced rotor speed.

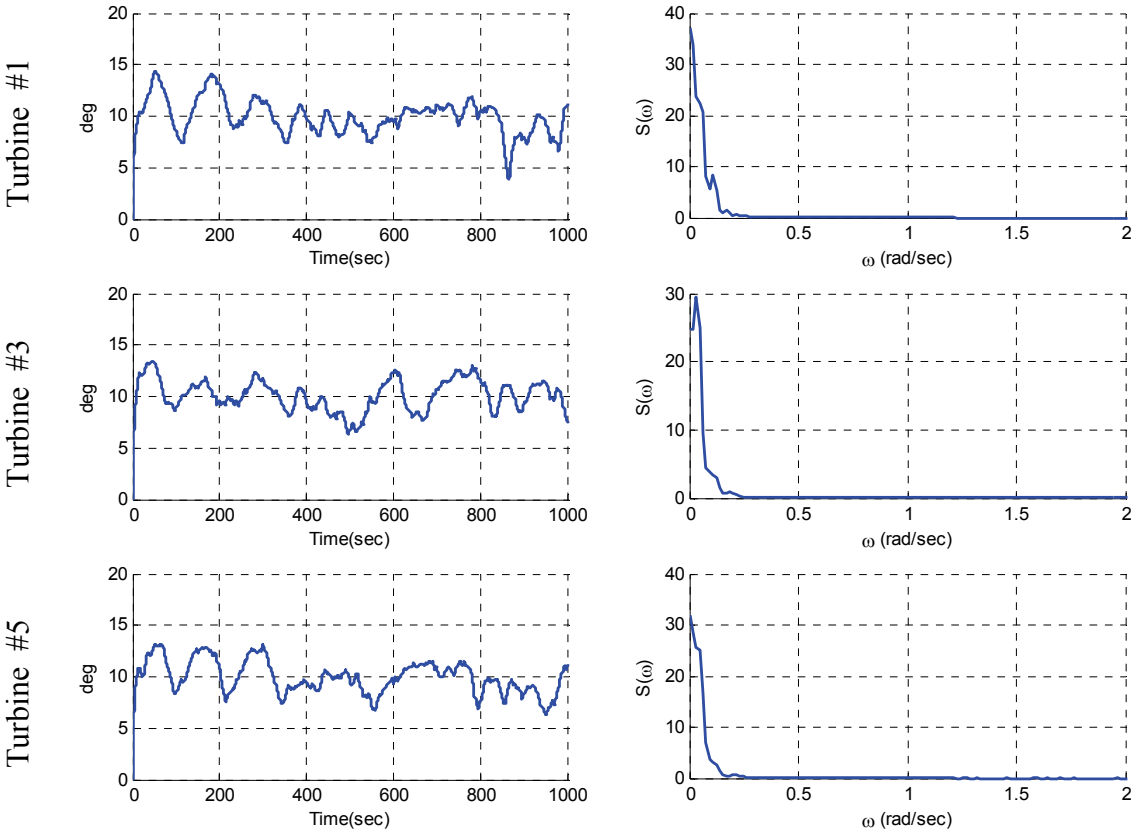

Figure 8.15 Blade pitch angle (a) and spectra (b) (Rectangular platform)

The variation of blade pitch angle of the selected turbine is depicted in Figure 8.15. As already mentioned, the control action of the blade pitch angle is very sensitive to low frequency wind energy. It can be confirmed by the spectra in Figure 8.15(b). To minimize the instability induced by the blade pitch angle control mentioned in the previous chapter, the same pitch control scheme, which was used in the Hywind spar case, was adopted because the platform pitch natural frequency in this platform was also very low with the possibility of interference from blade pitch control excitation.

As for the tower base loads in the in-line direction (fore-aft direction), the responses are mostly dependent on the incident wave energy. Figure 8.16 shows the time history and its spectra of tower base fore-aft shear force. Some fluctuations inside the wave frequency range in spectra were due to the geometry of the platform and the effect of trapped water inside the outer hull.

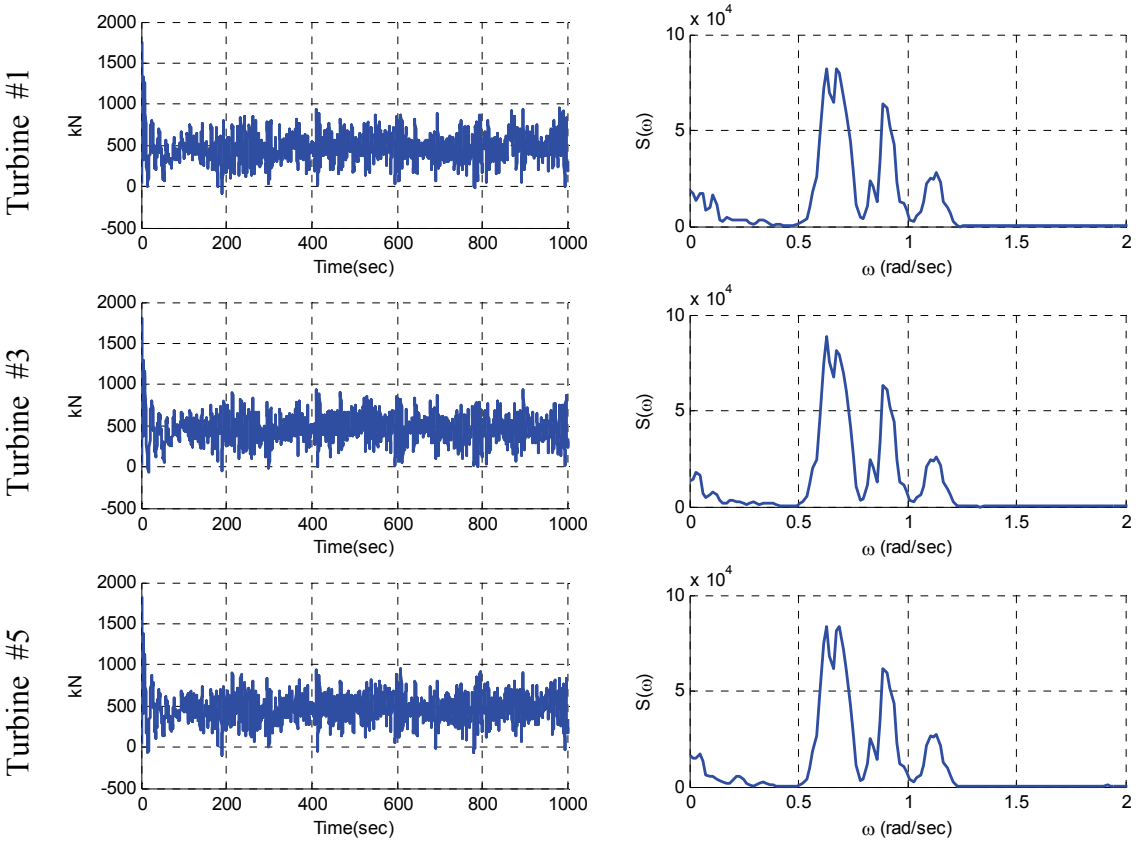

Figure 8.16 Tower base fore-aft shear force (a) and spectra (b) (Rectangular platform)

The tower base fore-aft (pitch) bending moment was also checked in Figure 8.17. The overall trends of the bending moment were very similar to those of the shear forces

in Figure 8.16. This showed that the tower base loads in normal operational conditions were nearly identical each other, thus the balance of the entire system was regarded to be well maintained. As already pointed out, the frequent drops of the spectra inside the wave frequency range were primarily due to the geometry of the semi-submersible.

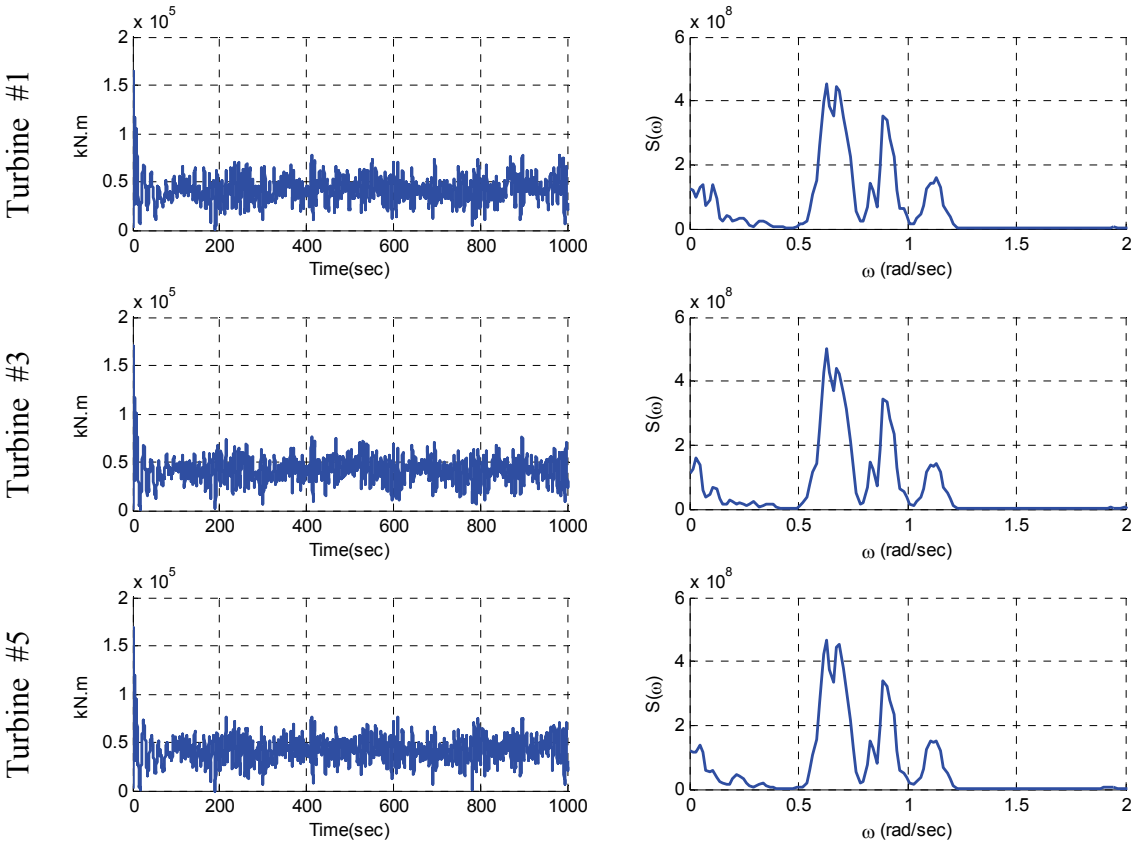

Figure 8.17 Tower base pitch moment (a) and spectra (b) (Rectangular platform)

In the case of the tower base torsional moment in Figure 8.18, the response was affected by low frequency wind energy. It shows that the structural design or fatigue

analysis of the local structure of the wind turbine should consider the sensitive frequency range that each structure is subjected to.

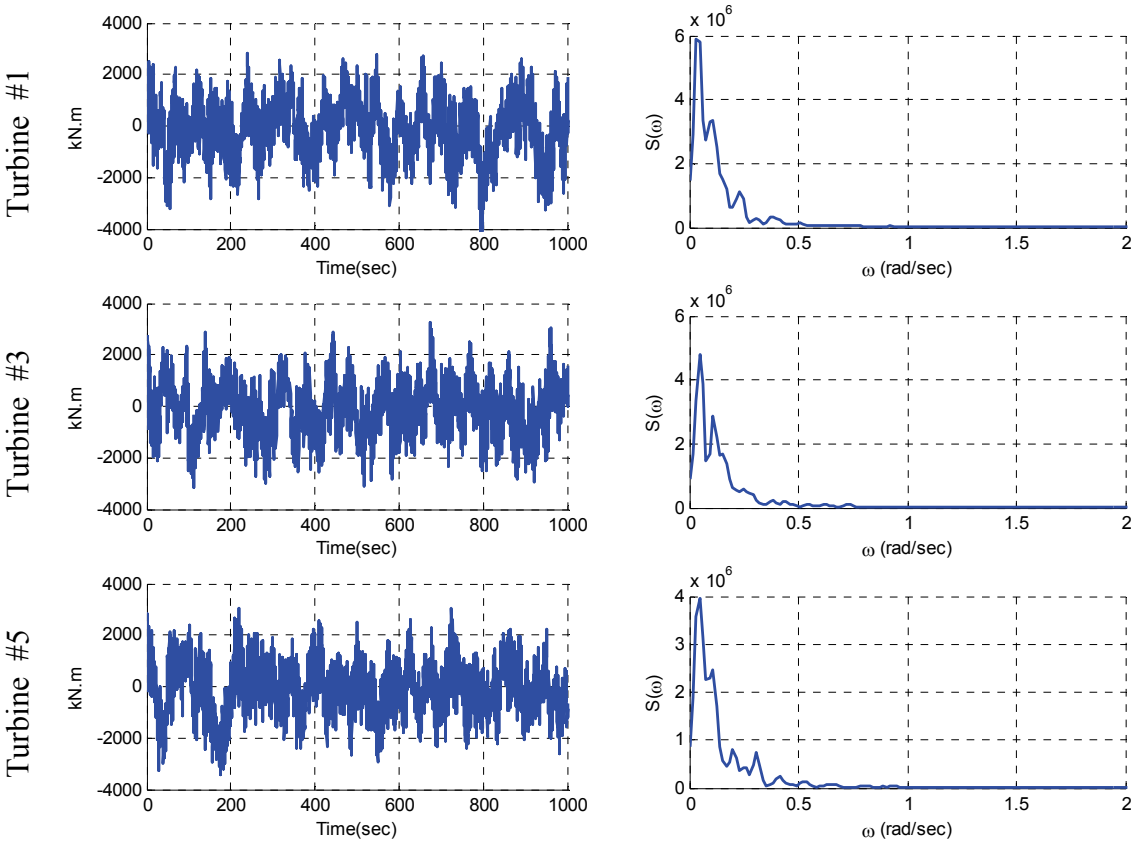

Figure 8.18 Tower base torsional moment (a) and spectra (b) (Rectangular platform)

8.5 One Turbine Failure Simulation

Similar to the previous chapter, the turbine failure case was selected and simulated to observe the overall performance of turbines and platform. In the previous chapter, the blade pitch angle of one turbine went wrong and locked at 30 degrees which showed the lack of drag force on that turbine and the progressive yaw rotation of the

platform was eventually detected. In this chapter, on the contrary, the blade pitch angle suddenly locked at 5 degrees, which is very small compared to the normal pitch angle action. In this case, the drag force on the blades will be significantly increased, and the fault turbine will be pushed backward. If that turbine is located in the centerline of the platform, then only the surge offset will be changed. However, if the fault turbine is off-centered, the floating platform may experience both translational force and rotational moment at the same time.

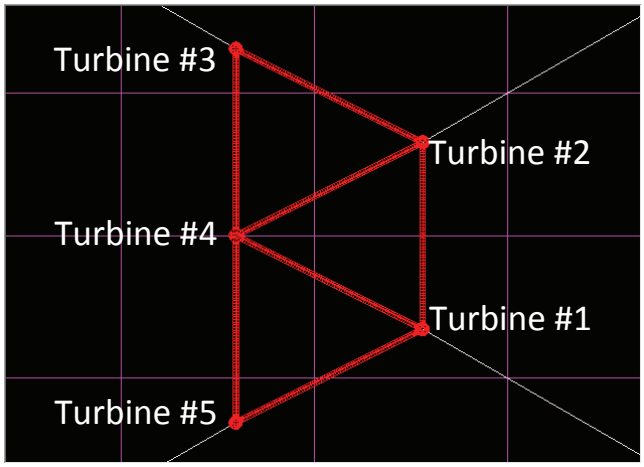

Figure 8.19 Turbine location (Rectangular platform)

Figure 8.19 shows the location of the five turbines. The fault turbine in this chapter is turbine #3 located at the upper front side of the platform. All other turbines remained intact during the whole simulation time of 1,000 seconds.

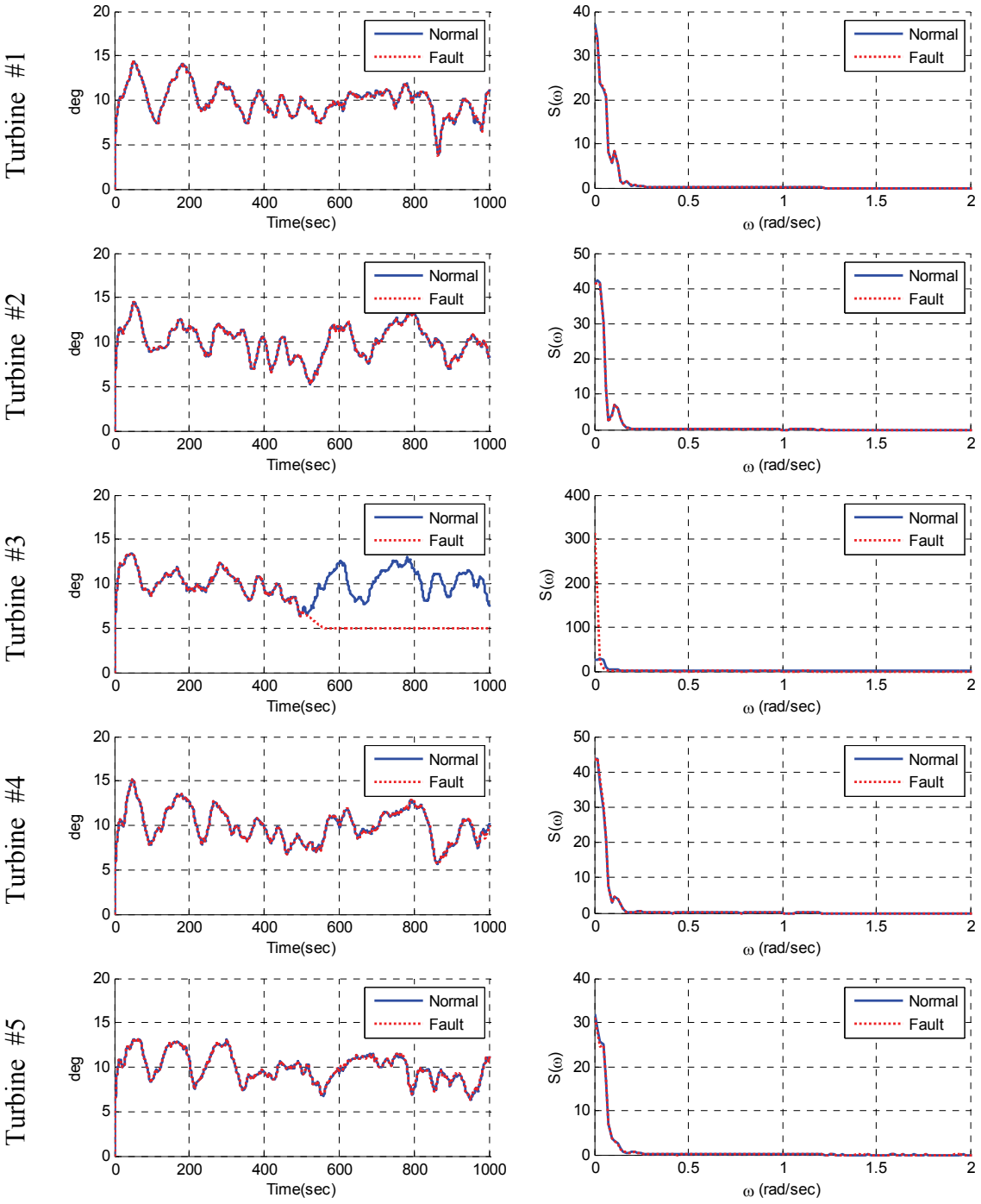

Figure 8.20 Blade pitch angle (a) and spectra (b) with blade control failure (Rectangular platform)

Figure 8.20 shows the change in the blade pitch angle of each turbine. It is seen that the pitch angle suddenly decreased 5 degrees at 500 seconds for turbine #3. All other turbines seemed to work normally even after the failure of turbine #3, but the trend of the pitch angle maneuvering after 500 seconds was slightly different from those of the normal case because all other turbines tried to compensate for the changes made by turbine #3.

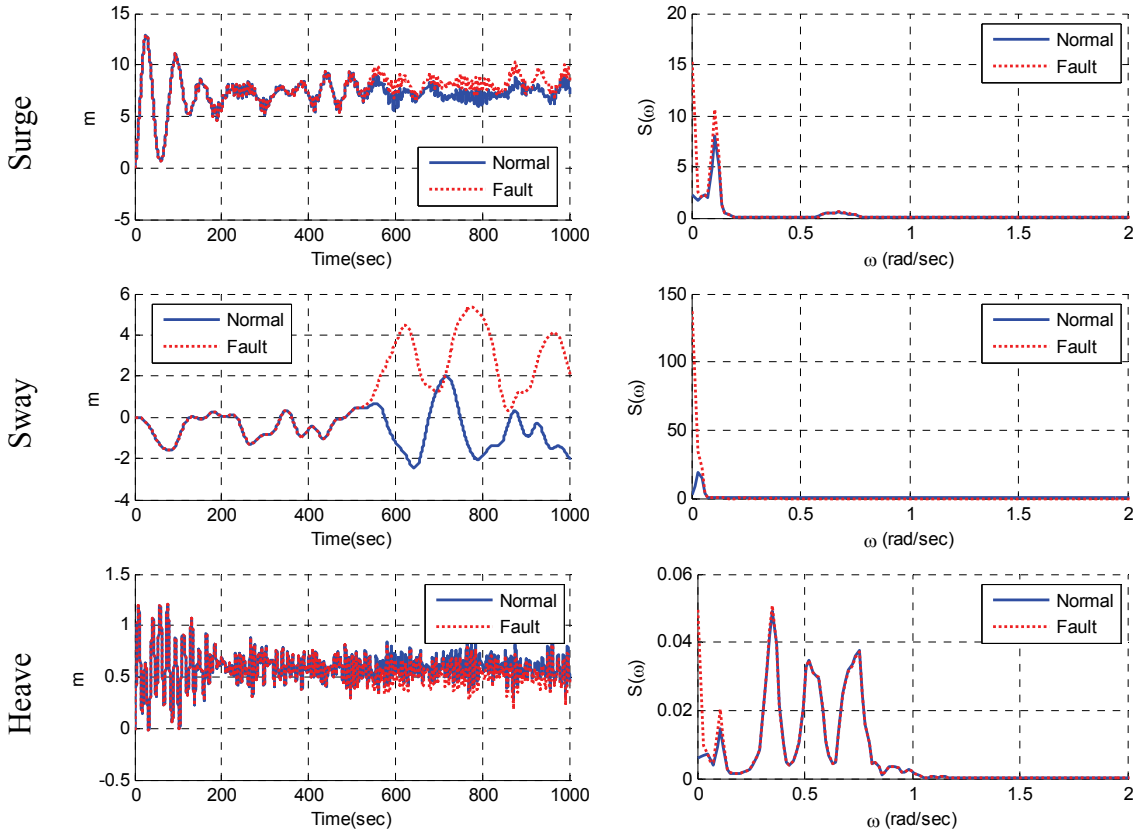

Figure 8.21 Platform translational motions (a) and spectra (b) with blade control failure (Rectangular platform)

Figures 8.21 ~ 8.22 show the overall platform responses after the failure event. In Figure 8.21, the platform sway shows a very rapid change from 0.33m to a maximum 5.38m after the failure event. Aside from the platform sway response, the maximum surge offset also increased from 9.21m to 10.29m due to the increased drag force from turbine #3.

Platform yaw changes after the failure event were also noticeable as can be seen in Figure 8.22. The yaw angle changed from -0.11 degrees at 500 seconds, and reached a minimum of -2.27 degrees in several minutes.

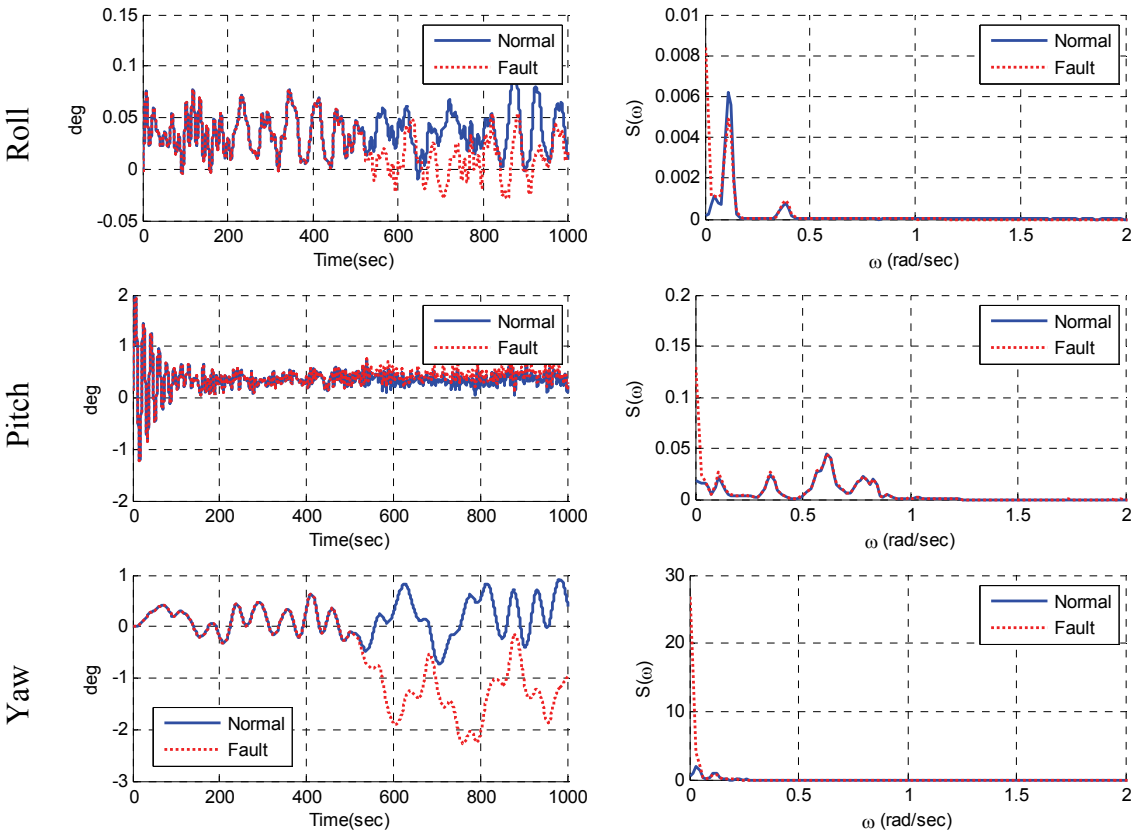

Figure 8.22 Platform rotational motions (a) and spectra (b) with blade control failure (Rectangular platform)

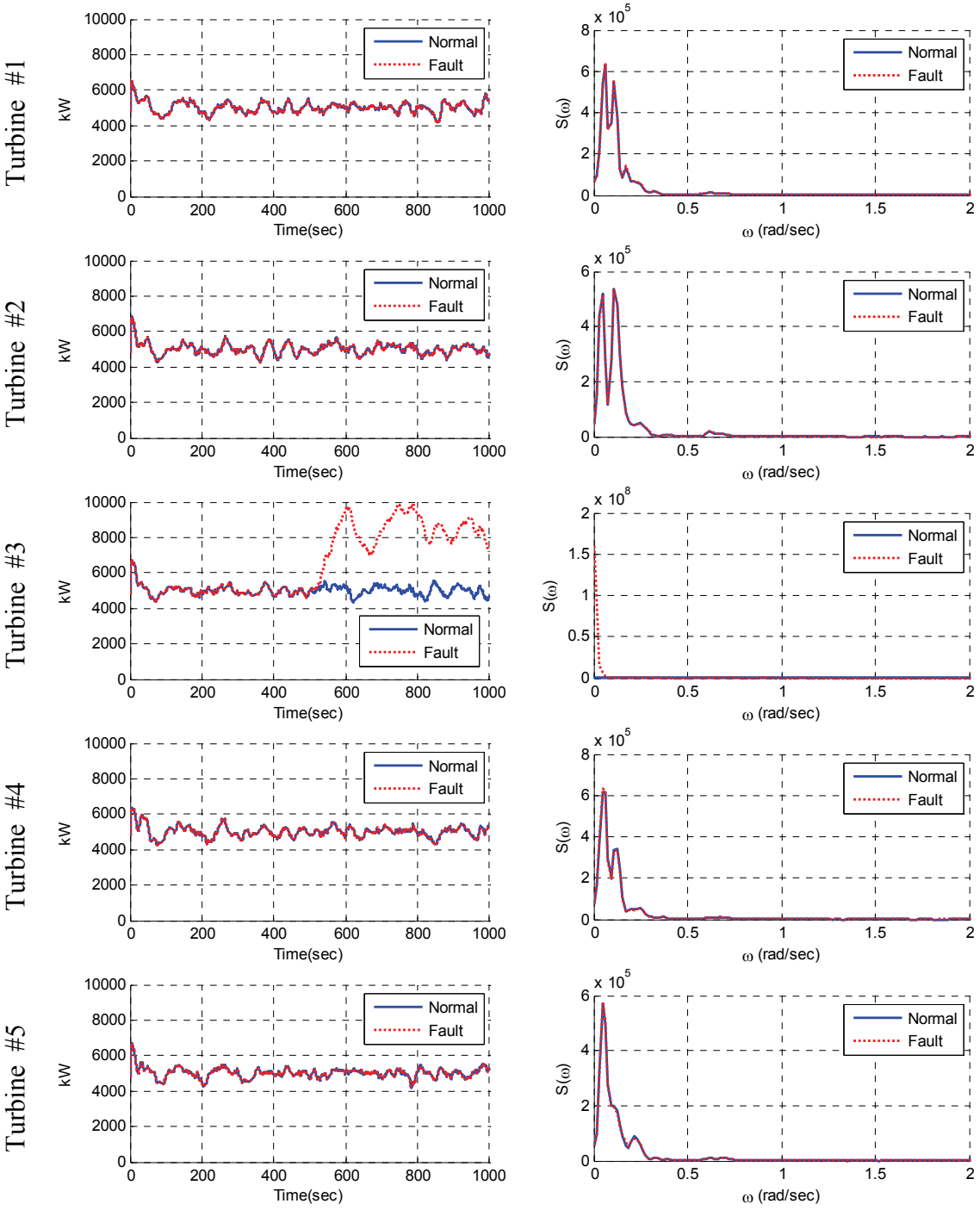

Figure 8.23 Generator power (a) and spectra (b) with blade control failure (Rectangular platform)

As pointed out in the previous chapter, the changes in yaw seem very small, approximately 2 ~ 3 degrees. However, this amount of yaw angle may induce appreciable changes in local structural responses. So, the overall balance of the MUFOWT system in terms of static and dynamic should be carefully checked in the design stage. Otherwise, a small problem in one turbine may affect the performance of the other turbines. To address these difficulties in system management, a more advanced turbine control method is necessary. For example, once unbalance of the platform is detected then control the blade pitch angle or rotor speed so that the system can minimize the loss of power production or reduce the local structural loadings.

As for the electric power output in Figure 8.23, all turbines except for #3 normally produced 5MW rated power during the entire simulation time, while turbine #3 produced very high electric power up to 10MW after locking the blade pitch angle. This change in electric power was primarily due to the fast rotation of the rotor due to the small blade pitch angle. However, this variation in electric power is unrealistic, and usually controlled by the shaft brake or tip brake. Otherwise, mechanical or electrical damage may occur and the entire system will be seriously damaged or may collapse.

The responses of the tower base force and moment were also checked as shown in Figures 8.24 ~ 8.26. As expected, the fore-aft shear forces and bending moments at the tower base in Figures 8.24 and 8.25 for turbine #3 increased appreciably due to the increased drag from the blades.

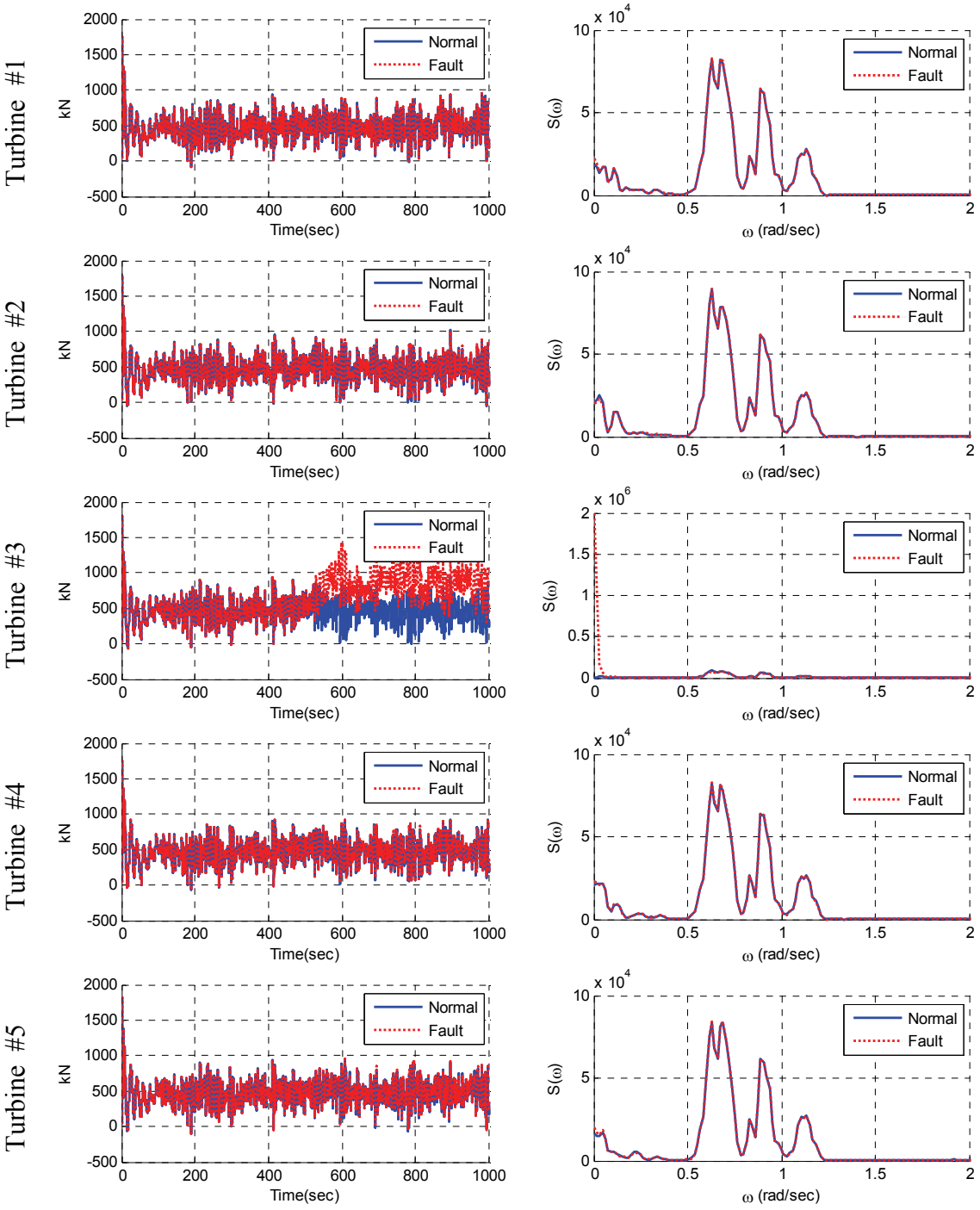

Figure 8.24 Tower base fore-aft shear force (a) and spectra (b) with blade control failure (Rectangular platform)

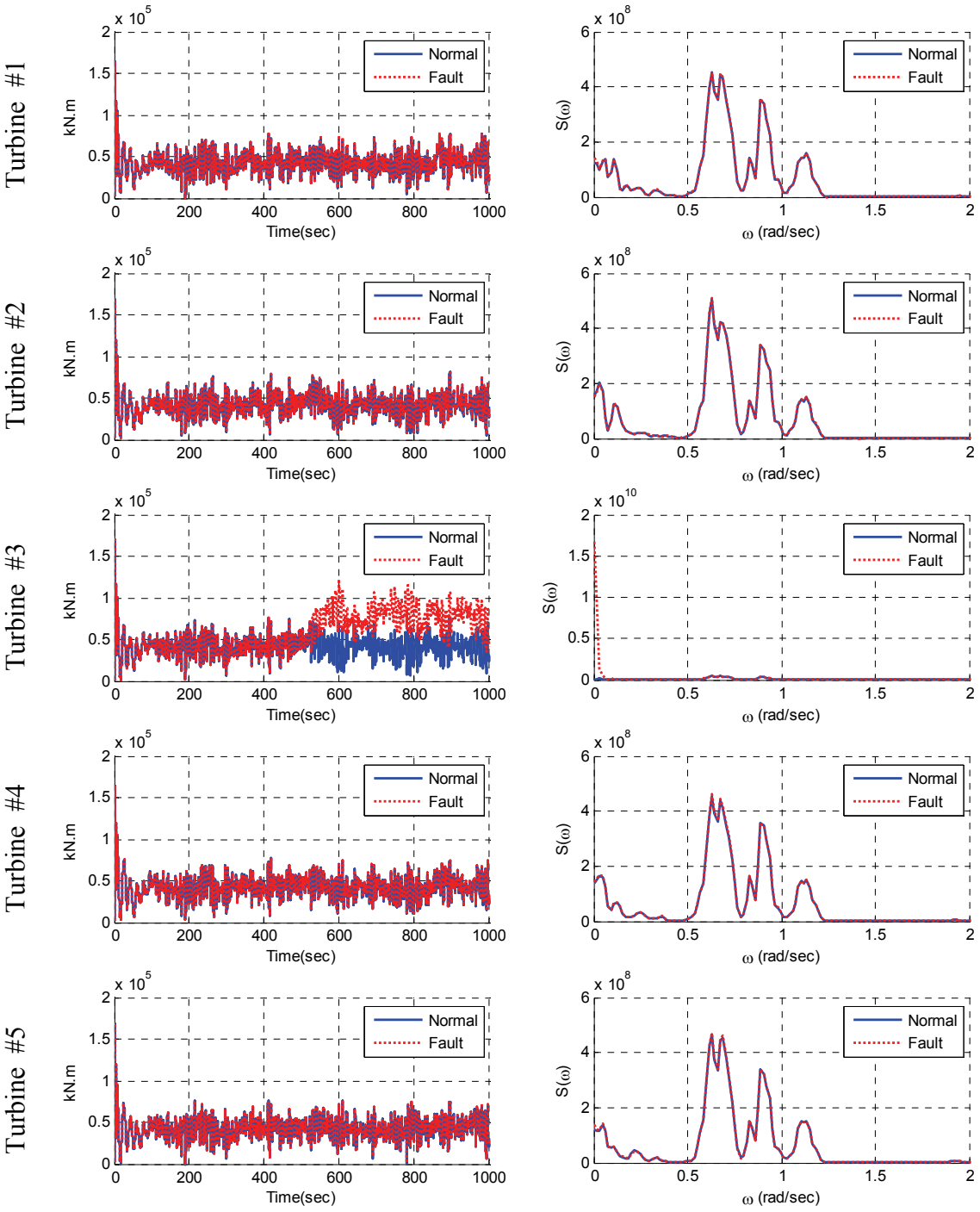

Figure 8.25 Tower base pitch moment (a) and spectra (b) with blade control failure (Rectangular platform)

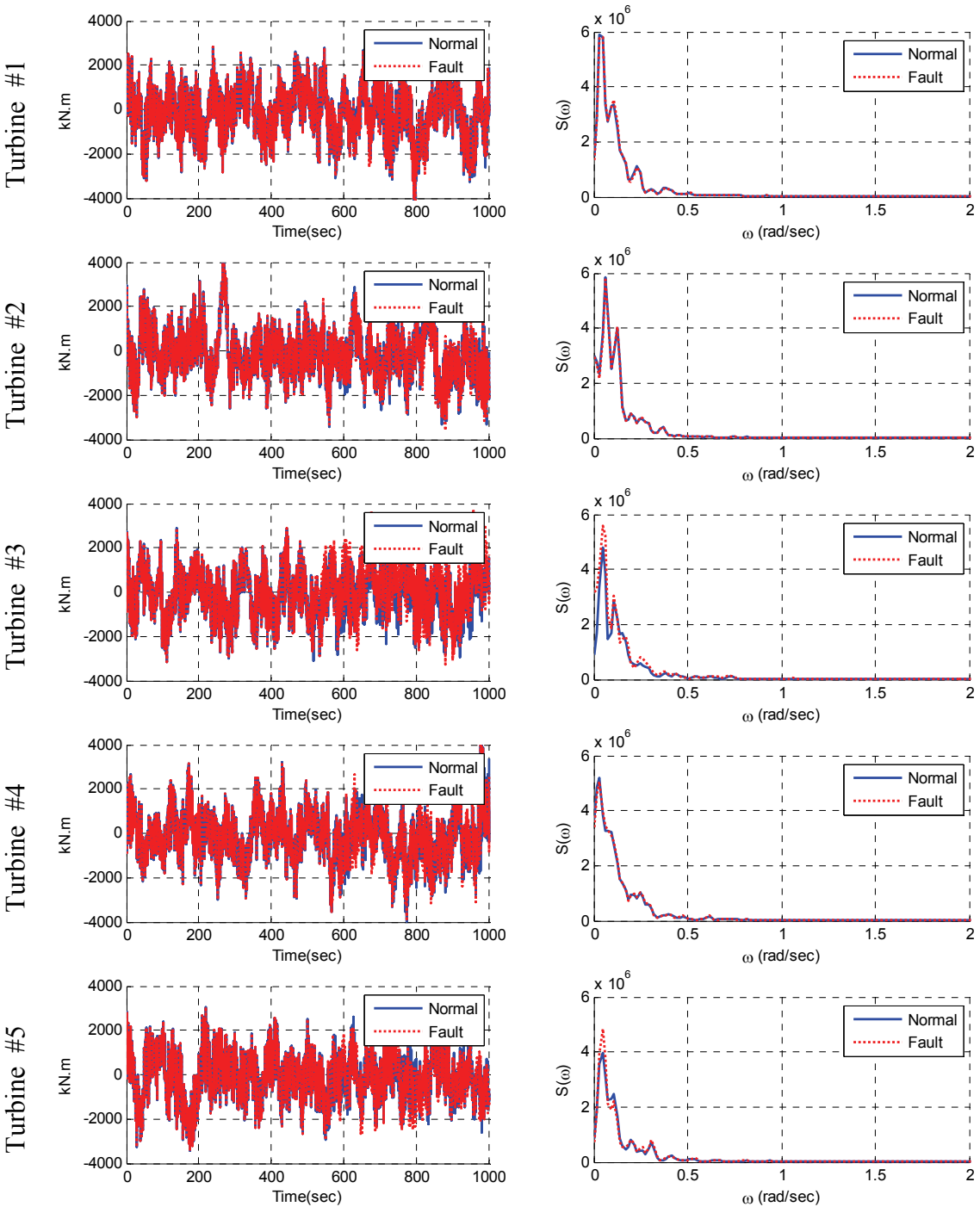

Figure 8.26 Tower base torsional moment (a) and spectra (b) with blade control failure (Rectangular platform)

For example, the mean tower base shear force of turbine #3 increased from 460.6 kN to 842.2 kN after the failure of the blade pitch control. This change is very critical for the structural integrity of the tower, and it may cause the collapse of the turbine tower.

Tower base torsional moment in Figure 8.26 shows that the changes after failure did not make a significant difference. The maximum moment of turbine #3 increased by 13.5% after the failure event; it was seen that this amount of change was relatively small compared to the responses presented earlier.

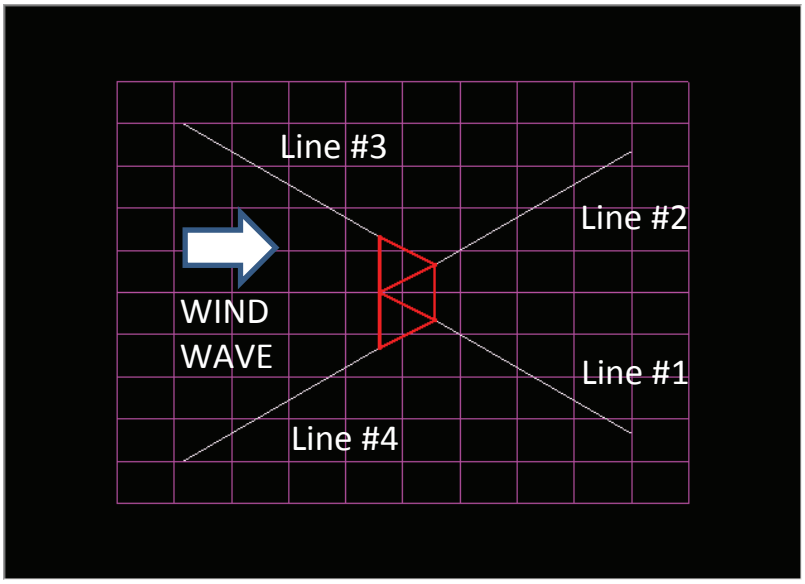

Figure 8.27 Top view of mooring-line arrangement (Rectangular platform)

When turbine #3 fails, the mooring line top tensions are also affected by that emergency. Since the blade pitch angle of turbine #3 is assumed to be decreased, the total aero dynamic force on this turbine is increased, and the platform yaw moment is induced. As a result, the mean top tensions of lines #1 and #3 in Figure 8.27 are

noticeably increased while the top tension of line #2 is reduced because of the shortened length between the fairlead and anchor position. The maximum top tension of line #1 increased from 1,299 kN to 1,410 kN and that of line #3 increased from 3,008 kN to 3,361 kN after the failure event. On the contrary, the maximum top tension of line #2 decreased from 1,351 kN to 1,234 kN. The time series and its spectra are presented in Figure 8.28.

In the case of line #4, the mean top tension slightly increased after the failure event due to the combination of larger surge drift and backward motion due to the negative platform yaw. Thus, the variations of mooring line top tensions in an emergency situation are very difficult to estimate without this numerical analysis tool for MUFOWT.

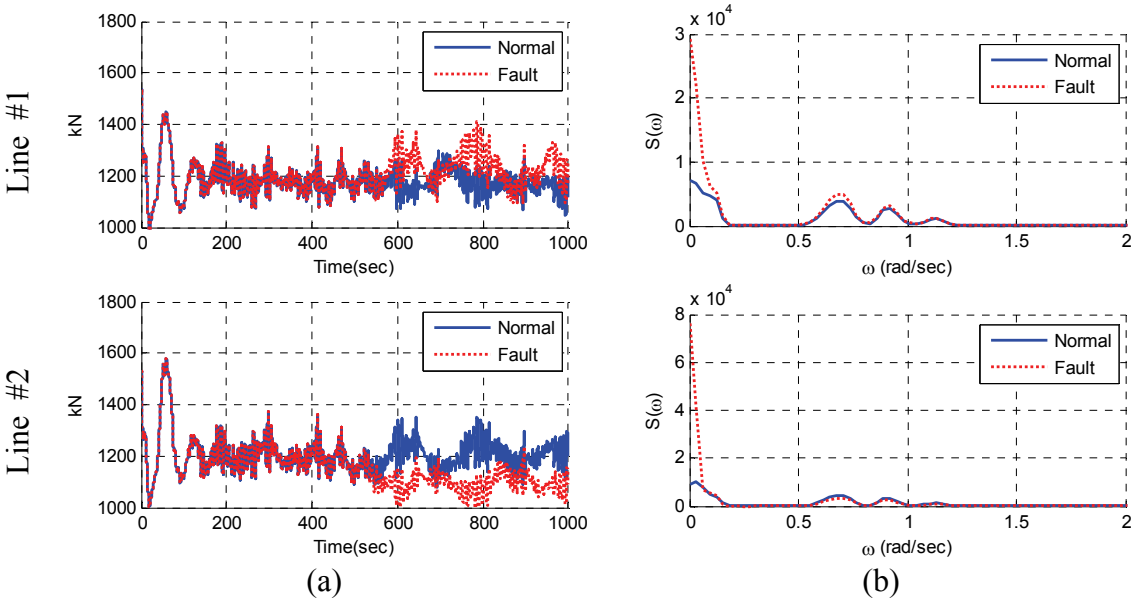

Figure 8.28 Top-tension (a) and spectra (b) with blade control failure (Rectangular platform)

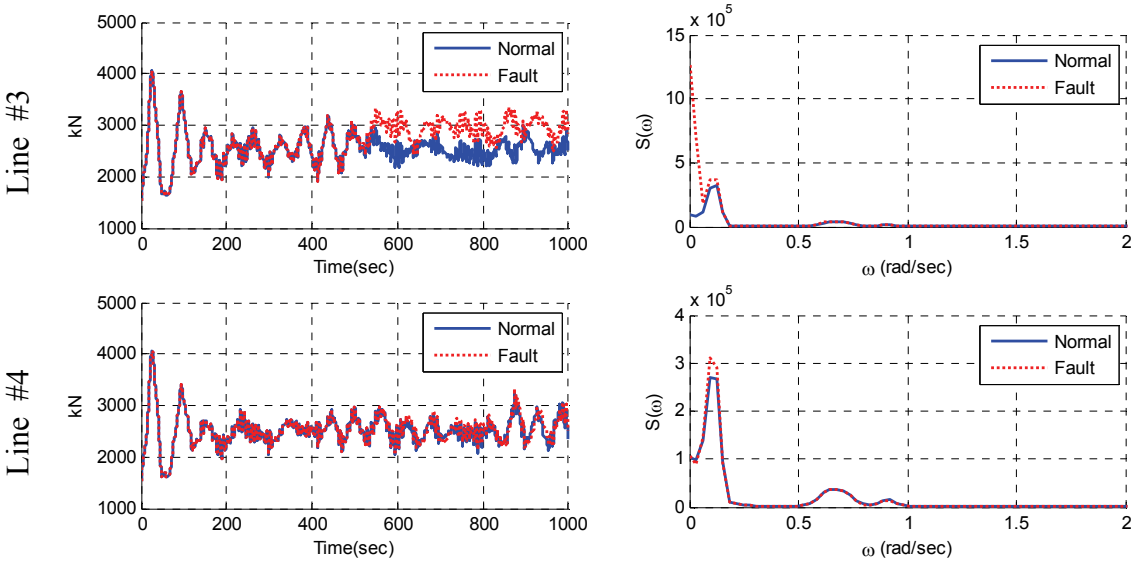

Figure 8.28 Continued

8.6 Discussion

So far, the coupled dynamic analysis of the five-turbine MUFOWT has been designed and analyzed in this chapter. This semi-submersible platform was equipped with five 5MW baseline turbines so the total rated power of this unit is equivalent to 25MW. The hydrostatic equilibrium was carefully checked by rigorous calculations of the mass properties of turbine and platform. The natural frequencies of the 6-DOFs of platform mode were obtained from the free decay test which revealed that the platform is well designed for the wind, wave environment. In normal operational conditions, the platform and turbine responses seemed to be stable and the power production of all turbines looked normal. The overall performance of MUFOWT with one turbine failure event is also investigated. If one of the turbines does not work normally, then the overall aerodynamic equilibrium cannot be guaranteed. As a result, unexpected platform yaw

moment is induced, and the turbine local structural loads can either be increased or decreased depending on the failure event. This failure also affects the mooring line top tensions. Depending on the mooring line arrangement and the direction of platform offset, the mooring line can be more taut or slackened as presented in this study.

9. CONCLUSION AND FUTURE WORK

9.1 Coupled Dynamic Analysis of MUFOWT

So far, most offshore wind turbine research has been limited to fixed towers in shallow-water areas. This study investigated a floating offshore wind turbine that can be used in deeper waters. The numerical tool combined with CHARM3D was able to analyze rotor-floater-tether coupled nonlinear dynamics in the time domain and was used for floater-motion, tower-acceleration and mooring-line-tension simulations in a collinear wind-wave environment. The coupled analysis has included time-varying aerodynamic loading, tower-blade elastic deformation, blade-control-induced loading, and gyroscopic effect in analyzing the global dynamics of the entire system. As a simple case study, the rotor-floater coupling effects of the Hywind spar were assessed through comparisons with the results of an uncoupled analysis in which the whole body was treated as a rigid body. The influence of control strategies were also simulated and reviewed.

The development of a numerical analysis tool for MUFOWT was one of the most challenging aspects of this study. One of the most popular wind turbine simulation tools 'FAST' was limited to a land-based turbine or single-turbine floating platform. Even so, various floating platforms including TLP, Spar, barge and semi-submersible were tested and performances were evaluated with this tool. To analyze multiple turbines on one floating platform, significant modification of current tools was required and was successfully done throughout this study.

The development of new analysis tools for MUFOWT started from the single turbine analysis tool FAST. It was then expanded to include a number of turbine variables and functions. In addition, the aerodynamic calculation module should also be expanded to calculate the aerodynamic loadings on different turbines. Above all, the design of the global matrix and forcing function of MUFOWT was the most important work. Based on the formation of a single turbine matrix, the global matrix for one floating platform with multiple turbines was suggested and implemented in this research. Similarly, the forcing function for MUFOWT was also designed and included. To evaluate this developed tool, two semi-submersible types of floating platforms with three and five turbines were proposed and analyzed. System identification work with a free decay test was conducted in advance followed by a time marching simulation with the wind, wave environment. All the dynamic aspects of multiple turbines with a floating platform were effectively captured with this numerical tool and the design of a semi-submersible platform was also validated.

9.2 Future Work

One of the important limitations of this study is the consideration of interference effects between adjacent turbines. Numerically, those effects cannot be included at this moment because the wake and turbulence wind field made by the rotor blade and the influence on the other rotating blade is difficult to measure with the current technology. Instead, the location of multiple turbines on one floating platform was carefully selected so that the shade effect was minimized. In the future, when more advanced aerodynamic

computations are available including the shade and interference effect, this tool can more accurately treat the dynamic aspects of MUFOWT. Furthermore, the floating platform can be also modeled as an elastic body. The current platform has only 6 degrees of freedom for translational and rotational motion, but as the platform gets bigger, the elastic modes of the platform should also be considered. Eventually, the fully coupled turbine-elastic platform-mooring can be utilized for the analysis of MUFOWT.

The development of remote structural health monitoring systems for MUFOWT can be also promoted using currently developed tools because the various scenarios of floating platform and multiple-turbine responses can be utilized as a database system using the simulation results. For example, the abnormal signal from the unmanned MUFOWT system can be detected by a monitoring system and a remote operator can analyze the specific problems of the turbine system using the generated database.

REFERENCES

Bae, Y.H., Kim, M.H., Shin, Y.S. 2010. Rotor-floater-mooring coupled dynamic analysis of mini TLP-type offshore floating wind turbines. In: Proceedings of the ASME 2010 29th International Conference on Ocean, Offshore and Arctic Engineering, Shanghai, China.

Bae, Y.H., Kim, M.H., 2011. Rotor-floater-mooring coupled dynamic analysis of mono-column-TLP-type FOWT (Floating Offshore Wind Turbine). J. Ocean Systems Engineering 1 (1), 95-111.

Bae, Y.H., Kim, M.H., Im, S.W., Chang, I.H. 2011a. Aero-elastic-control-floater-mooring coupled dynamic analysis of floating offshore wind turbines. In: Proceedings of the 21st (2011) International Offshore and Polar Engineering Conference, Hawaii, USA.

Bae, Y.H., Kim, M.H., Yu, Q., Kim, K. 2011b. Influence of control strategy to FOWT hull motions by aero-elastic-control-floater-mooring coupled dynamic analysis. In: Proceedings of the 21st (2011) International Offshore and Polar Engineering Conference, Hawaii, USA.

Barltrop, N., 1993. Multiple unit floating offshore wind farm. J. Wind Engineering 17 (4), 183-188.

Barthelmie, R., Frandsen, S., Rathmann, O., Hansen, K., Politis, E., Prospathopoulos, J., Cabezón, D., Rados, K., van Der Pijl, S., Schepers, J. 2008. Flow and wakes in large wind farms in complex terrain and offshore. In: Proceedings of the European Wind Energy Conference, Brussels, Belgium.

Barthelmie, R., Frandsen, S., Hansen, K., Schepers, J., Rados, K., Schlez, W., Neubert, A., Jensen, L., Neckelmann, S. 2009. Modelling the impact of wakes on power output at Nysted and Horns Rev. In: Proceedings of the European Wind Energy Conference, Marseille, France.

Butterfield, C.P., Musial, W., Jonkman, J., Sclavounos, P., Wayman, L., 2007. Engineering challenges for floating offshore wind turbines. National Renewable Energy Laboratory, Golden, CO.

Garrett, D., 1982. Dynamic analysis of slender rods. J. Energy Resources Technology 104, 302-306.

Global Energy Concepts, AWS Truewind LLC, 2005. Wind power project site : Identification and land requirements. NYS Energy Research & Development Authority, Albany, NY.

Henderson, A.R., Patel, M.H., Halliday, J.A., Watson, G.M. 1999. Multiple turbine floating offshore windfarms. In: Proceedings of the European Wind Energy Conference, Nice, France.

Henderson, A.R. 2000. Analysis tools for large floating offshore wind farms. Doctoral dissertation, University College London.

Henderson, A.R., Watson, G.M., Patel, M.H., Halliday, J.A. 2000. Floating offshore wind farms - an option? In: Proceedings of the Offshore Wind Energy in Mediterranean and Other European Seas, Siracusa, Sicilia, Italy.

Henderson, A.R., Leutz, R., Fujii, T. 2002. Potential for floating offshore wind energy in Japanese waters. In: Proceedings of the 12th (2002) International Offshore and Polar Engineering Conference, Kitakyushu, Japan.

Henderson, A.R., Patel, M.H., 2003. On the modelling of a floating offshore wind turbine. J. Wind Energy 6 (1), 53-86.

Henderson, A.R., Zaaijer, M., Bulder, B., Pierik, J., Huijsmans, R., van Hees, M., Snijders, E., Wijnants, G.H., Wolf, M.J. 2004. Floating windfarms for shallow offshore sites. In: Proceedings of the 14th (2004) International Offshore and Polar Engineering Conference, Toulon, France.

Ivanell, S., Sørensen, J., Henningson, D., 2007. Numerical computations of wind turbine wakes, Wind Energy : Proceedings of the Euromech Colloquium. Springer Berlin Heidelberg, 259-263.

Jagdale, S., Ma, Q. 2010. Practical simulation on motions of a TLP-type support structure for offshore wind turbines. In: Proceedings of the 20th (2010) International Offshore and Polar Engineering Conference, Beijing, China.

Jonkman, B.J., 2009. TurbSim user's guide: Version 1.50. National Renewable Energy Laboratory, Golden, CO.

Jonkman, J.M., 2003. Modeling of the UAE Wind Turbine for Refinement of FAST_AD. National Renewable Energy Laboratory, Golden, CO.

Jonkman, J.M., Buhl Jr, M.L., 2005. FAST user's guide. National Renewable Energy Laboratory, Golden, CO.

Jonkman, J.M., Sclavounos, P.D. 2006. Development of fully coupled aeroelastic and hydrodynamic models for offshore wind turbines. Paper presented at the 44th AIAA Aerospace Sciences Meeting and Exhibit, Reno, NV.

Jonkman, J.M., 2007. Dynamics modeling and loads analysis of an offshore floating wind turbine. National Renewable Energy Laboratory, Golden, CO.

Jonkman, J.M., 2008. Influence of control on the pitch damping of a floating wind turbine. National Renewable Energy Laboratory, Golden, CO.

Jonkman, J.M., 2010. Definition of the Floating System for Phase IV of OC3. National Renewable Energy Laboratory, Golden, CO.

Kane, T.R., 1961. Dynamics of Nonholonomic Systems. J. Applied Mechanics 28, 574-578.

Kim, M.H., Yue, D.K.P., 1991. Sum-and difference-frequency wave loads on a body in unidirectional Gaussian seas. J. Ship Research 35 (2), 127-140.

Kim, M.H., Ran, Z., Zheng, W., Bhat, S., Beynet, P. 1999, Mar. Hull/mooring coupled dynamic analysis of a truss spar in time domain. In: Proceedings of the 9th (1999) International Offshore and Polar Engineering Conference, Brest, France.

Kim, M.H., Tahar, A., Kim, Y.B. 2001. Variability of TLP motion analysis against various design methodologies/parameters. In: Proceedings of the 11th (2001) International Offshore and Polar Engineering Conference, Vol Iii, Stavanger, Norway.

Larsen, T.J., Hanson, T.D., 2007. A method to avoid negative damped low frequent tower vibrations for a floating, pitch controlled wind turbine. J. Physics: Conference Series 75, 012073.

Lee, C., Newman, J., Kim, M., Yue, D. 1991. The computation of second-order wave loads. In: Proceedings of the 10th International Conference on Offshore Mechanics and Arctic Engineering, Stavanger, Norway.

Lefranc, M., Torud, A. 2011. Three wind turbines on one floating unit, feasibility, design and cost. In: Proceedings of the Offshore Technology Conference, Houston, TX.

Malcolm, D., Hansen, A., Concepts, G.E., 2002. WindPACT Turbine Rotor Design Study: June 2000-June 2002. National Renewable Energy Laboratory, Golden, CO.

Manjock, A., 2005. Design codes FAST and ADAMS for load calculations of onshore wind turbines. Germanischer Lloyd WindEnergie GmbH.

Mikkelsen, R. 2003. Actuator disc methods applied to wind turbines. Doctoral dissertation, Technical University of Denmark.

Morison, J.R., Johnson, J., Schaaf, S., 1950. The force exerted by surface waves on piles. J. Petroleum Technology 2 (5), 149-154.

Musial, W.D., Butterfield, S., Boone, A. 2004. Feasibility of floating platform systems for wind turbines. Paper presented at the 42nd AIAA Aerospace Sciences Meeting and Exhibit, Reno, NV.

Nielsen, F.G., Hanson, T.D., Skaare, B. 2006. Integrated dynamic analysis of floating offshore wind turbines. In: Proceedings of the 25th International Conference on Offshore Mechanics and Arctic Engineering, Hamburg, Germany.

Rados, K., Larsen, G., Barthelmie, R., Schlez, W., Lange, B., Schepers, G., Hegberg, T., Magnisson, M., 2001. Comparison of wake models with data for offshore windfarms. J. Wind Engineering 25 (5), 271-280.

Ran, Z., Kim, M.H., Zheng, W., 1999. Coupled dynamic analysis of a moored spar in random waves and currents (time-domain versus frequency-domain analysis). J. Offshore Mechanics and Arctic Engineering 121, 194.

Roddier, D., Cermelli, C., Weinstein, A. 2009. Windfloat: A floating foundation for offshore wind turbines part I: Design basis and qualification process. In: Proceedings of the ASME 28th International Conference on Ocean, Offshore and Arctic Engineering, Hawaii, USA.

Shim, S., Kim, M.H. 2008. Rotor-floater-tether coupled dynamic analysis of offshore floating wind turbines. In: Proceedings of the 8th (2008) International Offshore and Polar Engineering Conference, Vancouver, Canada.

Tahar, A., Kim, M.H., 2003. Hull/mooring/riser coupled dynamic analysis and sensitivity study of a tanker-based FPSO. J. Applied Ocean Research 25 (6), 367-382.

Tong, K.C., 1998. Technical and economic aspects of a floating offshore wind farm. J. Wind Engineering and Industrial Aerodynamics 74-6, 399-410.

Wayman, E.N., Sclavounos, P.D., Butterfield, S., Jonkman, J., Musial, W. 2006. Coupled Dynamic Modeling of Floating Wind Turbine Systems. In: Proceedings of the Offshore Technology Conference, Houston, TX.

Wilson, B., Walker, S., Heh, P., 2000. FAST_AD advanced dynamics code. Technical Report OSU/NREL REPORT 99-01, NREL, Oregon State University, Corvallis, OR.

Wilson, R., Freeman, L., Walker, S., 1995. FAST2 Code validation. J. Wind Energy 16, 263-267.

Withee, J.E. 2004. Fully coupled dynamic analysis of a floating wind turbine system. Doctoral dissertation, Massachusetts Institute of Technology.

Yang, C.K., Kim, M.H., 2010. Transient effects of tendon disconnection of a TLP by hull-tendon-riser coupled dynamic analysis. J. Ocean Engineering 37 (8-9), 667-677.